NASA CR-179508

THERMAL BARRIER COATING LIFE PREDICTION MODEL DEVELOPMENT SECOND ANNUAL REPORT

Written by J.T. DeMasi
Approved by Dr. K.D. Sheffler

UNITED TECHNOLOGIES CORPORATION
Pratt & Whitney Group
Engineering Division

Prepared for
NATIONAL AERONAUTICS AND SPACE ADMINISTRATION

NASA LEWIS RESEARCH CENTER
21000 BROOKPARK ROAD
CLEVELAND, OHIO 44135

CONTRACT NAS3-23944

NASA

1.REPORT NO. CR-179508	2. GOVERNMENT AGENCY	3.RECIPIENT'S CATALOG NO.
4.TITLE AND SUBTITLE Thermal Barrier Coating Life Prediction Model Development		5. REPORT DATE April 1986 6. PERFORMING ORG. CODE
7.AUTHOR APPROVED BY: Jeanine T. DeMasi, Kjeth D. Sheffler		8. PERFORMING ORG. REPT. NO.
9.PERFORMING ORG. NAME AND ADDRESS UNITED TECHNOLOGIES CORPORATION Pratt & Whitney Engineering Division		10. WORK UNIT NO. 11. CONTRACT OR GRANT NO. NAS3-23944
12. SPONSORING AGENCY NAME AND ADDRESS National Aeronautics and Space Administration Lewis Research Center 21000 Brookpark Road, Cleveland, Ohio 44135		13. TYPE REPT./PERIOD COVERED Annual Report (Second) 14. SPONSORING AGENCY CODE

15. SUPPLEMENTARY NOTES
Project Manager: Dr. Robert A. Miller
NASA Lewis Research Center, Cleveland, Ohio

16. ABSTRACT

The objective of this program is to establish a methodology to predict thermal barrier coating life in an environment simulative of that experienced by gas turbine airfoils. Critical experiments were conducted to determine important failure modes of the thermal barrier coating. Analytical studies coupled with appropriate physical and mechanical property determinations were employed to derive a life prediction model relative to the predominant failure mode(s).

A review of experimental and flight service components as well as laboratory post evaluations indicates that the predominant mode of TBC failure involves thermo-mechanical spallation of ther ceramic coating layer. This ceramic spallation involves the formation of a dominant crack in the ceramic coating parallel to and closely adjacent to the topologically complex metal ceramic interface. This "mechanical" failure mode clearly is influenced by thermal exposure effects as shown by results of experiments conducted to study thermal pre-exposure and thermal cycle-rate effects.

17. KEY WORDS (SUGGESTED BY AUTHOR(S))	18. DISTRIBUTION STATEMENT
Thermal Barrier Coating Failure Mechanisms Life Prediction	

19. SECURITY CLASS THIS (REPT)	20. SECURITY CLASS THIS (PAGE)	21. NO. PGS	22. PRICE *
Unclassified	Unclassified	211	

* For sale by the National Technical Information Service, Springfield, VA 22161

16. ABSTRACT (continued)

The preliminary life prediction model developed focuses on the two major damage modes identified in the critical experiments task. The first of these involves a mechanical driving force, resulting from cyclic strains and stresses caused by thermally induced and externally imposed mechanical loads. The second is an environmental driving force based on experimental results, is believed to be related to bond coat oxidation. It is believed that the growth of this oxide scale influences the intensity of the mechanical driving force.

FOREWORD

The Second Annual Report contained in this document covers the activities performed during the second year of the NASA HOST Program, "Thermal Barrier Coating Life Prediction Model Development", under Contract NAS3-23944. The objective of this effort is to develop and verify Thermal Barrier Coating life prediction technology for gas turbine hot section components. The NASA program manager is Dr. Robert A. Miller. The program is being conducted in the Pratt & Whitney Materials Engineering and Research Laboratory under the direction of Mr. Allan H. Hauser. The Pratt & Whitney Project Manager is Dr. Keith D. Sheffler and the principal investigator is Jeanine DeMasi. Mr. Thomas Hajek serves as the Analytical Manager charged to this program. Mr. Milton Ortiz serves as the analytical investigator and is responsible for analytical modeling efforts. A note of thanks to Mr. Frederick Kopper and Leon Matysuk for the analytical efforts made early in this program. A substantial portion of the modeling effort is being conducted under sub-contract at the Southwest Research Institute, San Antonio, Texas, under the direction of Dr. Thomas A. Cruse. Substantial program contributions in the areas of structural interpretation and test instrumentation were made by Mr. Neal P. Anderson, Mr. Merritt Wight, and Mr. Russell Shenstone. Special thanks to Mr. Raymond Skurzeuski, Mr. Claude Clavette, Mr. Frederick Wiese and Mr. Arnold LaPete for their efforts in specimen preparation and testing.

TABLE OF CONTENTS

TABLE OF CONTENTS (Continued)

LIST OF ILLUSTRATIONS

LIST OF ILLUSTRATIONS (Continued)

LIST OF ILLUSTRATIONS (Continued)

LIST OF ILLUSTRATIONS (Continued)

LIST OF ILLUSTRATIONS (Continued)

LIST OF ILLUSTRATIONS (Continued)

LIST OF ILLUSTRATIONS (Continued)

LIST OF ILLUSTRATIONS (Continued)

LIST OF ILLUSTRATIONS (Continued)

LIST OF TABLES

LIST OF TABLES (Continued)

1.0 SUMMARY

The goals of this program are to identify and understand TBC failure modes, generate quantitative TBC life data, and developed and verify a TBC life prediction model.

The coating being studied on this program is a two layer thermal barrier system incorporating a nominal ten mil outer layer of seven percent yttria partially stabilized zirconia plasma deposited over an inner layer of highly oxidation resistant low pressure plasma sprayed NiCoCrAlY bond coating. This coating, designated PWA264, currently is in flight service on a number of stationary turbine components in Pratt & Whitney Commercial engines.

An initial review of experimental and flight service components indicates that the predominant mode of TBC failure involves thermomechanical spallation of the ceramic coating layer. This ceramic spallation involves the formation of a dominant crack in the ceramic coating parallel to and closely adjacent to the metal-ceramic interface.

Results from a laboratory test program designed to study the influence of various "driving forces" such as temperature, thermal cycle frequency, environment, coating thickness, etc. on ceramic coating spalling life suggest that bond coat oxidation damage at the metal-ceramic interface contributes significantly to thermomechanical cracking in the ceramic layer. Low cycle rate furnace testing in air and in argon clearly shows a dramatic increase of spalling life in a non-oxidizing environment. Elevated temperature pre-exposure of TBC specimens in air causes a proportionate reduction of cyclic thermal spalling life, whereas pre-exposure in argon does not.

Interrupted cyclic thermal exposure (burner rig) testing showed that thermo mechanical ceramic spallation is a progressive damage mode. Subcritical microcrack link-up is proposed as the mode of failure. Initial metallographic observations showed major subcritical cracking initiating above the metal-ceramic interface and not at the bond-coat asperities which are inherent in the TBC system being studied. Since early experimental results showed that bond coat oxidation is a significant factor in the cyclic spalling life of the ceramic coating it is assumed that this environmental driver magnifies the mechanical driving force due to thermal loading in the burner rig.

Mechanical property tests show that the bulk as-plasma sprayed 7w/o Y_2O_3 $-ZrO_2$ exhibits a highly non linear stress strain response in pure tension and compression. Also, it was shown that this material exhibits a significant creep response. Low cycle fatigue characteristics were observed over a narrow stress range indicating that stress levels above a critical stress threshold will result in rapid damage accumulation. This result supports the model approach, which will be discussed in the proceeding paragraphs, and in itself is supported by the interrupted burner rig test metallographic observations.

The preliminary life prediction model developed focuses on the two major damage modes identified in the laboratory testing described above. The first of these modes involves a mechanical driving force, resulting from cyclic strains and stresses caused by thermally induced and externally imposed loads. The second is an environmental driving force which appears, based on the experimental results, to be related to "oxidation damage", due to the in-service growth of a NiCoCrAlY oxide scale at the metal-ceramic interface. Based on the apparently "mechanical" mode of ceramic failure, (near inter facial cracking), and on the difficulty in finding metallographic evidence of a direct physical link between the growing oxide scale and incipient cracking in specimens exposed to a relatively small fraction of expected life, it was elected to employ an existing phenominological fatigue model (Manson - Coffin) as the basis for the TBC life model. In traditional form, this model relates cyclic inelastic strain range to number of cycles to fatigue failure. The model does incorporate an environmental effect, in that the mechanical driver is analytically modified in such a way as to reduce the apparent fatigue strength of the ceramic layer. The use of inelastic strain range as a damage driver for the ceramic coating layer is considered justified in view of the previously mentioned nonlinearity observed in constitutive tests conducted on the material.

The mathematical form of the model is shown below and it expresses a relationship between the number of cycles, cyclic inelastic strain and bond coat oxide accumulation.

$$(\Delta\epsilon_i / \Delta\epsilon_f)^b = N$$

where $\Delta\epsilon_i$ = Total cyclic inelastic strain range
$\Delta\epsilon_f$ = failure strain

and $$\Delta\epsilon_i = \Delta(\alpha\Delta T) + \Delta\epsilon_c + \Delta\epsilon_h - 2(\sigma y.s./E)$$

The total cyclic inelastic strain $\Delta\epsilon_i$, is the sum of the $\Delta\alpha\Delta T$ strain plus the heat up and cool down strains, $\Delta\epsilon_h$ and $\Delta\epsilon_c$ respectively, due to the initial heat up and cool down transient part of the burner rig thermal cycle.

$$\Delta\epsilon_f = \Delta\epsilon_{fo}(1-\delta/\delta_c)^c + \Delta\epsilon_i(\delta/\delta_c)^d$$

The failure strain, $\Delta\epsilon_f$, is a function of the inelastic strain and is reduced by the strain due to the oxide thickness ratio, δ/δ_c, where δ_c is the critical oxide thickness which will cause ceramic failure in a single thermal cycle. The static failure strain, $\Delta\epsilon_{fo}$, is the strain required to fail the ceramic in the absence of bond coat oxidation.

For a mission comprised of n cycles, the damage accumulated by cyclic inelastic strain and oxide growth will equal 1/N. The Miner's Rule assumption is used in that failure of the TBC occurs when $1/N \geqslant 1.0$.

2.0 INTRODUCTION

Ceramic coatings have been utilized in aircraft gas turbine engines for over twenty years, primarily as an add-on technique to increase the durability of already reliable coatings. More recently, thermal barrier coating usage was extended to protect selected high pressure turbine components as well as combustors and augmentors. For these early turbine applications, no specific design methodology was needed, and coating lives (ceramic spalling resistance) were determined adequate (or not) based on experimental engine testing. Future applications for thermal barrier coatings, which emphasize performance improvement (as apposed to durability extension), will require more sophisticated design tools and lifetime prediction methods.

The objective of this program is to establish a methodology to predict thermal barrier coating life in an environment simulative of that experienced by gas turbine airfoils. Specifically, work is to be conducted to determine failure modes of thermal barrier coatings in the aircraft engine environment. Analytical studies coupled with appropriate physical and mechanical property determinations will be employed to derive coating life prediction model(s) for the important failure mode(s).

The program to accomplish these objectives is divided into two phases. Phase I (36 months) will be directed towards identification and modeling of the predominant failure mode(s), including verification. Phase II (24 months), which will proceed at the option of the government following the conclusion of Phase I, will develop and verify an integrated design capable life prediction model accounting for all important contributions to coating failure.

Phase I, which currently is in progress, includes the following three technical tasks, plus a fourth reporting task.

- Task I - The objective of this task is to identify the relative importance of various TBC degradation and failure modes, and to develop a preliminary life prediction model for further development Phase II. Specific modes to be addressed include degradation resulting from static and cyclic thermal exposure and hot corrosion.

- Task II - The objective of this task is to design, conduct and analyze experiments to obtain data for major mode life prediction model development. Design of the experiments will be based on results of Task I. Test parameters will be varied as appropriate to failure mode(s) being modeled to cover the range of parameters anticipated on thermal barrier coated turbine components. Transient thermal and stress analyses will be conducted for each test condition. The analytical results will be used to construct life prediction model(s) for the predominant mode(s).

- Task III - The validity of models developed in Task II will be assessed through a series of approved benchmark engine mission simulation tests. The basis for judgment of model validity shall be how closely the model predicts TBC life for each benchmark engine simulation test. Recommendations for further research or refinement required to arrive at a fully satisfactory engine life prediction methodology shall be made if necessary.

Phase II, if exercised, will include the following five technical tasks, plus a sixth reporting task.

- Task V - The objective of this task is to develop fracture and continuum mechanics life prediction models based on the design and performance of approved experiments to determine mechanical/material properties and analyze loads resulting from the coating deposition process and those that arise in service.

- Task VI - The objective of this task is to develop oxidation and hot corrosion failure models both under steady state and simulated engine conditions. Mechanical property implications of bond coat oxidation shall be determined to permit incorporation of oxidation response into an integrated life prediction model. A semi-empirical hot-corrosion model will be developed to include effects of corrodent infiltration and the dilation pressure produced by phase changes of the corrodent during temperature cycling.

- Task VII - The objective of this task is to design and conduct a series of experiments to develop a data base from which the erosion and foreign object damage models can be developed. Erosion test results will be extrapolated to construct a correlation model to predict TBC erosion life at typical operating conditions. The correlation shall include the velocity, temperature, erodent intensity, impingement angle and temperature-dependent ceramic properties. The degree to which the occurrence of an FOD incident reduces the life of the TBC will be predicted through development of a debit based life prediction model.

- Task IX - The objective of this task is to integrate the appropriate combinations of models into a comprehensive, design capable, causal, life prediction model. This model shall incorporate the sub-models having the best predictive capability for each failure mode. A modular structural design shall be used in constructing the integrated model for flexibility and ease of incorporation in available thermal and structural computer programs. The integrated models developed and a test plan for their verification shall be subject to NASA Project Manager approval before initiating Task X.

- Task X - The objective of this task shall be to verify the models proposed under simulated engine conditions including benchmark engine mission simulation tests. Based on these results a model or series of models will be recommended for adequate TBC life prediction as used in design engineering. The utility of the model shall be demonstrated by evaluating its applicability to design of a new hot section component. This demonstration will involve application of the model to an advanced turbine blade design to assess how overall life could be improved by the use of a TBC system. The blade design developed under NASA contract NAS3-23057 entitled "Preliminary Design of a Supersonic Aircraft High Pressure Turbine Program" shall be used. The study shall include the determination of the life fractions for each failure mode. Also, trade-off studies will be carried out to determine changes in the life distribution if the TBC was modified to eliminate certain failure modes.

3.0 PHASE I - FAILURE MODES ANALYSES AND MODEL DEVELOPMENT

The objectives of this phase are to identify thermal barrier coating degradation modes which lead to coating failure, to determine the relative importance of these degradation modes in aircraft engine applications, and to develop and verify life prediction model(s) for the predominant mode(s) of engine failure.

These objectives are being accomplished in three tasks. The objective of the first task is to identify and determine the relative importance of TBC failure modes, including development and verification of preliminary correlative life prediction model(s) for the predominant mode(s) of failure. The objective of the second task is to refine the model(s) developed in Task I, including generation of a substantial body of experimental failure data for model calibration. Additional data will be generated in the third task to verify the model(s) developed in Task II. A fourth reporting task also is included in Phase I of the program. Task I is substantially complete; results are discussed in detail in section 3.1. Task II has been initiated; the experimental approach and initial results obtained on this task are described in Section 3.2.

The thermal barrier coating being evaluated on all of these tasks is designated PWA 264. It consists of an air plasma sprayed 7 w/o Y_2O_3 - partially stabilized ZrO_2 layer and a low pressure chamber sprayed metallic inner layer. The ceramic outer layer is nominally 0.010 $\pm$0.002 inches thick, and is approximately 80% dense. The NiCoCrAlY inner layer is nominally fully dense and is 0.005 $\pm$ 0.001 inches thick with appropriate surface roughness. The TBC coating system is shown in Figure 1. The substrate alloy being used for this program is PWA 1455. It's composition as well as the NiCoCrAlY bond coat composition is shown in Table I.

TABLE I
NOMINAL COMPOSITION OF PROGRAM MATERIALS
(Weight Percent)

	Ni	Co	Cr	Al	Mo	Ta	Hf	Ti	B	C	Y
PWA 1455	Remainder	10.0	8.0	6.0	6.0	4.25	1.15	1.0	0.015	0.1	-
PWA 1376	Remainder	22	18	12	-	-	-	-	-	-	0.4

3.1 Task I - Failure Mechanism Determination

The objectives of this task were to identify thermal barrier coating degradation modes which lead to coating failure, to determine the relative importance of these modes in aircraft engine applications, and to develop and verify preliminary correlative life prediction model(s) for the predominant failure mode(s).

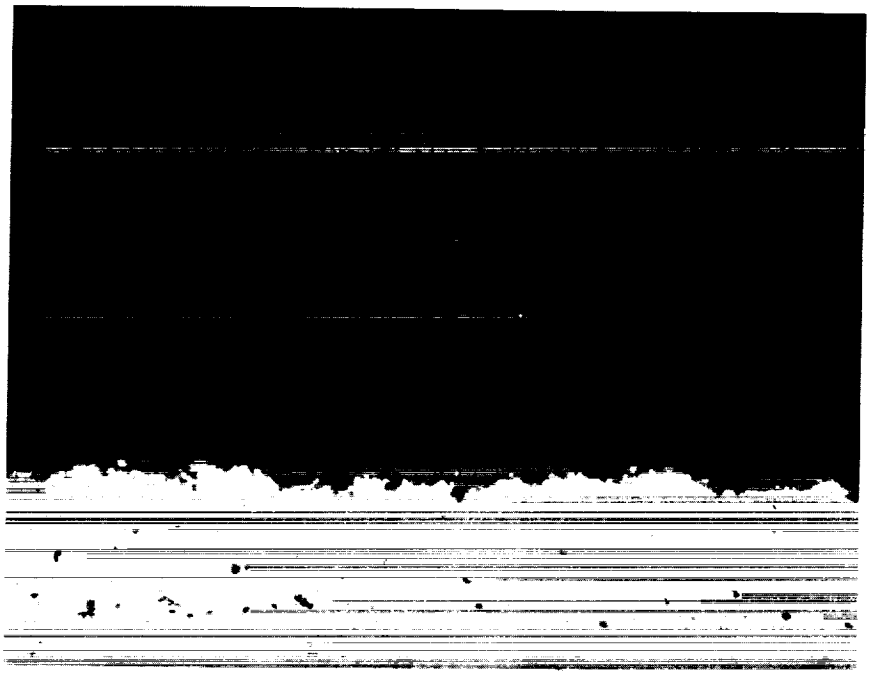

Pre-Test 200X

Figure 1 Thermal Barrier Coating System Microstructure

The approach to accomplish these objectives included an initial review of the thermal barrier coating literature and of Pratt & Whitney engine experience with thermal barrier coated turbine components to identify potential modes of thermal barrier coating degradation and to determine which of these modes appear to predominate in engine service (Task IA). This review has been completed, and results have been used to establish a laboratory simulative engine test program (Task IB). Results of this test program were used to critically assess the relative importance of various degradation modes as they relate to coating service life. Also included in Task IB was a subtask to measure physical and mechanical properties of coating system materials which were required for analytical modeling and preliminary correlative life prediction system development which was conducted in the first part of Task IC. This effort was followed by additional laboratory testing to verify the preliminary model and to provide a basis for model refinement in Task II.

3.1.1 Task IA- Experimental Design

The objectives of this subtask, which has been completed, were to review the TBC literature and Pratt & Whitney experience with thermal barrier coated turbine components, and based on this review, to establish an experimental program to determine the relative importance of various TBC degradation mechanisms as they relate to coating service life.

Early work on thermal barrier coatings describes numerous material and process developments, and identifies several potential degradation and failure modes (Refs. 1-14). These modes include thermomechanically induced structural failure of the ceramic coating layer, oxidative degradation of the underlying metallic bond coating, thermochemically (hot corrosion) induced ceramic degradation, foreign object damage (FOD), and erosion.

Examination of experimental and flight serviced engine components indicates the first of these degradation modes to be the predominant cause of coating failure, resulting in spallation of the ceramic coating layer due to formation of a dominant crack in the ceramic parallel and adjacent to the metal-ceramic interface (Figure 2). Laboratory test results reported in the literature suggest that this thermomechanical spallation mode is accelerated by time/temperature dependent interfacial oxidation of the metallic bond coat (Refs. 15-16). The examination of engine exposed components indicates that hot corrosion, FOD, and erosion do not represent life-limiting modes of degradation in engine service. Based on these observations, an experimental program was designed to separately assess and quantify the relative contributions of mechanical and oxidation degradation to TBC failure. While hot corrosion was not identified as a major failure mode in commercial engine service, experimental tests were included in the program to identify the threshold contaminant level for corrosion damage, thus providing a basis for prediction of flight environments where this degradation mode might be important. Details of findings from the literature and engine component review and of the experimental program designed to assess critical mode importance, are provided in the following paragraphs.

200X

Figure 2 Typical Thermal Barrier Coating Engine Failure Mode

In reviewing the available literature, laboratory data, and engine hardware, there was general agreement that the major TBC failure mode is thermomechanical ceramic coating spallation due to dominant crack propagation parallel to but not coincident with the ceramic-metal interface. Crack driving forces are presumed due to thermal expansion differences between the ceramic and metal components of the system, with the coefficient of thermal expansion of the ceramic being significantly lower than that of the underlying metallic system.

It is also hypothesized that the stresses resulting from thermal expansion mismatch during thermal cycling are augmented by oxidation of the NiCoCrAlY bond coat, which has an irregular roughened surface topology (Refs. 15, 16, 17, 18). Miller and Lowell (see Ref. 15) were the first to discuss the role of the irregular bond coat/ceramic interface on oxidation related failure.

Despite the observation that the predominant thermal barrier coating failure mode involves thermomechanical spalling, resulting from thermal cycle induced stresses, some laboratory evidence exists to indicate a time and environmental dependence of the mechanical failure mode. Early evidence of time dependence was provided by McDonald & Hendricks (Ref. 19), who showed, at least for some compositions, a substantial decrease in the number of thermal cycles caused ceramic spallation failure as cycle duration increased from 7 minutes to 60 minutes. Similar results have been obtained at Pratt & Whitney. Gedwill (Ref. 20) confirmed this effect with a more durable coating of similar composition. Miller & Lowell (see Ref. 15) postulated time dependent changes of "stress free temperature," resulting from time dependent bond coat flow, as being responsible at least in part for interaction between thermal exposure and thermal cycling effects, but also noted that exposure in an oxidizing atmosphere was much more damaging than exposure on a non-oxidizing environment. Early results from Pratt & Whitney also indicate a cyclic life reduction for both oxidizing and non-oxidizing pre-exposure, with the oxidizing atmosphere being much more deleterious. A preliminary thermal barrier coating oxidation/thermal stress life prediction model has been proposed by Miller (see Ref. 18).

Andersson (Ref. 21) analyzed the stresses of typical thermal barrier coated heat engine components and found that the stresses are tensile in directions parallel to metal-ceramic interface for elevated temperature steady state operating conditions and during the cool down portion of the cycle, and in tangential compression during the heatup portion of the cycle.

The stresses induced in coatings are hypothesized to be dependent not only on material properties but also heat flux or degree of thermal loading. The latter was addressed by Miller and Berndt (Ref. 22). They reported that "good" ZrO_2-8 w/o Y_2O_3 coatings have remarkable tolerance to an extremely high heat flux plasma torch test.

The geometry of the component and the coating thickness are also important life variables. For thinner coatings (< 5 mils) the stresses due to temperature gradients in the coating have been shown to be less severe so that increased service life can be expected (Ref. 23). Normal stresses are introduced in the coating of a curved surface by the tangential compressive stresses present resulting in ceramic spallation. In coated airfoil applications this is seen at the leading and trailing edges where the convex radii of curvature are minimized. (It should be noted that even a flat surface would have radial stresses due to surface roughness.)

Ceramic thermal stability is an important characteristic effecting coating life. Thermal stability refers to the ability of ceramic layer to endure prolonged high temperature exposure without the occurrence of damaging morphological, chemical, or phase changes. Ceramic sintering is a thermally activated processes which can also limit cycle life. However, it has not been observed in laboratory/engine testing. Phase studies have determined that the presence of large amounts of monoclinic phase correlate to poor performing coatings (Refs. 24,25,26 also Ref 8).

Room temperature x-ray diffraction studies of 7YSZ coatings indicate a two phase structure consisting primarily of the cubic and metastable tetragonal phases together with 0 to 5% monoclinic. Because of the extremely rapid cooling rates associated with deposition of the ceramic coating layer, the tetragonal phase formed in the coating contains a relatively high percentage of Y_2O_3, and is not readily transformed to monoclinic. With prolonged exposure at elevated temperature in the cubic plus tetragonal phase field, yttrium diffusion occurs and the high Y_2O_3 tetragonal phase transforms to cubic plus low Y_2O_3 tetragonal, with the low Y_2O_3 tetragonal phase being readily transformed to monoclinic upon cooling (Refs. 24, 25, see also Ref. 27).

Stecura (28) studied TBC systems and hypothesized that compositional changes in various bond coats and substrates play a more important role in coating durability than does the coefficient of thermal expansion of the substrate material. It was hypothesized that yttrium, aluminum and chromium in the bond coat critically affect the TBC life. Aluminum, chromium and yttrium oxides are formed at the interface during thermal testing. Yttrium diffuses toward the bond coat-ceramic interface, chromium diffuses towards the substrate and molybdenum into the bond coat. These events are considered to have an adverse effect on coating life. It has been shown that yttria in the bond coat moves coating failure location from the bond coat-substrate interface to just above the ceramic bond coat interface (see Ref. 16). It is hypothesized that the location of major crack initiation, whether within the bond coat oxide layer or in the ceramic, is dependent on the stress state at the roughened interface which is at the very least changed by oxide growth.

Other degradation modes noted in several studies include secondary failure modes i.e., hot corrosion, erosion, FOD. Results from several laboratories (Refs. 29-34), have demonstrated an apparent susceptibility of thermal barrier coatings to failure in hot corrosion environments. The responsible mechanism appears to involve infiltration of the porous ceramic with liquid corrodent deposited on the coating surface at intermediate exposure temperatures, and subsequent "mechanical" spalling resulting from alternate freezing and thawing of the infiltrated corrodent (see Refs. 34,32,30,14).

Some evidence has been reported which supports "thermochemical" ceramic spallation in hot corrosion environments; i.e., the infiltrated (Na_2SO_4) reacts with the ceramic at high SO_3 partial pressures (Refs. 35,36, also Refs. 34,30), resulting in destabilization of ZrO_2. This degradation is attributed to acid leaching of yttrium from the ceramic.

Thermal barrier coating degradation and failure modes and mechanisms observed in prior Pratt & Whitney laboratory tests were found to be in general agreement with analysis from the literature. The major mode of failure in PWA264 is spallation of the ceramic layer resulting from in-plane cracking adjacent to but not coincident with the metal ceramic interface. Prior or concurrent bond coat oxidation appears to play a major role in cyclic thermal stress induced spallation cracking. The Task IB testing is designed to identify the relative importance of these two degradation modes and to provide the quantitative data required to develop a preliminary model which will predict spalling life under varying exposure conditions.

While the Task IA study included reviews of TBC literature and prior laboratory experience, primary emphasis was placed on the evaluation of failure mode as observed on ground based experimental engine and field service exposed components. Engine exposed PWA 264 coated parts have been evaluated from the commercial engines; JT9D-7R4G2, -7R4D -7R4D1, 7R4E1, 7R4H and PW2037, and the military engines; F-100, ATEGG (F-100) and TF-30. Details of the reviewed parts are documented in Table II. Where available, components representing the unexposed coating in each of the engine exposed components also have been examined to identify changes which occurred in coating structure during engine test. Significant observations form this review of engine exposed components are as follows:

a) Ceramic sintering was not observed in any case

b) Oxidation of the low pressure chamber sprayed PWA276 bond coat contributed to coating failure to a lesser degree than as seen in the laboratory

c) Coating failure due to oxidation of substandard, air plasma sprayed bond coat was a major life limiting factor found in PW2037 first vane platform

d) Geometry effects were considered to play a significant role in coating degradation.

Examination of numerous engine tested components indicates that thermal barrier failures are almost exclusively of the "thermomechanical" type shown in Figure 2. In only one case has engine component thermal barrier coating failure been attributable directly to bond coat oxidation alone. That particular failure occurred on a vane airfoil which was operated under unusually severe thermal conditions and was, for reasons of processing convenience, coated with an air sprayed bond coat.

3.1.2 Task IB. 1 Conduct Critical Experiments

The objective of this subtask was to conduct a series of critical experiments and tests designed in Task IA to determine the relative importance of various thermomechanical and thermochemical coating degradation modes. Failure life data from these tests was also used to develop a preliminary life prediction model in Task IC. The test program included clean fuel and salted burner rig tests as well as static furnace testing of thermal barrier coated specimens to establish the relative importance of thermal stress cycling versus thermal and thermochemical degradation in determining thermal barrier coating life. The overall Task I test plan is shown in Figure 3.

The specimen used for all static and cyclic exposure testing in this sub-task is illustrated in Figure 4. For cyclic burner rig testing, this specimen is thermal barrier coated on all surfaces except for the butt end, where coating is optional but not required. For static furnace exposure testing, the application of a tapered coating to only the cylindrical portion of the bar was employed to minimize the possibility of premature coating failure at the edge of the ceramic layer.

Prior to use in this task, all raw materials were thoroughly characterized and tested to ensure acceptability. Table III presents ceramic and metallic powder analysis which include: chemistry, particle size distribution and x-ray diffraction results.

TABLE II
EVALUATION OF ENGINE EXPOSED PWA 264 COATED COMPONENTS

Date	Engine Type	Part Name	Engine #	Operator	Material	Remarks
12/02/83	2037	1st Vane Paired Platform	X-666-1C	P&W	647/264 modified bond coat	265.89 hrs/1500 cycles endurance testing. APS/LPCS bond coat - APS severely oxidized. Spalling at A.P.S. - LPCS bond coat interface. Ceramic thick in some areas.
09/01/82	2037	1st Vane platform N/C	X-664-1A			36.97 hrs/136 cycles endurance testing. Limited spallation of the ceramic on O.D. T.E., ceramic microstructure meets specifications.
09/01/82	2037	1st Vane platform N/C	X-664-1A			36.97 hrs/136 endurance. Limited spallation of the ceramic on O.D. T.E., ceramic microstructure meets specifications.
01/10/84	2037	1st Vane Paired platform	X-662-6			Ceramic Spallation on ID platform bond coat oxidation of the A.P.S. layer.
05/10/84	2034	1st Turbine Vane platform	X-671-5		647/264	485 cycles limited ceramic spallation. Ceramic structure meets specification.
10/25/82	TF30	2nd Vane	P-559-4 1B		633/264	1000 F.H./2171 A/B squirts. Ceramic thickness; 16-20 mils. Spallation around most of C.V. side of airfoil, C.C. L.E. In plane cracking. Metal bond coat has thin oxide layer ceramic microstructure meets specifications.
10/25/82	TF30	2nd Vane	P-559-4 1B	P&W (FAA)	633/264	1000 F.H./2171 A/B squirts. Spallation at L.E.
01/17/83	F-100 (ATEGG)	1st Vane	P-686-2		1422/264	910 TAC cycles/53.7 hot time. Spallation at I.D. L.E. only; due to specimen geometry and thermal cycling stress. Coating structure meets specifications. Bond coat has very thin oxide layer.
01/17/83	F-100 (ATEGG)	1st Blade	P-686-2		1422/264	910 TAC cycles/53.7 hot time. Spallation at I.D. L.E. only due to specimen geometry and Thermal cycling stress. Coating microstructure meets specifications. Bond coat has very thin oxide layer.
05/18/83	F100	1st Vane	-		1480/264 modified bond coat	2000 TAC cycles ceramic spalled L.E.; bond coat failures.
04/20/82	JT9D-7R4D	1st Vane platform	X-491-45	P&W	647/264	246.9 hrs/1500 cycles spalled after engine run. Spalling location - corners of platforms. Ceramic structure meets specifications. Very thin oxide layer/thin Beta depleted zone. Some segmentation and in plane cracking in ceramic. *(Rec'd vacuum H.T./1975°F F/4 hrs.)

TABLE II (Continued)
EVALUATION OF ENGINE EXPOSED PWA 264 COATED COMPONENTS

Date	Engine Type	Part Name	Engine #	Operator	Material	Remarks
04/20/82	JT9D-7R4D	1st Vane platform	X-491-45	P&W	647/264	246.9 hrs/1500 cycles spalled after engine run. Spalling location - corners of platforms. Ceramic structure meets specifications. Some segmentation and in plane cracking in ceramic. Ceramic Thickness 16-18 mils.*rs.)
04/21/82	JT9D-7R4D	1st Vane platform	X-491-45			Ceramic not distressed after engine run. Ceramic structure meets specifications (Rec'd Ar H.T./1975°F/4hrs). Ceramic thickness 8 mils.
04/19/82	JT9D-7R4G2	Wide Chord 1st Vane Platform	X-579-29			FAA 1000 cycle Test (Bond Coat - A.P.S./L.P.C.S.) A.P.S. portion is severely oxidized. In plane cracking of the ceramic. Ceramic structure meets specification.
05/82	JT9D-7R4G2	Wide Chord 1st Vane Platform	X-579-29A			114 hrs./19 cycles, substantial spallation on OD/ID. Good ceramic porosity but layered in - plane cracking. Spallation due to oxidizable inclusions; $ZrCN_2$ (Starck #5399 + Union Carbide 1365-1).
01/12/83	2037	1st Vane (Paired) Platform	X-666-1C			265.89 hrs/1500 cycles endurance testing. Limited spallation on O.D. T.E. and I.D.L.E. due to F.O.D. - (not apparent from microstructure). Spallation adjacent to areas where ceramic thickness 7 mils. Some in plane cracking. A.P.S./L.P.C.S. bond layer-thick A.P.S. 5 mils. Microstructure adjacent to spalled areas was acceptable.
01/07/83	2037	1st Vane Paired platform/airfoil coated also	X-667-1A		647/264 (modified bond coat)	325.3 hrs/1500 cycles endurance testing. Spallation on O.D.T.E. and I.D.L.E. (A.P.S./L.P.C. - bond coat) also hidden pressure airfoil. Metallic thickness specifications not met. Spallation - chipping documented as FOD. Some areas of thick ceramic.
01/12/83	2037	1st Vane Paired platform/airfoil coated also	X-667-1A			325.3 hrs/1500 cycles endurance testing. Spallation on O.D.T.E. and I.D.L.E. (A.P.S./L.P.C. - bond coat) also hidden pressure airfoil. Metallic thickness specifications not met. Spallation - chipping documented as FOD. Some areas of thick ceramic. Note: layer of engine debris
09/06/83	2037	1st Vane Paired platform/airfoil coated also	X-667-1A,B 2,3, X-670-2A			593.6 hrs/1947 cycles endurance testing. Spallation limited but did occur in bond coat at APS/LPCS bond coat interface due to bond coat oxidation. Some in plane cracking some cracking at bond coat - ceramic interface also ceramic thick in some areas. O.D., I.D., T.E. hidden pressure airfoil. FOD.
09/11/84	JT9D-7R4E1	1st Vane Platform	716102	Airbus A-310	264	2355 hrs/411 cycles coating looks excellent.
09/13/84	JT9D-7R4D	1st Vane Platform	709643	TW	264	227 hrs/868 cyles coating looks excellent.
5/1/85	JT9D-7R4D	1st Vane	708603	SR	264	9300 hrs/2328 cycles coating looks excellent.
10/25/85	JT9D-7R4D1	1st Vane Platform	7077714	SR	264	4978 hrs/4109 cycles coating looks excellent.

TEMPERTURE	EXPOSURE	STATIC		CYCLIC						FRACTIONAL EXPOSURE							
	TEST	FURNACE		BURNER RIG						FURNACE		BURNER RIG					
	ATMOSPHERE	OXIDIZING	NON-OXIDIZING	OXIDIZING				HOT CORROSION		OXIDIZING	NON-OXIDIZING	OXIDIZING				HOT CORROSION	
	CYCLE LENGTH			SHORT		LONG						SHORT		LONG			
	HEATING RATE			FAST	SLOW	FAST	SLOW					FAST	SLOW	FAST	SLOW		
	CORRODENT LEVEL							LOW	HIGH							LOW	HIGH
1650								J	H								K
2000				D_2													
2100		A_1	A_2	D_1	E	F				C		G					
2200		B															

CYCLIC OXIDATION BURNER RIG TEST SPECIMEN SET FOR CONDITIONS D1, D2, E & F-12 SPECIMENS PER TEST

- 4 10 MIL VIRGIN CERAMIC (''BASELINE'' COATING)
- 2 5 MIL VIRGIN CERAMIC
- 2 15 MIL VIRGIN CERAMIC
- 2 10 MIL AIR PRE-EXPOSED FOR APPROXIMATELY ½ ESTIMATED BURNER RIG HOT TIME LIFE
- 2 10 MIL Ar PRE-EXPOSED FOR APPROXIMATELY ½ ESTIMATED BURNER RIG HOT TIME LIFE

CYCLE LENGTH

SHORT: 6 MINUTE CYCLE = 4 MINUTES IN THE FLAME + 2 MINUTES FORCE AIR COOLED

LONG: 60 MINUTE CYCLE = 57 MINUTES IN THE FLAME + 3 MINUTES FORCE AIR COOLED

CYCLE RATE

FAST: NOMINAL 60 SECOND HEAT-UP TO MAXIMUM TEMPERATURE

SLOW: NOMINAL 180 SECOND HEAT-UP TO MAXIMUM TEMPERATURE

CORRODENT LEVEL

LOW: 10 PPM % SYNTHETIC SEA SALT

HIGH: 35 PPM % SYNTHETIC SEA SALT

Figure 3 Task I Test Plan to Evaluate Thermal Barrier Coating Failure Life

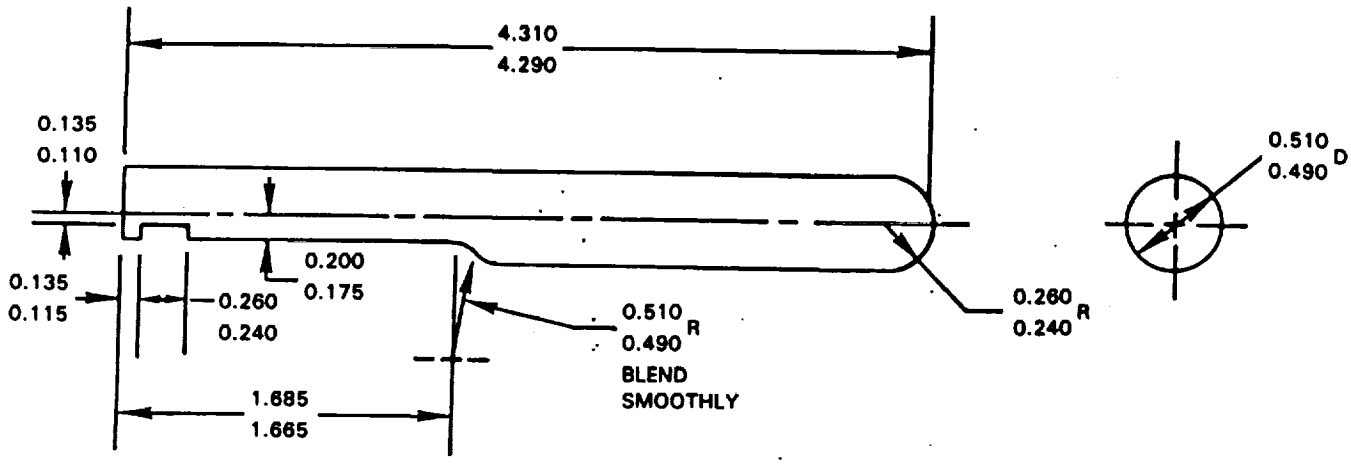

All Dimensions Shown In Inches

Figure 4 Burner Rig Coating Evaluation Specimen

TABLE III
METALLIC AND CERAMIC POWDER ANALYSES

Material	Chemical Analysis	Particle Size Analysis	
		Cumulative % Finer	Microns
NiCoCrAlY	21.60 w/o Co	100	176
(Alloy Metals	17.50 w/o Cr	100	125
Lot #6192)	13.00 w/o Al	100	88
	0.66 w/o Y	100	62
	Bal. - Ni	93	44
		72.2	31
		41.5	22
		21.9	16
		11.8	11
		5.5	7.8
		2.3	5.5
		0.7	3.9
		0.0	2.8
7 w/o Y_2O_3- ZrO_2	7.2 w/o Y_2O_3	100%	176
(Zircoa Lot #30656)	1.7 w/o HfO_2	94.7%	125
	0.1 w/o CaO	86.1%	88
	0.2 w/o TiO_2	63.7%	62
	0.1 w/o Fe_2O_3	39.4%	44
	0.3 w/o Al_2O_3	29.0%	31
	Bal. -ZrO_2	11.8%	22
		5.3%	16
		2.7%	11
		1.3%	7.8
		0.5%	5.5
		0.5%	3.9
		0%	2.8

X-RD Results

80-85 v/o fcc ZrO_2
20-15 v/o monoclinic ZrO_2

Following raw material qualification, all burner rig standard erosion bars used in Task I testing were LPCS with NiCoCrAlY metallic bond coat (AMI Lot No. 6192). Low pressure chamber spray conditions and parameters are presented in Table IV. Sample tip sections were taken from selected specimens from each batch of bars for verification of thickness and microstructure.

The test bars were air plasma sprayed with ZrO_2-7w/o Y_2O_3. Air plasma spray deposition parameters are given in Table V. A statistical program designed to randomize coating sequence, and hence any uncontrolled variability of deposition parameters, was used to coat and select test bars.

To document uniformity of structure, a pre-test sample was obtained from every specimen tested in this program. Selected samples (about 10%) were examined metallographically using a statistically designed selection plan. The balance of the samples are available for metallographic examination if needed.

TABLE IV
LOW PRESSURE PLASMA SPRAY CONDITIONS

Standard erosion bar specimens coated using a Electroplasma High Energy Gun.

Gun Voltage (V)	58
Gun Current (A)	1500
Standoff (in.)	15
Workpiece Temperature	1500-1700°F

Helium and Argon arc gases used

TABLE V
AIR PLASMA SPRAY CONDITIONS

Standard erosion bar specimens coated using a Plasmadyne SG-100 Gun.

Gun Voltage (V)	42
Gun Current (A)	900
Standoff (in.)	3
Workpiece Temperature	500°F

Helium and Argon arc gases used.

3.1.2.1 Furnace Exposure Tests

These tests were performed to determine the influence of static thermal exposure on TBC degradation and failure. Specimens were furnace exposed at two temperatures for various times in various combinations of oxidizing and non-oxidizing environments as shown in Figure 5 and described below. Baseline tests designated "A" were conducted at 2100°F in oxidizing and non-oxidizing environments. These tests involved furnace exposure of two thermal barrier coated specimens per test condition for times sufficient to cause failure of the ceramic coating. Failure in this context is defined as development of "delamination" cracking over a significant area. In order to observe delamination damage, specimens were infrequently cycled to room temperature. Cycle frequency/inspection intervals are presented in Table VI.

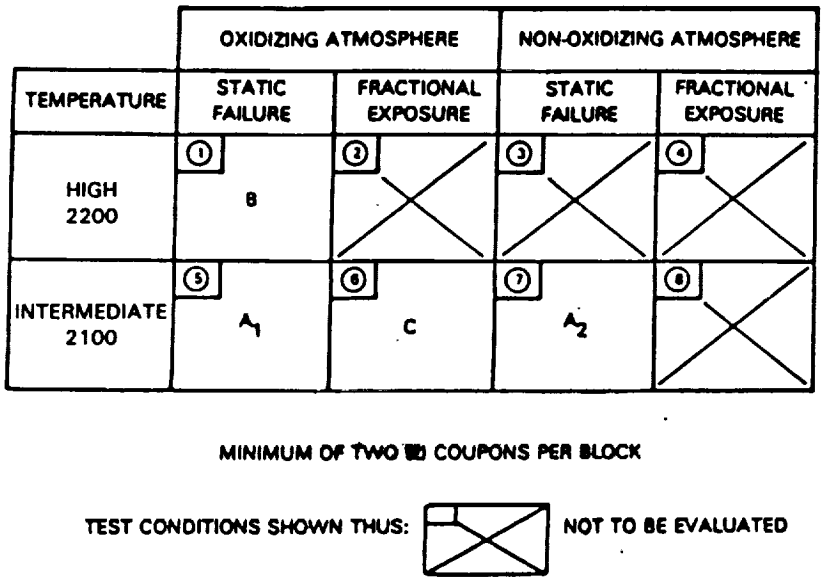

Figure 5 Task I Furnace Exposure Test Plan to Evaluate Thermal Barrier Coating Static Failure Life

TABLE VI
INSPECTION INTERVALS FOR TASK IB FURNACE TESTS

Test Code	Condition	Inspection Interval
A1.A	2100°F/Air	10 hrs.
A1.B	2100°F/Air	80 hrs.
A2	2100°F/Argon	80 hrs.
B	2200°F/Air	10 hrs.

Examination involved visual observation to look for areas of delaminated ceramic. To determine the influence of temperature on static coating failure life in air, an additional furnace exposure test designated "B" was conducted at 2200°F. To evaluate progressive damage accumulation, a fractional exposure test designated "C" was conducted in the oxidizing environment at 2100°F.

This fractional exposure test involved metallographic examination of specimens successively removed at approximate decile fractions of the "static failure" life as defined in the corresponding "A" test. The primary goal of the examination was to find evidence of incipient delamination cracking; in addition, specimens were examined to determine oxide scale growth at the interface between the metal and ceramic coating layers and beta phase depletion in the metallic coating layer.

3.1.2.1.1 Furnace Test Results and Microstructural Evaluation

Furnace exposure test results are summarized in Table VII and Figure 6. Note that independent of this program, data generated in-house for 2000°F has been included in Figure 6. Spallation failure of the ceramic coating layer did not occur during isothermal exposure; all specimen failures occurred upon cool-down, initiating at the tip area where there is a radius change. A photograph of a typical failed coating is shown in Figure 7. Weight gain measurements were made at each inspection interval for every specimen.

TABLE VII
SUMMARY OF AIR AND ARGON FURNACE EXPOSURE TEST RESULTS

Specimen I.D. #	Code/ Condition	Exposure Time/(hrs) # of Cycles	Results	Metallographic Observations
TP07 TP08	A1.A/Air-2100°F (10 hr inspection)	140/14 160/16	Failed	Major crack just above interface within ceramic oxide layer
TP01 TP02	A1.B/Air-2100°F (80 hr inspection)	240/3 160/2	Failed	Major crack just above interface within ceramic
TP05 TP06	A2/Ar-2100°F (80 hr. inspection)	1040/13	No Failures	Incipient cracking near interface noted
TP03 TP04	B/Air-2200°F (10 hr inspection)	40/4 60/6	Failed	Major crack just above interface within ceramic
TP16	C/Air-2100°F Fractional	90/1	No Failures	(60%)No major cracking; some incipient cracking near the ceramic oxide interface
TP19	C/Air-2100°F Fractional	135/1	No Failures	(90%)No major cracking; some incipient cracking near the ceramic oxide interface
TP20	C/Air-2100°F Fractional	150/1	No Failures	Incipient failure observed at suspected bond coat defect; Major cracking extending from "blister" through aligned Kirkendall voids
TP21	C/Air-2100°F Fractional	165/1	Failed	Major cracking/ delamination
TP22	C/Air-2100°F Fractional	180/1	Failed	Major cracking/ delamination
TP23	C/Air-2100°F (10hr inspection)	120/12	Failed	Incipent cracking at the tip
TP24	C/Air-2100°F (10hr inspection)	150/15	Failed	Major cracking with some delamination at tip

Although the tapered coating scheme prevented premature coating failure, the design allowed for exposed substrate; thus the weight gain data will only give a rough indication of oxide accumulation. These weight gain data are summarized in Appendix A.

Review of the failure time data in Table VII clearly shows the influence of temperature, exposure environment and cycle frequency on ceramic spallation life. The results show that thermal exposure in Argon does not cause coating failure for an extended period of time compared to air exposure. For furnace exposure conducted in air, frequent thermal cycling appears to slightly decrease the total exposure time to failure, as shown by comparison of 2100°F air tests with 10 hour and 80 hour inspection intervals. Thermal barrier coating life was shown to be more dramatically dependent on "cyclic content" by previous work conducted by Miller, (Ref. 37) and McDonald and Henricks (Ref. 19).

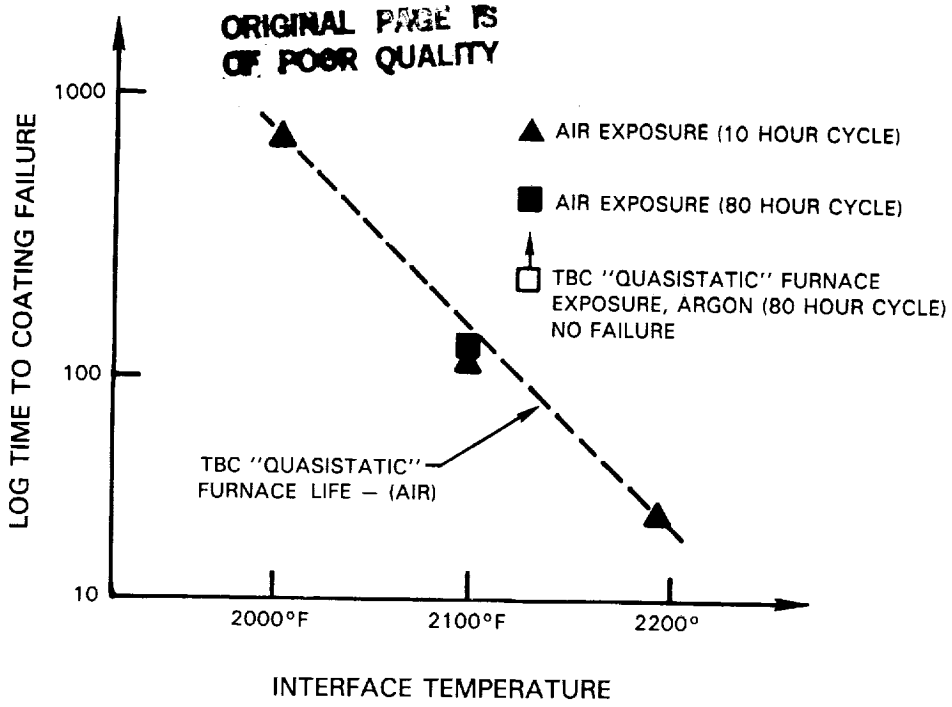

Figure 6 Test Data Showing Thermal Exposure Atmosphere Effects on Coating Durability

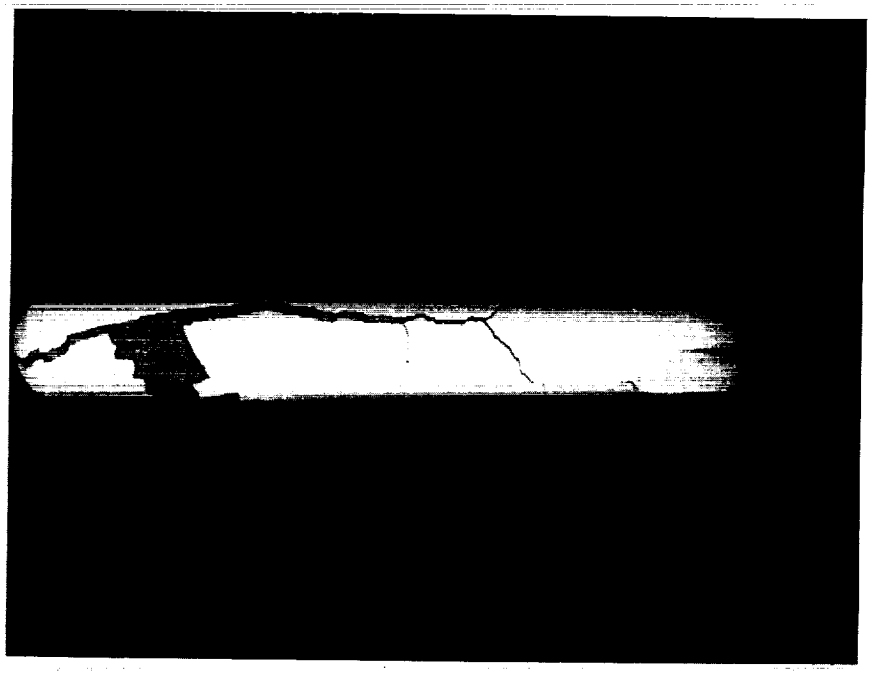

0.9X

Figure 7 Photomicrograph of Typical Furnace Tested Failed Coating (TP-08, 16 cycles, 10 hrs/cycle, Total Hours = 160 at 2100°F in Air)

The high temperature (2200°F in air) furnace exposure results show a significant decrease in TBC life. This life decrease is attributed to a combination of more rapid oxidation at the high temperature and larger thermal strain excursion on cooling to ambient from the higher temperature. The Argon environment significantly reduces the weight gain (oxidation) rate as compared to an air environment so that exposure time and cycle life increase dramatically without causing ceramic spallation.

To aid in interpretation of static furnace exposure results, metallographic and x-ray diffraction analyses were conducted on pre-and post-exposure specimens. X-ray diffraction results are summarized in Figure 8. In the air exposed specimens, the v/o of monoclinic ZrO_2 increases with increasing exposure time. In individual comparisons between these tested specimens and the pre-test specimen, there is an apparent decrease in the tetragonal phase which accompanies the increase in the monoclinic phase and a slight increase in the FCC phase, suggesting that existing metastable tetragonal phase is undergoing transformation. In looking at the two specimens tested at 2100°F (different cycle lengths; 80 hrs. and 10 hrs.), one failing at 160 hours and the other at 240 hours, there appears to be not only an increase in the v/o monoclinic phase with time but an associated decrease in the v/o FCC phase and no change in the v/o tetragonal phase with increasing time.

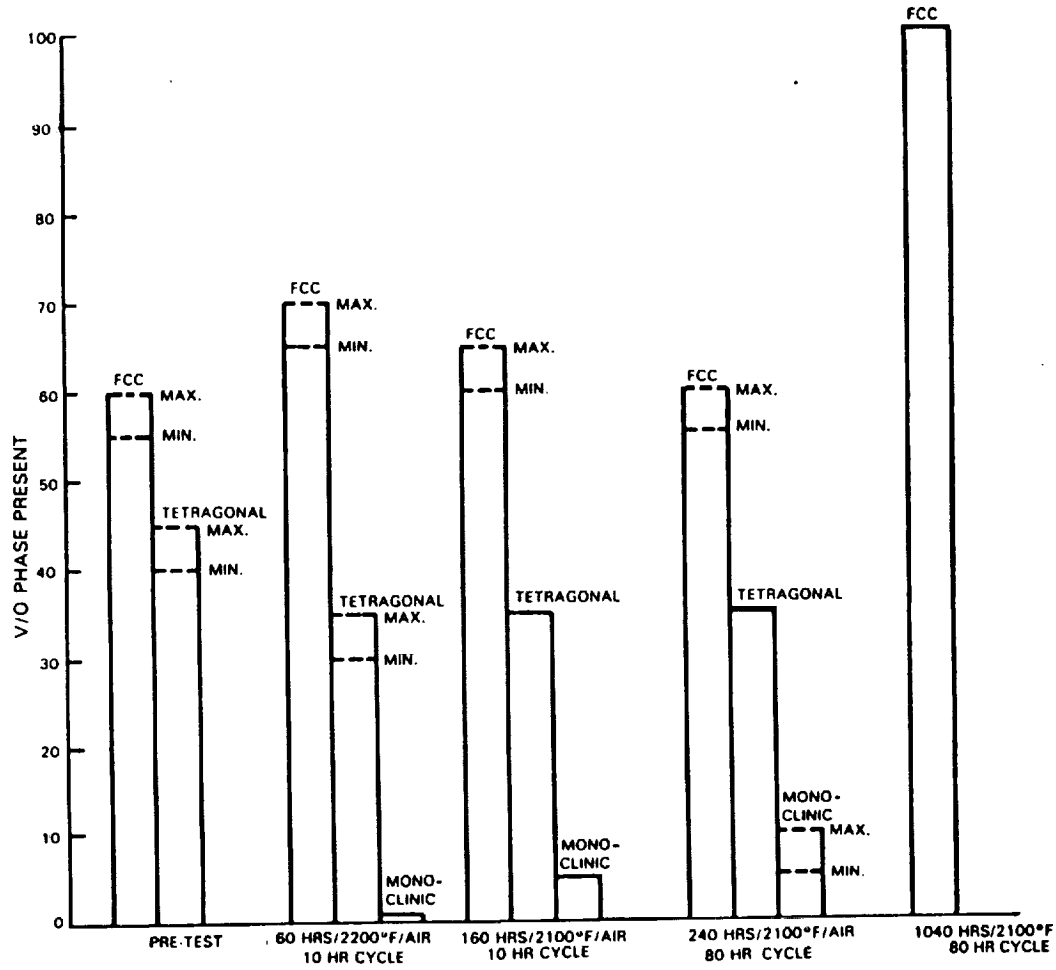

Figure 8 X-Ray Diffraction Results of Furnace Exposed Test Specimens

These observations are consistent with those presented by Miller (Ref. 24), suggesting that homogenization resulting from heat treatment may have resulted in an increase in both the low Y_2O_3 transformable tetragonal and the high Y_2O_3 cubic phase. Upon cooling, the transformable tetragonal then would transform to the monoclinic phase, while the cubic phase is retained.

X-ray diffraction analysis of the Argon exposed specimen revealed 100% FCC ZrO_2. This result is consistent with other studies which suggest that the equilibrium phase distribution may be sensitive to oxygen partial pressure (Ref. 38).

Thermal exposure effects including oxidation, beta (NiAl) depletion, bond coat substrate interdiffusion, and ceramic structure were metallographically studied. Electron Microprobe analyses was conducted to study time dependent chemical changes occurring in the substrate-bondcoat-ceramic system. Table VIII presents a summary of the metallographic evaluation of selected post-test furnace exposed specimens which are shown in Figures 9 through 15. Thermal barrier coating failure was observed to be associated with increased time at temperature which resulted in increased beta depletion, average oxide thickness, interdiffusion zone width and average void size. An increase in Kirkendall void population is seen with the high exposure temperature. Specific examples of these various changes are discussed in the following paragraphs.

TABLE VIII
METALLOGRAPHIC EVALUATION OF SELECTED FURNACE EXPOSURE SPECIMENS AFTER EXPOSURE

Specimen I.D.#	Test Code/ Conditions	Average Oxide Thickness(mils)	Beta (NiAl) Depletion	Interdiffusion Zone (mils)	Average Void Width (Mils)
TP01	A1.A/240 hrs in Air 2100°F/3 80 hr. inspections	0.25 - 0.50	100%	4	0.50 - 1.00
TP08	A1.B/160 hrs in Air 2100°F/16 10 hr. inspections	0.25 - 0.50	100%	3	0.50
TP05	A2/1040 hrs. in Ar 2100°F/13 80 hr. inspections	1.0 - 1.25 *very irregular discontinuous	100%	7	0.75 - 1.00
TP04	B/60 hrs Air 2200°F/6 10 hr. inspection	0.25	Overall 60 - 70% 40-50 depleted MCrAlY to ceramic 10-25% depleted MCrAlY to substrate interface	4.5 - 5.0	0.50 - 0.75 *void population is high
TP16	C/90 hrs. in Air 2100°F 60%	0.25 - 0.50	Overall 80 - 100% 60 - 70% depleted MCrAlY to ceramic interface 10-20% depleted MCrAlY to substrate interface	2.5 - 3	0.25 - 0.75
TP19	C/135 hrs. in Air 2100°F 90%	0.25 - 0.50	100%	2.5 - 3.0	0.25 - 0.50
TP20	C/150 hrs. in Air 2100°F	0.25	100%	2.5 - 3.0	0.25 - 0.50

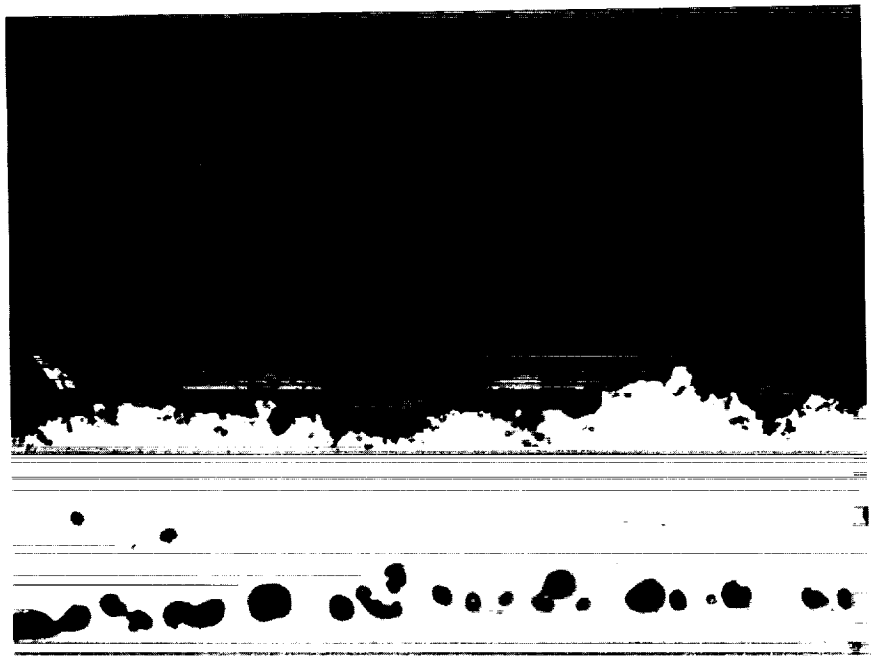

200X

Figure 9 Light Photomicrograph of Post-Test Microstructure. Failed After Furnace Exposure in Air at 2100°F with 80 Hours Inspection Intervals (240 hrs/3 cycles)

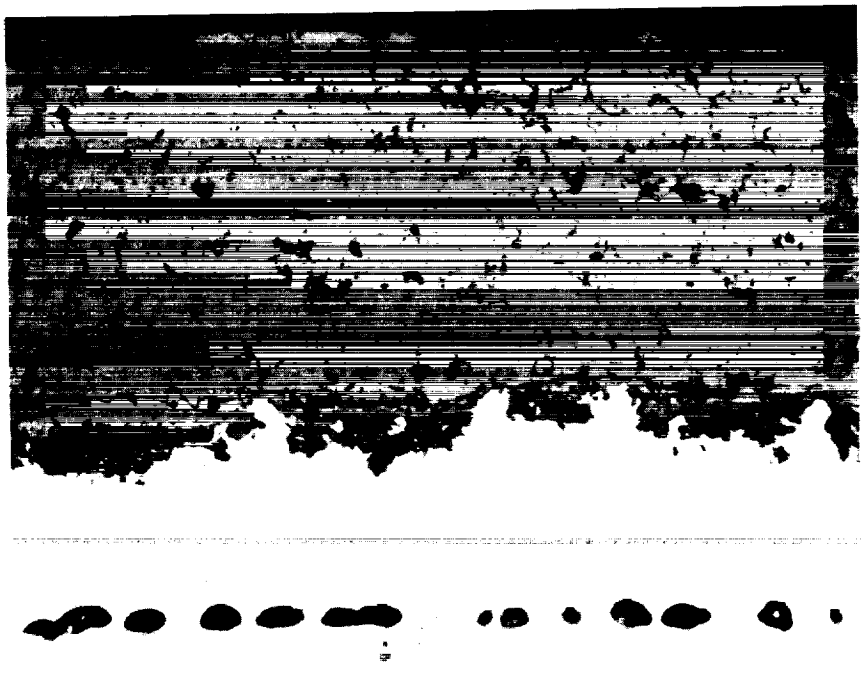

200X

Figure 10 Light Photomicrograph of Post-Test Microstructure. Furnace Exposure in Argon of 2100°F with 80 Hours Inspection Intervals (1040 hrs/13 Cycles)

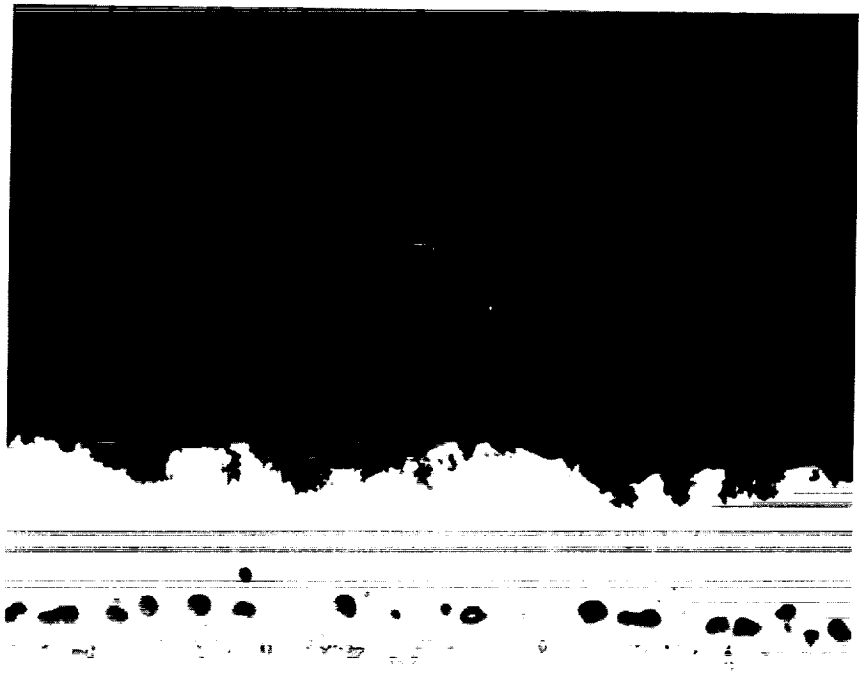

Figure 11 Light Photomicrograph of Post-Test Microstructure. Failed After Furnace Exposure in Air at 2100°F with 10 Hours Inspection Intervals (160 hrs/16 cycles)

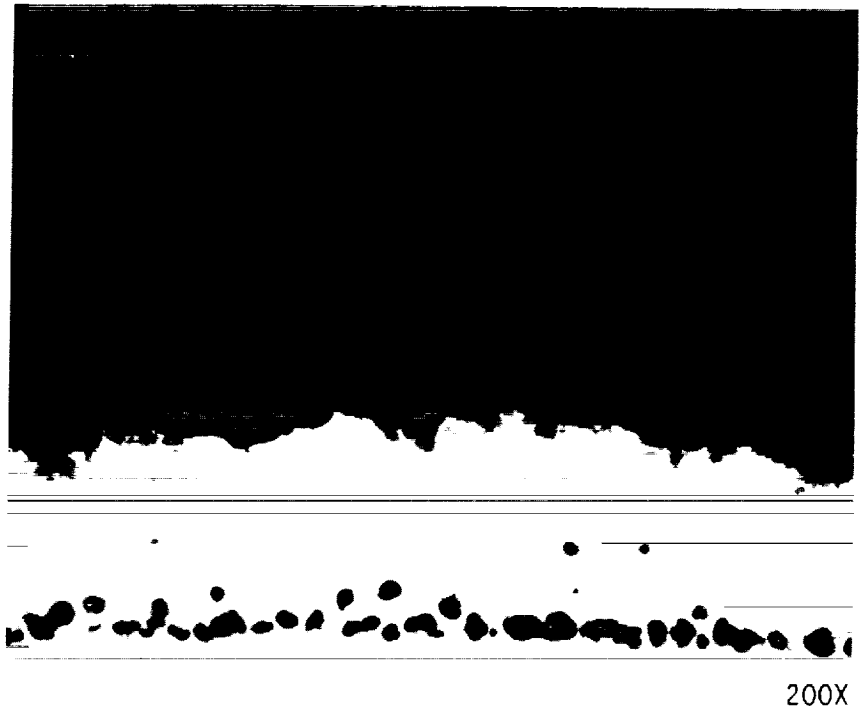

Figure 12 Light Photomicrograph of Post-Test Microstructure. Failed After Furnace Exposure in Air at 2200°F with 10 Hours Inspection Intervals (60 hrs/6 cycles)

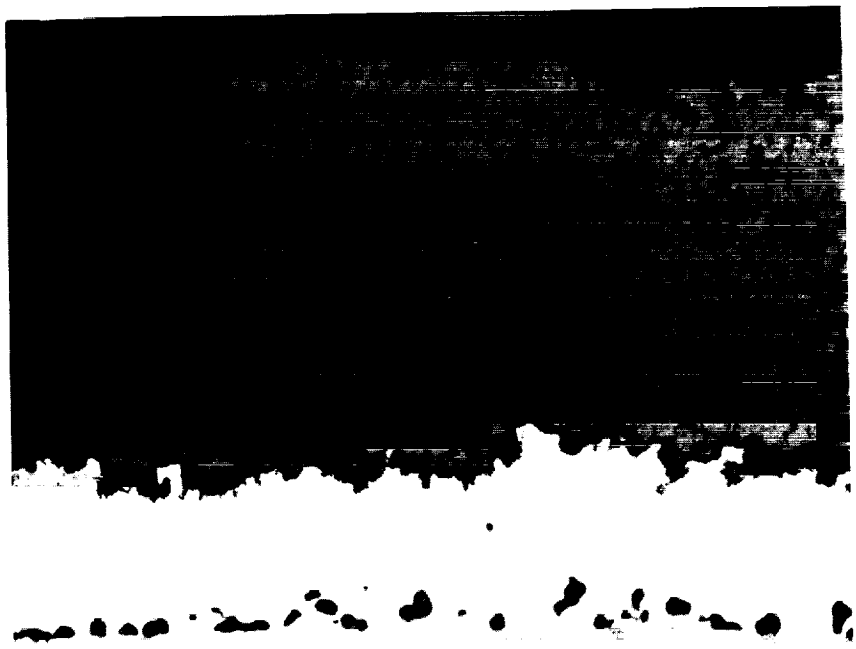

200X

Figure 13 Light Photomicrograph of Post-Test Microstructure After Furnace Exposure in Air (90 hrs/2100°F/1 cycle 60%)

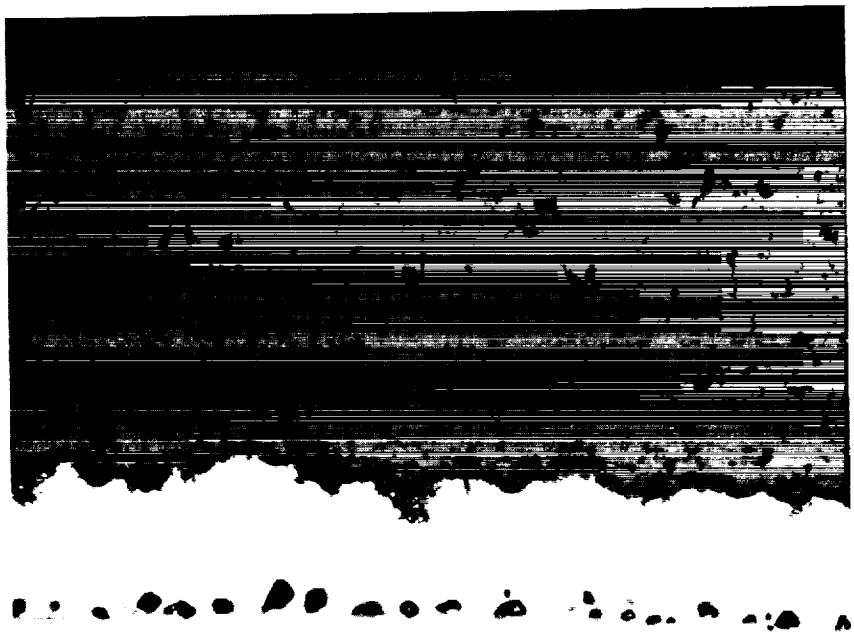

200X

Figure 14 Light Photomicrograph of Post-Test Microstructure After Fractional Furnace Exposure in Air (135 hrs/2100°F/1 cycle 90%)

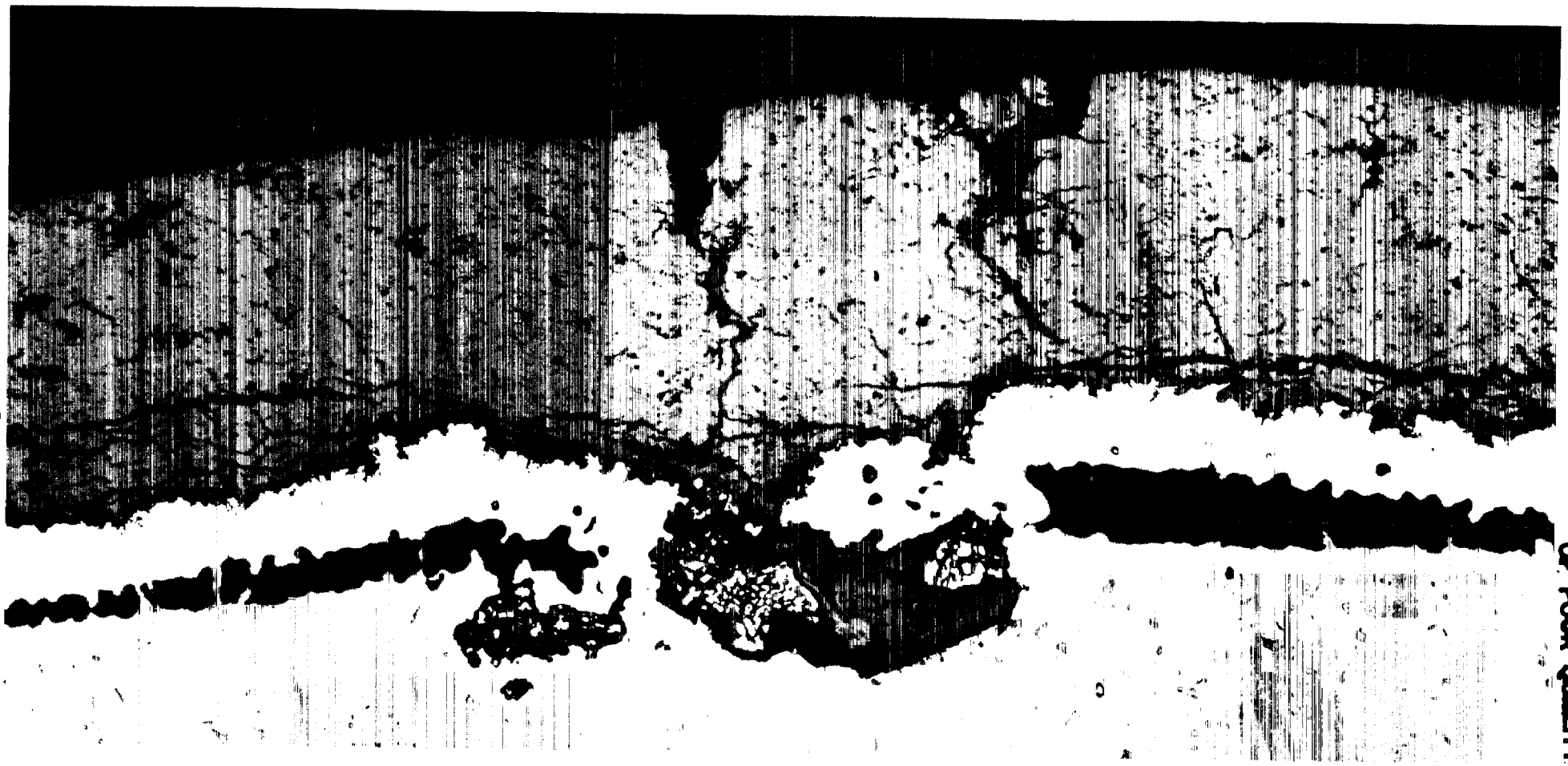

Figure 15 Light Photomicrograph of Post-Test Microstructure After 150 Hrs Fractional Exposure at 2100°F in Air

Figures 16a through 16c show the back scatter image photomicrographs for the post-test microstructure for the specimen furnace tested in Argon for 1040 hours at 2100°F. Although thermal exposure in Argon did not result in TBC failure, the microstructure reveals major crack formation at near-interface locations. Upon examination of the Back Scatter Image (BSI) photomicrographs, the bond-coat oxide appears to be a two-phase system. The first or major phase is dark and discontinuous. The second phase, or light areas in the oxide are believed to be unoxidized bond-coat evident by the polishing marks which are visable in Figure 16c. Figures 16d through h show the energy dispersion specra graphs for the various elements present, corresponding to the locations marked 1-5 on Figure 16b. Figures 17a through 17j show the X-ray maps for various elements present. It becomes clear from these maps that the dark interface phase is predominantly Al_2O_3. Cobalt, Ni, Cr are the major bond-coat elements and show a strong x-ray image, while Molybdenum, Hf, Ti and Ta are substrate elements which have clearly diffused into the bond coat. Some Ti and Hf enrichment is occurring at the bond coat-ceramic interface and many Hf enriched phases are also visible.

Figures 18a through 18c show back scatter images for the post-test micro-structure for the specimen furnace tested in air for 240 hours at 2100°F The figures show a thick, well defined, continuous, dual oxide layer. The dual layer oxide consists of a light oxide phase and a dark oxide phase. The light oxide seems almost porous and shows a network of extensions reaching into the ceramic. The darker phase however is very dense but with some secondary phases or "islands". A previous analysis showed that they seem to be either Hf-rich oxides or spinel-type oxide particles. Figures 18d through k, show the energy dispersion spectragraphs for the various elements present corresponding to the locations marked 1-8 on Figure 18c. Figures 19a through 19j show the X-ray maps for the various elements present. The maps show clearly that the "dark" portion of the oxide is Al_2O_3. Kirkendall voids are present at the substrate-bond coat interface. The x-ray map for Al shows a strong image of Al picked up in the void area. This assumed to be an artifact resulting from entrapment of Al_2O_3 polishing media. The "light" portion of the oxide appears to consist of spinel i.e., Ni or Co chromates. Hafnium, Ti and Ta appear to have diffused into the bond coat but do not appear to have greatly enriched any particular area at the bond coat-ceramic interface.

As shown previously Figures 13 and 14 represent the "fractional" exposure test specimen microstructures after exposure for 60% and 90% of the total exposure time. These specimens were not cycled periodically for inspection as were those discussed previously. Presumably as a consequence, they show less microcracking than the cycled specimens. Figure 15 shows the post-test specimen microstructure in cross-section through a blister which developed during the high temperature exposure for 100% of the total life time; 150 hours. It is highly probable that this blister was caused by an initial bond coat defect.

Two additional specimens were tested at 2100°F in air for 165 hours and 180 hours with one thermal cycle achieved upon removal from the furnace. These additional tests were conducted in order to verify the single cycle ceramic spalling life in terms of hours exposed in the furnace. Both of these specimens exhibited ceramic spallation after a single thermal cycle. Additional"cyclic" fractional exposure tests were also conducted where tests life was estimated 150 hrs at 2100°F with ten hour inspection intervals used.

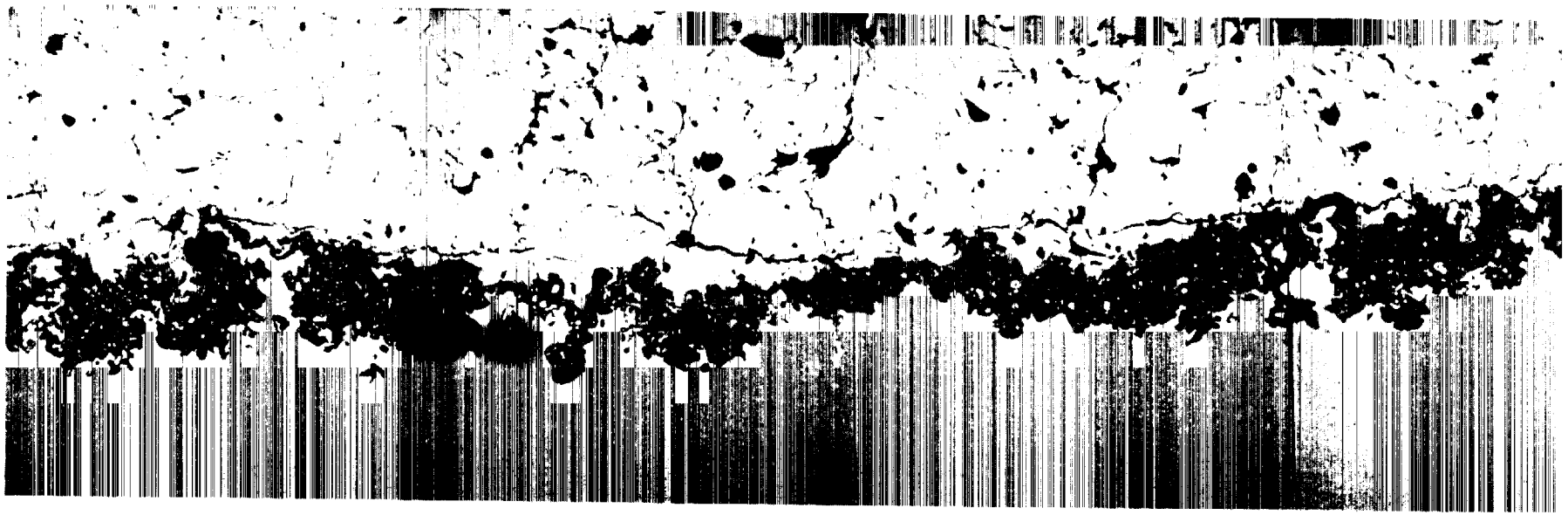

500X

Figure 16a Back Scatter Image of Post-Test Microstructure. Furnace Exposure in Argon at 2100°F for 1040 Hours (80 hour cycles - 13 cycles)

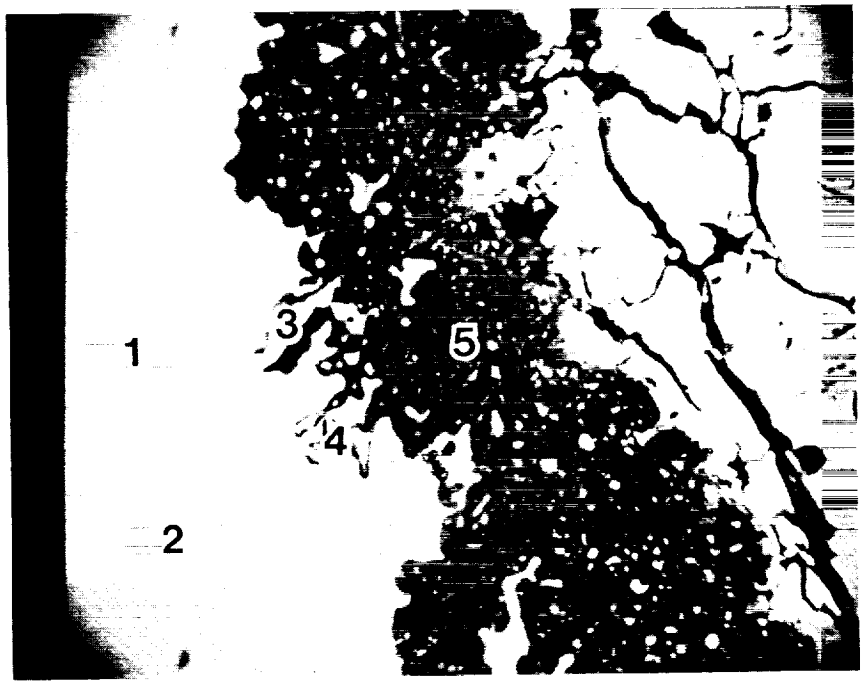

(b) 1200X (BSI)

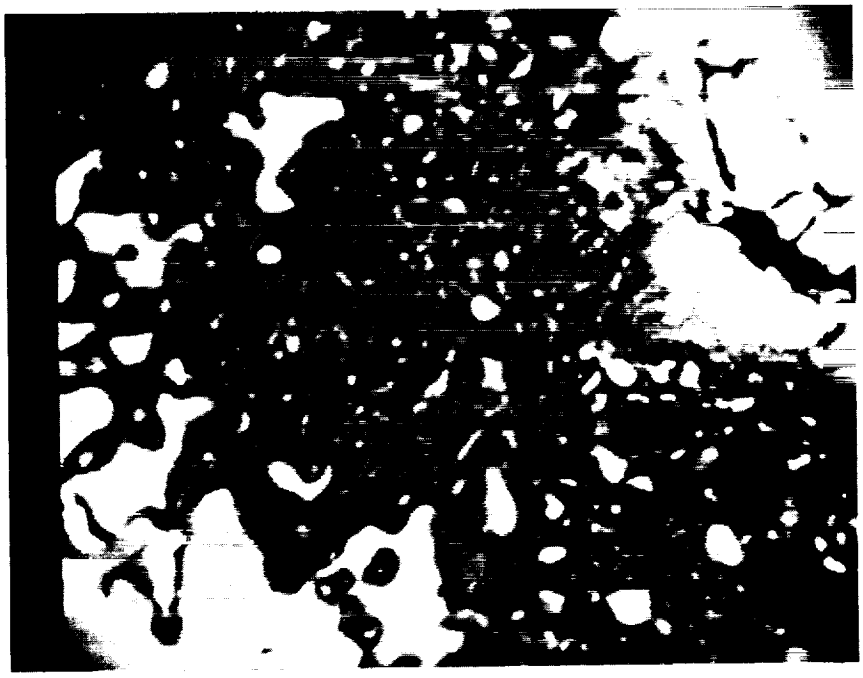

(c) 3000X (BSI)

Figure 16b and c Back Scatter Images of Post-Test Microstructure. Furnace Exposure in Argon at 2100°F for 1040 Hours (80 hour cycles - 13 cycles)

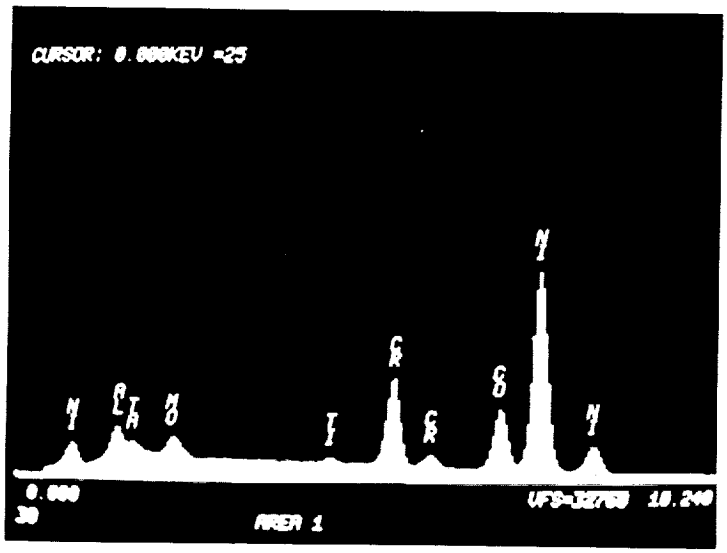

(d)

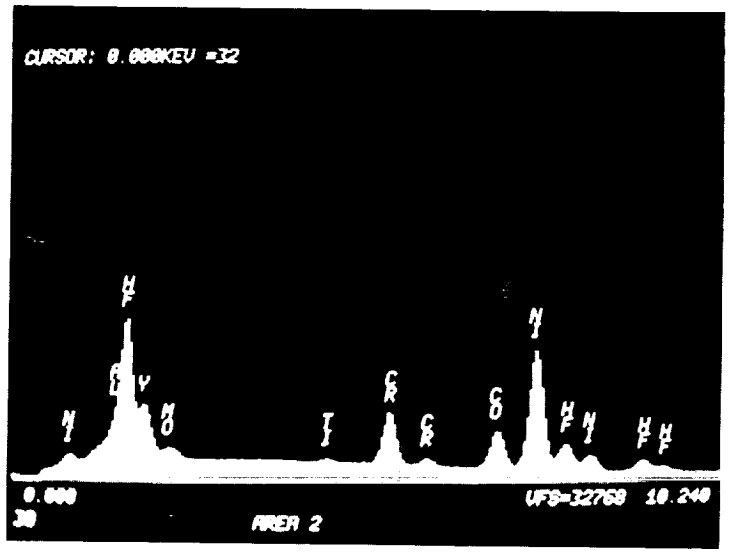

(e)

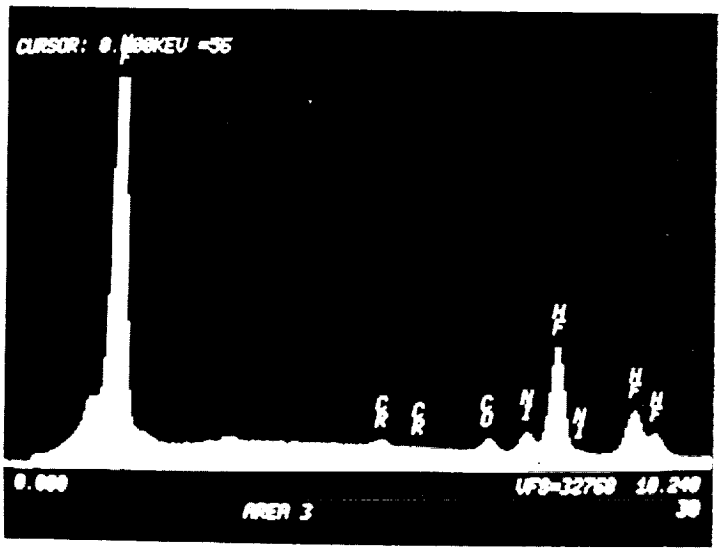

(f)

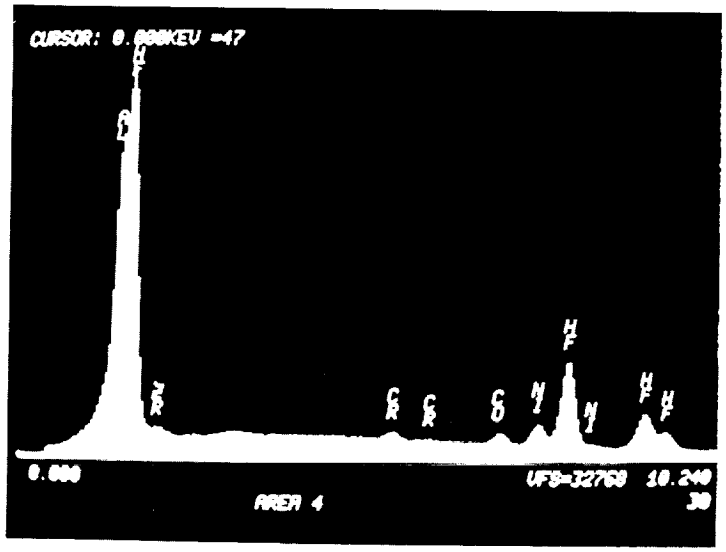

(g)

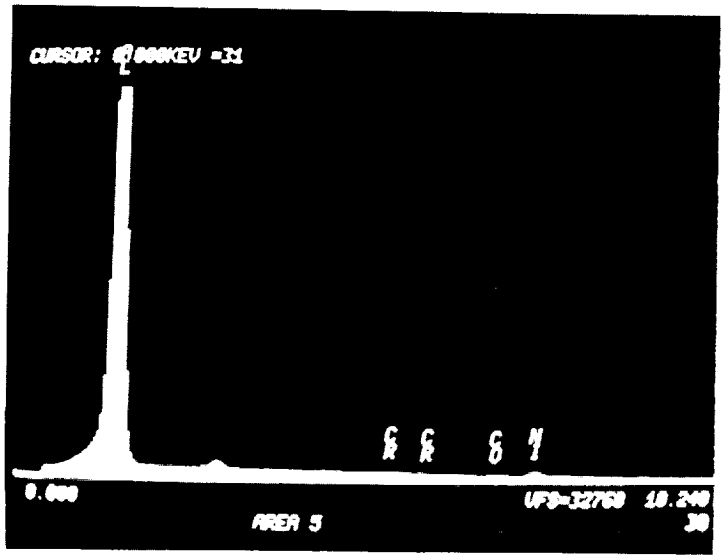

(h)

Figure 16d and h Energy Dispersion Spectragraphs for Elements Present at Various Locations Corresponding to Figure 16b. Argon Exposed 2100°F for 1040 Hours (80 hour cycles - 13 cycles)

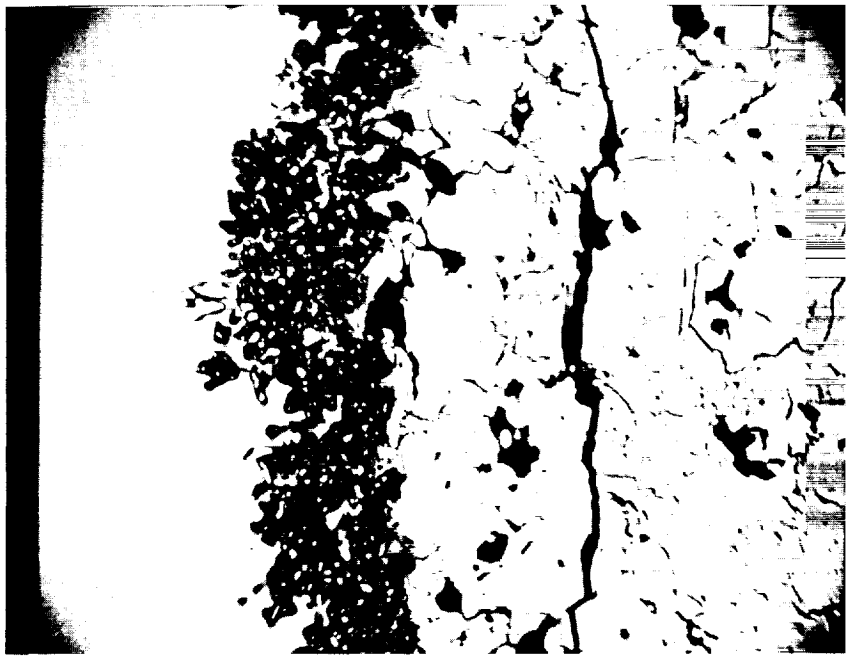

BACK SCATTER IMAGE (a) 800X

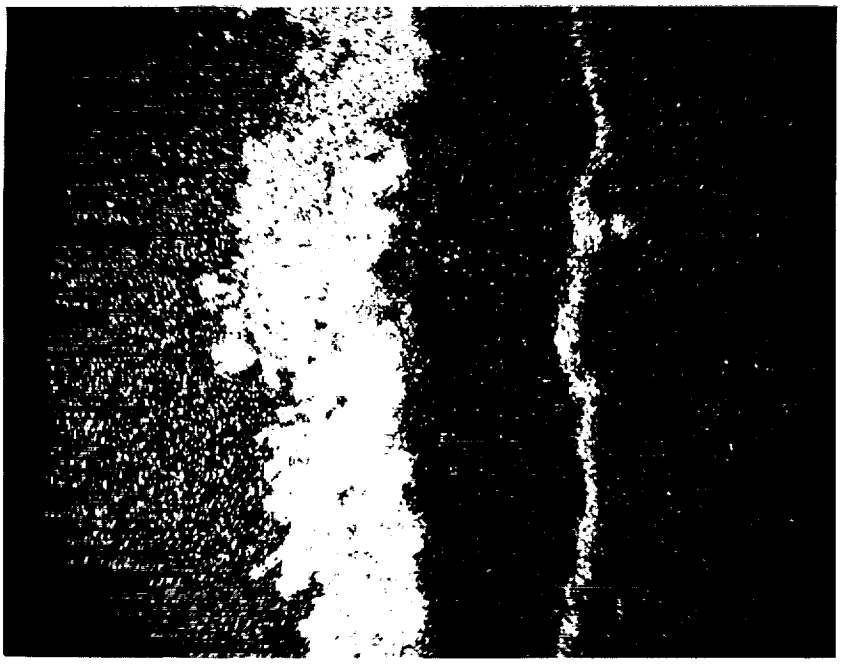

Al X-ray Map (b) 800X

Figure 17 a - j Post-Test Microstructure. Furnace Exposure in Argon at 2100°F for 1040 Hours (80 hour cycles - 13 cycles)

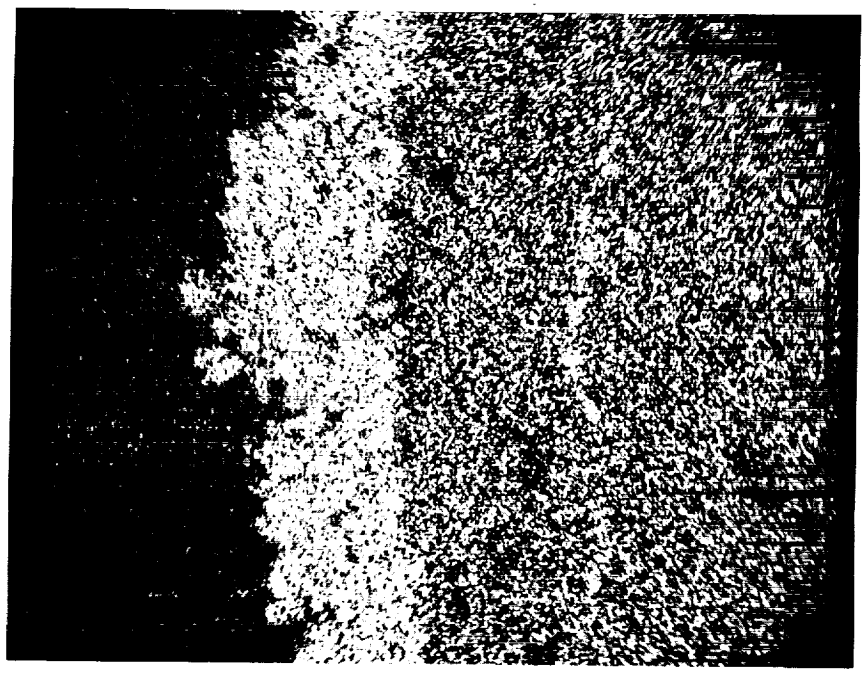

O X-ray Map (c) 800X

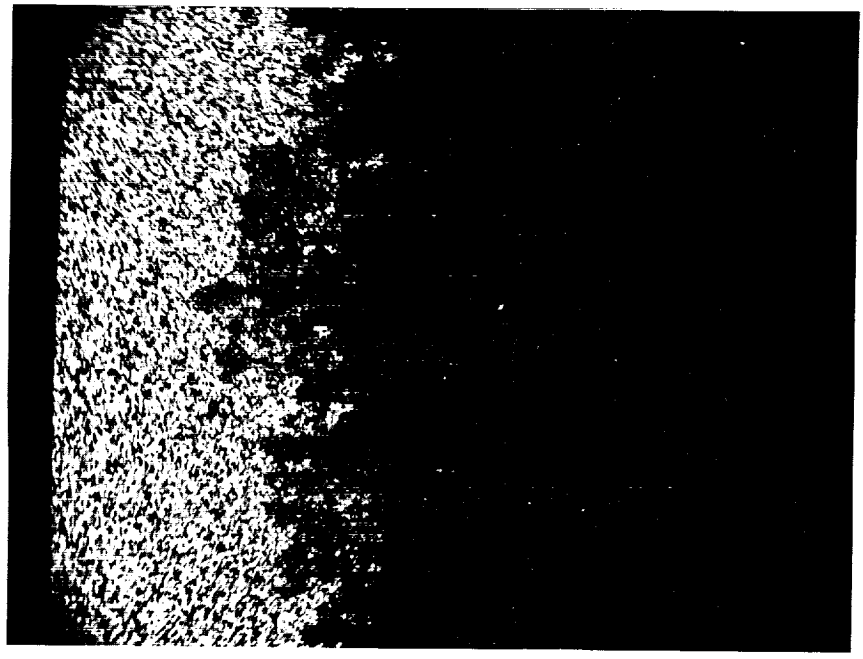

Co X-ray Map (d) 800X

Figure 17 (continued)

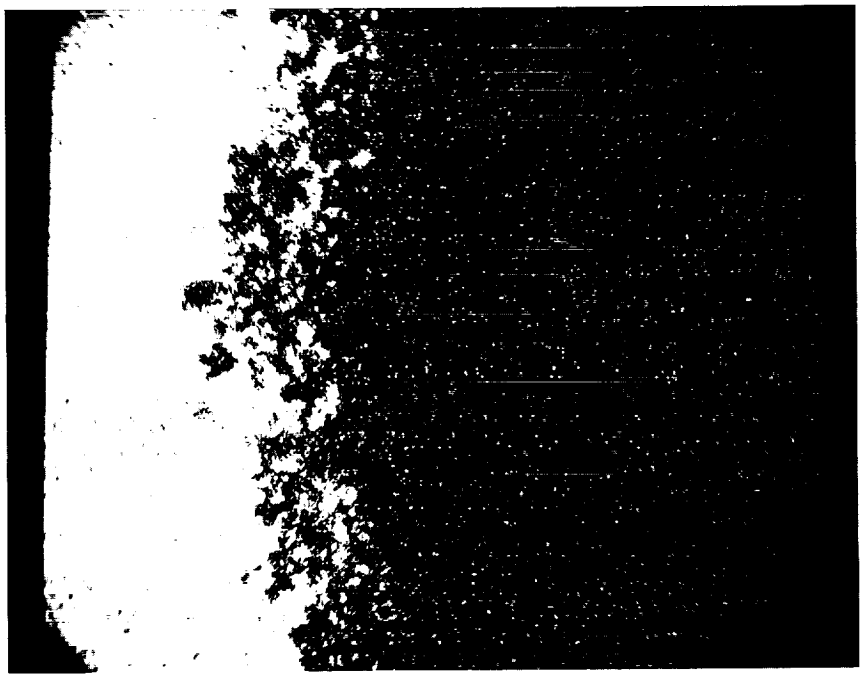

Ni X-ray Map (e) 800X

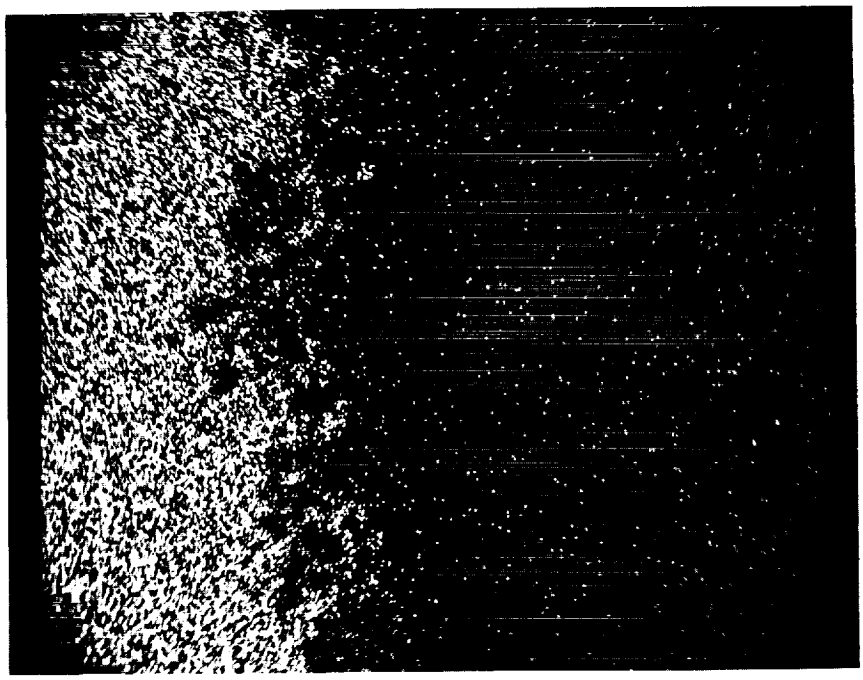

Cr X-ray Map (f) 800X

Figure 17 (continued)

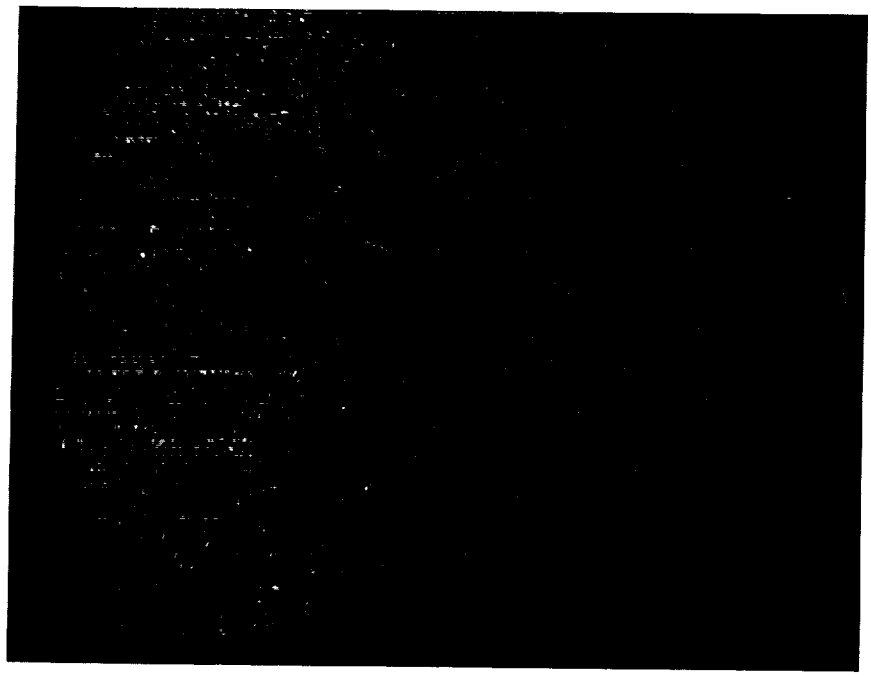

Mo X-ray Map (g) 800X

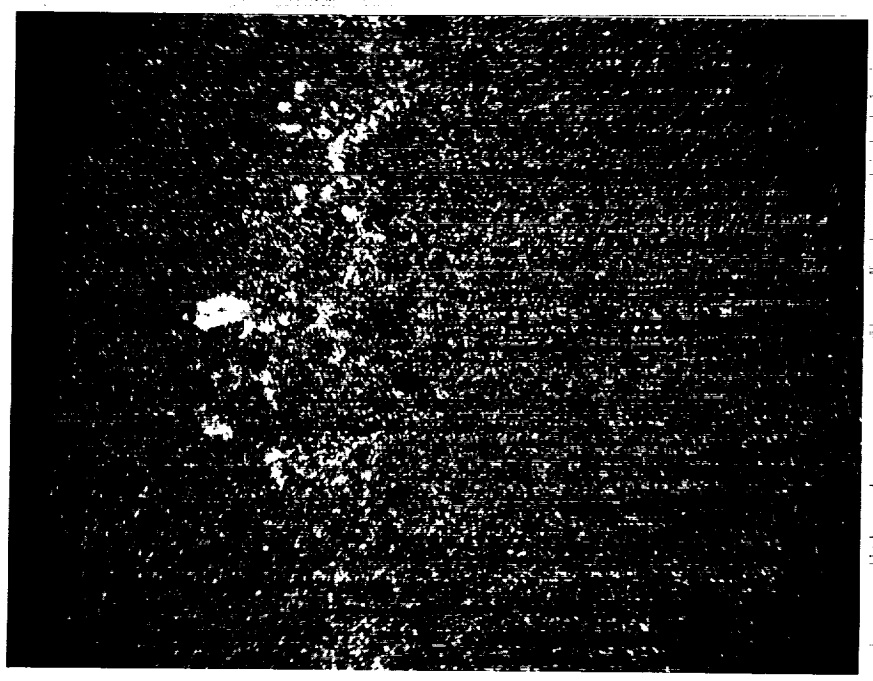

Hf X-ray Map (h) 800X

Figure 17 (continued)

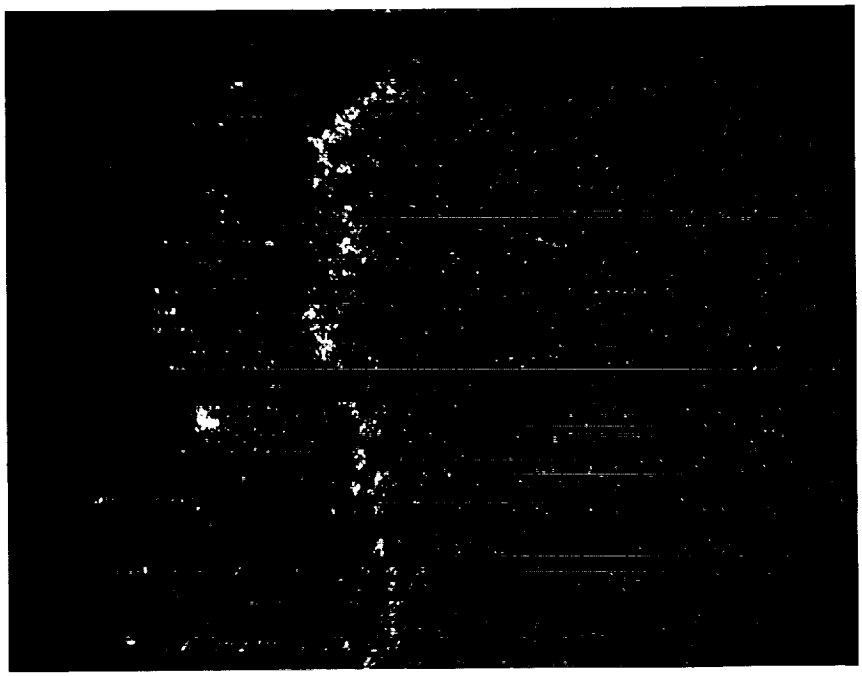

Ti X-ray Map (i) 800X

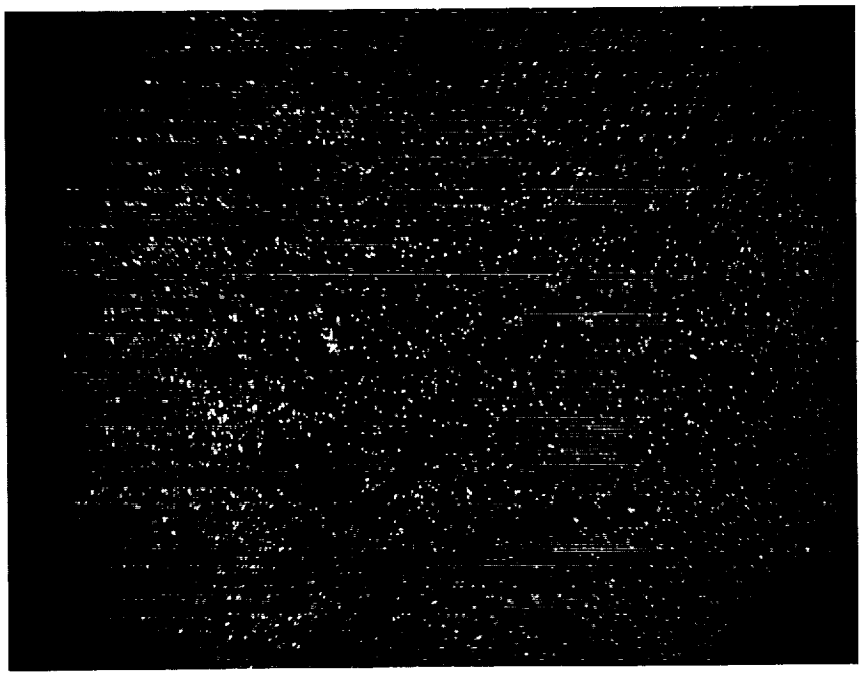

Ta X-ray Map (j) 800X

Figure 17 (continued)

500X

Figure 18a Back Scatter Image of Post-Test Microstructure. Furnace Exposure in Air at 2100°F for 240 Hours (80 hour cycles - 3 cycles)

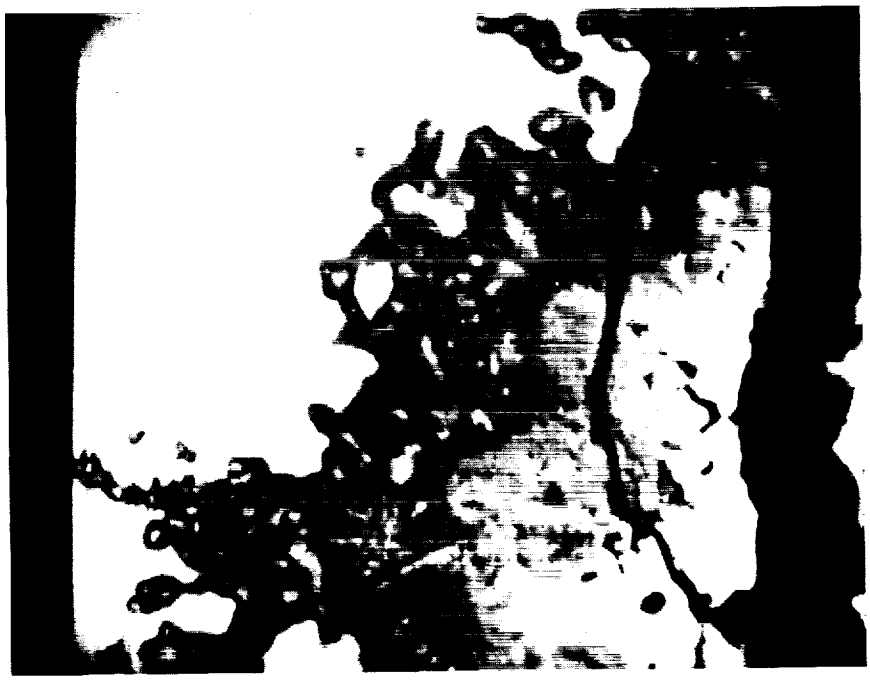

(BSI) (b) 2000X

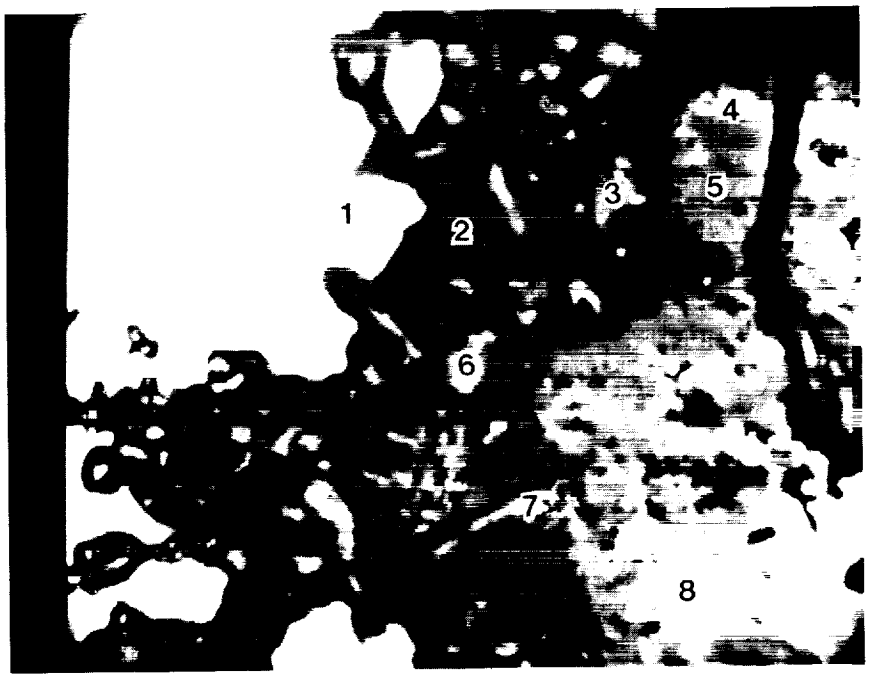

(BSI) (c) 2000X

Figure 18b - c Back Scatter Image of Post-Test Microstructure. Furnace Exposure in Air at 2100°F for 240 Hours (80 hour cycles - 3 cycles)

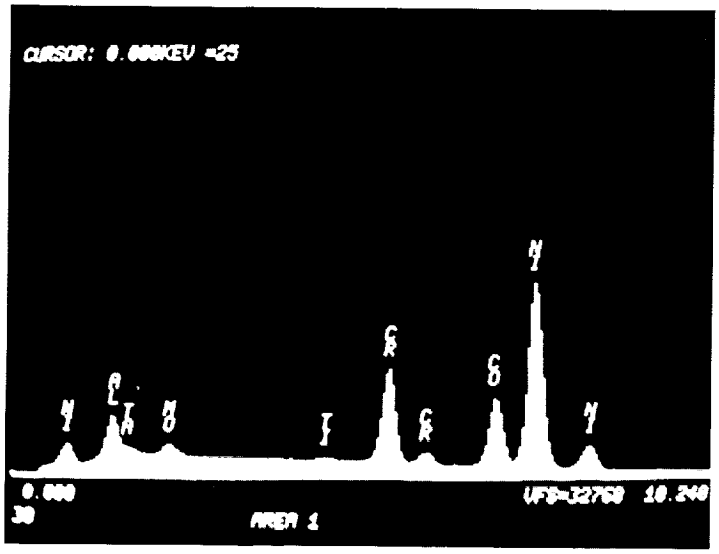

(d)

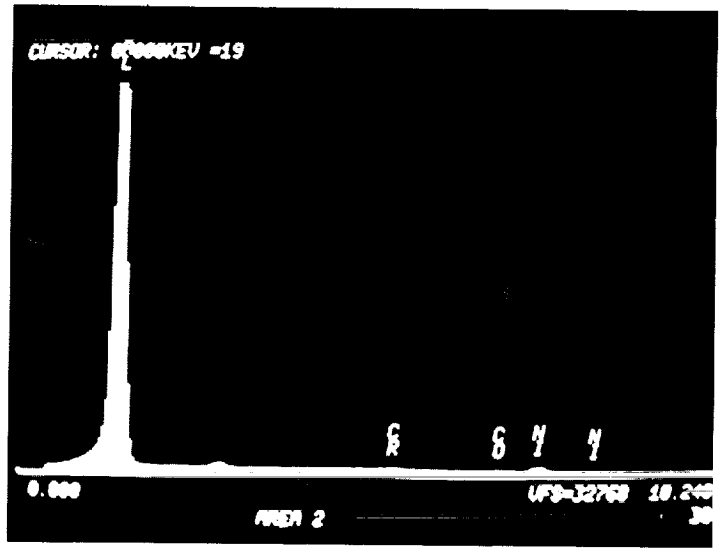

(e)

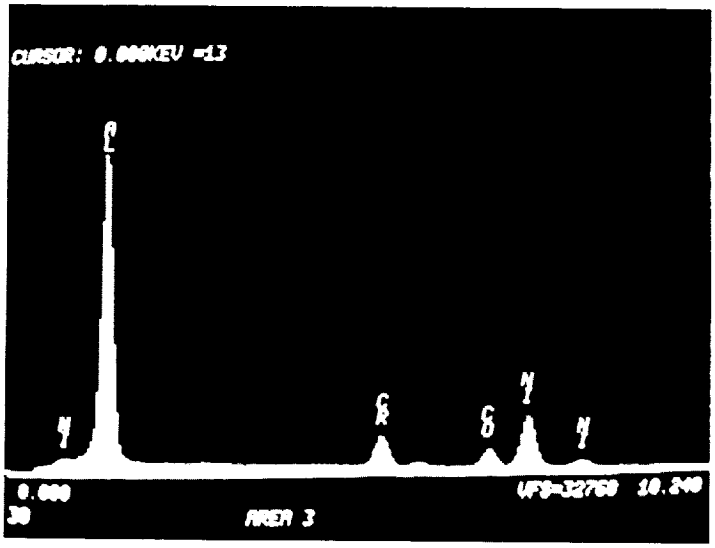

(f)

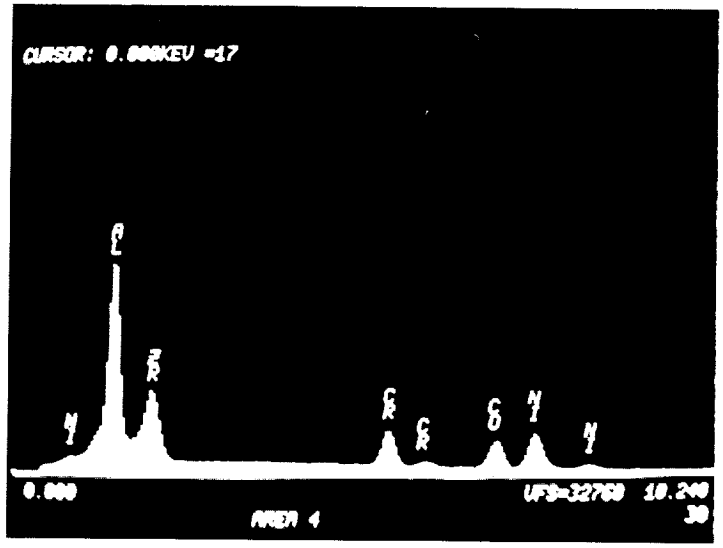

(g)

Figure 18d and g Energy Dispersion Spectragraphs for Elements Present at Various Locations Corresponding to Figure 18c. Air Exposed 2100°F for 240 Hours (80 hour cycles - 3 cycles)

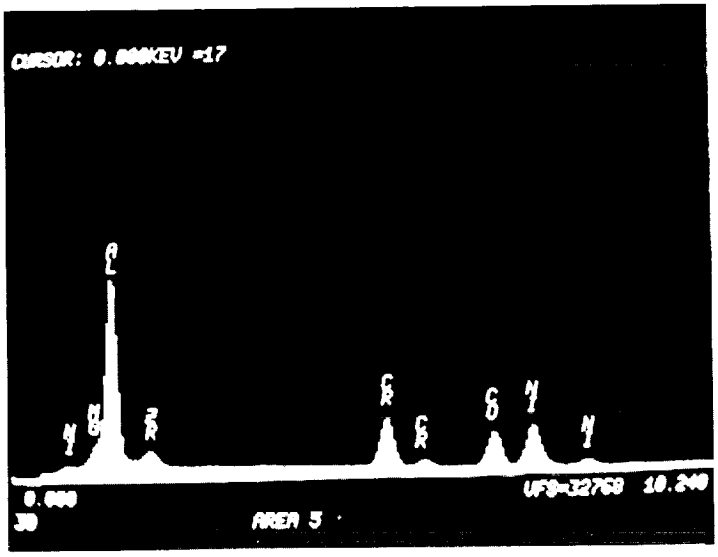

(h)

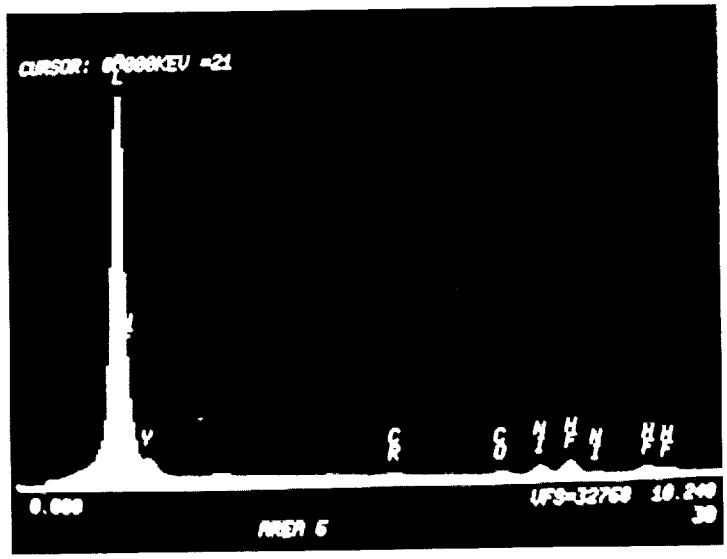

(i)

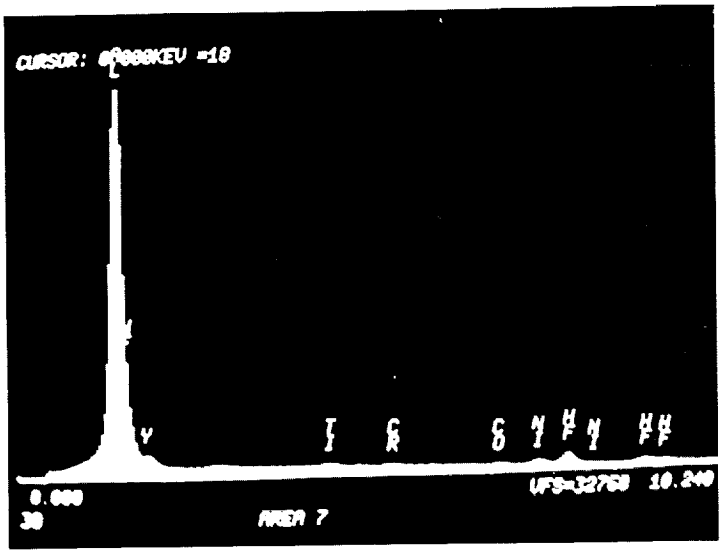

(j)

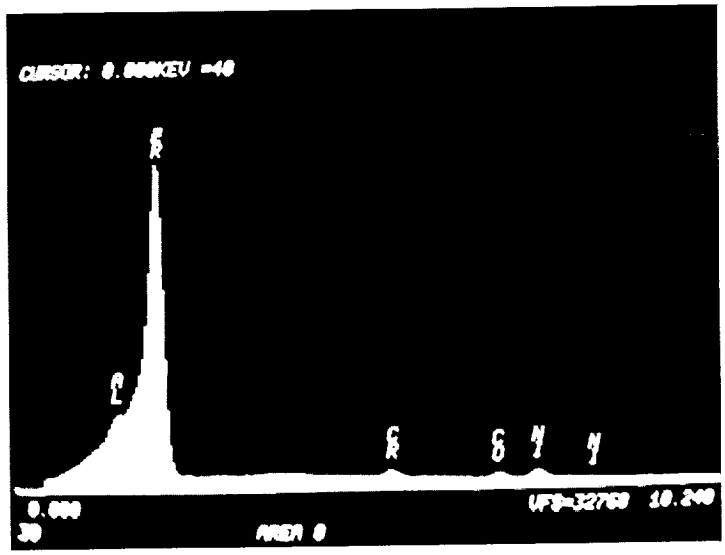

(k)

Figure 18h and k Energy Dispersion Spectragraphs for Elements Present at Various Locations Corresponding to Figure 18c. Air Exposed 2100°F for 240 Hours (80 hour cycles - 3 cycles)

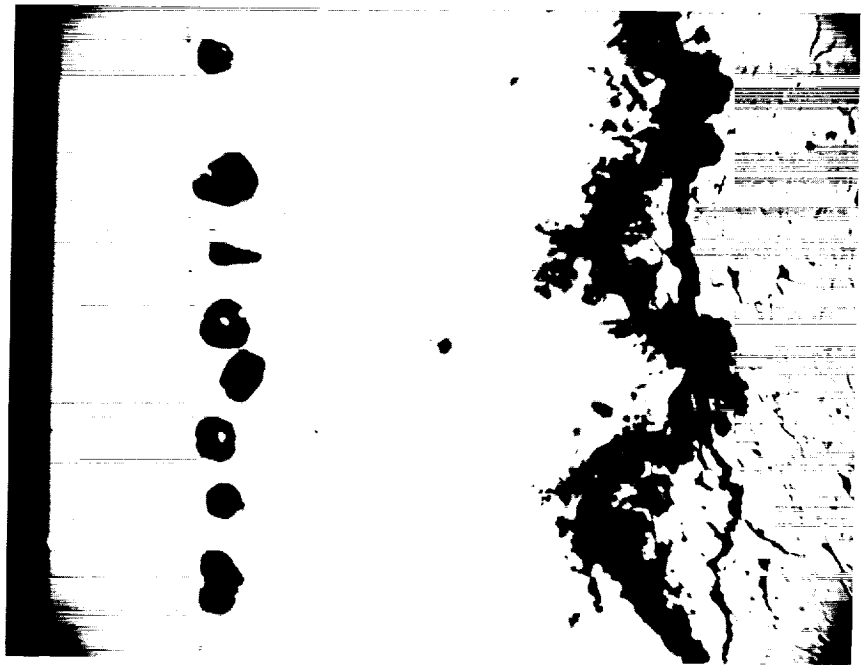

BACK SCATTER IMAGE (a) 400X

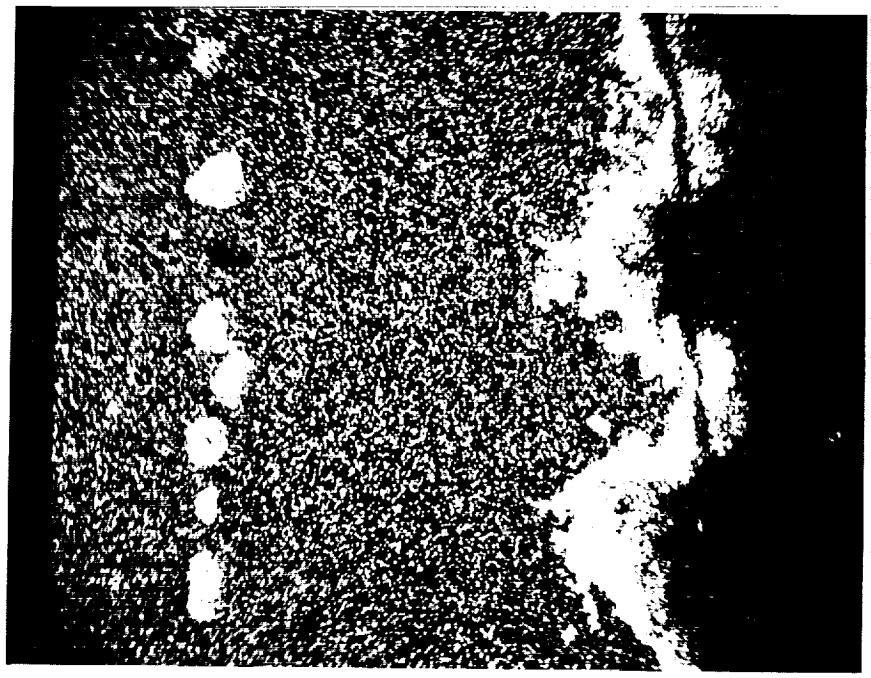

Al X-RAY MAP (b) 400X

Figure 19a - j BSI of Post-Test Microstructure. Furnace Exposure in Air at 2100°F for 240 Hours (80 hour cycles - 3 cycles)

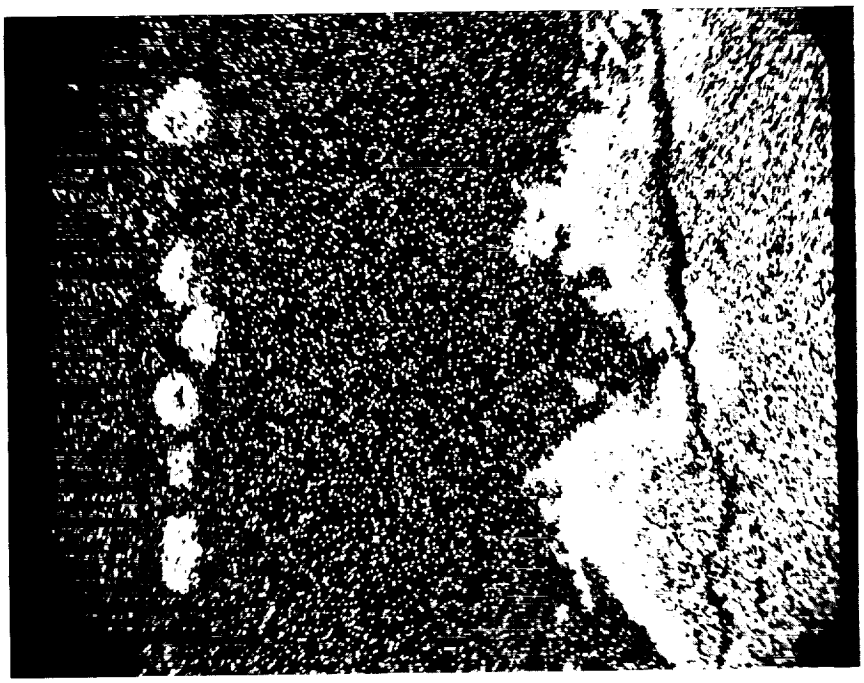

O X-RAY MAP (c) 400X

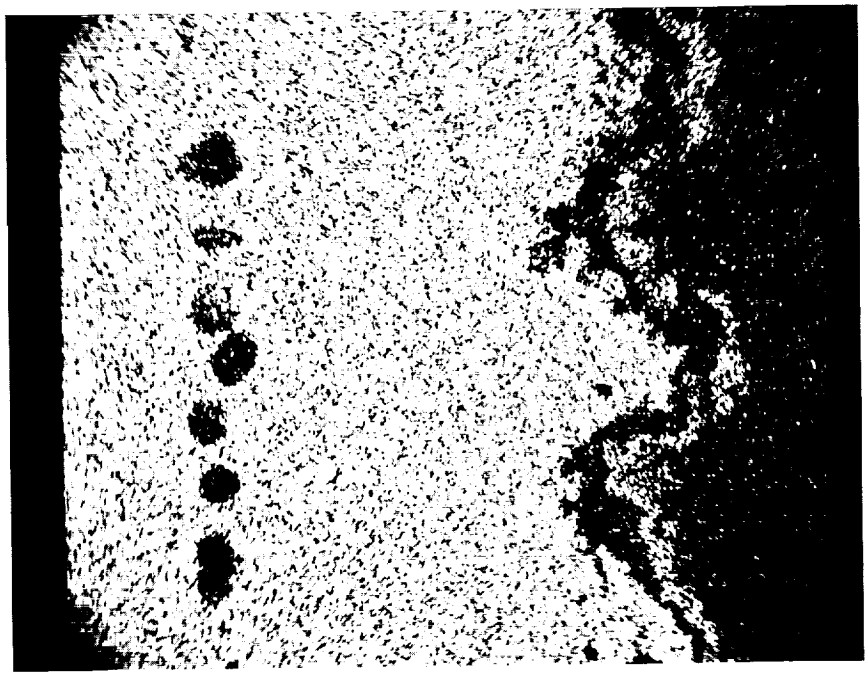

Co X-RAY MAP (d) 400X

Figure 19 (continued)

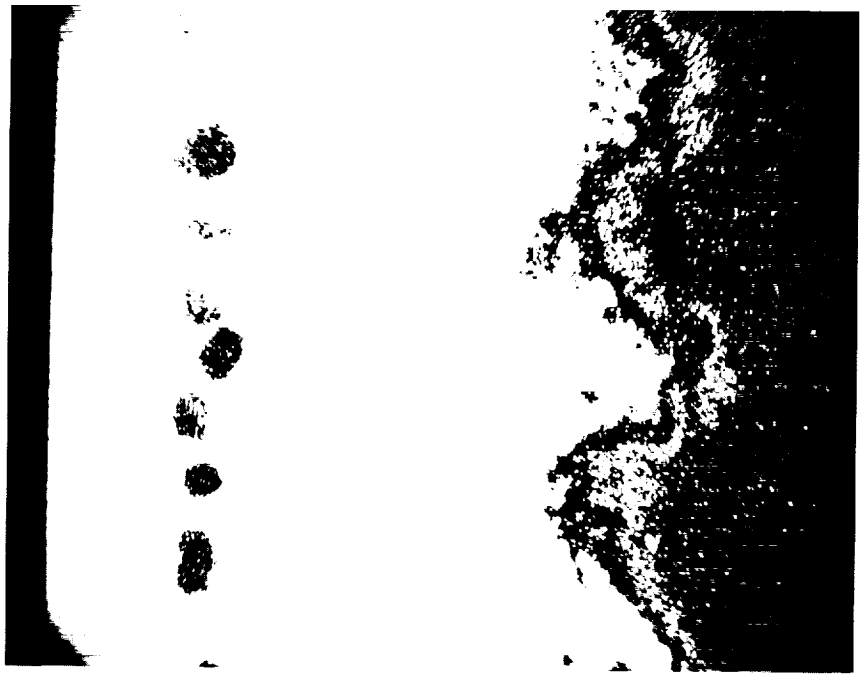

Ni X-RAY MAP (e) 400X

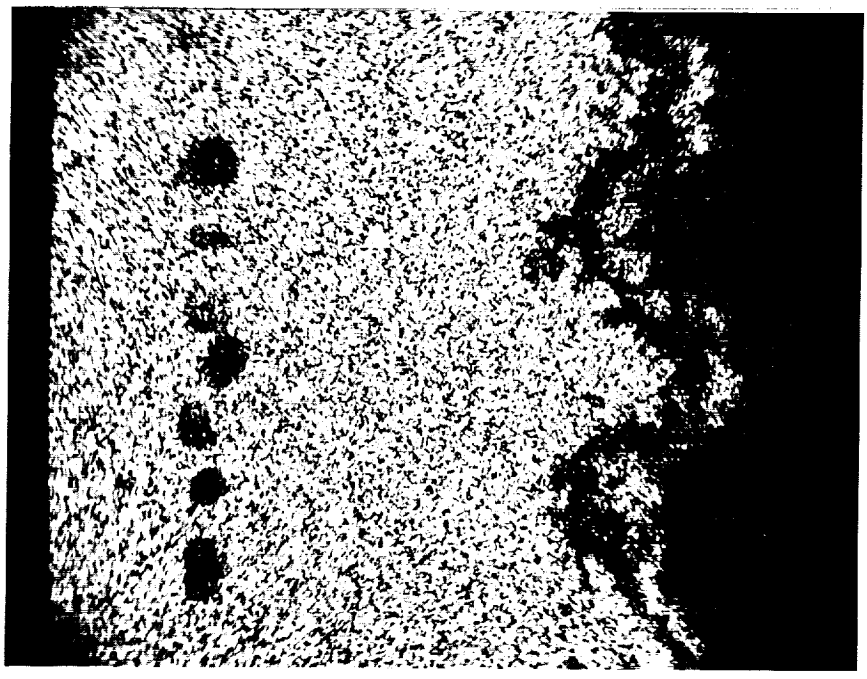

Cr X-RAY MAP (f) 400X

Figure 19 (continued)

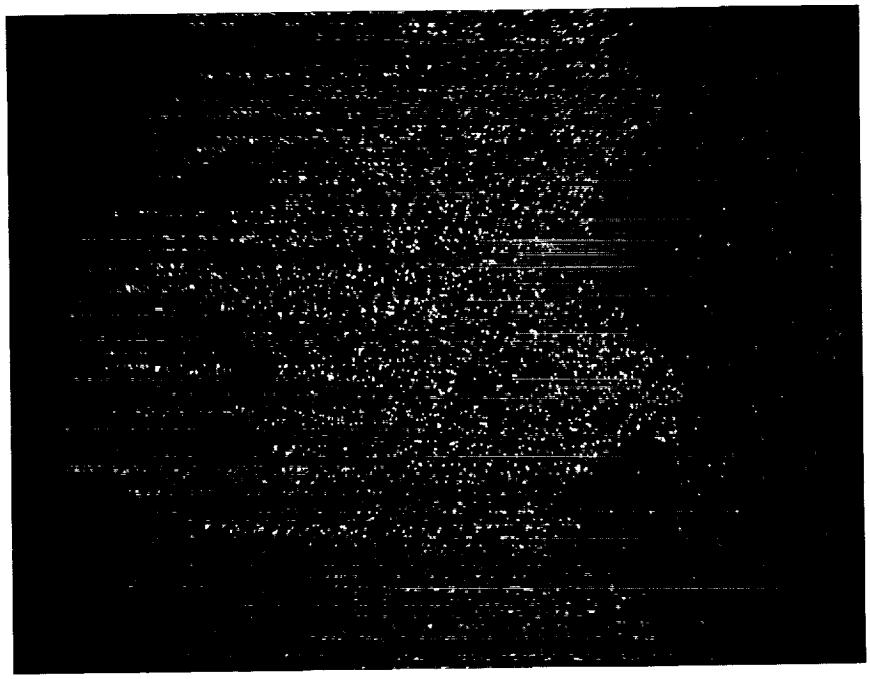

Mo X-RAY MAP (g) 400X

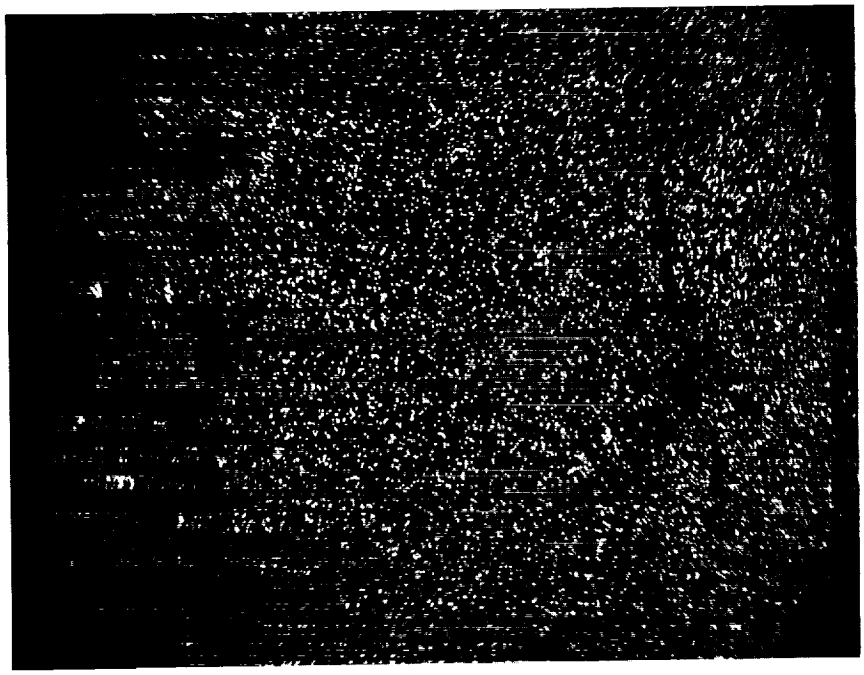

Hf X-RAY MAP (h) 400X

Figure 19 (continued)

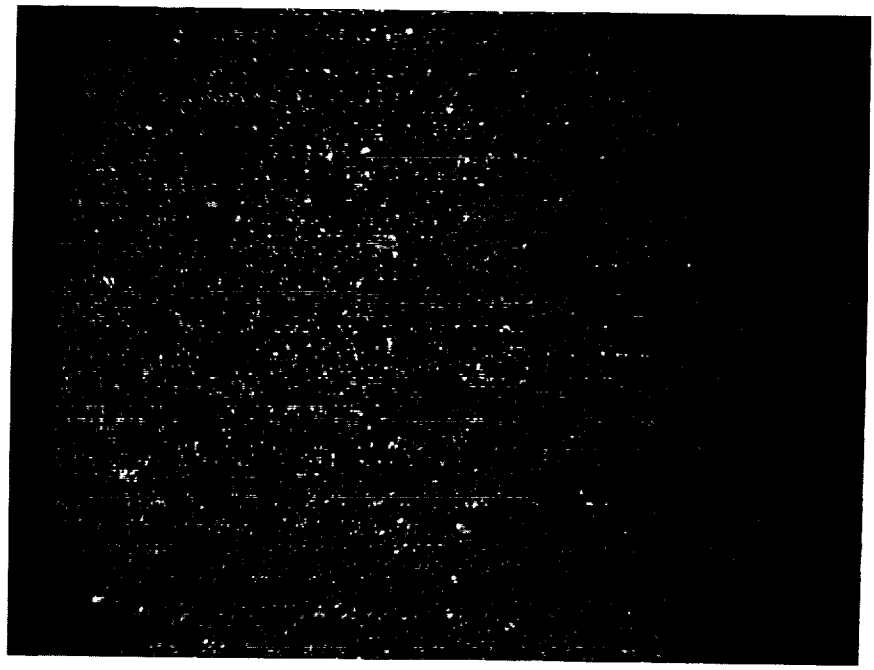

Ti X-RAY MAP (i) 400X

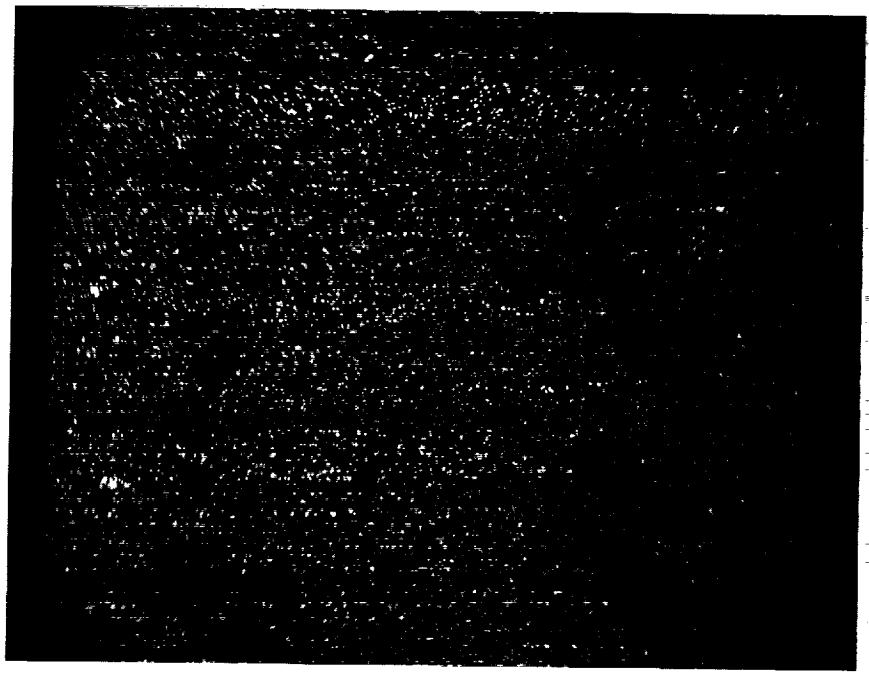

Ta X-RAY MAP (j) 400X

Figure 19 (continued)

As noted in Table VII, cracking occurred at the tip location for the 80% (120 hrs) specimen and major cracking and delamination was observed for the 100% (150 hrs) specimen. The metallographic results of the fractional exposure furnace test specimens showed near interface cracking was occurring at exposure times which are relatively short as compared with the total exposure lifetime of the coating. These "incipient" cracks appear to be a direct physical result of oxidation of the bond coat asperities. The subcritical cracks seen are short, fine and are directly linked to bond coat asperities. However, no "dominant" major subcritical cracking is observed, nor is the gradual growth of singularly large cracks, which may result in spallation, seen.

3.1.2.2 Cyclic Thermal Exposure Tests

A partial factorial test program shown in Figure 20 was conducted to determine the influence of temperature, cycle rate, coating thickness and static pre-exposure on coating cyclic thermal failure life and to provide preliminary information concerning interactions between static and cyclic thermal failure modes.

MAXIMUM CYCLE TEMPERATURE	TRANSIENT HEATING RATE	SHORT CYCLE		LONG CYCLE	
		CYCLE TO FAILURE	FRACTIONAL EXPOSURE	CYCLE TO FAILURE	FRACTIONAL EXPOSURE
2100	FAST	⑨ D_1	⑩ G	⑪ F	⑫ X
	SLOW	⑭ E	⑬ X	⑮ X	⑯ X
2000	FAST	⑰ D_2	⑱ X	⑲ X	⑳ X
	SLOW	㉑ X	㉒ X	㉓ X	㉔ X

CONDITION D,E,F – 12 SPECIMENS PER TEST.

4 – 10 MIL VIRGIN CERAMIC ("BASELINE" COATING)
2 – 5 MIL VIRGIN CERAMIC
2 – 15 MIL VIRGIN CERAMIC
2 – 10 MIL AIR PRE-EXPOSED CERAMIC } 40 HR AT 2100 °F FOR 2100°F TESTING
2 – 10 MIL ARGON PRE-EXPOSED CERAMIC } 100 HR AT 2000°F FOR 2000 °F TESTING

CONDITION G:

FRACTION EXPOSURE TEST, DESCRIBED IN TEXT

Figure 20 Task I Clean Fuel Cyclic Burner Rig Test Program

The test method used to measure cyclic coating life involved uncooled cyclic burner rig testing as described in Appendix B. The Jet A fueled burner employed in this test simulates the clean fuel combustor environment in which most hot section components operate. The primary method of temperature control in this test involved optical measurement of specimen surface temperature. To ensure consistent test conditions, a thermocoupled specimen was employed at all times during testing to monitor/calibrate test temperature. To provide

specimen temperature distributions required for subsequent preliminary life prediction modeling (Task IC), instrumented specimens were tested, as needed, to characterize specimen temperature distributions for each of the test conditions studied.

Baseline cyclic life of the TBC was determined as a function of maximum substrate temperature by exposure of eight baseline coated burner rig test specimens to the test condition identified as "D1" and five baseline coated specimens to test condition "D2" in Figure 20. Cycle duration in these tests was 6 minutes, with 4 minutes of flame immersion (1 - 1.5 minutes to temperature + 2.5 - 3 minutes at temperature) and 2 minutes forced air cooling. Each specimen was cycled to failure, with failure being defined as spallation of the TBC over approximately 50% of the specimen hot zone which amounts approximately to a 1/2" X 1/2" size patch. A photograph of a typical failed burner rig test specimen is shown in Figure 21.

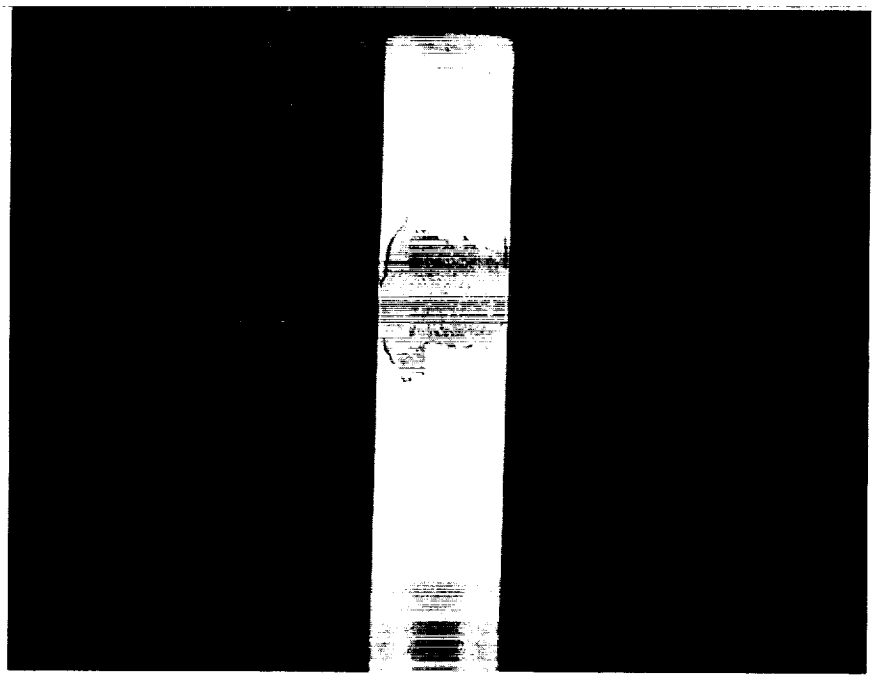

~1.5 X

Figure 21 Photomicrograph of Typical Burner Rig Failed Specimen

To provide information on the influence of transient heating rate on thermal barrier coating spalling life, six specimens were tested to failure at a transient heating rate which was approximately three minutes instead of one minute. Results of these tests, identified as "E" in Figure 20, were used in Task IC and subsequent life prediction modeling analyses.

Two approaches were employed to evaluate interaction(s) between thermal exposure and cyclic degradation modes. The first of these involved cyclic exposure as defined above with a longer cycle duration (identified as "long cycle" in Figure 20). The long cycle employed was 60 minutes, involving 57

minutes flame immersion (approximately 1 - 1.5 minutes to temperature + 55.5 - 56 minutes at temperature) and 3 minutes forced air cooling. Four "baseline" thermal barrier coated specimens were cycled to failure at the condition identified as "F" in Figure 20.

A second approach to evaluate interactions between cycling and thermal exposure involved cyclic testing of furnace pre-exposed specimens at the same cyclic conditions as the baseline specimens. The test plan involved pre-exposure of test specimens in air and in argon to approximately one-half of the estimated respective total hot times which were anticipated for failure of the baseline coating in the corresponding test. Pre-exposure durations were selected on the basis of prior experience. The actual pre-exposure "life fraction" was calculated from baseline test results after testing was completed. Four pre-exposed specimens, two each exposed in oxidizing and non-oxidizing environments, were tested at each of the test conditions identified in Figure 20.

To determine the influence of ceramic thickness on coating life, two specimens coated with a nominal 5 mil thick ceramic and two specimens coated with a nominal 15 mil thick ceramic were included in each of the four burner rig tests indentified as 9, 11, 13, and 17 in Figure 20.

To provide information concerning the nature and rate of accumulation of coating damage, a fractional exposure test, identified as "G" was conducted. In this test, two groups of specimens were exposed to approximate decile fractions of the cyclic failure life and examined metallographically to identify possible progressive damage mode(s) which cause ceramic spalling failure. In the first group, specimens were cycled to each of the approximately 10%, 20%, 30%, 40%, 50%, 60%, 70%, 80%, and 90% fractions of the estimated cyclic failure life defined in the "D1" test. A single specimen was included in this first group which was tested until failure and then life fractions of the other specimens in this group were adjusted accordingly. The second group of specimens were cycled to life fractions exposure times which were chosed to focus on giving better resolution to the actual failure time.

3.1.2.2.1 Cyclic Thermal Exposure Test Results

A comparative summary of the Task IB burner rig test results is presented in Table IX. Detailed results for each test are listed in Table X.

Review of these data clearly indicates exposure temperature to have a strong influence on spallation life. Comparison of baseline coating lives at 2000°F and 2100°F (D2 versus D1 results in Table IX) indicates approximately 60 percent reduction in life for a 100°F increase in exposure temperature. This temperature effect is shown graphically in Figure 22, where estimated total hot time to failure is plotted versus exposure temperature for the D1 and D2 baseline tests together with results from other tests conducted on internal programs. Also included for comparison in Figure 22 are results of the quasi-static failure tests shown previously in Figure 6. This comparison clearly shows the influence of thermal cycling of spallation life. The reason for the apparent curvature of the cyclic data in Figure 22, as opposed to the apparently linear behavior of the static data, is not presently understood.

TABLE IX
COMPARATIVE SUMMARY OF TASK IB BURNER RIG TEST RESULTS
TOTAL HOURS TO FAILURE/CYCLES TO FAILURE/
ESTIMATED HOURS OF HOT TIME TO FAILURE*

TEST CODE/ CONDITION	STANDARD "BASELINE" AVERAGE	THIN AVERAGE	ARGON PRE-EXPOSED AVERAGE	THICK AVERAGE	AIR PRE-EXPOSED AVERAGE
D1/2100°F I.D., Short Cycle - Fast Heat Up Rate	186/1860/77	238/2380/99	215/2150/130	132/1320/55	50/500/61
D2/2000°F I.D., Short Cycle - Fast Heat Up	471/4710/235	525/5250/263	694/6940/447	470/4700/235	205/2050/203
E/2100°F I.D., Short Cycle Slow Heat Up	135/1350/22	162/1620/27	142/1420/64	121/1210/20	29/290/45
F/2100°F I.D., Long Cycle Fast Heat Up	72/72/67	119/119/110	98/98/162	59/59/55	16/16/55

*Estimated hours of hot time to failure include time for Air and Argon thermal exposure prior to burner rig testing.

TABLE X
BURNER RIG TEST RESULTS

TEST CODE/ TEST CONDITION	"BASELINE" STANDARD	AIR PRE-EXPOSED	ARGON PRE-EXPOSED	THICK CERAMIC	THIN CERAMIC
D1/2100°F, Short Cycle - Fast Heat Up Rate	182, 172, 213, 175, 172, 193, 182, 198 } AVG = 186	50, 50 } AVG = 50	75, 67, 279, 279, 279, 279, 221, 199, 199, 271 } AVG = 215	104, 160 } AVG = 132	243, 232 } AVG = 238
D2/2000°F, Short Cycle - Fast Heat Up Rate	386, 443, 435, 557, 536 } AVG = 471	194, 215 } AVG = 205	679, 708 } AVG = 694	515, 425 } AVG = 470	557, 492 } AVG = 525
E1/2100°F, Short Cycle Fast Heat Up Rate	156, 129, 142, 142, 121, 121 } AVG = 135	39, 18 } AVG = 29	142, 142 } AVG = 142	121, 121 } AVG = 121	162, 162 } AVG = 162
F1/2100°F, Long Cycle Fast Heat Up Rate	70, 60, 59, 98 } AVG = 72	16, 16 } AVG = 16	93, 102 } AVG = 98	54, 64 } AVG = 59	116, 122 } AVG = 119

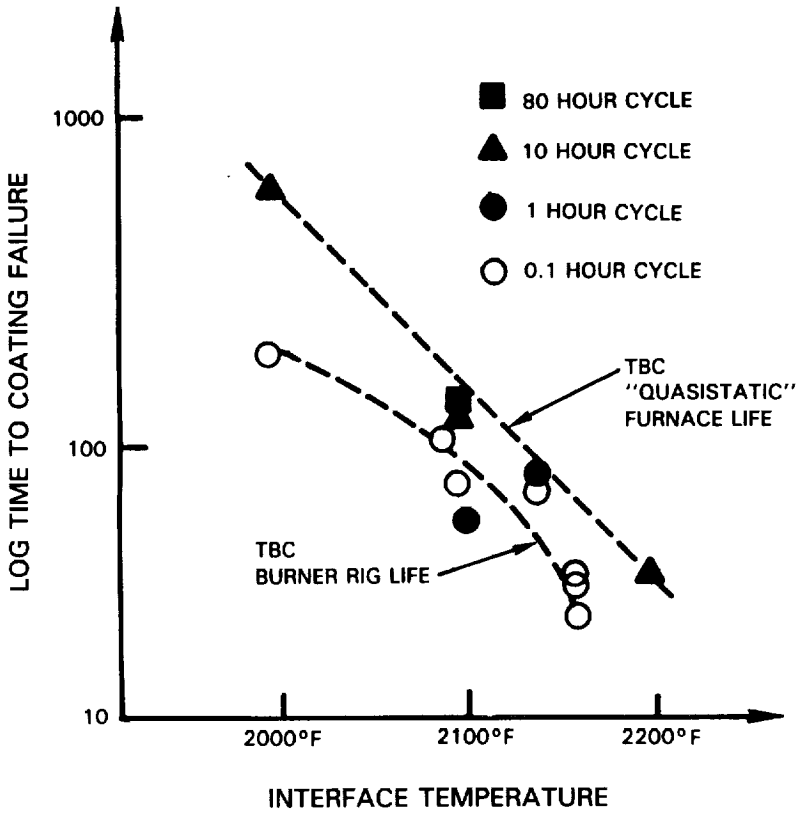

Figure 22 Test Data Showing Coating Life Dependent on Temperature, "Cyclic Content"

The effect of cycle frequency on spallation life is shown by comparison of the D1 and F test results in Table IX. When compared on the basis of cycles to failure, a dramatic life reduction is seen; however, when compared on the basis of estimated time at maximum exposure temperature, cyclic frequency is seen to have a relatively little influence on life in the frequency range and at the temperature studied, as seen in Figure 22. This latter observation must be interpreted with some caution, as the 2100°F temperature where the frequency effect was studied is, by coincidence, the temperature of closest approach of the cyclic and quasi-static life data. It is possible that, had the effect of frequency been measured at a lower or higher temperature, a more significant influence on life might have been seen.

As described previously, Test E was conducted to assess the influence of transient heating rate on spallation life. It was expected that the slower transient and reduced time at temperature would increase life; however, as seen in Table IX, spallation life appears to have been slightly reduced by this change of test parameters. This result is not fully understood at the present time; however, evaluation of this data set by the subsequently discussed preliminary prediction system indicates that the difference of life between the baseline and reduced transient results could be accounted for by a temperature error of less than ten degrees, which is within the inherent accuracy of the thermocouple based instrumentation system used to establish temperature for these two tests. Based on this observation, it seems reasonable to conclude at this point that the reduction of transient heating rate appears to have no significant influence on life within the range of scatter inherent in the burner rig test.

In an effort to assess the influence of thermal exposure on spallation life, and to separate thermal from environmental effects, coated specimens which were thermally pre-exposed in both oxidizing and non-oxidizing environments were included in several of the burner rig tests discussed above. As illustrated in Figures 23 and 24, results of these tests indicate that isothermal pre-exposure in air causes a significant reduction of subsequent cyclic spalling life, while pre-exposure in a non-oxidizing environment does not reduce life. It is interesting to note in Figure 23 that the total time at temperature for spallation of the air pre-exposed specimens is roughly comparable to hot time to failure for cyclically tested baseline specimens. This observation, coupled with the absence of a life debit for non-oxidizing pre-exposure, strongly suggests that oxidization is a primary thermal barrier coating degradation mechanism.

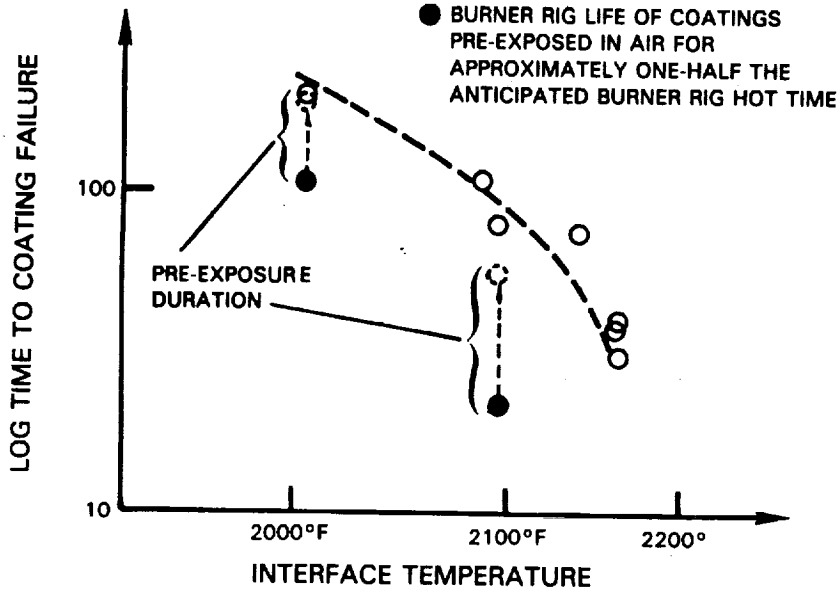

Figure 23 Test Data Showing Air Pre-Exposure Degrades Cyclic Life

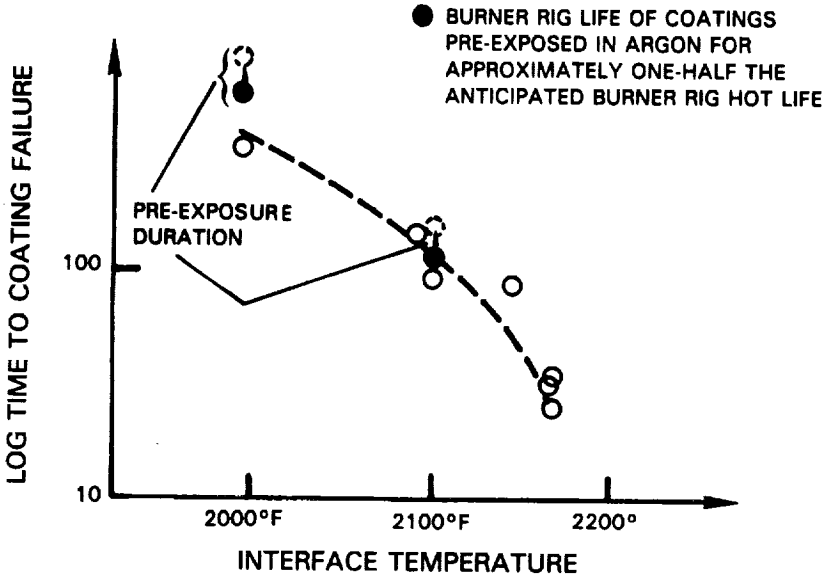

Figure 24 Test Data Showing "INERT" (ARGON) Pre-Exposure Does Not Affect Coating Performance

The influence of ceramic thickness on baseline test spallation life is illustrated in Figure 25. As expected, reducing ceramic thickness provides a small increase of life, while increasing thickness reduces life. Examination of the data in Table IX indicates that this effect is consistent for the various test parameters investigated.

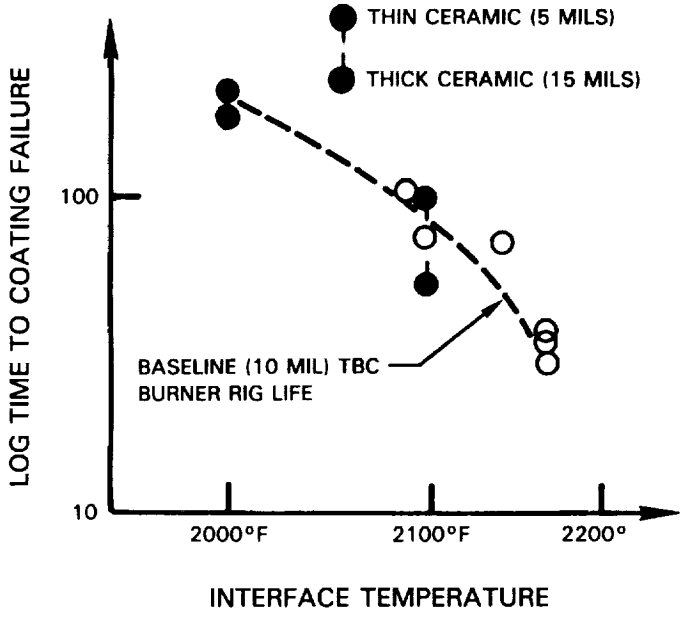

Figure 25 Test Data Showing Ceramic Thickness Effects

3.1.2.2.2 Microstructural Evaluation for Cyclic Thermal Exposure Tests

In an effort to better understand the phenomenological observations discussed above, failed burner rig specimen were examined metallographically. All burner rig specimens exhibited "typical" near interface ceramic spallation, with a thin layer of ceramic remaining adherent to the bond coat after failure.

Figures 26 through 29 show representative baseline pre-test and post-test microstructures for all four burner rig test conditions. In comparing the baseline laboratory post test microstructures with engine exposed failures, "oxidation damage" (oxide thickness) appears to be somewhat greater for the laboratory test specimens. This is attributed to the relatively high interface temperatures employed in the accelerated laboratory spallation life testing. Oxide thickness is on the order of 0.0003 inches for all the tests except for the long cycle 2100°F test in which oxide thickness was estimated to be twice as thick. Thermal gradient testing to be conducted in Task II is expected to more closely simulate engine exposure condition. The microstructures also show Kirkendall voids which have aligned themselves at the original bond coat-substrate interface suggesting bond-coat/substrate compositional changes.

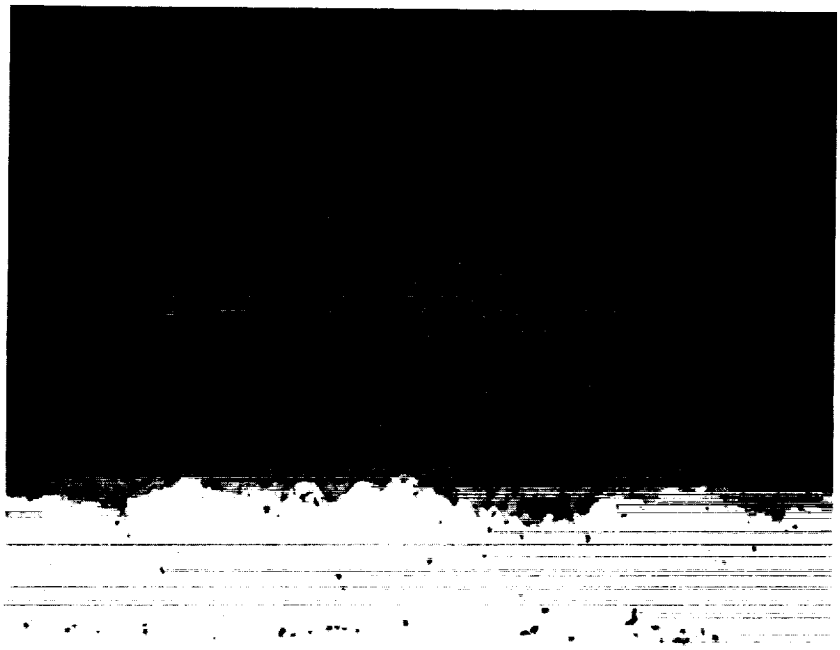

200X
Unetched

Figure 26a Light Photomicrograph of Baseline Pre-Test Microstructure (D1 Test)

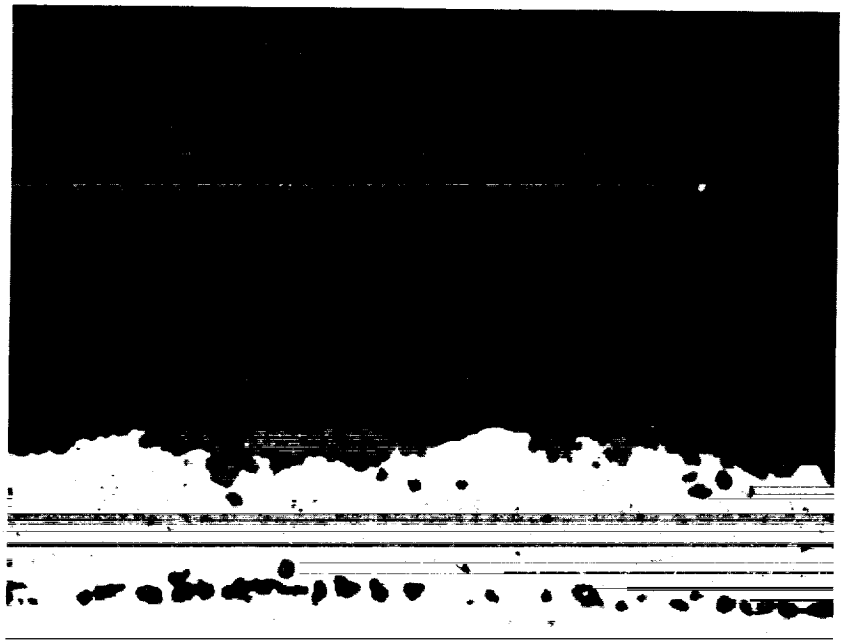

D1 Baseline Post-Test
175 hrs/2100°F - I.D./Short Cycle
HST 004 (85-18)

200X
Etched - AG 21

Figure 26b Light Photomicrograph of Baseline Post-Test Microstructure (D1 Test) After 175 hrs at 2100°F/Short Cycle/Fast Heatup

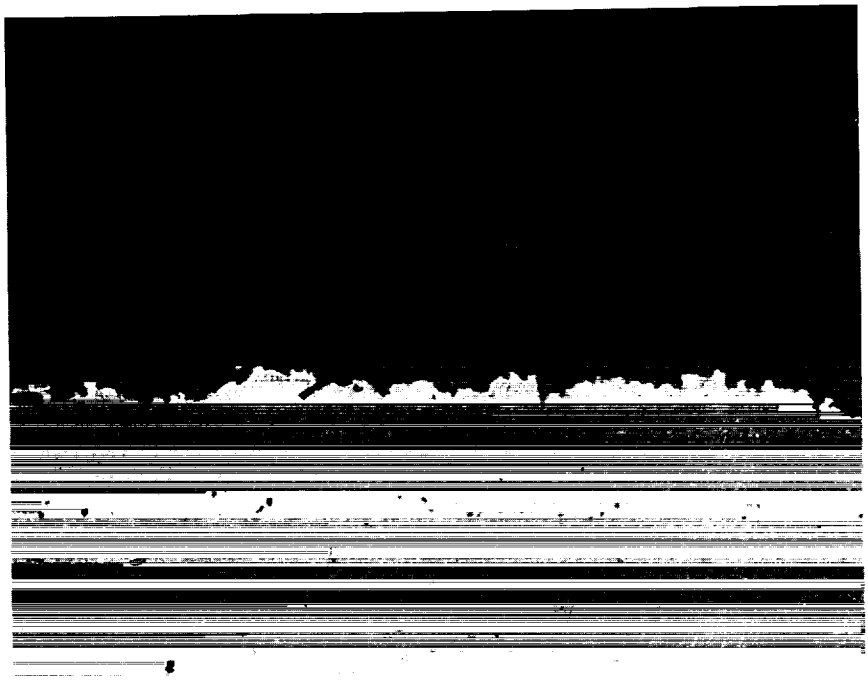

Figure 27a Light Photomicrograph of Baseline Pre-Test Microstructure (D2 Test)

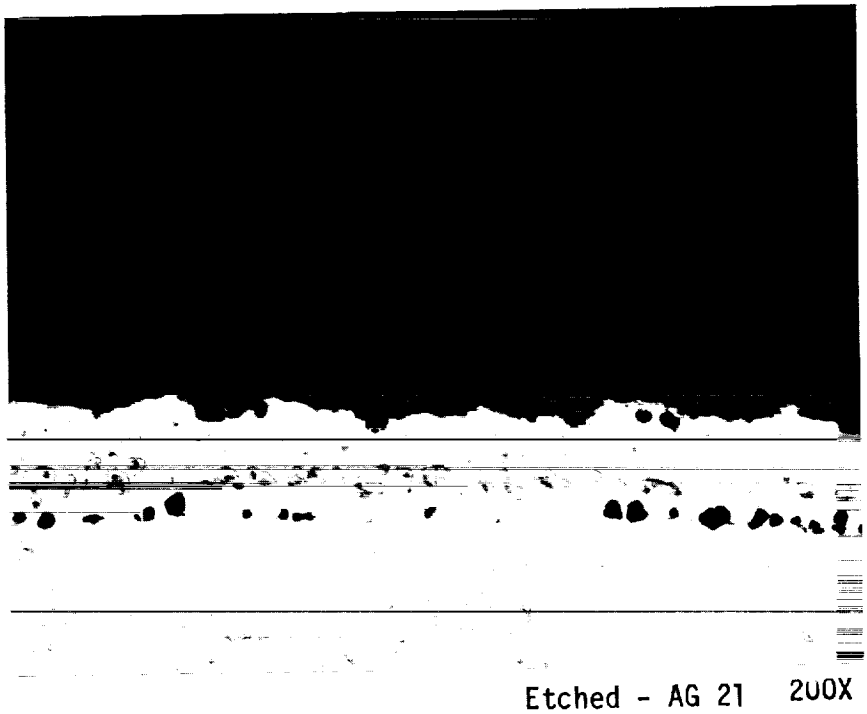

Figure 27b Light Photomicrograph of Baseline Post-Test Microstructure (D2 Test) After 435 hrs at 2000°F/Short Cycle/Fast Heatup

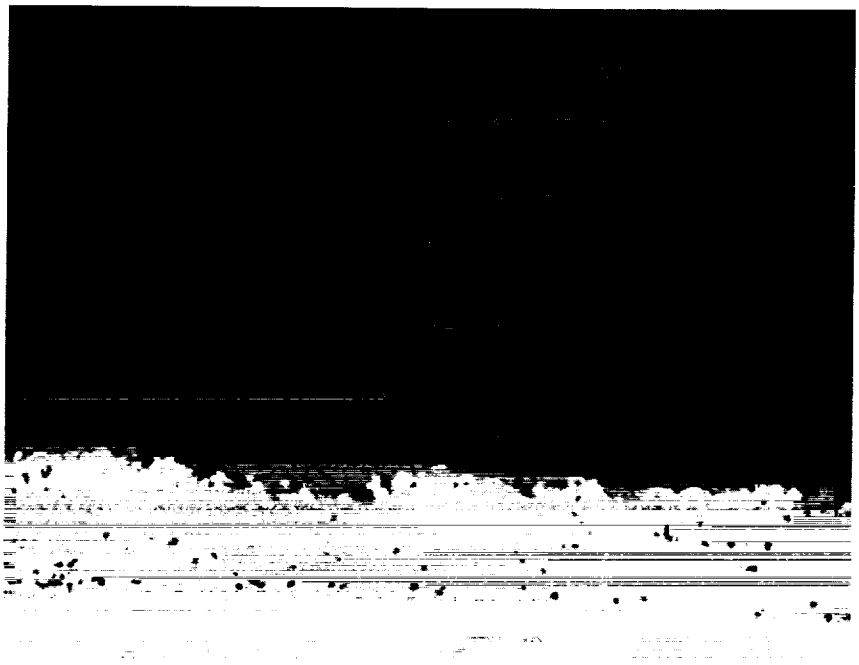

Etched - AG 21 200X

Figure 28a Light Photomicrograph of Baseline Pre-Test Condition

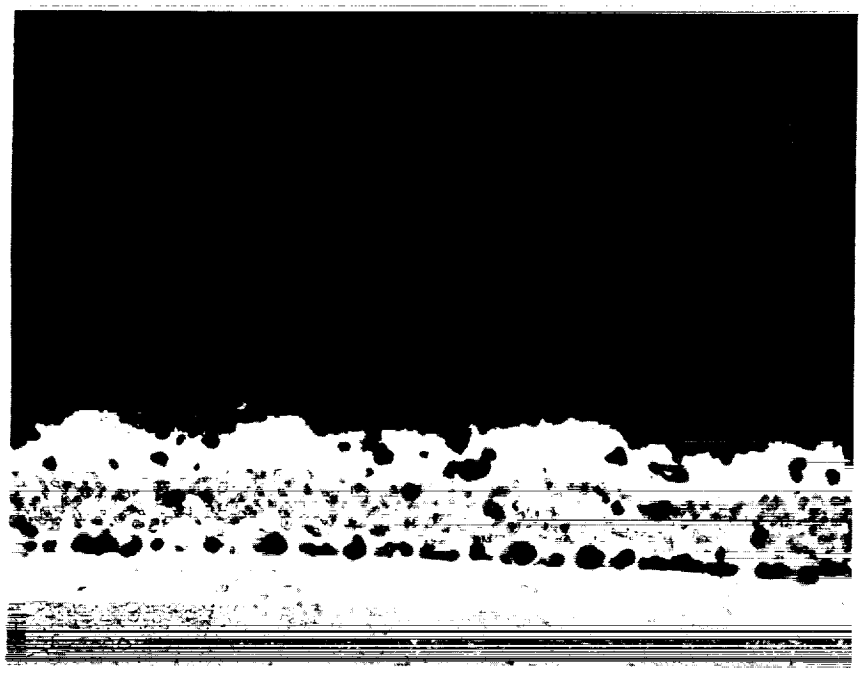

Etched - AG 21 200X

Figure 28b Light Photomicrograph of Baseline Post-Test Microstructure (E Test) After 142 hrs at 2100°F/Short Cycle Slow Heat Uprate

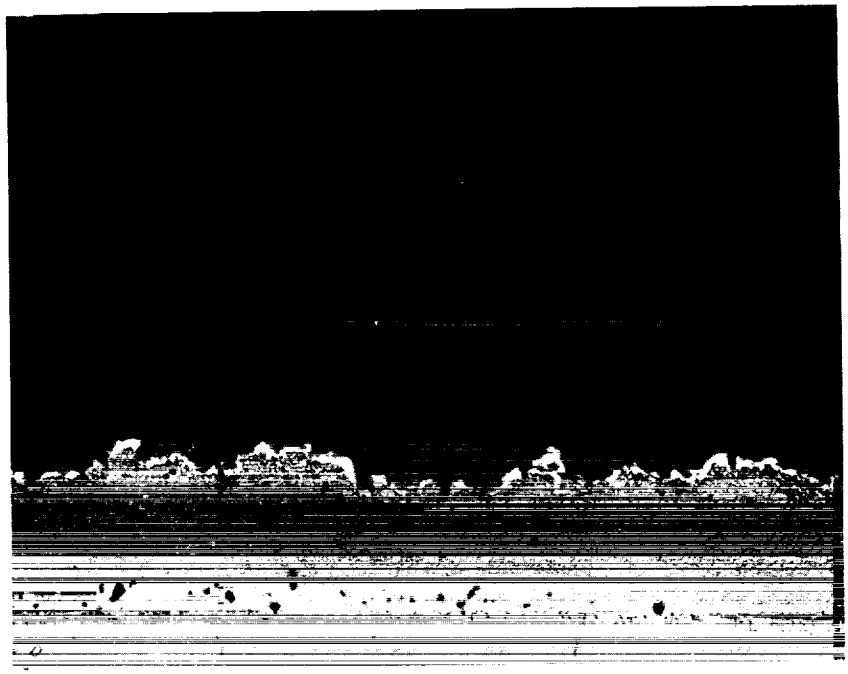

Etched - AG 21 200X

Figure 29a Light Photomicrograph of Baseline Pre-Test Microstructure (F Test)

Etched - AG 21 200X

Figure 29b Light Photomicrograph of Baseline Post-Test Microstructure (F Test) After 70 hrs at 2100°F/Long Cycle Fast Heat Uprate

In the laboratory test conducted to study environmental effects, results suggested that oxidation damage contributes significantly to thermomechanical cracking in the ceramic layer. Figures 30 through 33 show the pre-test (post furnace exposure) and post burner rig test microstructures of representative air pre-exposed specimens for each test condition. Figures 34 through 37 show the pre-test (post-furnace exposure) and post burner rig test microstructures for representative argon pre-exposed specimens. Evaluation of the specimen microstructures pre-exposed in air and in argon, prior to burner rig testing, showed that the former has a well defined thick oxide layer at the metal ceramic interface which the latter does not. This oxide layer is on the order of 0.0003 mils thick prior to laboratory testing. The air pre-exposed microstructures also show a beta (NiAl) depleted zone in the bond coat about 1.5 mils wide directly below the oxide layer, suggesting that the composition of the oxide may be predominantly Al_2O_3 or alumina spinel. This near-interface beta depletion is clearly absent in those specimens which were argon heat treated. Coarsening of the beta phase was observed for both types of pre-exposure.

The air and argon pre-exposed microstructures, exhibited an interdiffusion zone at the area adjacent to and below the bond coat-substrate interface, marked by Kirkendall void alignment. This suggests that the bond coat and substrate composition has changed. It is possible that the slight increase in coating life found with the argon pre-exposed specimens is due to these compositional changes which may result in changes in the bond coat strength properties. For the air pre-exposed specimens, any benefits obtained due to these compositional changes would be over ridden by the thick oxide developed at the interface.

Figures 38 through 41 show the pre-test and post-test microstructures for representative thin ceramic coated specimens. The post-test microstructures all show wide beta (NiAl) depleted zones and substrate inter diffusion layers as compared with the baseline 10 mil thick coating microstructures. This is attributed to the greater exposure time experienced by these specimens. Bond coat oxide thickness ranged from 0.0002 inches to 0.0006 inches for the D1 (2100°F, short cycle, fast heat-up) and F (2100°F, long cycle, fast heat-up) test specimens respectively. Figures 42 through 45 shows the pre-test and post-test microstructures for representative thick ceramic coated specimens. The microstructures shown in these figures show distinct differences in bond coat oxide growth and beta depletion as well as the degree of beta phase coarsening. The D2 (2000°F/short cycle/fast heat-up) test specimen microstructure shows a larger degree of beta phase coarsening as compared with the other specimen microstructures. The F (2100°F/long cycle/fast heat-up) test specimen microstructure shows the greatest oxide scale thickness as seen earlier. The bond coat microstructure from the specimen in the E test (2100°F/short cycle/slow heat-up) shows excessive porosity, believed to be due to poor bond coat deposition. No differences in the ceramic microstructures are observed in either the pre-test or post-test condition as compared with the other microstructures which have been discussed in preceeding paragraphs.

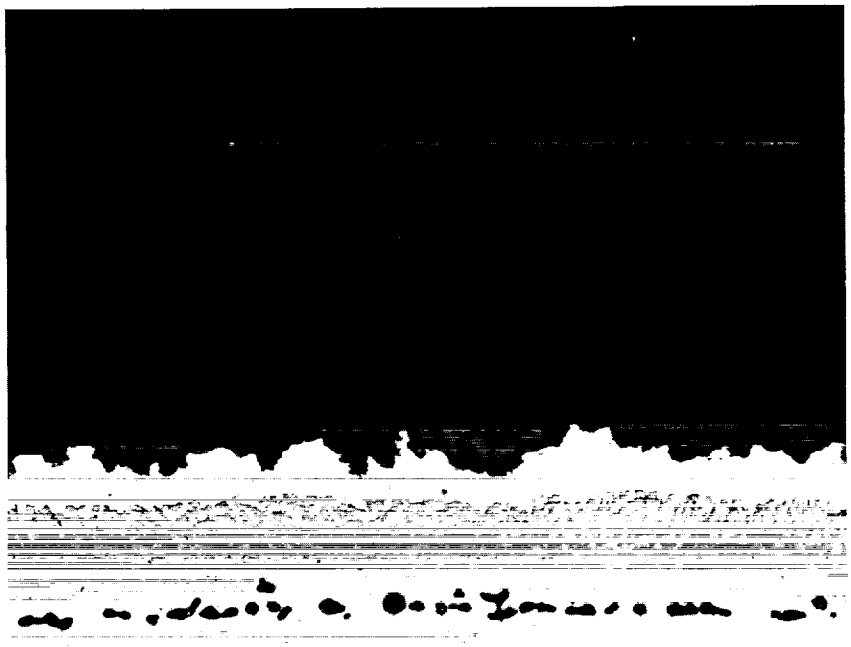

Etched - AG 21 200X

Figure 30a Light Photomicrograph of Pre-Burner Rig Microstructure (D1 Test) for Air Pre-Exposed Specimen (2100°F/40hrs)

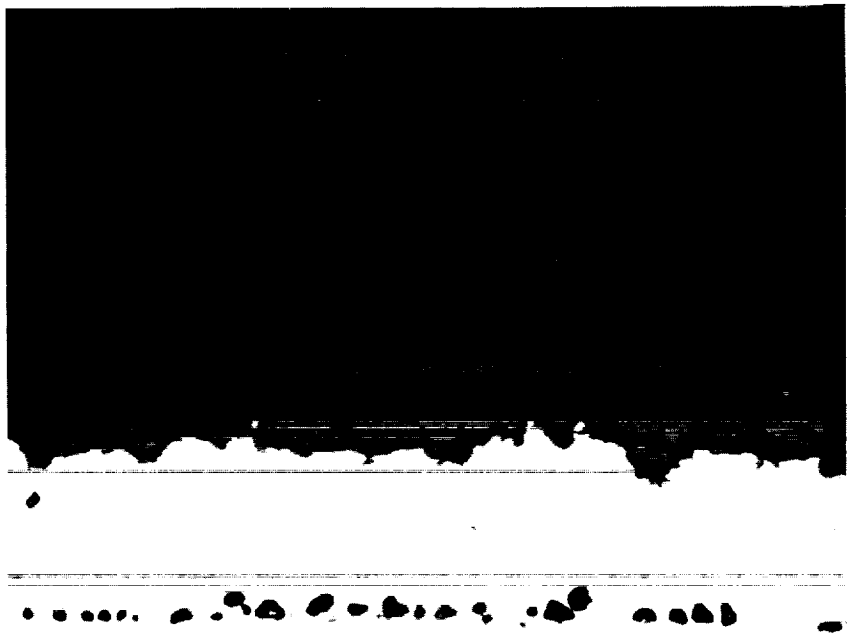

Etched - AG 21 200X

Figure 30b Light Photomicrograph of Post-Burner Rig Microstructure (D1 Test) for Air Pre-Exposed Specimen (2100°F/40 hrs) After 50 hrs at 2100°F/Short Cycle/Fast Heatup

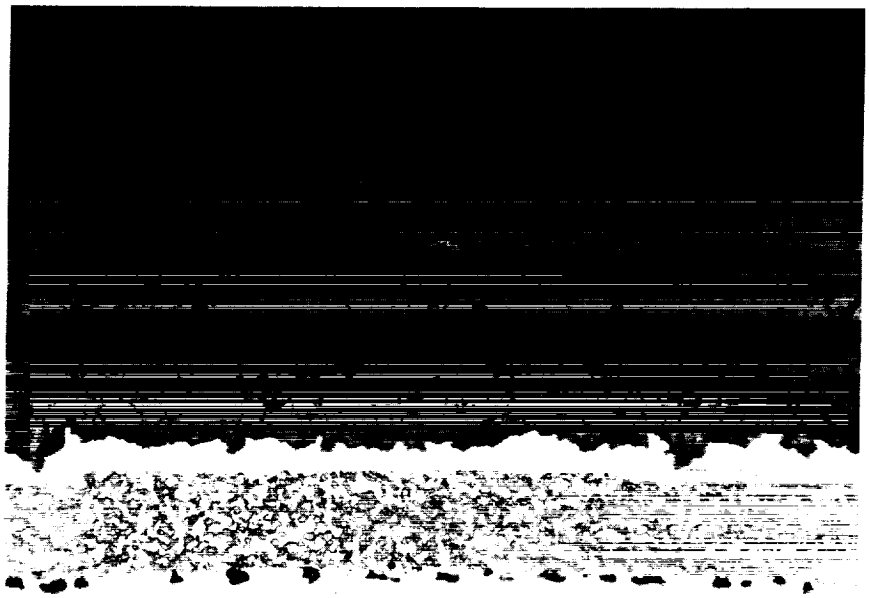

Etched - AG 21 200X

Figure 31a Light Photomicrograph of Pre-Burner Rig Microstructure (D2 Test) for Air Pre-Exposed Specimen (2000°F/100hrs)

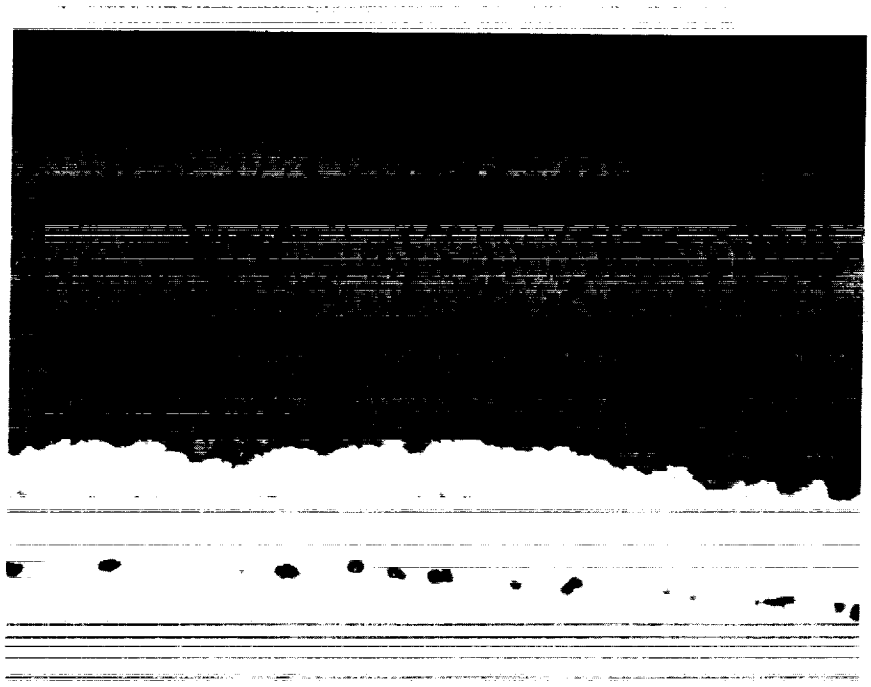

Etched - AG 21 200X

Figure 31b Light Photomicrograph of Post-Burner Rig Microstructure (D2 Test) for Air Pre-Exposed Specimen (2100°F/100 hrs) After 215 hrs at 2000°F/Short Cycle/Fast Heatup

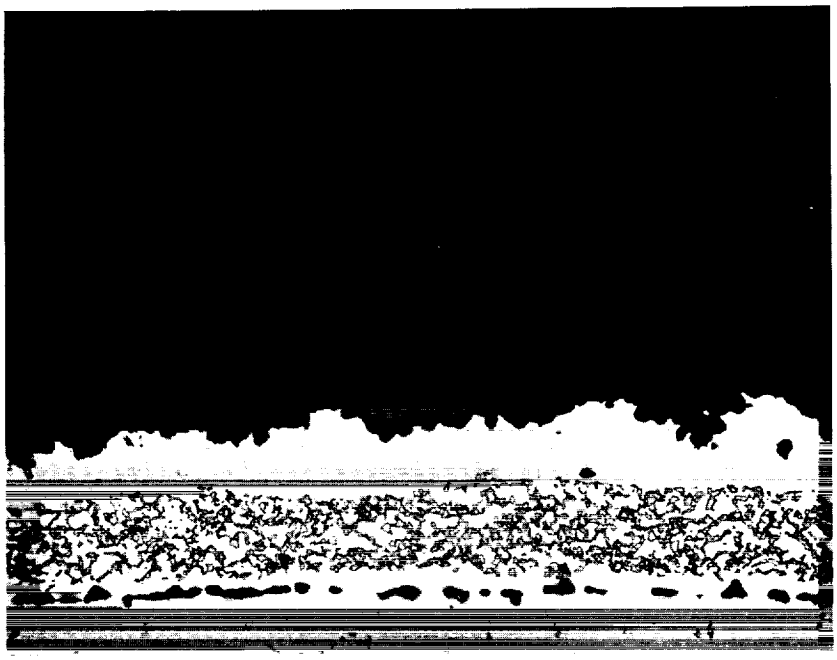

Etched - AG 21 200X

Figure 32a Light Photomicrograph of Pre-Burner Rig Microstructure (E2 Test) for Air Pre-Exposed Specimen (2100°F/40 hrs)

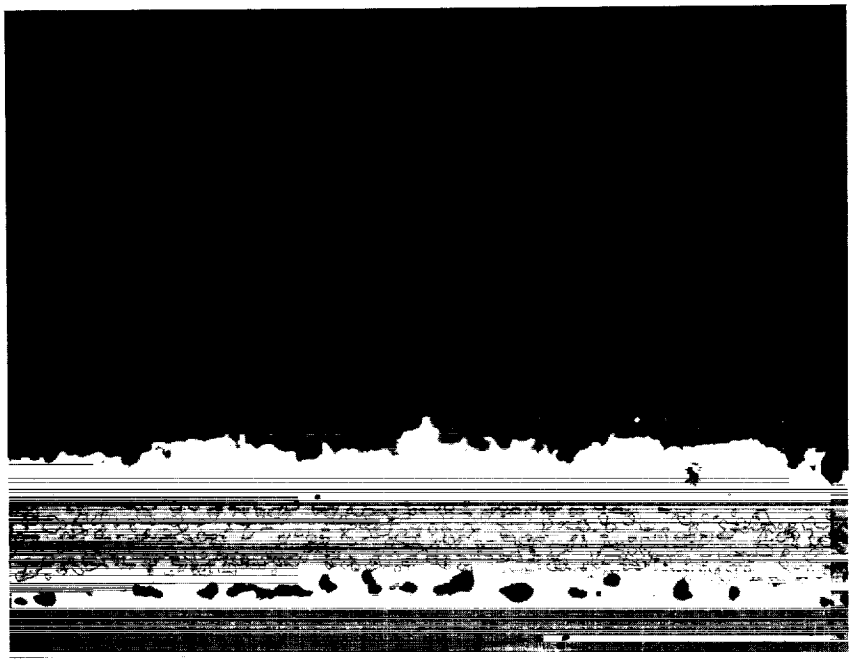

Etched - AG 21 200X

Figure 32b Light Photomicrograph of Post-Burner Rig Microstructure (E2 Test) for Air Pre-Exposed Specimen (2100°F/40 hrs) After 39 hrs at 2000°F/Short Cycle/Slow Heatup

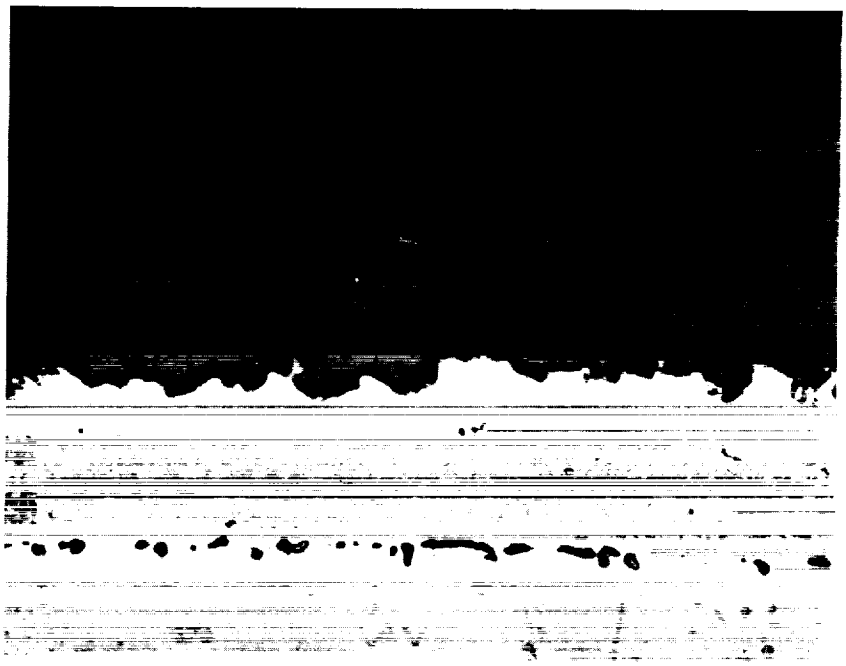

Etched - AG 21 200X

Figure 33a Light Photomicrograph of Pre-Burner Rig Microstructure (F1 Test) for Air Pre-Exposed Specimen (2100°F/40 hrs)

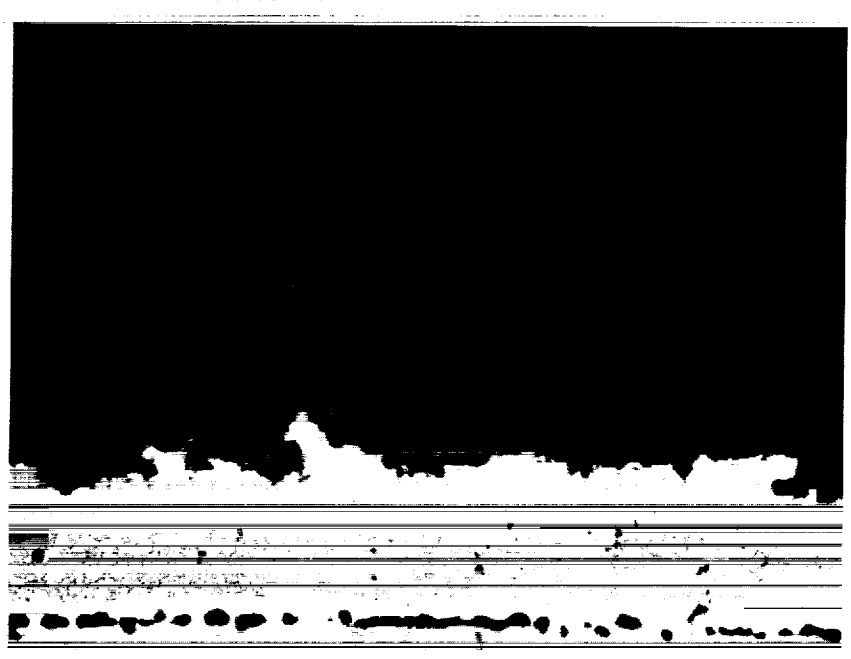

Etched - AG 21 200X

Figure 33b Light Photomicrograph of Post-Burner Rig Microstructure (F1 Test) for Air Pre-Exposed Specimen (2100°F/40 hrs) After 16 hrs at 2100°F/Long Cycle/Fast Heatup

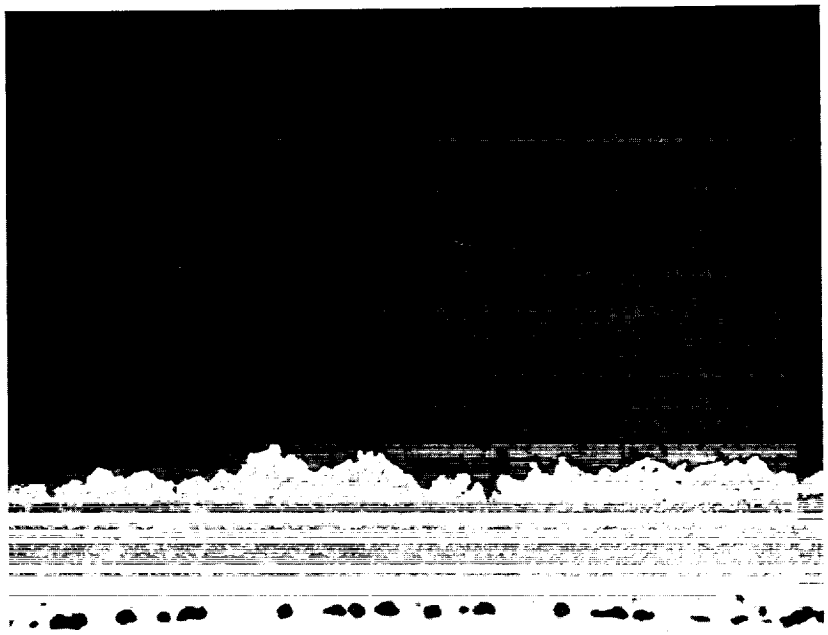

Etched - AG 21 200X

Figure 34a Light Photomicrograph of Pre-Burner Rig Microstructure (D1 Test) for Argon Pre-Exposed Specimen (2100°F/40 hrs)

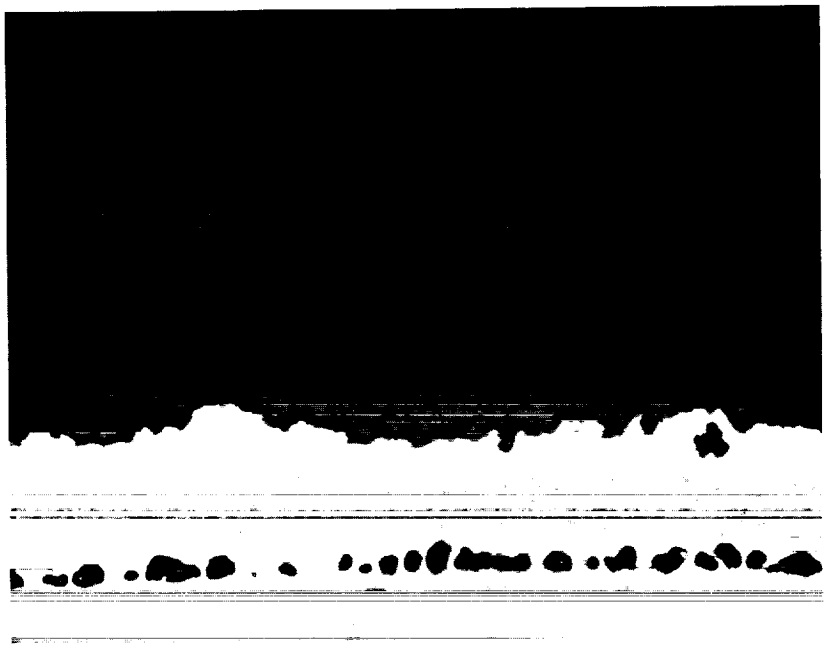

Etched - AG 21 200X

Figure 34b Light Photomicrograph of Post-Burner Rig Microstructure (D1 Test) for Argon Pre-Exposed Specimens After 67 hrs at 2100°F/Short Cycle/Fast Heatup

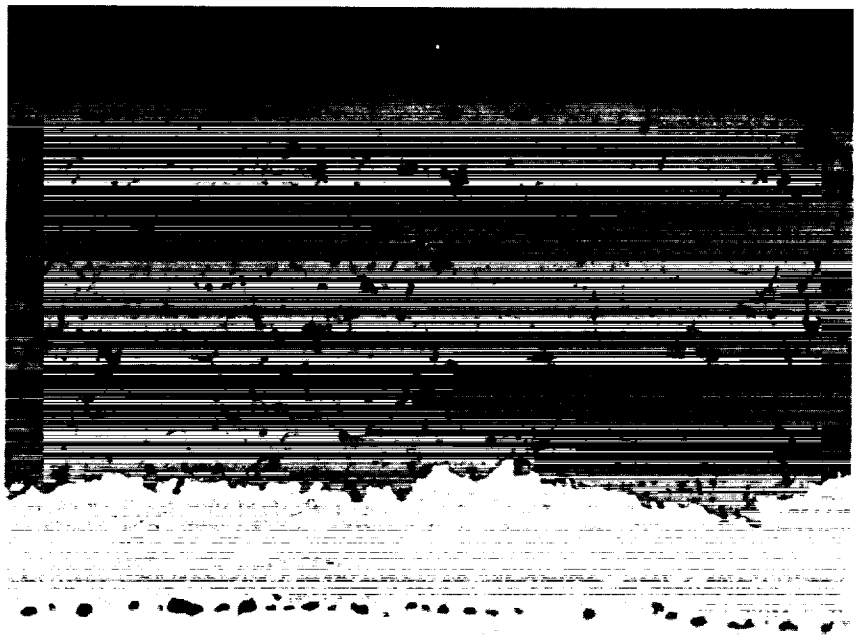

Etched - AG 21 200X

Figure 35a Light Photomicrograph for Pre-Burner Rig Microstructure (D2 Test) for Argon Pre-Exposed Specimen (2000°F/100 hrs)

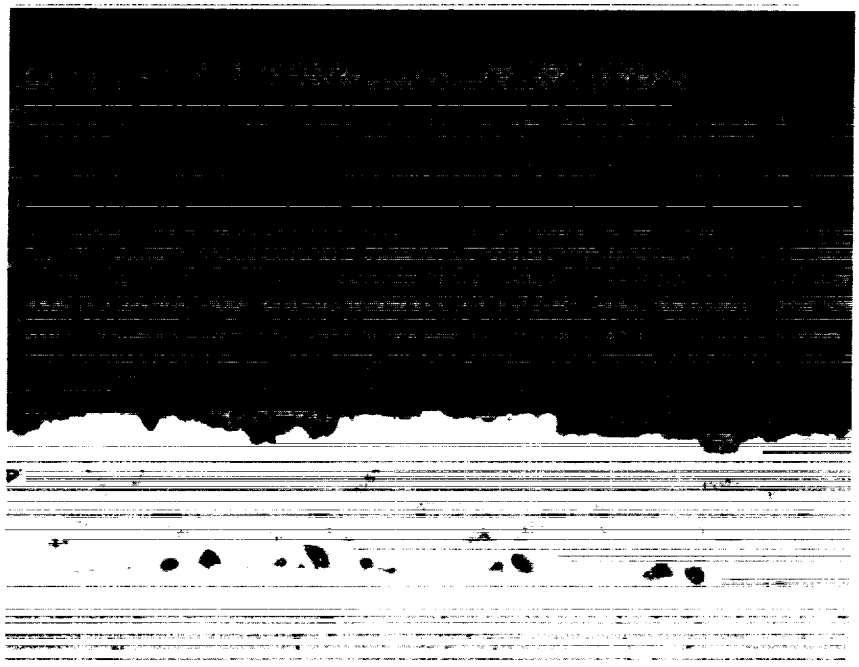

Etched - AG 21 200X

Figure 35b Light Photomicrograph of Post Burner Rig Microstructure (D2 Test) for Argon Pre-Exposed Specimen (2000°F/100 hrs) After 708 hrs at 2000°F/Short Cycle/Fast Heatup

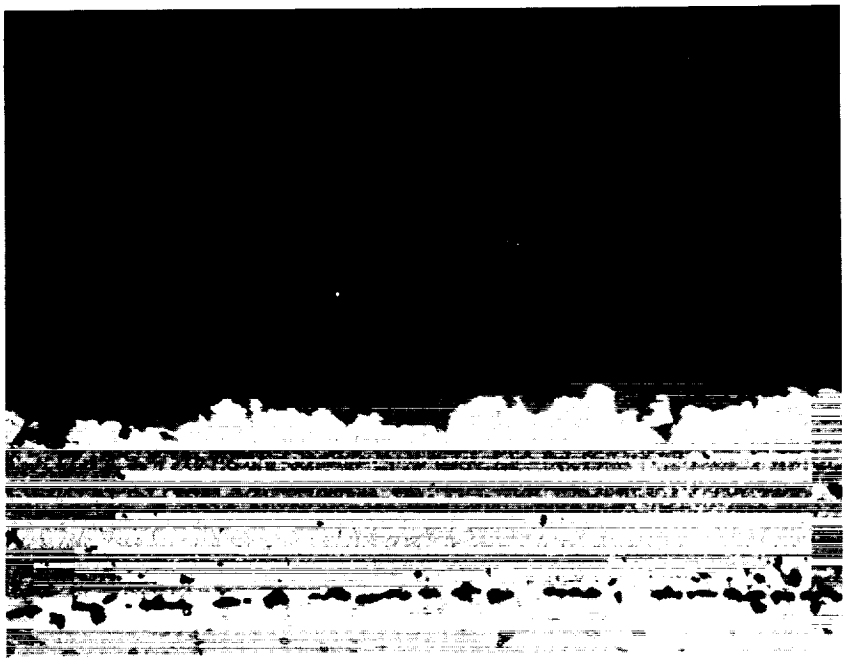

Etched - AG 21 200X

Figure 36a Light Photomicrograph for Pre-Burner Rig Microstructure (E Test) for Argon Pre-Exposed Specimen (2100°F/40 hrs)

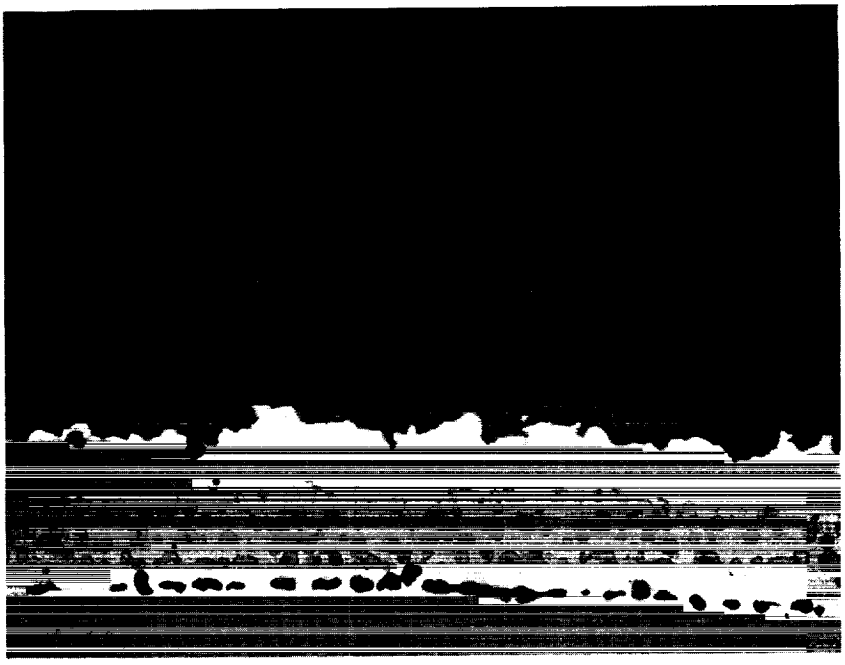

Etched - AG 21 200X

Figure 36b Light Photomicrograph of Post Burner Rig Microstructure (E Test) for Argon Pre-Exposed Specimen (2100°F/40 hrs) After Short Cycle/Slow Heatup

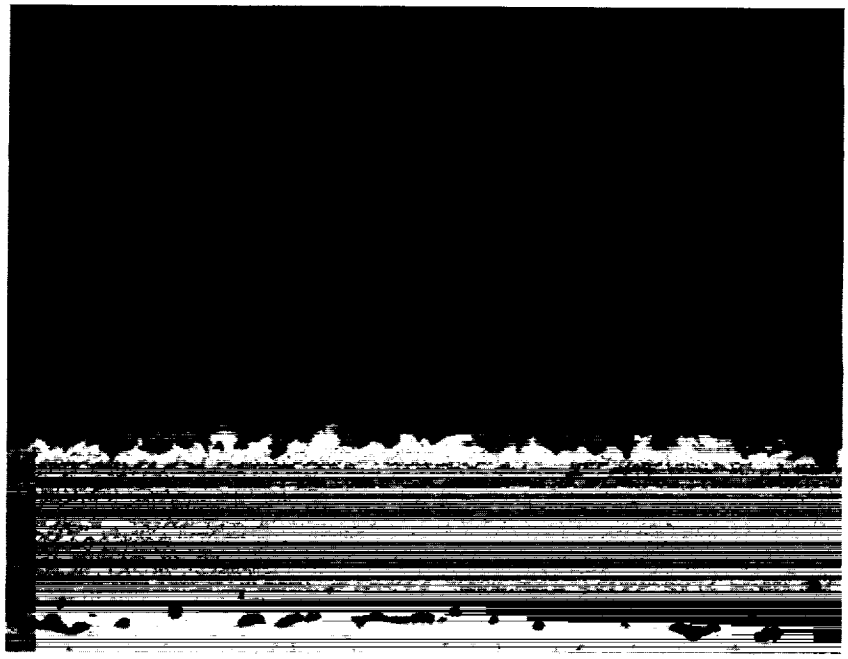

Etched - AG 21 200X

Figure 37a Light Photomicrograph for Pre-Burner Rig Microstructure (F Test) for Argon Pre-Exposed Specimen (2100°F/40 hrs)

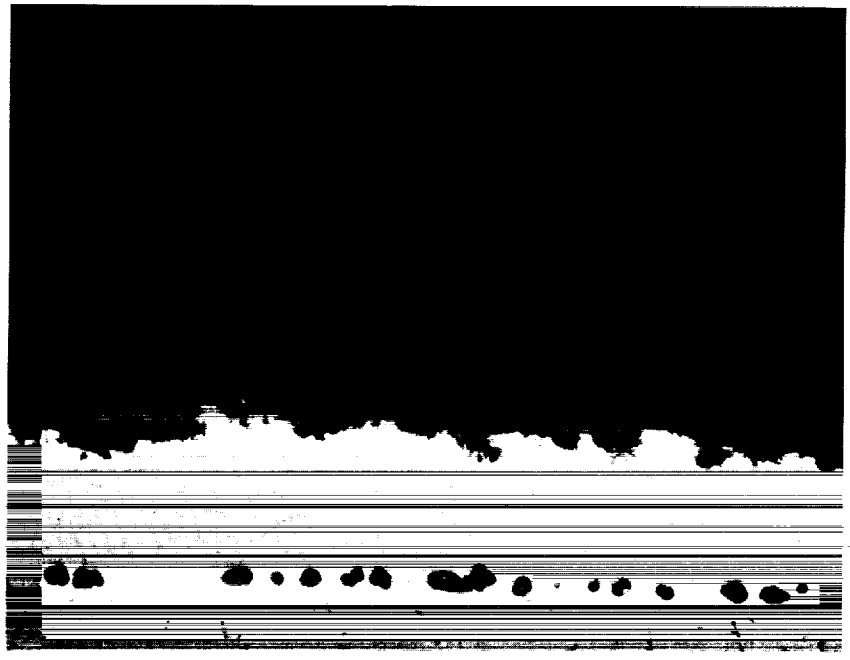

Etched - AG 21 200X

Figure 37b Light Photomicrograph of Post Burner Rig Microstructure (F Test) for Argon Pre-Exposed Specimen (2100°F/40 hrs) After Long Cycle/Fast Heatup

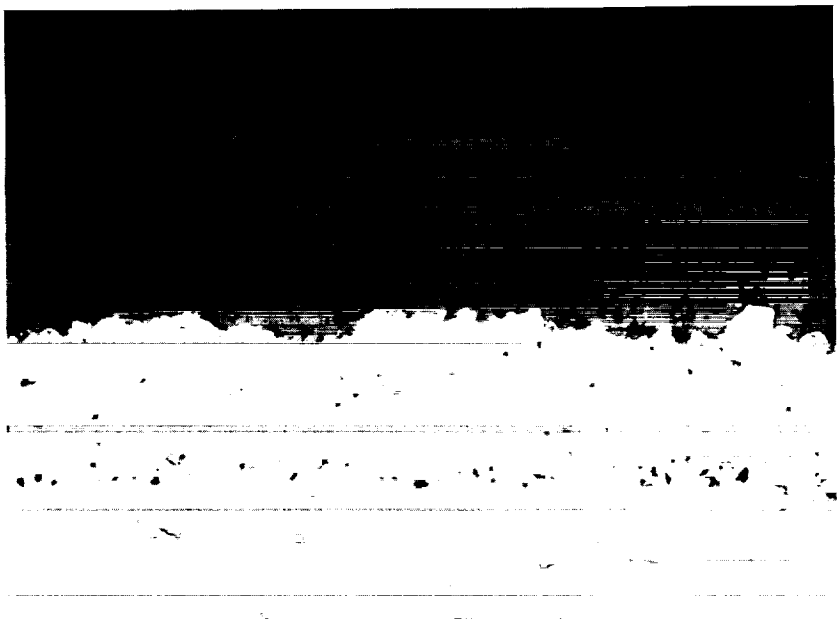

Etched 200X

Figure 38a Light Photomicrograph of Pre-Test Microstructure (D1 Test) for Thin Ceramic Specimen

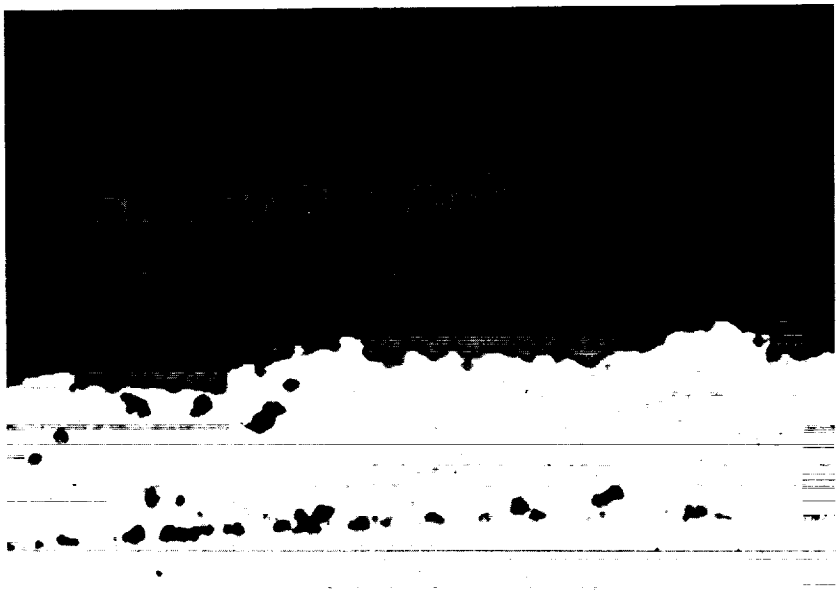

Etched - AG 21 200X

Figure 38b Light Photomicrograph of Post-Test Microstructure (D1 Test) for Thin Ceramic Specimen After 243 hrs at 2100°F/Short Cycle/Fast Heatup

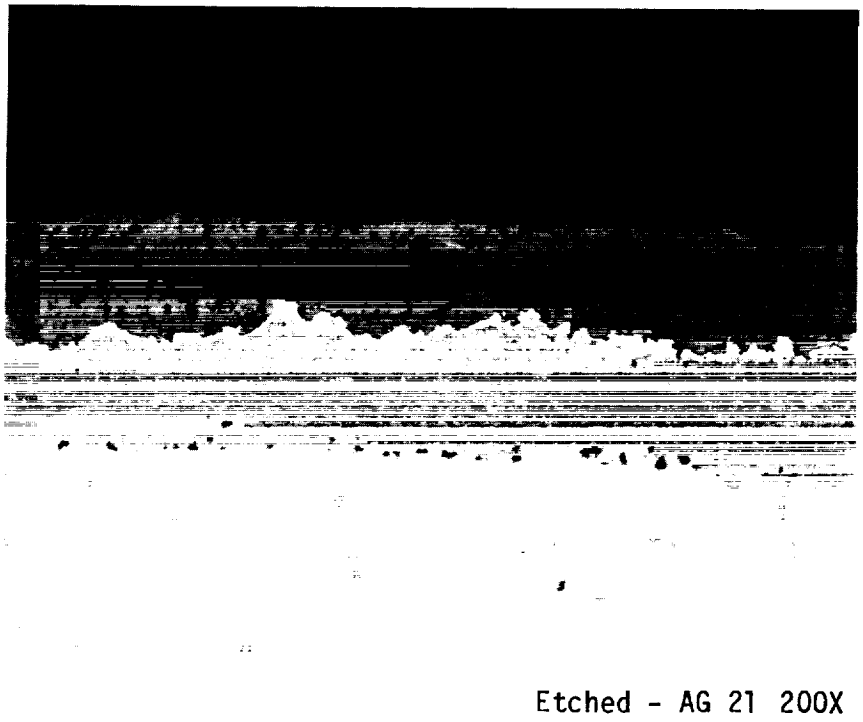

Etched - AG 21 200X

Figure 39a Light Photomicrograph of Pre-Test Microstructure (D2 Test) for Thin Ceramic Specimen

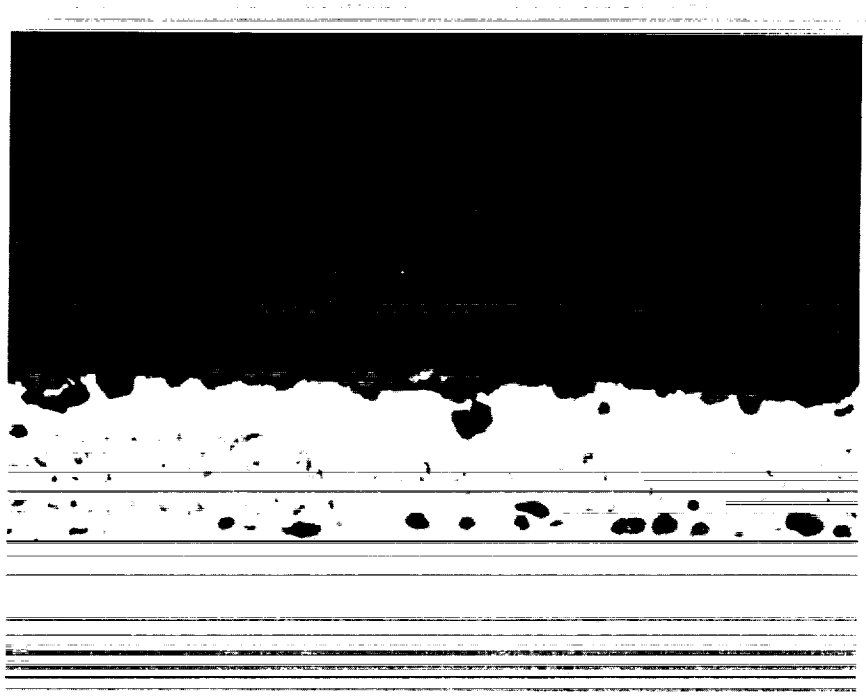

Etched - AG 21 200X

Figure 39b Light Photomicrograph of Post-Test Microstructure (D2 Test) for Thin Ceramic Specimen After 492 hrs at 2000°F/Short Cycle/Fast Heatup

Etched - AG 21 200X

Figure 40a Light Photomicrograph of Pre-Test Microstructure (E Test) for Thin Ceramic Specimen

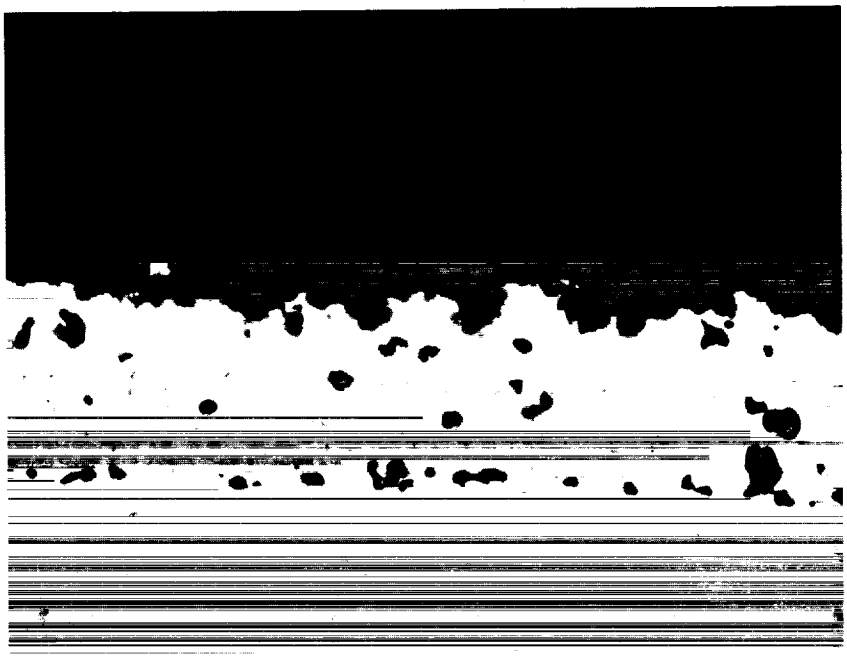

Etched - AG 21 200X

Figure 40b Light Photomicrograph of Post Burner Rig Test Microstructure (E Test) for Thin Ceramic Specimen After 162 hrs at 2100°F/Short Cycle/Slow Heatup

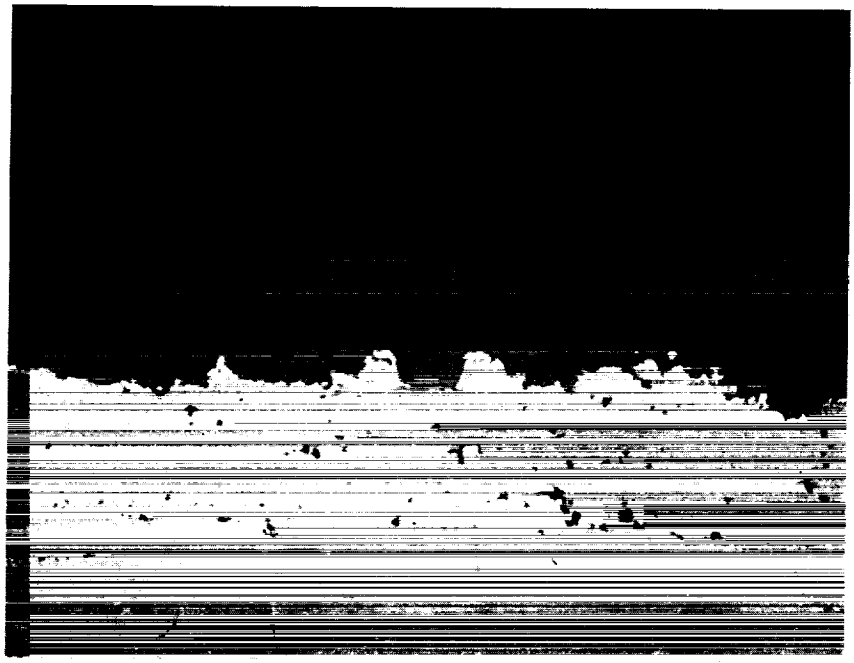

Etched - AG 21 200X

Figure 41a Light Photomicrograph of Pre-Test Microstructure (F Test) for Thin Ceramic Specimen

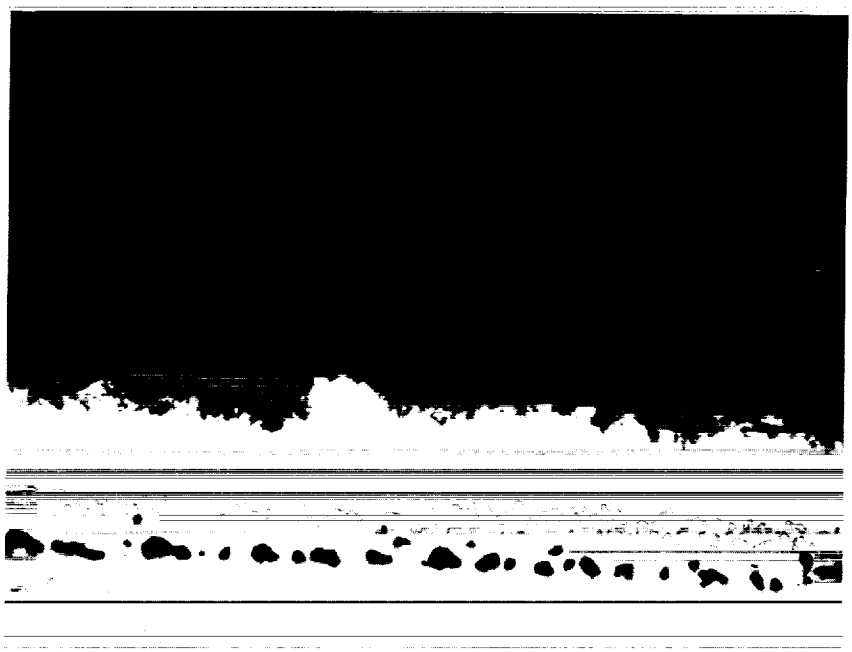

Etched - AG 21 200X

Figure 41b Light Photomicrograph of Post Burner Rig Test Microstructure (F Test) for Thin Ceramic Specimen After 116 hrs at 2100°F/Long Cycle/Fast Heatup

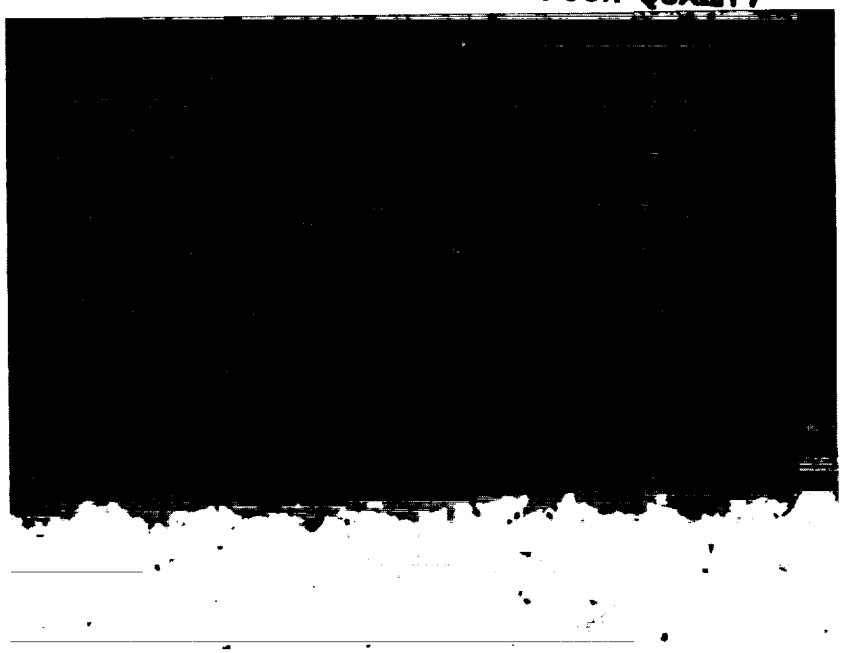

Unetched 200X

Figure 42a Light Photomicrograph of Pre-Test Microstructure (D1 Test) for Thick Ceramic Specimen

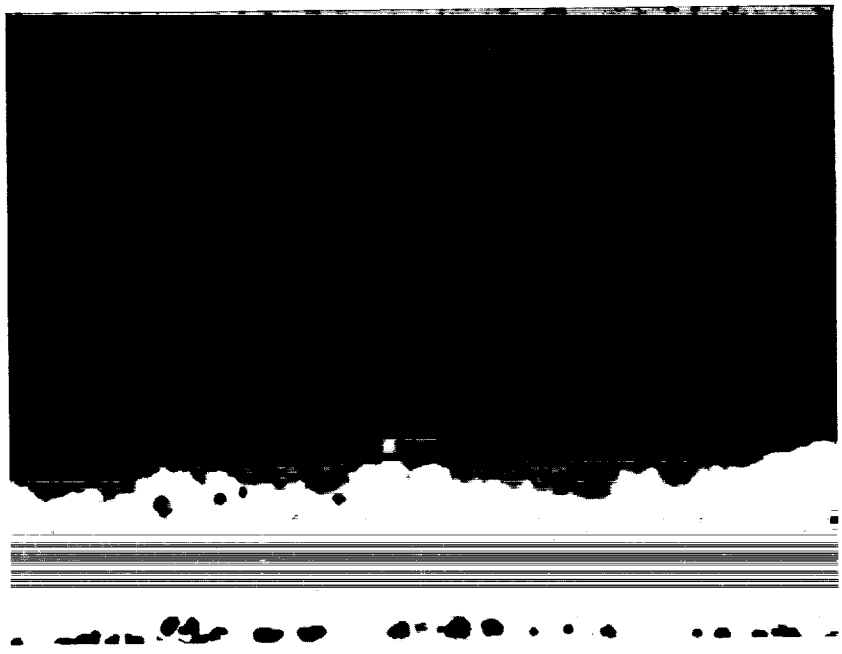

Etched - AG 21 200X

Figure 42b Light Photomicrograph of Post Burner Rig Test Microstructure (D1 Test) for Thick Ceramic Specimen After 160 hrs at 2100°F/Short Cycle/Fast Heatup

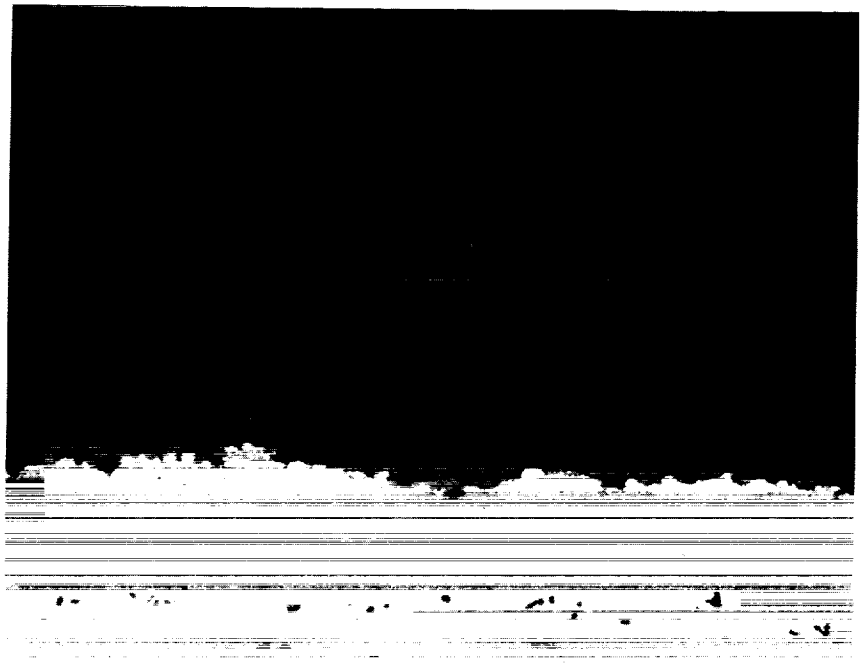

Unetched 200X

Figure 43a Light Photomicrograph of Pre-Test Microstructure (D2 Test) for Thick Ceramic Specimen

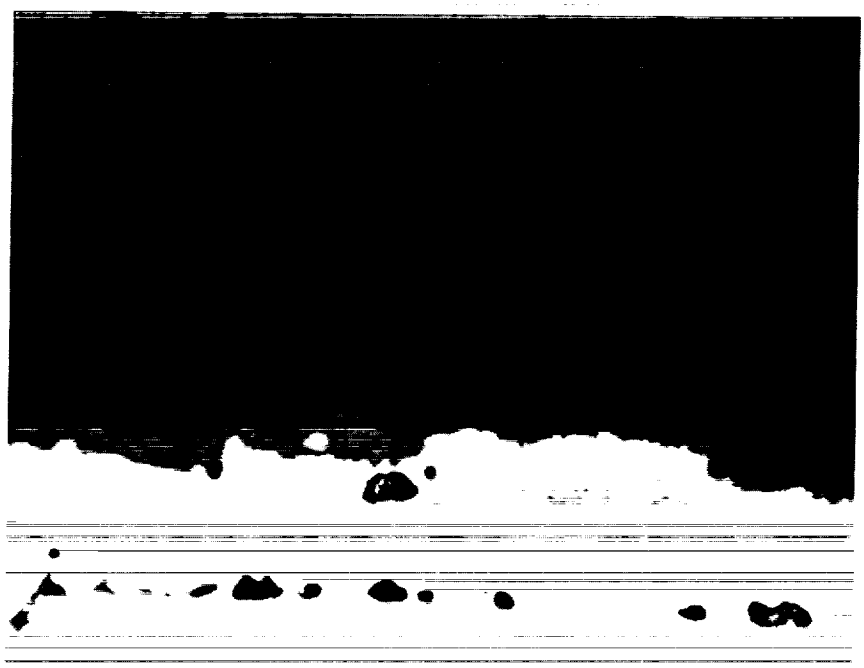

Etched - AG 21 200X

Figure 43b Light Photomicrograph of Post Burner Rig Test Microstructure (D2 Test) for Thick Ceramic Specimen After 454 hrs at 2100°F/Short Cycle/Fast Heatup

Etched - AG 21 200X

Figure 44a Light Photomicrograph of Pre-Test Microstructure (E Test) for Thick Ceramic Specimen

Etched - AG 21 200X

Figure 44b Light Photomicrograph of Post Burner Rig Test Microstructure (E Test) for Thick Ceramic Specimen After 121 hrs at 2100°F/Short Cycle/Slow Heatup

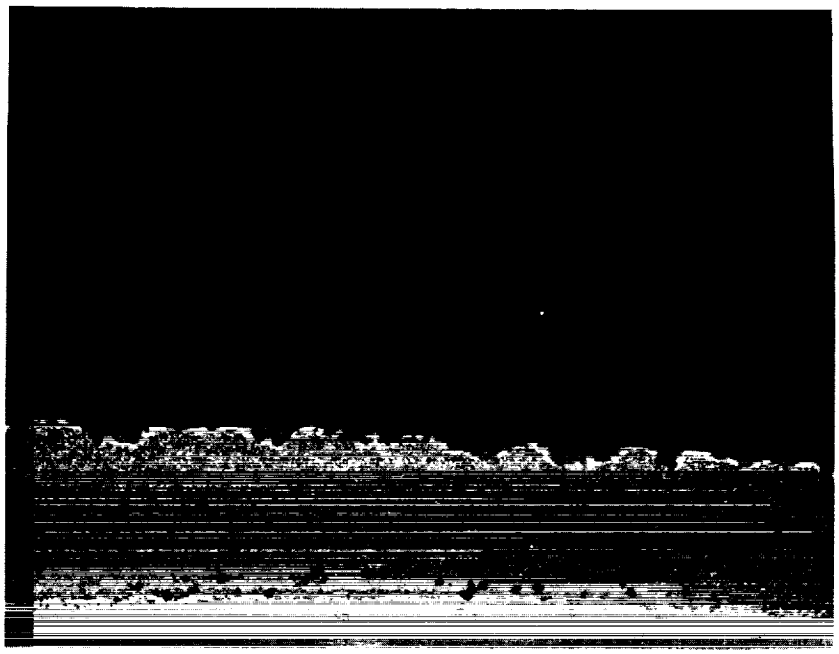

Etched - AG 21 200X

Figure 45a Light Photomicrograph of Pre-Test Microstructure (F Test) for Thick Ceramic Specimen

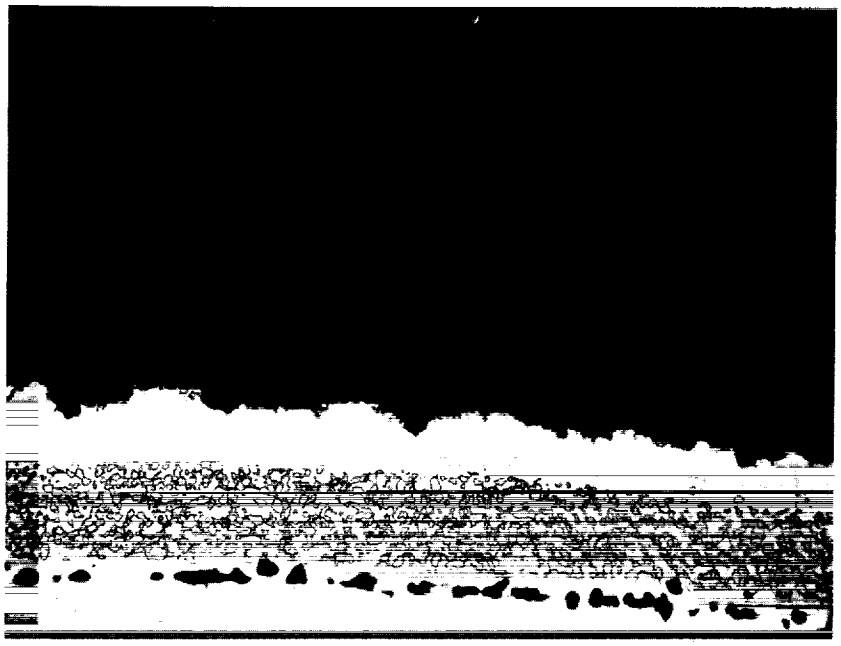

Etched - AG 21 200X

Figure 45b Light Photomicrograph of Post Burner Rig Test Microstructure (F Test) for Thick Ceramic Specimen After 54 hrs at 2100°F/Long Cycle/Fast Heatup

X-ray diffraction analyses for all representative post-test specimens is presented in Table XI. It is believed that no significant amount of monoclinic ZrO_2 was formed. Although it should be noted that for most cases, 1 v/o monoclinic phase was present adjacent to the spall and absent away from the spalled location.

In summary, the comparative post-test specimen evaluation has shown that increased exposure time results in: 1) increased MCrAlY oxide scale thickness, 2) increased beta depletion and/or coarsening, 3) some increase in Kirkendall void population and size occurring at the original bondcoat-substrate interface, 4) no significant phase changes in the ceramic, and 5) no gross microstructural changes in the ceramic. Also, it is clear from the post-test microstructures studied that more bond coat oxidation has occurred for the long cycle (F) test than for the more rapid cycle tests, even though total "hot" life was similar.

3.1.2.2.3 Fractional Exposure Burner Rig Test Results

The purpose of this test was to investigate the occurrance and accumulation of microstructural damage resulting from cyclic thermal burner rig exposure for various fractions of spalling life. The approach involved burner rig exposure of test bars for various fractions of life as measured in the D1 (2100°F/short cycle/fast heat up) test. There were two series of test conducted. The first set provided a broad survey of damage throughout life, with the specimens being exposed for approximate decile fractions of the average D1 test life (180 hours). The second set focused more closely on high life fractions, with the specimens being exposed at life fractions in the range of 58% - 100%.

Both series of tests were conducted at the D1 test conditions. At least one specimen was tested to failure in each group, to assure the validity of the estimated life. Specific exposure times are listed in Table XII, together with estimates of life fractions represented by each exposure. In the first group, the control specimen failed very close to the D1 test average. In the second group, life fraction estimates were less exact, two specimens exceeded the D1 baseline average and the control specimen failed at 130% of the average, suggesting test conditions may have shifted slightly. As calculated by the preliminary life prediction model discussed in succeeding sections, the 30% shift in life for Group II specimens would correspond to a temperature shift of 10°. Table XII shows two Group II calculated life fractions. The first is based on the nominal 180 hour life at 2100°F and the second is based on the observed failure life of the reference bar in the Group II test.

Microstructural examination of fractionally exposed specimens shows incipient/subcritical cracking as early as 20-30 percent of the burner rig test life (Figure 46). Examination of crack morphology at successively increasing life fractions suggests that ceramic spallation may result from progressive link-up of adjacent subcritical cracks, as opposed to subcritical growth of a single dominant crack. Quantitative measurement of average crack length shows a progressive increase with increasing exposure. "Young" specimens contain cracks on the order of 2-3 mils; longer exposure times yield average crack

TABLE XI
X-RAY DIFFRACTION ANALYSIS OF SOME REPRESENTATIVE POST TEST SPECIMENS

Specimen/ Location	v/o FCC ZrO_2	v/o Tetragonal ZrO_2	v/o Monoclinic ZrO_2	Failure Time (hours)
2100°F Short Cycle, Fast Heat-up Test (D1)				
Baseline Pre-test	60-55 (a_o = 5.122A)	40-45 (a_o = 5.1172A c_o=5.1646A)	Not detected	N/A
Baseline: adjacent to spall	60-65 (a_o = 5.13263A)	35-30	5	175
180° from spall	55-60 (a_o = 5.13575A)	45-40	1	
Air pre-exposed: adjacent to spall	60-65 (5.13907A)	35-30	5	
180° from spall	55-60 (5.13910A)	45-40	Not detected	50
Thick: adjacent to spall	60-65 (a_o = 5.13762A)	40-35	Not detected	
adjacent to spall (other side)	60-65 (a_o = 5.14152A)	40-35	--	104
2100°F Short Cycle, Fast Heat-up Test (D2)				
Air pre-exposed: adjacent to spall	65-70	35-30	1	194
Argon pre-exposed: adjacent to spall	60-65	35-30	1 (Possibly monoclinic ZrO2 or hexagonal Y_2O_3)	679
Thick ceramic: adjacent to spall	50-70	45-40	Not detected	443
Thin ceramic: adjacent to spall	50-55	50-45	Not detected	557

TABLE XI (continued)
X-RAY DIFFRACTION ANALYSIS OF SOME REPRESENTATIVE POST TEST SPECIMENS

Specimen/ Location	v/o FCC ZrO_2	v/o Tetrogonal ZrO_2	v/o Monoclinic ZrO_2	Failure Time (hours)
2100°F Short Cycle, Slow Heat-up Test (E)				
Baseline: Away from Spall	60-65	40-35	Not detected	142
Spalled Area	60-65	40-35	1	
Air Pre-Exposed: Away from Spall Area	60-65	40-35	1	18
Spalled Area	60-65	40-35	1	
Argon Pre-Exposed: Away from Spall Area	60-65	40-35	Not detected	142
Spalled Area	65-70	35-30	1	
Thick: Away from Spall	55-60	45-40	Not detected	121
Spalled Area	60-65	40-35	1	
Thin: Away from Spall	55-60	45-40	Not detected	121
Spalled Area	60-65	40-35	Not detected	
2100°F Short Cycle, Fast Heat-up Test (F)				
Baseline: Away from Spall	55-60	45-40	Not detected	98
Spalled Area	65-70	35-30	1	
Air Pre-Exposed: Away from Spall Area	55-60	45-40	Not detected	18
Spalled Area	60-65	40-35	1	
Argon Pre-Exposed: Away from Spall Area	55-60	45-40	Not detected	102
Spalled Area	60-65	40-35	1	
Thick; Away from Spall	55-60	45-40	Not detected	64
Spalled Area	65-70	35-30	1	
Thin: Away from Spall	55-60	45-40	Not detected	122
Spalled Area	60-65	40-35	1	

TABLE XII
FRACTIONAL EXPOSURE TEST (Condition G) RESULTS
(2100°F/Short Cycle/Fast Heat-Up Rate)

Specimen Identification Number	Total Test Hours (TTH)	Percent Life (TTH/180 X 100)	(TTH/235 X 100)
GROUP I			
214	15	8%	
215	30	17%	
216	45	25%	
217	60	33%	
218	75	42%	
219	90	50%	
220	105	58%	
221	120	67%	
227	135	75%	
223	150	83%	
224	165	92%	
225	180	100% Failed	
GROUP II			
290	136	76%	58%
292	143	80%	61%
296	145	81%	62%
297	151	84%	64%
298	171	95%	73%
299	174	97%	74%
300	177	98%	75%
301	180	100%	77%
303	215	120%	91%
302	235	130%	100% - Failed

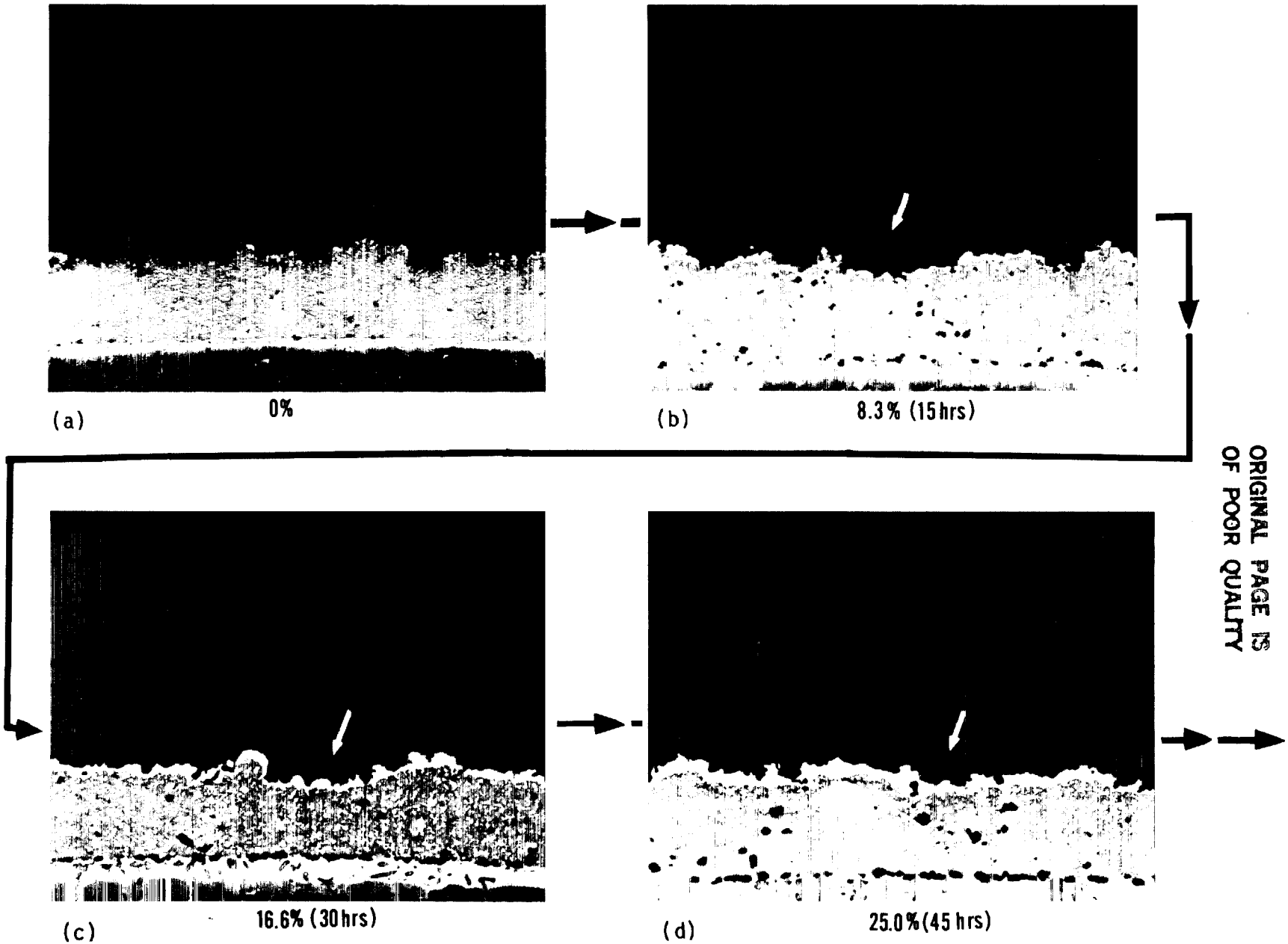

Figure 46 Thermal Barrier Coating Damage Progression

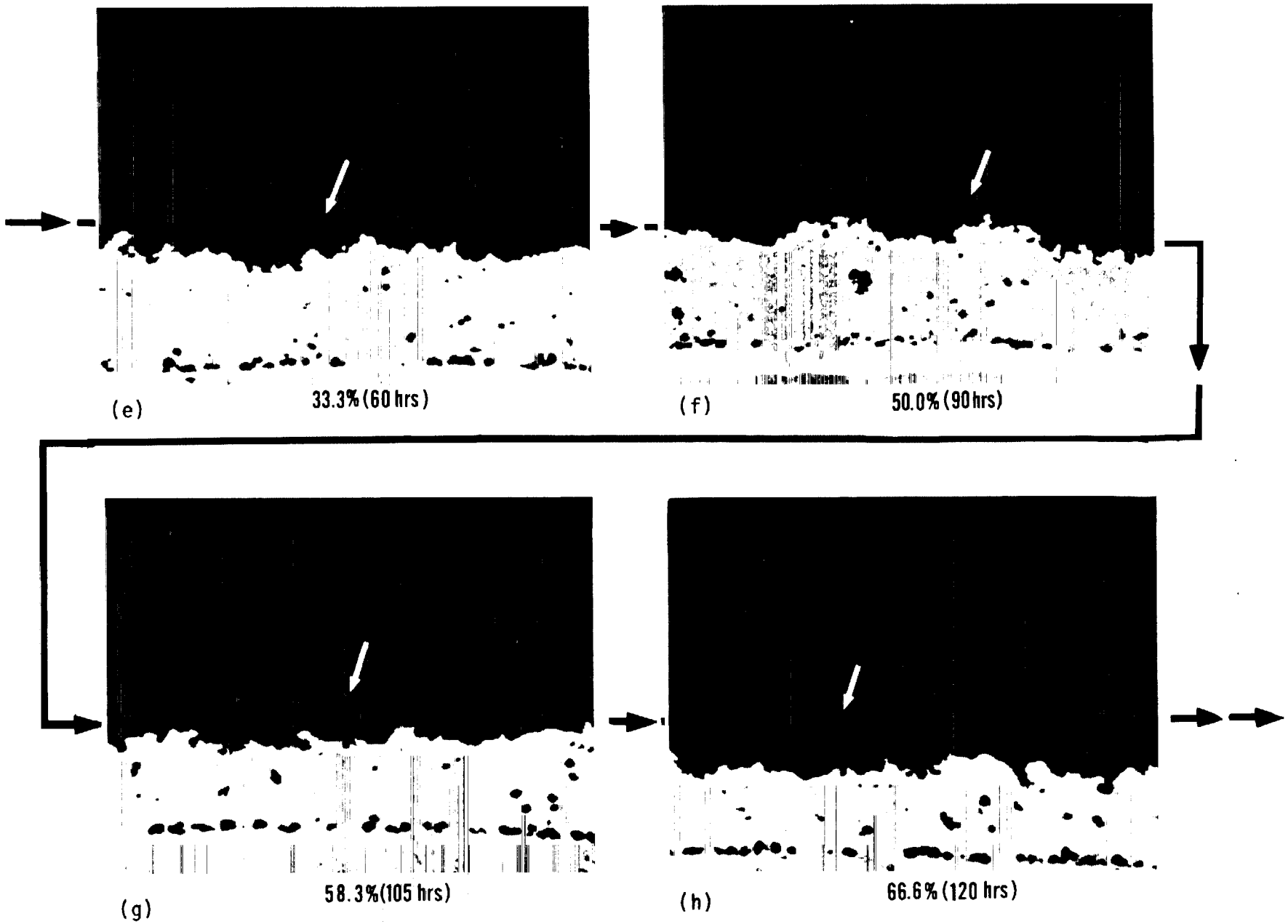

Figure 46 (Continued)

Figure 46 (Continued)

sizes of 6-10 mils. The number of cracks also appears to increase with exposure time. "Old" specimens show large isolated cracks on the order of 12.5 mils, together with shorter (2-3 mil) cracks. The "oldest" unfailed specimen evaluated showed one major crack ≈ 38 mils long and some 6-7 mil cracks.

Because previously discussed phenomenological evidence clearly indicated a significant influence of oxidative environment on coating "damage" accumulation, substantial effort was devoted to investigation of the relationship between incipient cracking and the growing oxide scale. Most of the observed ceramic cracking occurred parallel to and about 1 to 2 mils above the zirconia-oxide scale interface with no obvious linkage between cracks and oxide. While scanning electron microscope studies, discussed below, did show a few isolated cases of scale initiated cracking, these examples were sufficiently difficult to find as to lead to the conclusion that this is not the major mode of crack initiation in the ceramic layer. It is interesting to note that examples of scale initiated cracking were easier to find in older specimens, occurring in the same structure together with larger numbers of well developed longer cracks which appeared to be isolated from the interface. The observation could suggest that the thicker oxide scale developed at larger exposure times can initiate cracks, but that this is not the "critical" damage mode in the sense that those cracks which propogate to failure are initiated early in life and appear to be isolated from the interface.

Scanning electron micrographs of typical crack structures are shown in Figures 47 through 50. Shown in Figure 47 is the structure found in a specimen exposed for 90 hours (≈ 50% life), in which subcritical cracks are noted in the vicinity of (but not clearly initiated at) the bond coat peaks. Figure 49 is the same specimen as seen in Figure 48 but shows a different area; fine layered cracking in the bond coat oxide is noted at higher magnifications. "Older" specimens with more oxide accumulation frequently showed this type of layered type cracking within the oxide, but these cracks were in general not associated with the major subcritical cracks seen in Figure 46. Figure 48 shows the BSI for the specimen exposed for 105 hours and two large cracks are observed to extend from either edge of a particular bond coat asperity. Figure 50 shows the BSI for the specimen exposed for 135 hours. This figure also shows a subcritical crack extending from the edge of a bond coat peak with cracking observed in the bond coat oxide.

Another interesting structural feature observed in "older" specimens was an apparent increase in the amount of near-interface porosity, usually associated with major cracks. Critical examination of this porosity indicates that it is an artifact, resulting from pull-out in polishing rather than being an inherent feature of the structure. This apparent increased sensitivity of the ceramic to pull-out suggests that the ceramic may be somewhat "weakened" in the vicinity of the interface. At the time of writing, it appeared that the suggested near interface weakening may correspond physically to a progressive increase of localized near-interface microcrack density. Additional metallographic studies currently are in progress to further investigate this phenomenon.

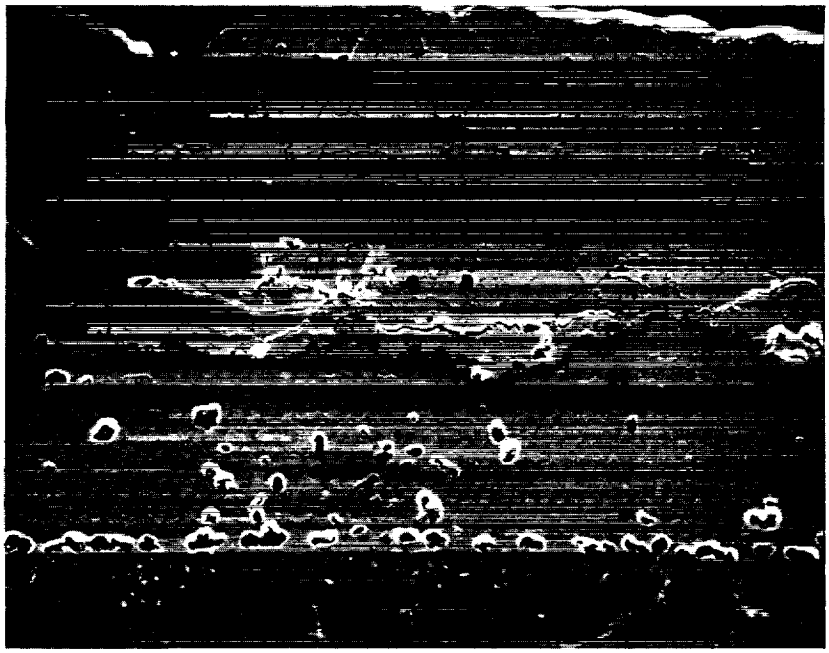

85-196 200X

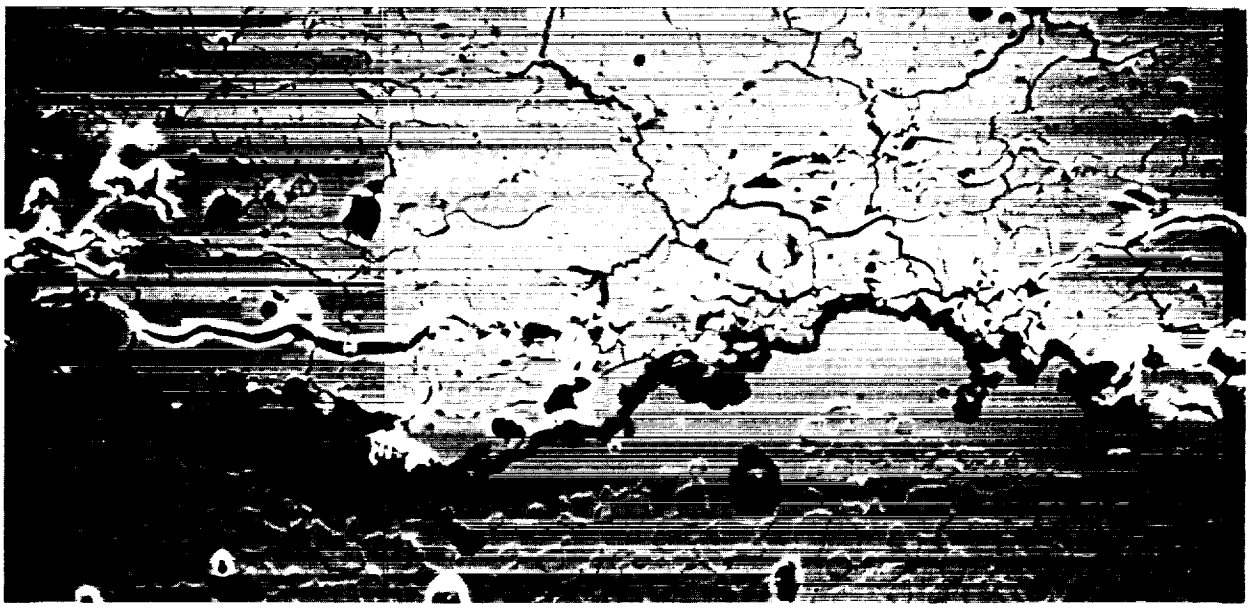

85-196 500X

Figure 47 BSI of Thermal Barrier Coating After 90 Hours of Burner Rig Test Time 2100°F/Short Cycle/Fast Heatup

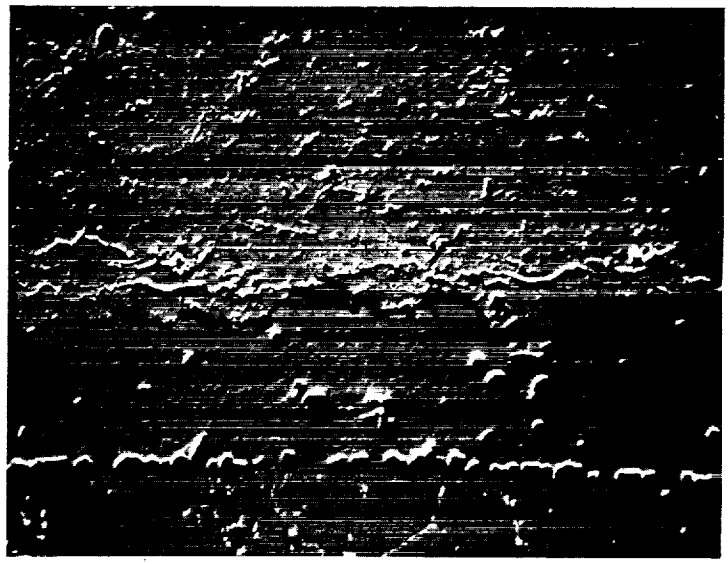

85-197
200X

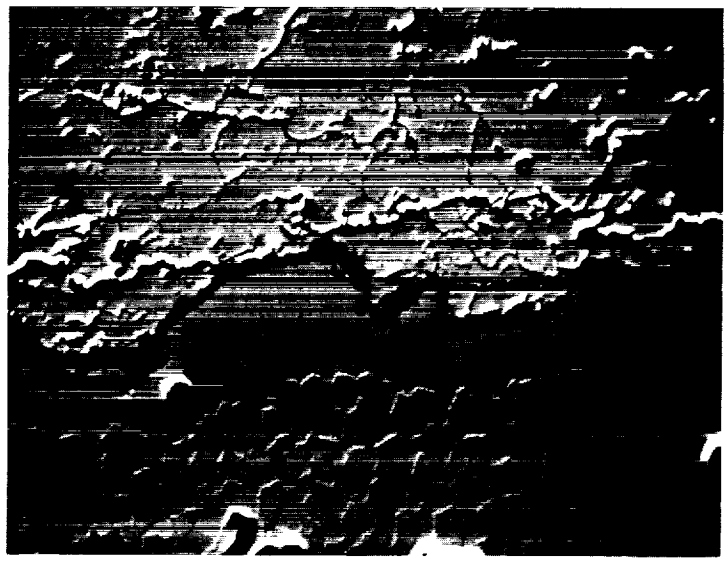

85-197
500X

85-197
1000X

Figure 48 BSI of TBC After 105 Hours of Burner Rig Test Time at 2100°F/Short Cycle/Fast Heatup

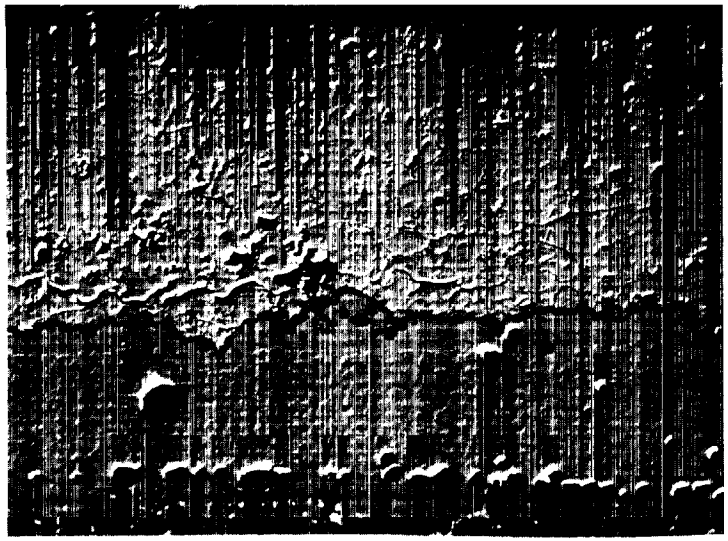

85-197 200X

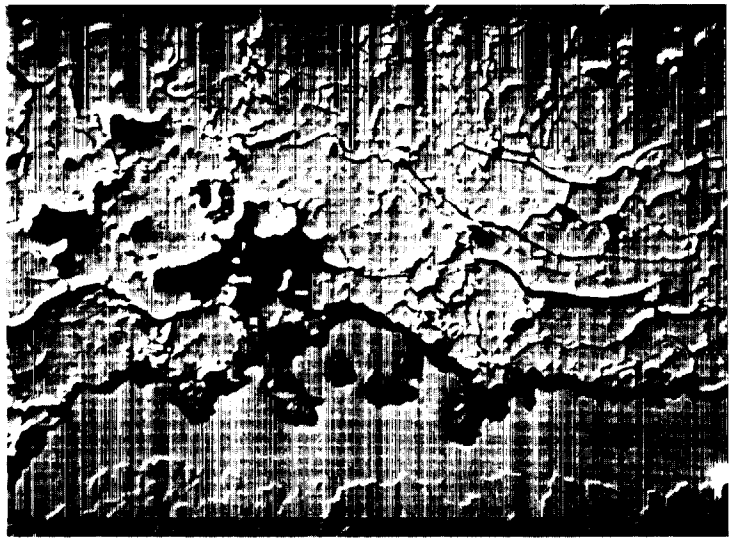

85-197 500X

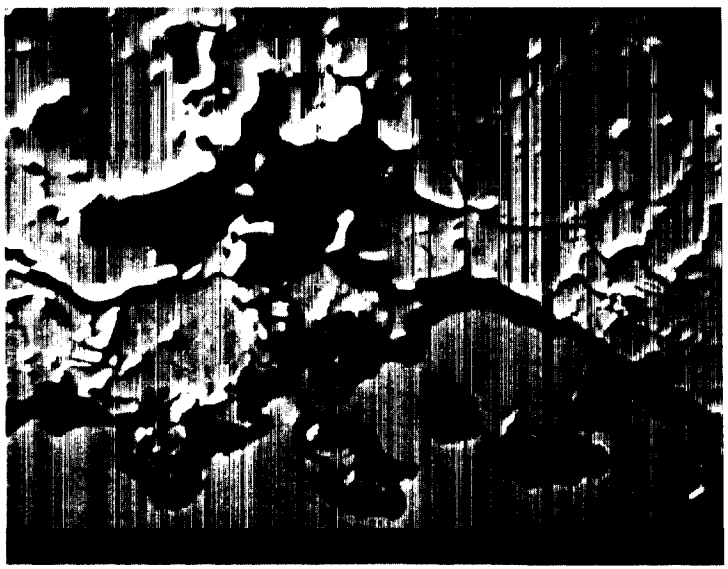

85-197 1000X

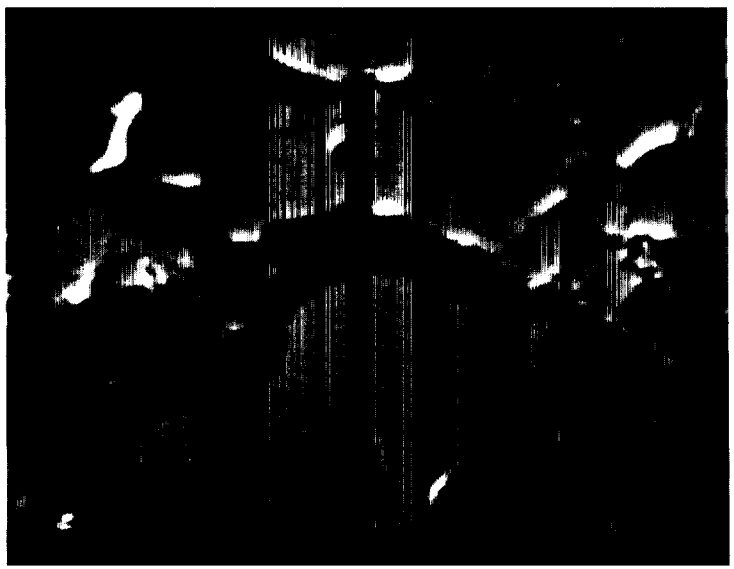

85-197 2000X

Figure 49 BSI of TBC After 105 Hours of Burner Rig Test Time at 2100°F/Short Cycle/Fast Heatup

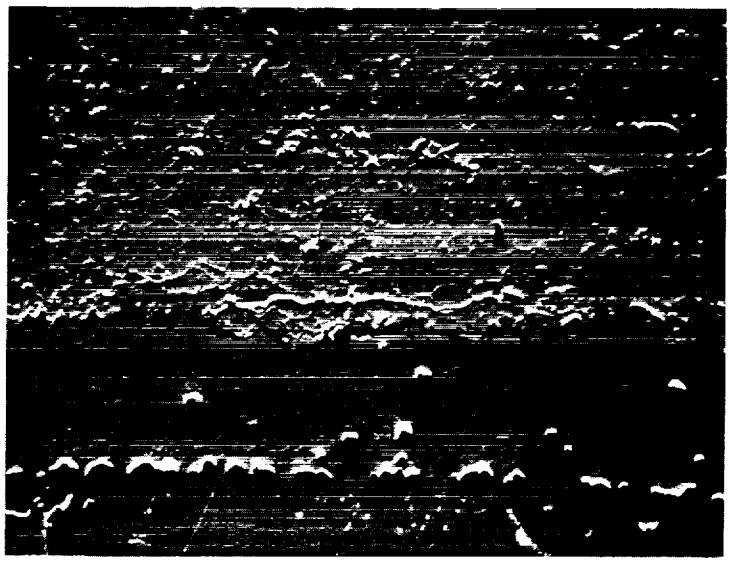

85-199
200X

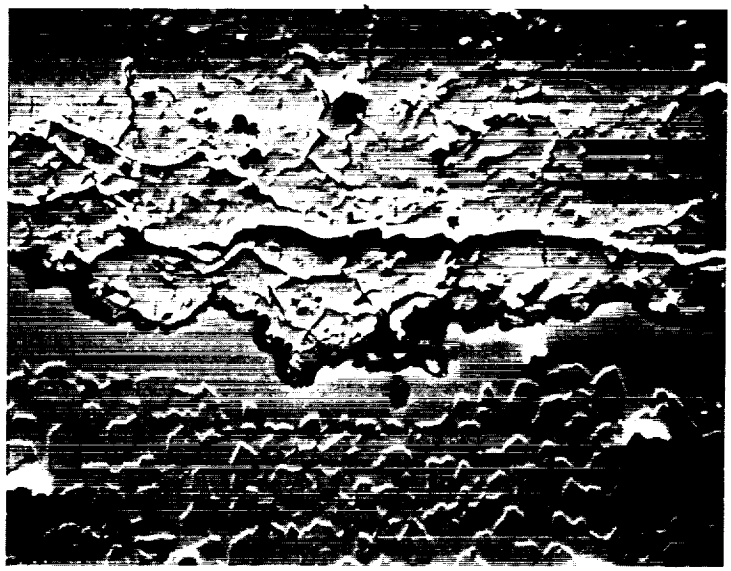

85-199
500X

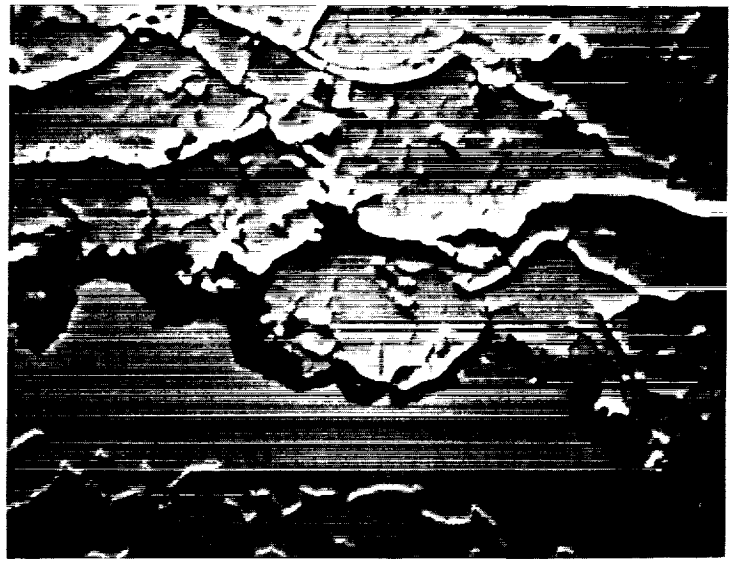

85-199
1000X

Figure 50 BSI of TBC After 135 Hours of Burner Rig Test Time at 2100°F/Short Cycle/Fast Heatup

3.1.2.3 Cyclic Hot Corrosion Tests

This subtask was designed to determine the relative importance of hot corrosion as a thermal barrier coating failure mechanism and provide test data from which a preliminary life prediction model might be developed. Nine specimens were exposed to a high corrodent level and six specimens were exposed to a low corrodent level. Twenty additional specimens were then exposed to various cyclic life fractions.

The test method involved ducted burner rig testing as described in Appendix C. To maximize the potential for hot corrosion damage, these tests were conducted with a surface temperature of 1650°F. A partial factorial test program is shown in Figure 51. Testing to spallation failure was conducted at a "high" corrodent level; 35 ppm synthetic sea salt, condition "H" in Figure 51, and at a lower corrodent level; 10 ppm synthetic sea salt identified as "J" in Figure 51. To provide information concerning the nature and rate of accumulation of hot corrosion damage, a fractional exposure test, identified as "K" in Figure 51 also, was conducted. In this test, specimens exposed to decile fractions of the high corrodent level hot corrosion life were examined metallographically to identify and characterize progressive damage mode(s) which cause thermal barrier coating hot corrosion failure. Two specimens were cycled to each of the approximate 10%, 20%, 30%, 40%, 50%, 60%, 70%, 80%, and 90% fractions of the average cyclic failure life defined in the "H" test. Two additional specimens were cycled to 100% of the "H" test life, however, after 1000 hrs of exposure no failures had occurred.

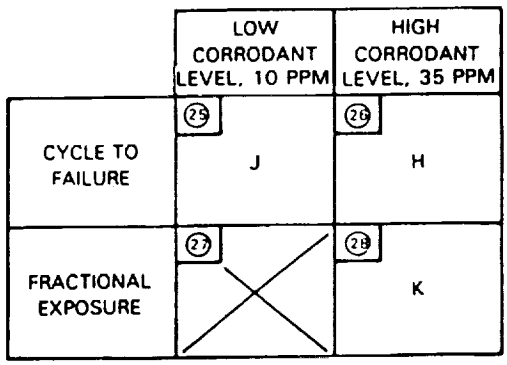

Figure 51 Task I Hot Corrosion Test Program

3.1.2.3.1 High Corrodent Level Test Results

Results of the High corrodent level test (1650°F, 35 ppm artificial sea salt, 1.3%SO_3, 1 hour cycle (57 minutes in the flame + 3 minutes FAC)) are summarized in Table XIII. These results contain significant scatter with five specimens failing between six and seven hundred hours, and two specimens surviving to 1000 hours, when testing was terminated with no failure.

A photograph of a typical high corrodent level failure is shown in Figure 52. Failures occurred well above the ceramic-metallic interface with large amounts of ceramic remaining adherent. Small visually observable cracks grew in length as testing continued until discrete patches of ceramic spalled around the bar, favoring leading edge locations.

TABLE XIII
CYCLIC HOT CORROSION TEST RESULTS (Condition H) HIGH CORRODENT LEVEL
(1650°F/Long Cycle/35ppm Artificial Sea Salt/1.3% SO_3)

Failure Time (Hrs)	
693	Avg = 618
693	
638	
615	
450	
1000	No Failure Observed
1000	
1000	

Figure 52 Cyclic Hot Corrosion Test Specimen Showing Multi-level Flaking of the Ceramic

Figures 53 and 54(a and b) show the pre-test and post-test microstructures of specimens tested 693 and 1000 hours respectively. The ceramic spallation mode seen in these structures clearly is different from that observed in clean fuel burner rig test failures, exhibiting multi-level in plane, ceramic cracking and flaking, as opposed to the predominent near interface cracking seen in clean fuel failure.

Figure 53a Pre-Test Hot Corrosion Test Specimen; 35 ppm Artificial Sea Salt/ 1650°F/1 Hour Cycle

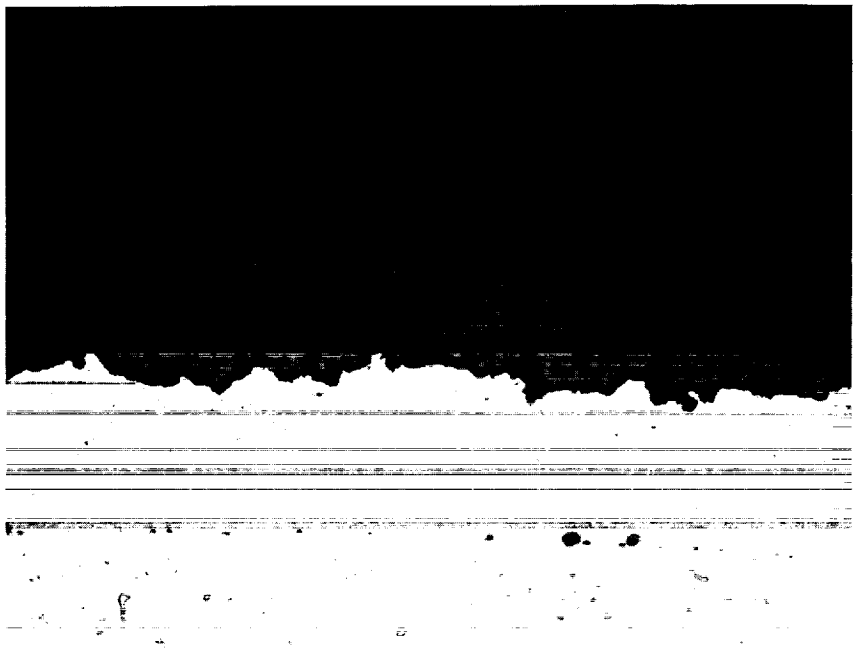

Figure 53b Post-Test Hot Corrosion Test Specimen Showing In-Plane Ceramic Cracking in Central and Upper Portion of Ceramic Layer After 693 hrs at 35 ppm Artificial Sea Salt/1650°F/1 Hour Cycle

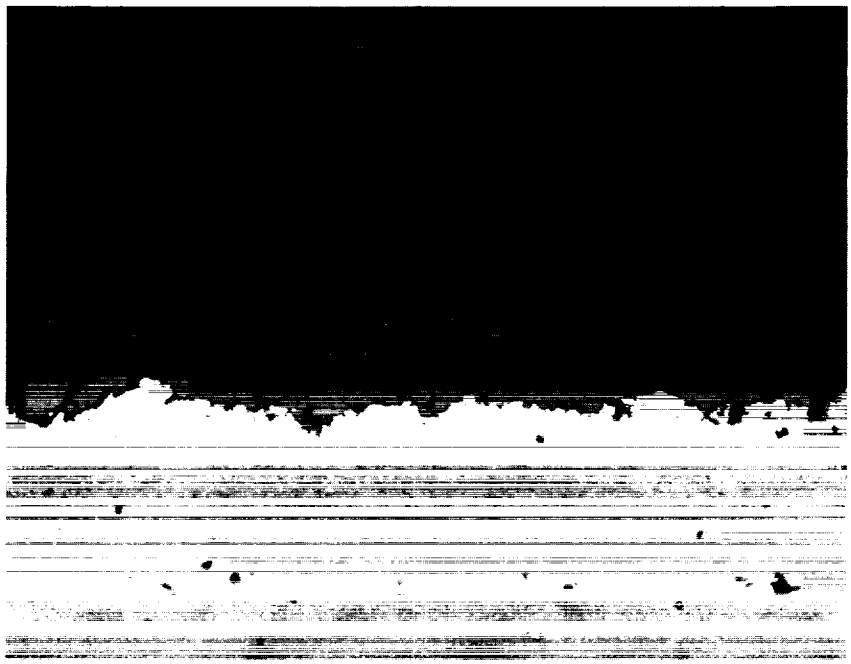

Figure 54a Pre-Test Hot Corrosion Test Specimen; 35 ppm Artificial Sea Salt/ 1650°F/1 Hour Cycle

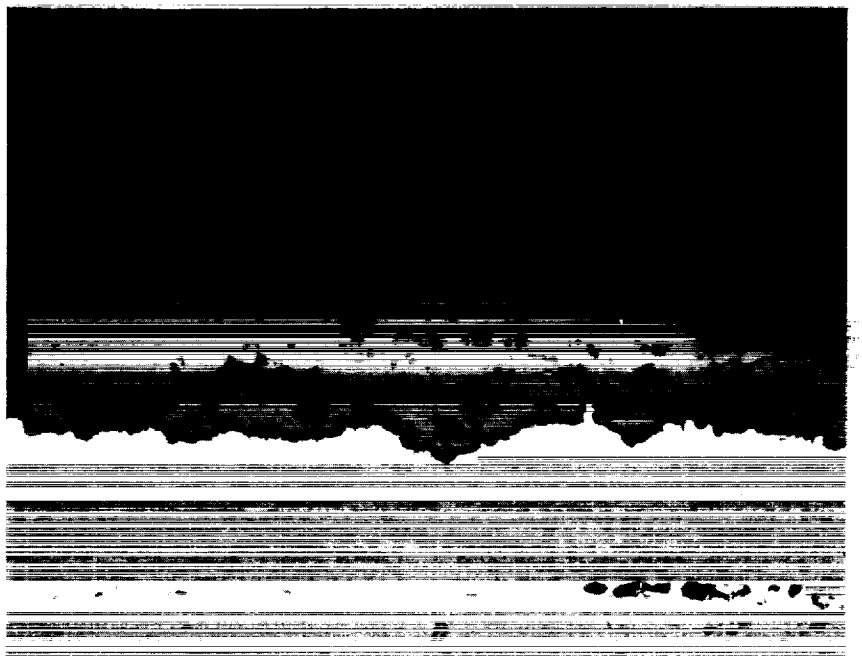

Figure 54b Post-Test Hot Corrosion Test Specimen After 1000 hrs at 35 ppm Artificial Sea Salt/1650°F/1 Hour Cycle

Figures 55(a-c), and 56(a-d) show post-test surface structure and transverse microstructure for a test specimen exposed for 450 hrs in the high corrodent level test (Condition H). The EMP results as seen in the x-ray maps clearly show the infiltration of sodium and sulfur in the pores and microcracks.

Further post corrosion test specimen evaluations have confirmed infiltration of sodium and sulfur in localized areas of porosity and microcracking throughout the thickness of the ceramic coating. Increased exposure time shows increased infiltrent concentration in these areas. Magnesium, contained in synthetic sea salt as $MgCl_2$ (see Table XIV), was generally not detected in the zirconia layer but was found concentrated at the oxide layer between the ceramic/bond coat interface. As shown in Figures 57(a-g), x-ray maps for Al and Mg may suggest the predominance of the formation of $MgAl_2O_4$ spinel.

Table XV shows x-ray diffraction analysis for representative post test high corrodent level test specimens (condition H). It is noted that "higher" time specimens show a significant increase in v/o monoclinic and also up to 10 v/o of other phases; i.e., fcc NiO, or the orthorhombic $NiCrO_4$, Ca_2SiO_4. This increase in monoclinic phase (stabilization of ZrO_2) is believed to influence coating spalling life.

TABLE XIV
ARTIFICIAL SEA SALT COMPOSITION

NaCl	58.4%
$MgCl_2$	26.4
Na_2SO_4	9.7
$CaCl_2$	2.7
KCl	1.6
$NaHCO_3$	.4
KBr	.23
H_3BO_3	.07
$SrCl_2$	.09
Na F	.007

TABLE XV
X-RAY DIFFRACTION ANALYSIS FOR SOME REPRESENTATIVE CYCLIC HOT CORROSION POST-TEST SPECIMENS
(High Corrodent Level)

Specimen/ Location	v/o fcc ZrO_2	v/o Tetragonal ZrO_2	v/o Monoclinic ZrO_2	Other	Failure Time (hrs)
(HST #086) Spalled Area	60-65	35-40	5	1 v/o Unidentified	450
(HST #088) Spalled Area	50	25-35	15-10	10 v/o fcc and /or MgO 1 v/o orthorhombic $NiCrO_4$	615
(HST #091) Spalled Area	45-50	45-50	10	1 v/o fcc NiO, MgO and/or Ca_2SiO_4	693

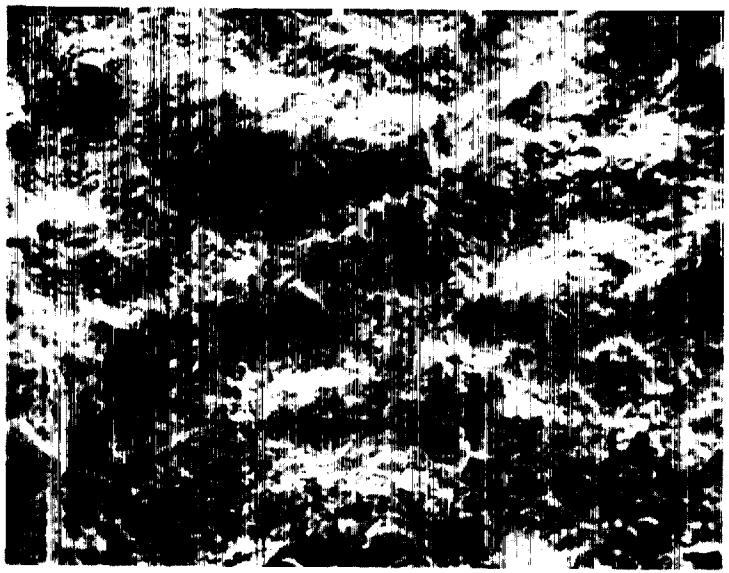

a) SEI Detailed Image Of Coating On Test Bar Surface 800X

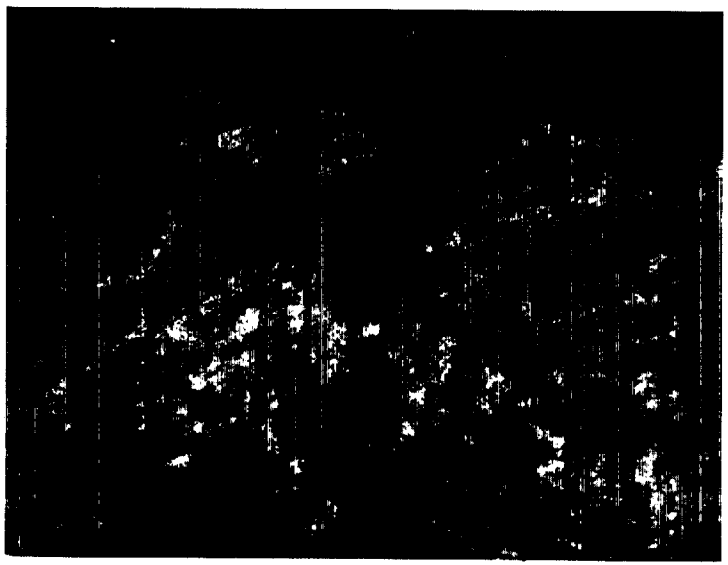

b) Na X-Ray Map 800X

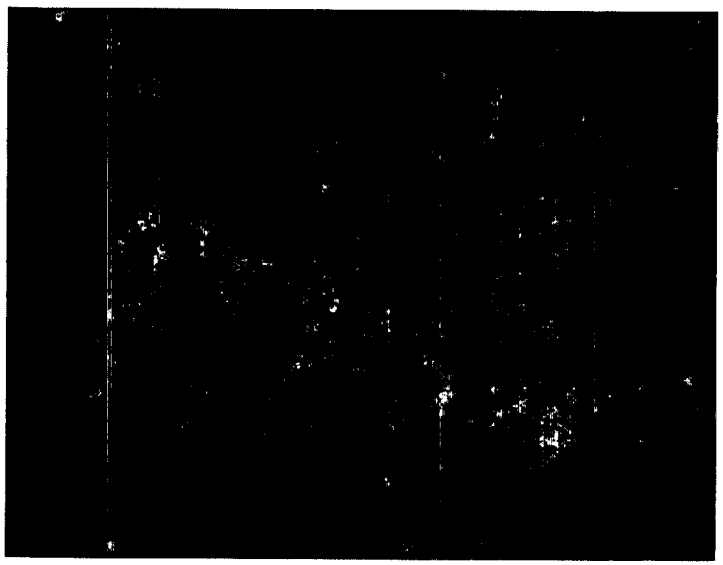

c) Sulfur X-Ray Map 800X

Figure 55 Cyclic Hot Corrosion Test Specimen Surface (HST-086) After 450 Hrs/1650°F - High Corrodent Level Test

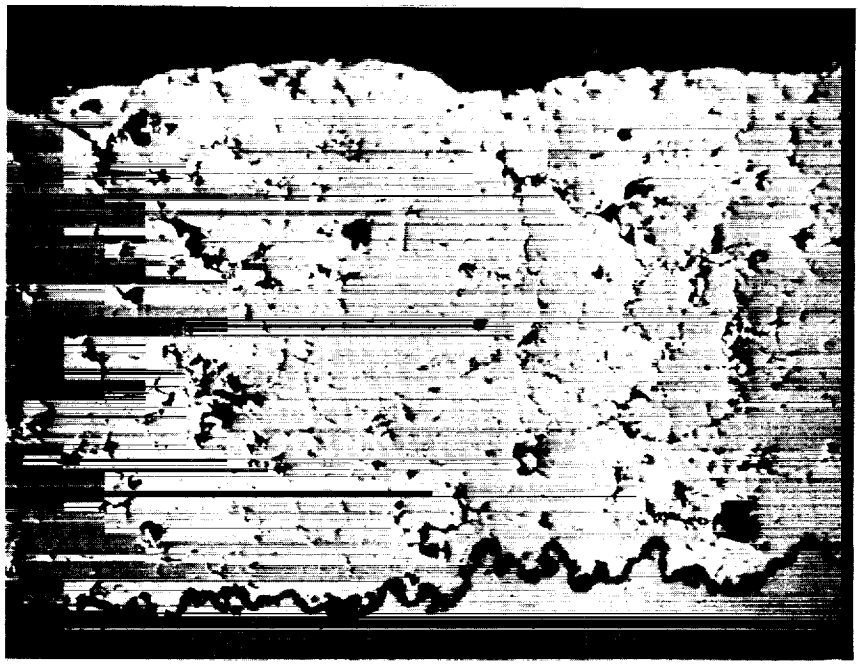

a) BEI 300X

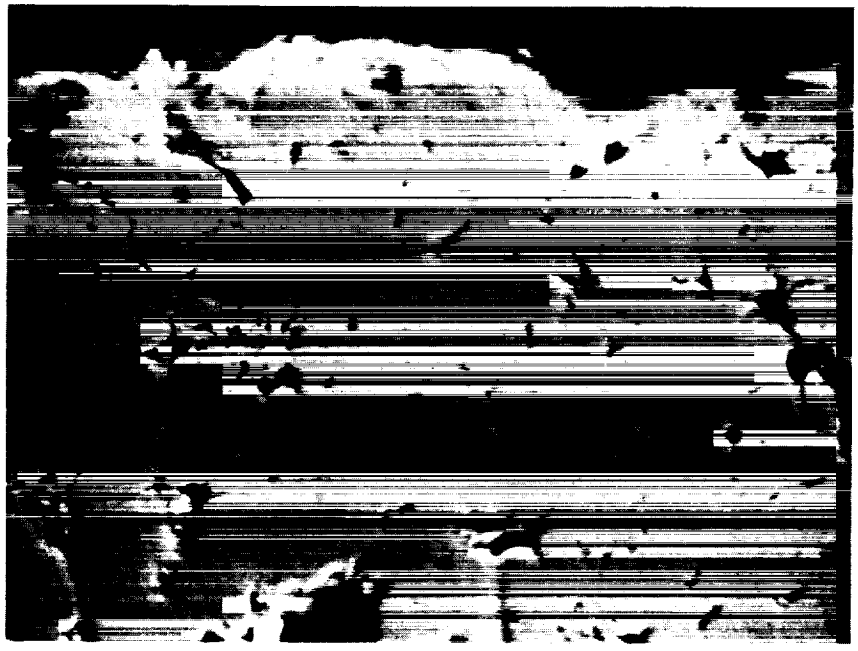

b) BEI Detailed Image Of Outer Surface Of Coating 1000X

Figure 56 Cyclic Hot Corrosion Test Specimen After 450 Hrs at 1650°F. High 35 ppm Corrodent Level in Area Near Failure.

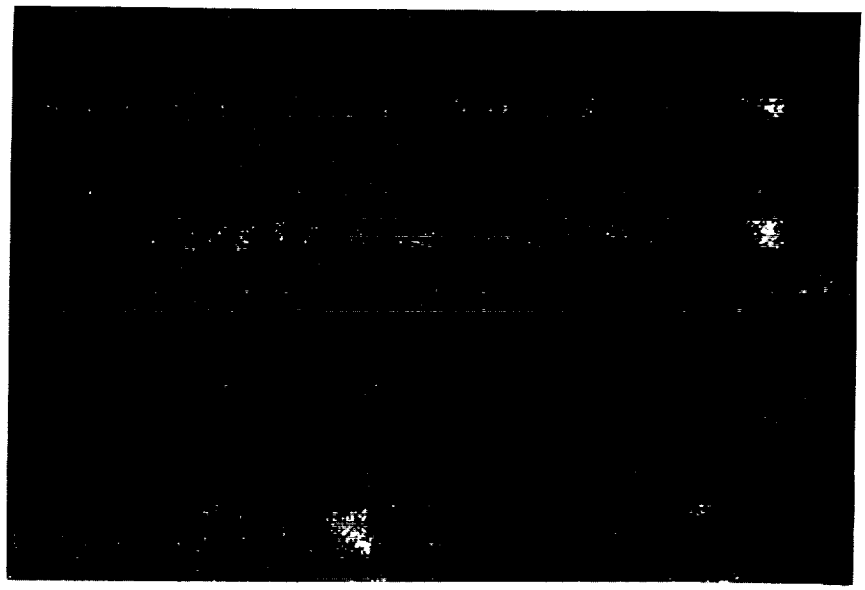

c) Na X-Ray Map 1000X

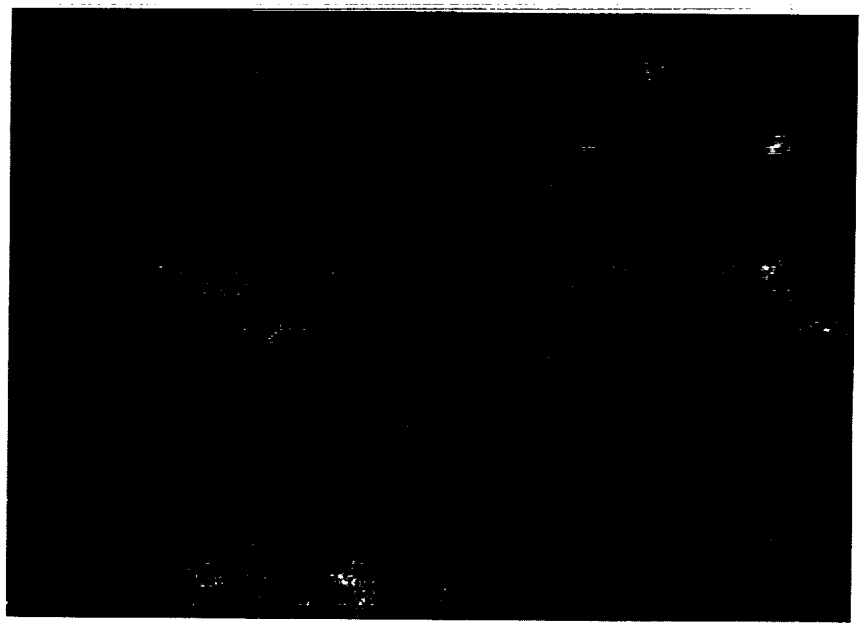

d) Sulfur X-Ray Map 1000X

(continued)

Figure 56 Cyclic Hot Corrosion Test Specimen After 450 Hrs at 1650°F. High Corrodent Level in Area Near Failure.

a) BEI 300X

b) BEI Detailed Image of Oxide Layer 2000X

c) Al X-Ray Map 2000X

d) Mg X-Ray Map 2000X

Figure 57 Cyclic Hot Corrosion Post-Test Specimen After 1000 hrs at 1650°F/ Long Cycle/35 ppm Artificial Sea Salt/1.3% SO_3

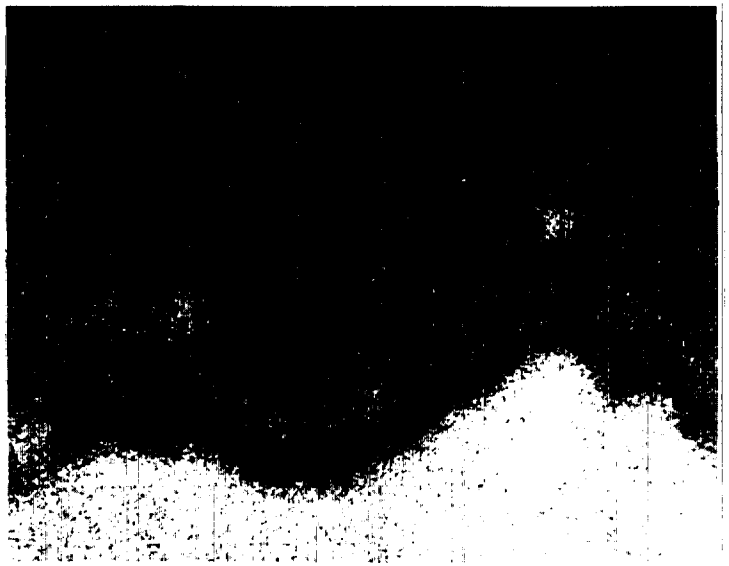

e) Cr X-Ray Map 2000X

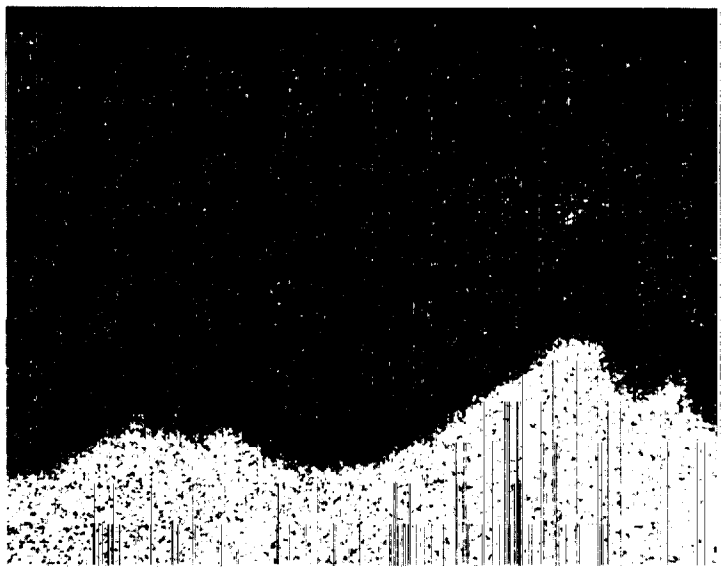

f) Ni X-Ray Map 2000X

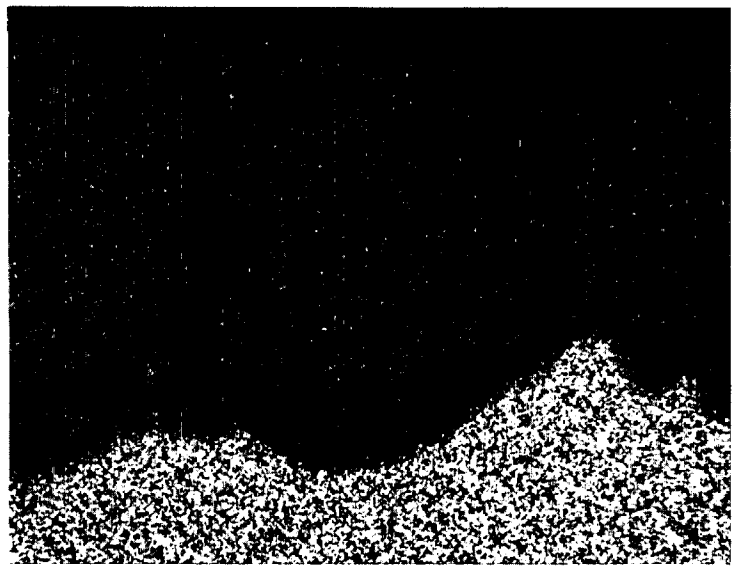

g) Co X-Ray Map 2000X

Figure 57 (continued) Cyclic Hot Corrosion Post-Test Specimen After 1000 hrs at 1650°F/ Long Cycle/35 ppm Artificial Sea Salt/1.3% SO_3

3.1.2.3.2 Low Corrodent Level Test Results

The low corrodent level test (Condition J) 10 ppm artificial sea salt, 1.3% SO_3, was terminated after completing 1000 hrs of test time, with none of the six specimens tested exhibiting any evidence of coating degradation. The specimens did show, however, a dark brown surface appearance, Figure 58 shows a photomicrograph of one of these specimens after over 1000hrs of exposure.

Electron microprobe analysis conducted on the cross-sectional microstructure of an unfailed low corrodent level specimen indicated less corrodent infiltration than found in high corrodent level specimens.

As seen in Figures 59 through d, low levels of Na and S were detected in areas of porosity and microcracking. Magnesium was detected not only within pores and cracks, but also at the ceramic-bond coat interface. It appears that this element is in the form of an oxide and at the interface forms spinel; $MgAl_2O_4$, as shown in Figures 60a through 60d.

Table XVI presents X-ray diffraction data for two representative low corrodent level samples. The phase distribution as shown is not consistent for these two specimens exposed for the same length of time. It was observed that for at least one specimen a high v/o monoclinic ZrO_2 (20-25 v/o) was detected.

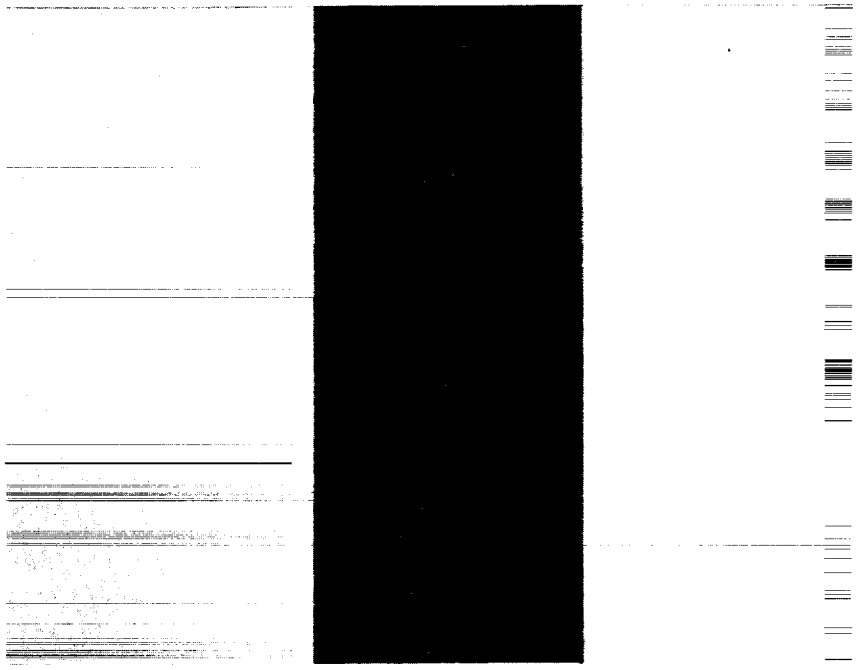

Figure 58 Light Photomicrograph of Test Specimen After 1000 hrs at 1650°F/ Long Cycle/10 ppm Synthetic Sea Salt/1.3% SO_3 - Condition J

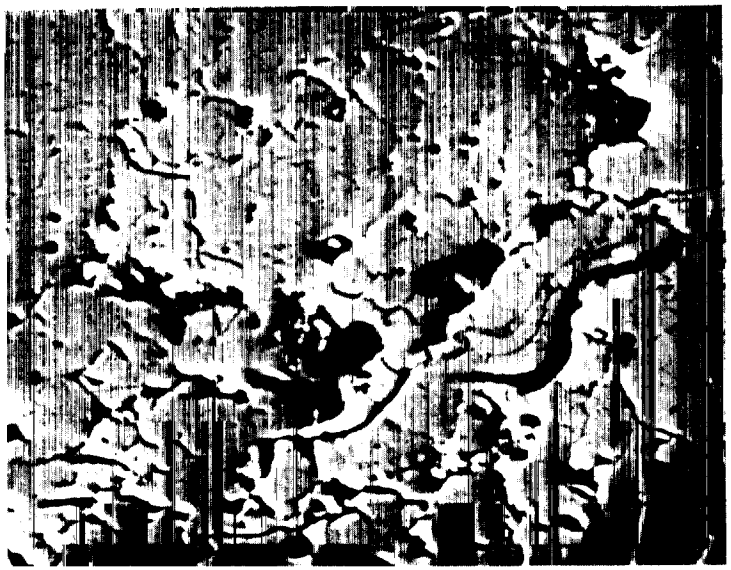

(a) Detailed Image of Coating 800X

(b) Na X-ray Map 800X

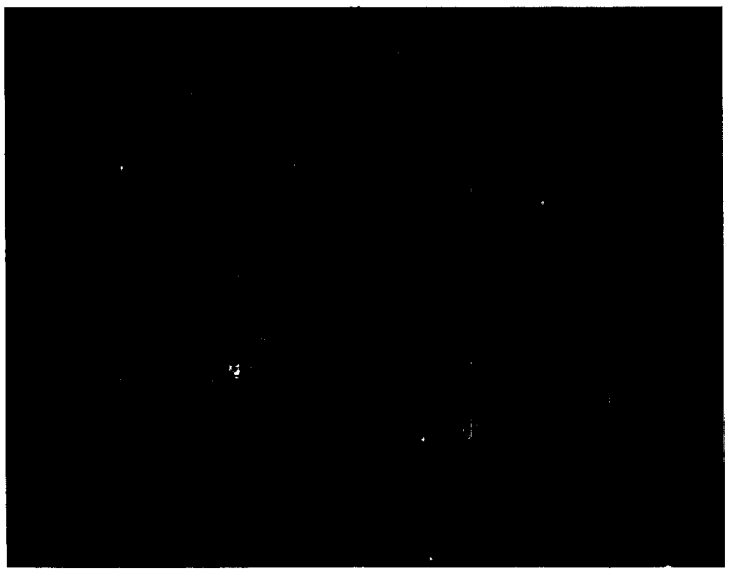

(c) Sulfur X-ray Map 800X

(d) Mg X-ray Map 800X

Figure 59 Post Test Specimen Microstructure After 1000 hrs with Artificial Sea Salt 10ppm and 1650°F Host Test "J"

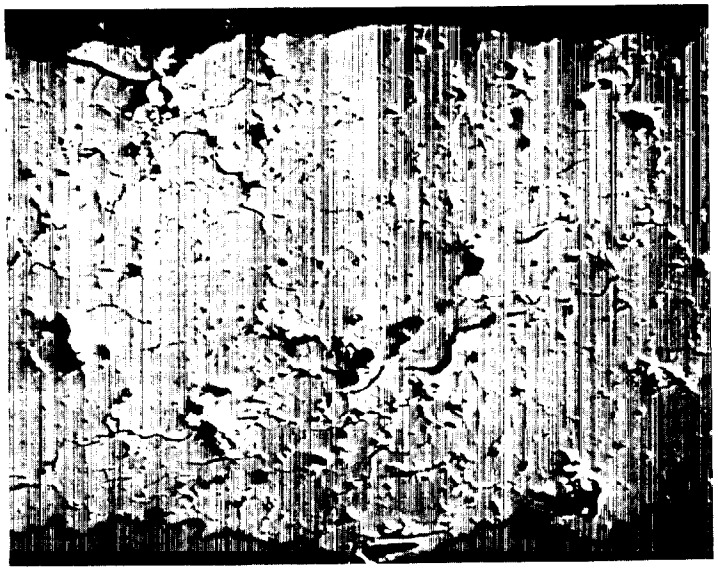

(a) BEI 300X

(b) BEI Detailed Image of Oxide Layer 2000X

(c) Al X-ray Map 2000X

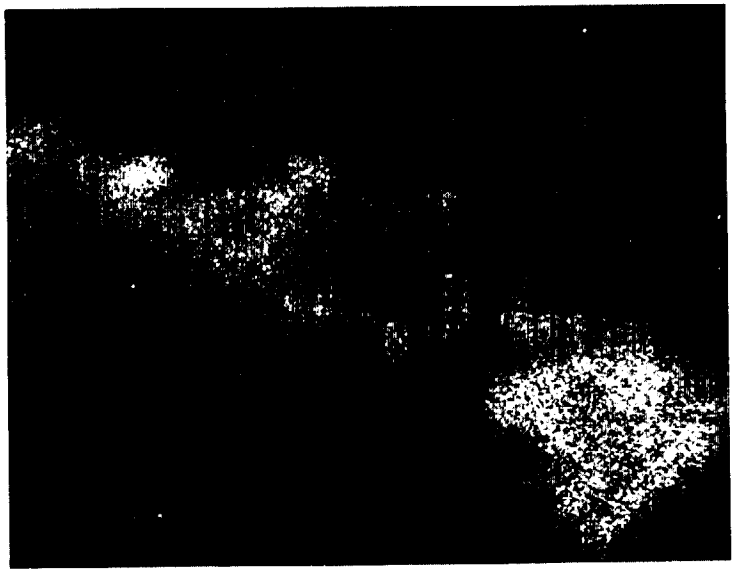

(d) Mg X-ray Map 2000X

Figure 60 Post Test Specimen Microstructure After 1000 hrs with Artificial Sea Salt 10ppm and 1650°F Host Test "J"

TABLE XVI
X-RAY DIFFRACTION ANALYSES OF SOME REPRESENTATIVE POST-TEST SPECIMENS, CYCLIC HOT CORROSION TEST (Low Corrodent Level)

Specimen/ Exposure Time	v/o FCC ZrO_2	v/o Tetragonal ZrO_2	v/o Monoclinic ZrO_2	v/o Other
HST 113/ 1000 hrs	42-45	32-35	5	10-7 fcc $NiCr_2O_4$ and/or $NiFe_2O_4$ spinel), 5 fcc NiO and and/or MgO, 3-1 hexagonal NiS, 2-1 bcc Y_2O_3, 1 tetragonal TiO_2, and possibly 1 hexagonal - Al_2O_3
HST 131/ 1000 hrs	30-35	25-20	25-20	5 fcc $NiFe_2O_4$ and/or $NiFe_2O_4$ (spinel), 5 hexagonal NiS, 10-15 fcc $(Fe,Ni)S_2$

3.1.2.3.3 Fractional Exposure Hot Corrosion Test Results

The fractional exposure corrosion test K (35ppm artificial sea salt, 1650°F, long cycle) was terminated with over 1000 hours of test time accumulated.

Two of the twenty specimens planned for this test were to be reference specimens taken to failure to confirm the previously determined average test life (from the H test: 35ppm artificial sea salt, long cycle, 1650°F). The other 18 specimens were to be tested to decile fractions of this life.

However, these two specimens did not fail after over 1000 hours of testing and in accordance with the statement of work this test was terminated. Thus there is an uncertainty as to the actual life fractions of the eighteen specimens, evaluated.

Post-test metallographic analysis was conducted for one of the specimens exposed to each fraction of the coating life. Figures 61a through i show the typical post-test microstructures for specimens exposed to the estimated 10%-90% of TBC life. These specimens were polished using standard procedures except that an oil-based polishing slurry replaced water to prevent leaching of infiltrated corrodent. This metallographic analysis was conducted to look for subcritical crack development. Fractionally exposed specimen metallography showed some accumulated damage after 515 - 585 test hours; large in-plane cracks with several minor extensions were noted above the "typical" failure location. Note that the large crack in Figure 61i has several smaller extensions. Also, this crack is far from the interface in comparison with the typical clean fuel burner rig test failure mode. Figure 61h shows what may be considered the start of microcrack "link up" at the center of the ceramic. Also note the patch of ceramic which has flaked off at the outer surface. Most of the rest of the photomicrographs show some segmentation cracking which is thought to have developed during exposure.

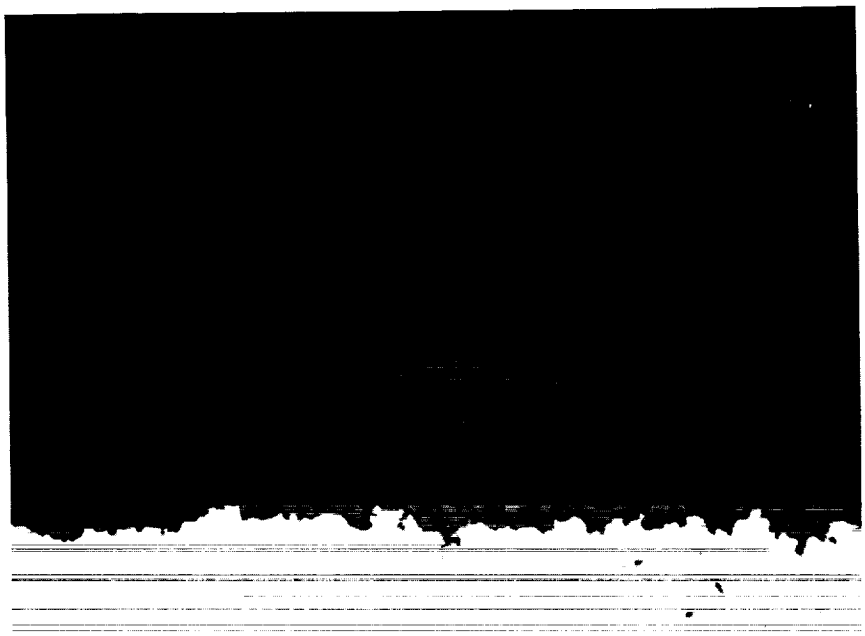

200X

Figure 61a Post-Test Fractional Hot Corrosion Specimen Microstructure 10%, 65 hrs/1650°F/35 ppm Na_2SO_4

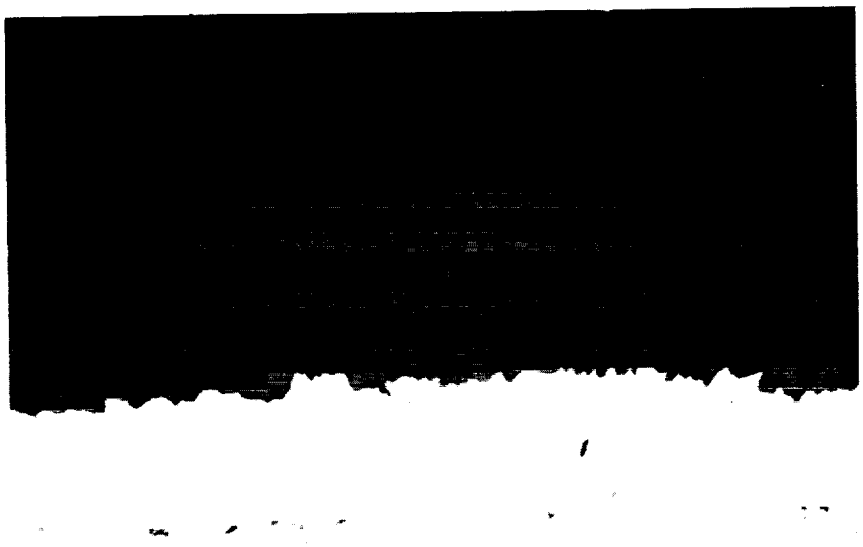

200X

Figure 61b Post-Test Fractional Hot Corrosion Specimen Microstructure 20%, 130 hrs/1650°F/35 ppm Na_2SO_4

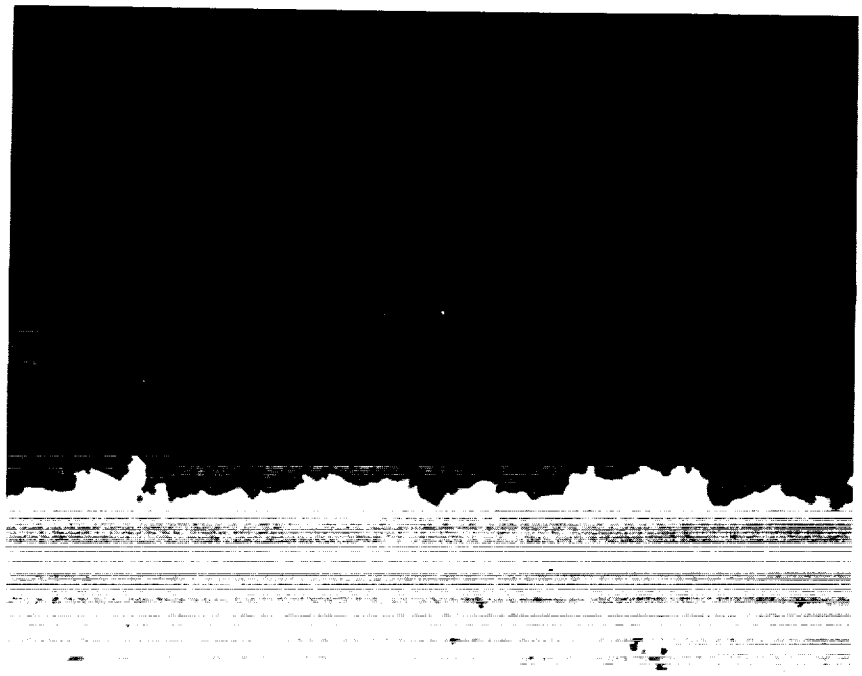

200X

Figure 61c Post-Test Fractional Hot Corrosion Specimen Microstructure 30%, 185 hrs/1650°F/35 ppm Na_2SO_4

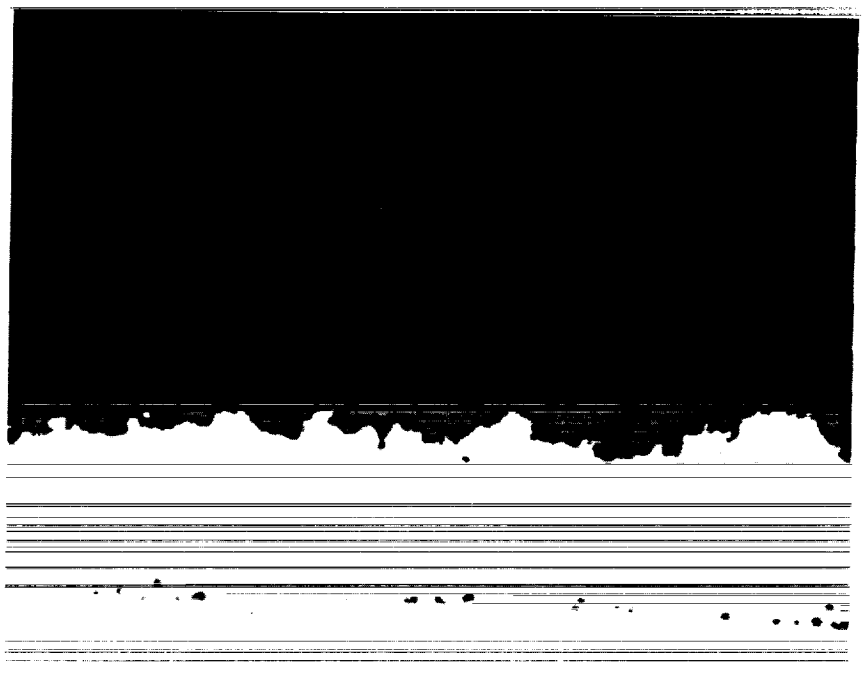

200X

Figure 61d Post-Test Fractional Hot Corrosion Specimen Microstructure 40%, 250 hrs/1650°F/35 ppm Na_2SO_4

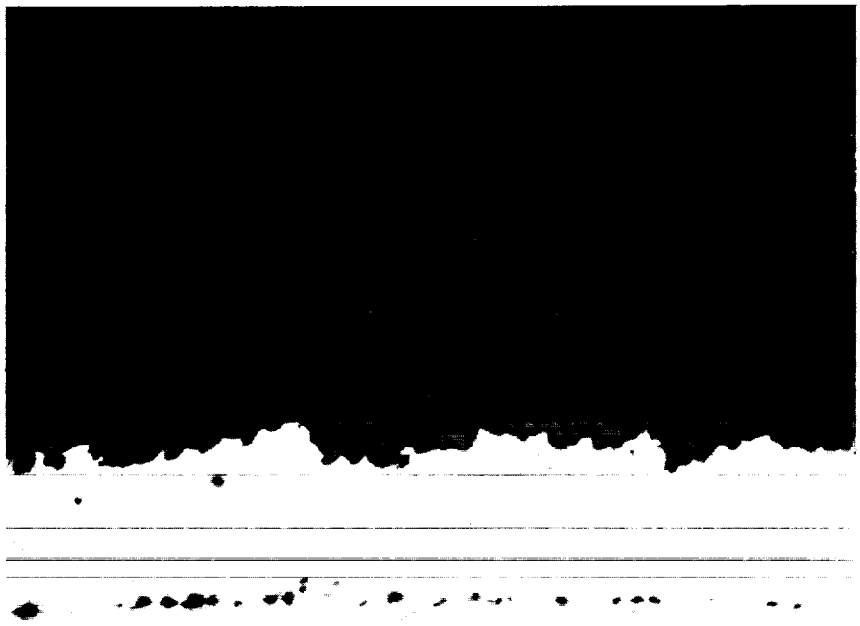

200X

Figure 61e Post-Test Fractional Hot Corrosion Specimen Microstructure 50%, 315 hrs/1650°F/35 ppm Na_2SO_4

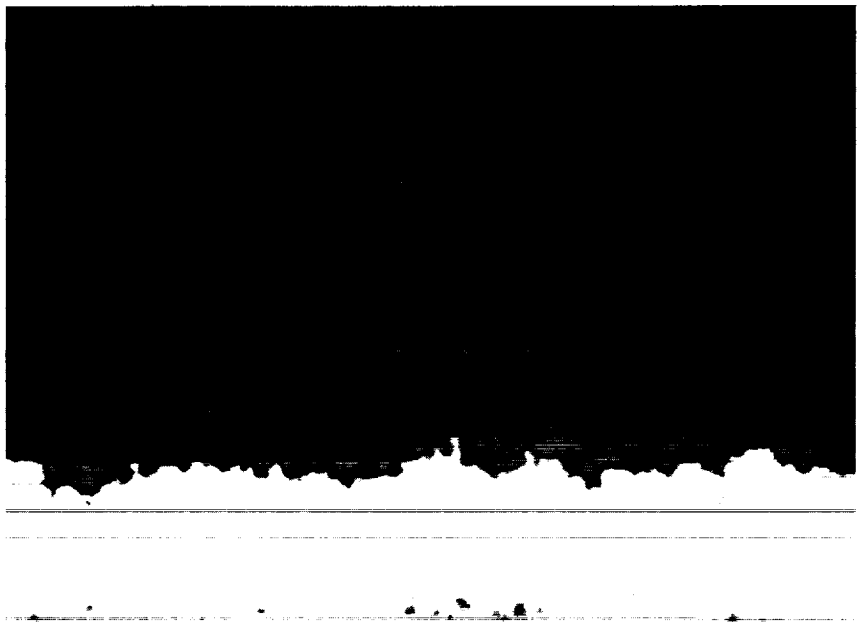

200X

Figure 61f Post-Test Fractional Hot Corrosion Specimen Microstructure 60%, 380 hrs/1650°F/35 ppm Na_2SO_4

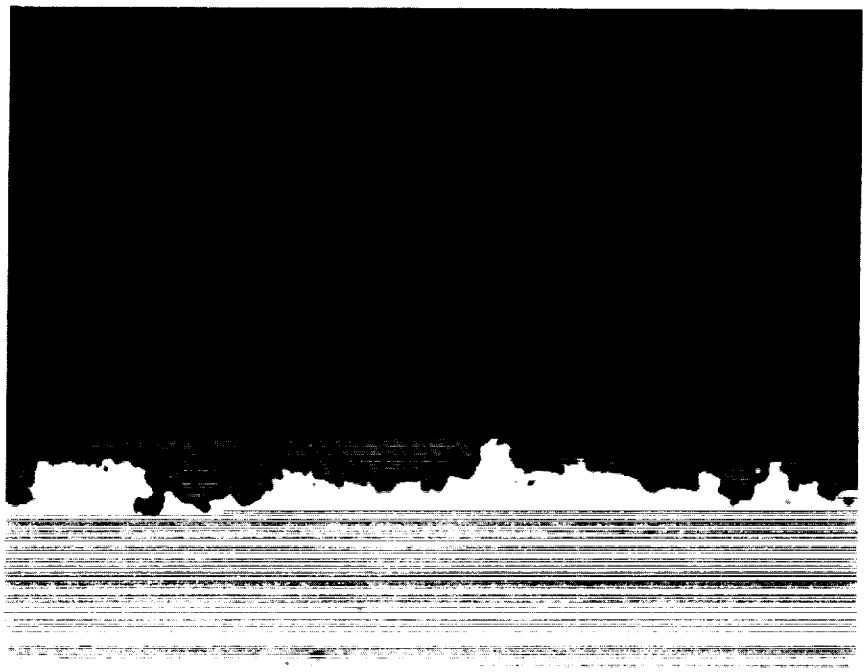

200X

Figure 61g Post-Test Fractional Hot Corrosion Specimen Microstructure 70%, 445 hrs/1650°F/35 ppm Na_2SO_4

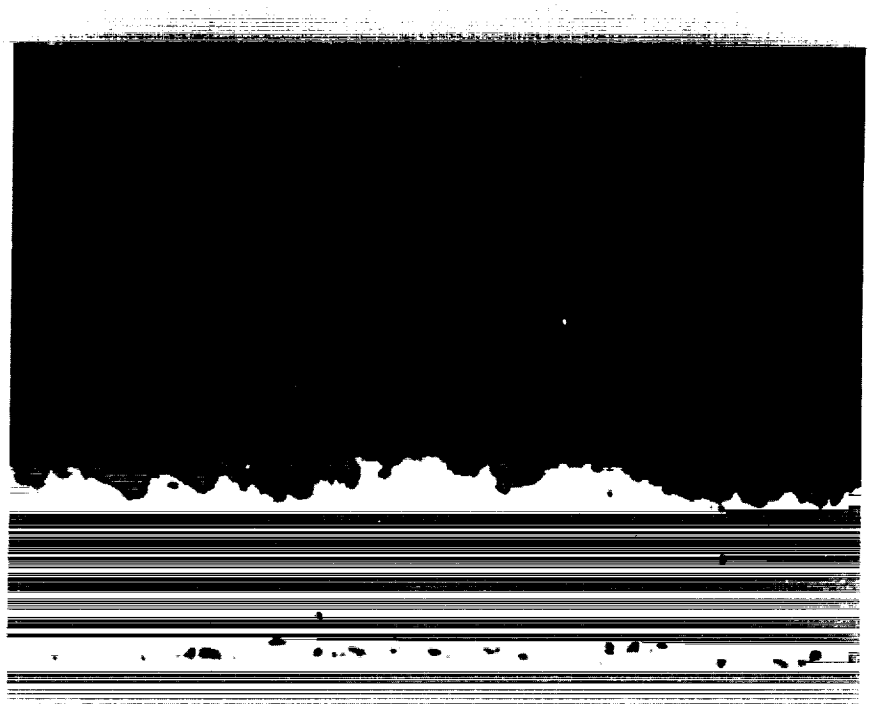

200X

Figure 61h Post-Test Fractional Hot Corrosion Specimen Microstructure 80%, 510 hrs/1650°F/35 ppm Na_2SO_4

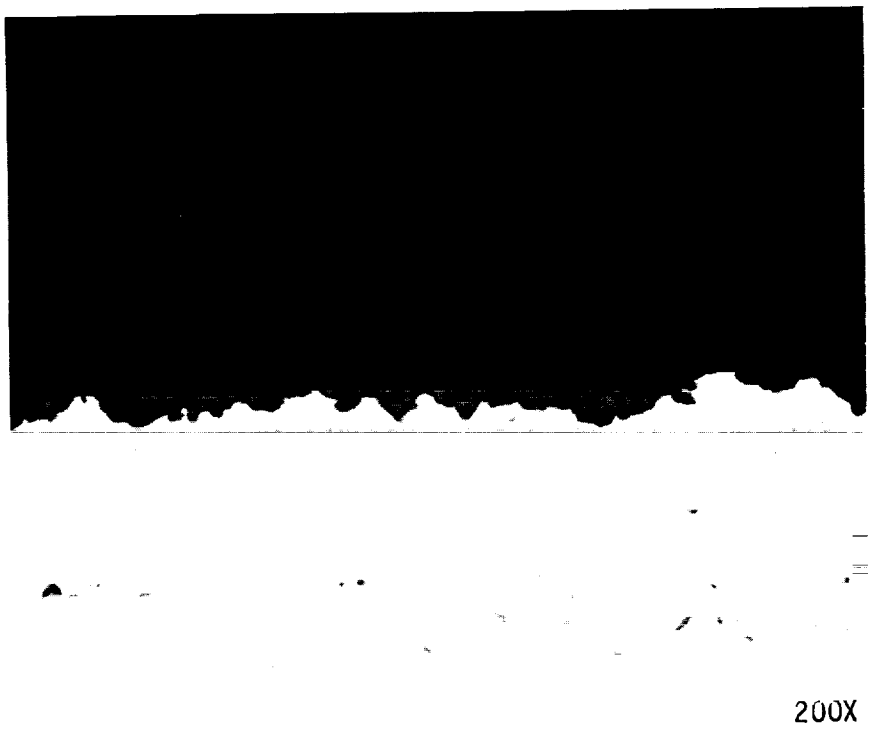

Figure 61i Post-Test Fractional Hot Corrosion Specimen Microstructure 90%, 575 hrs/1650°F/35 ppm Na_2SO_4

The results of the X-ray diffraction analysis for the fractionally exposed specimens is included in Table XVII. It is apparent from the data that increased exposure times show increased v/o monoclinic ZrO_2.

The analysis of the fractionally exposed specimens (10% - 90%) removed from the test showed a minimum of 5 v/o monoclinic ZrO_2 for smaller fractions of exposure and up to 9 v/o monoclinic ZrO_2 for higher fractions of exposure. This result is consistent with earlier suggestions of thermochemical interaction of the corrodent with the ceramic (Ref. 30, 34, 35, 36), i.e., selective "leaching" of Y_2O_3 by the corrodent.

In summary, the results of the contaminated fuel burner rig test conducted showed that 7YsZ is extremely spall resistant in hot corrosion environments. When TBC failure did occur, only in high corrodent level testing, the TBC failure mode consisted of multilevel flaking of the ceramic. This mode is unique to cyclic hot corrosion testing and has not been seen in clean fuel burner rig, furnace test, or more importantly in any of the engine exposed hardware examined to date. X-ray diffraction analysis has shown higher levels of monoclinic ZrO_2 forming upon cool down, however, ceramic spallation was unobserved. Thus a predominant failure mechanism may more likely involve mismatch between infiltrate and ceramic as reported in earlier studies (Ref. 14, 30, 32, 34) than selective leaching of Y_2O_3 causing destabilization (Ref. 35, 36). Although the latter is occurring there seems to be no correlation to actual failure life. However, failure life of the ceramic is most probably governed by the interaction of these two mechanisms.

TABLE XVII
X-RAY DIFFRACTION ANALYSES OF FRACTIONAL EXPOSURE, CYCLIC HOT CORROSION TEST SPECIMENS

SPECIMEN ID/ EXPOSURE TIME	V/O PHASE PRESENT			
	FCC ZrO_2	TETRAGONAL ZrO_2	MONOCLINIC ZrO_2	OTHER
HST-004A - 65 hrs	55-53	40-42	5	1 unidentified (possibly fcc NiO)
HST-007A 130 hrs	54-56	39-37	6-4	1-2 NiO and $\leq$ 1fcc (Ni, Fe) S_2
HST-009A - 185 hrs	54-56	39-37	6-4	$\leq$ 1 Hexagonal Na_2SO_4 and/or Hexagonal α - $NaFeO_2$
HST-012A - 250 hrs	53-55	38-36	5-3	2-4 fcc NiO, 2-1 tetragonal γ - Fe_2O_3 $\leq$ 1 fcc FeS_2
HST 017A 315 hrs	53 55	37-35	4-6	2 Tetragonal γ - Fe_2O_3 2-1 Hexagonal α - $NaFeO_2$, 2-1 fcc (Ni,Fe) S_2
HST 019A - 380 hrs	43-45	45-43	7-9	3-1 fcc (Ni,Fe) S_2, 2 Tetragonal γ - Fe_2O_3 $<<$ 1 fcc NiO
HST 022A 445 hrs	52-54	38-36	6-8	2-1 Tetragonal γ - Fe_2O_3
HST-025A - 510 hrs	Poor Profile trace, major phase-fcc ZrO_2, minor phases- tetragonal ZrO_2, monoclinic ZrO_2 and hexagonal Na_2SO_4			
HST-027A - 575 hrs	Poor profile trace major phase hexagonal Na_2SO_4, fcc ZrO_2 - trace			
HST-032A - 1000 hrs	30	45-50	15 10	$\leq$10 [2 $(Mg_{96}$ $Fe_{0.04})$ 0.SiO_2] ~1 βNiAl ~1 NiO
HST-032A - 1000 hrs	30	45-50	15 10	$\leq$10 [2 $(Mg_{96}$ $Fe_{0.04})$ O. SiO_2] ~1 βNiAl ~1 NiO

3.1.3 Task IB.2 Determine Physical/Mechanical Properties

The purpose of this subtask was to measure values of physical and mechanical properties required for subsequent analytical and life modeling. Measured physical properties include thermal conductivity, specific heat, and thermal expansion of bulk porous zirconia and dense NiCoCrAlY specimens fabricated to simulate structures found in the respective TBC coating layers. Mechanical tests were conducted only on bulk porous zirconia and included fracture toughness, uniaxial tension and compression, tensile and compressive creep, and "derived" tensile fatigue in the range of ambient to 2200°F. All needed base alloy properties and mechanical properties of the metallic coating were available from prior internally funded programs and were not remeasured in this program. All physical property testing was conducted by Dynatech Corporation, Cambridge, Mass. With the exception of an ambient temperature four point bend test conducted early in the program to gain needed preliminary insight into basic ceramic constitutive behavior, all mechanical property tests were conducted at Southwest Research Institute, San Antonio, Texas.

Bulk ceramic and metallic property test specimens were fabricated by plasma deposition using the same parameters as used to make the respective TBC coating layer. Coating thickness of up to one half inch were accumulated on mild steel panels and then the test specimens were machined off and ground to required dimensions. Shown in Figure 62 is a bulk ceramic specimen microstructure which can clearly be seen to quite closely simulate the microstructure of the 10 mil ceramic coating.

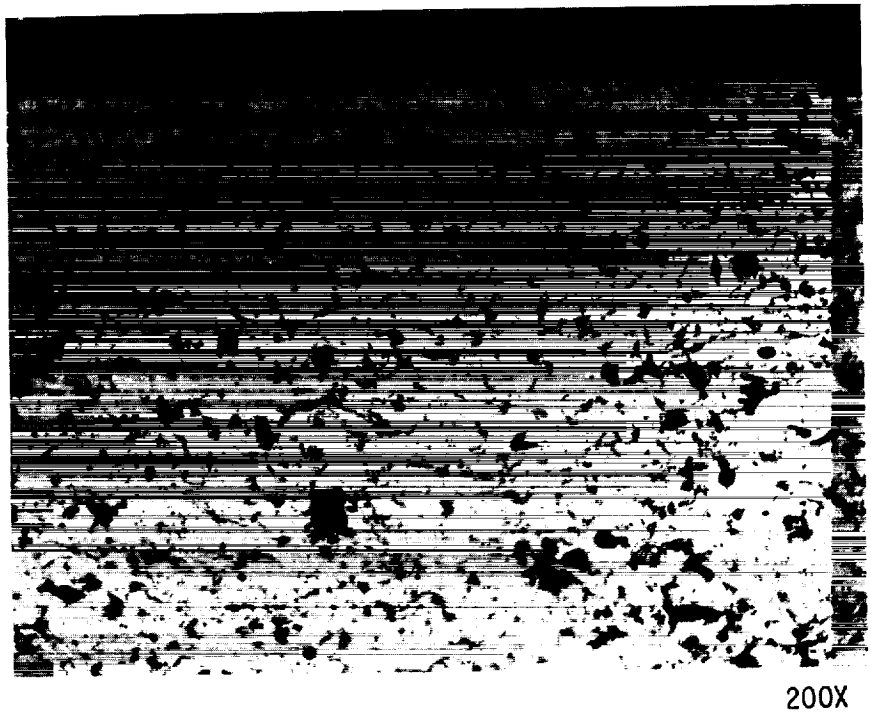

Figure 62 Bulk Ceramic Microstructure Used for Physical/Mechanical Property Tests

3.1.3.1 Physical Property Tests

Procedures used by Dynatech to measure physical properties are summarized in Appendix D. Specific numbers of physical tests conducted and the corresponding temperature ranges investigated are summarized in Table XVIII. Results of these tests are presented in Tables XIX through XXIV.

TABLE XVIII
COATING PROPERTY TESTS

	Virgin Ceramic (Bulk Specimen)	Virgin Bond Coat (Bulk Specimen)
o Thermal Conductivity	3 Tests: 1000°F, 1600°F, 2100°F	3 Tests: 1000°F, 1600°F, 2100°F
o Thermal Expansion	2 Tests: 1000°F, 2100°F	2 Tests: 1000°F, 2100°F
o Specific Heat	3 Tests: 1000°F, 1600°F 2100°F	3 Tests: 1000°F, 1600°F, 2100°F

TABLE XIX
THERMAL CONDUCTIVITY OF 7 w/o Y_2O_3 -ZrO_2

Temperature (°C/°F)	Thermal Conductivity (W/mK)	(Btu in/hr ft^2°F)
538/1000	0.645	4.47
871/1600	0.675	4.68*
1100/2012	0.660	4.58

*The accuracy of these measurements ranges from ±8-10% and therefore the apparant peak at 1600°F is not considered to be significant. This judgment is based in part on previous work done at Dynatech for Pratt & Whitney, which showed no thermal conductivity peaks at intermediate temperatures.

TABLE XX
SPECIFIC HEAT OF 7 w/o Y_2O_3 -ZrO_2

Temperature (°C/°F)	Specific Heat J/g °C	cal/g C (Btu/lb °F)
538/1000	0.582	0.139
871/1600	0.593	0.142
1149/2100	0.603	0.144

TABLE XXI
THERMAL EXPANSION OF 7 w/o Y_2O_3 -ZrO_2

Temperature (°C/°F)	Thermal Expansion T. E. x 10^4	Coefficient of* Thermal Expansion x 10^6 ($°C^{-1}$)
25/77	0	-
100/212	7.26	9.68
200/392	17.53	10.02
300/572	27.00	9.82
400/752	36.39	9.70
500/932	45.77	9.64
600/1112	56.25	9.78
700/1292	66.72	9.88
800/1472	77.64	10.02
900/1652	89.15	10.19
1000/1832	100.82	10.34
1100/2012	110.64	10.29
1175/2147	116.12	10.10

*Average-from ambient temperature to temperature indicated

TABLE XXII
THE THERMAL CONDUCTIVITY OF NiCoCrAlY

Sample thickness = 9.47mm (.373 inch)

Temperature (°C/°F)	Thermal Conductivity (W/mK)	(Btu in/hr ft^2°F)
538/1000	20.5	142
871/1600	24.3	168
1100/2012	34.2	237

TABLE XXIII
THE SPECIFIC HEAT OF NiCoCrAlY

Temperature (°C/°F)	Specific Heat (Btu/lb °F)
538/1000	.150.
871/1600	.161
1149/2100	.170

TABLE XXIV
THERMAL EXPANSION OF NiCoCrAlY

Temperature (°C/°F)	Thermal Expansion TE x 10^4	Coefficient of Thermal Expansion x 10^6 [1/°C]/[1/°F]
25/77	0	
100/212	2.56	12.75 / 6.94
200/392	22.17	12.67 / 7.03
300/572	36.83	13.39 / 7.40
400/752	52.38	13.97 / 7.76
500/932	67.53	14.22 / 7.90
600/1112	85.15	14.81 / 8.23
700/1292	104.62	15.5 / 8.60
800/1472	126.27	16.29 / 9.05
900/1652	148.15	16.93 / 9.41
1000/1832	168.72	17.30 / 9.60
1100/2012	191.13	17.78 / 9.87
1175/2150	202.02	17.96 / 9.97

3.1.3.2 Preliminary Mechanical Testing

As mentioned previously, a preliminary room temperature four point bend test was conducted at the United Technologies Research Center to gain early insight into the constitutive behavior of the strain tolerant ceramic. The geometry of the test specimen is illustrated in Figure 63. A plot of outer fiber tensile stress (calculated from applied load using classical elastic bending relationships) vs. outer fiber tensile strain (measured by bonded strain gage) is shown in Figure 64a. The stress-strain relationship differs dramatically from the completely elastic ambient temperature behavior typically observed for fully dense structural ceramic materials. The strain tolerant ceramic deformation appears to be non-linear even at very low stress levels, with no clearly definable linear elastic segment of the stress-strain curve. Unloading of another partially loaded specimen showed substantial permanent offset with no visually observable micro-cracking on the tensile side, indicating that the curvature seen in Figure 64a represents truly inelastic behavior.

Despite the occurrence of significant inelastic deformation, the ultimate strength and fracture strain of the strain tolerant ceramic are quite low, 6.9 ksi and 0.26% respectively. The material also is highly compliant with an initial stiffness of 5.8 x 10^6 psi. Measurements from multiply oriented strain gages indicate a relatively small Poisson's ratio of 0.091. An interesting fractograph from the tensile side of a broken specimen shows a highly columnar structure with "splats" of the plasma deposited ceramic (Figure 64b).

3.1.3.3 SouthWest Research Institute Mechanical Test Program

The mechanical test program conducted by Southwest is summarized in Figure 65. Test methods and results are described in the following paragraphs. All tests were conducted with the primary loading axis in the plane of the splat structure.

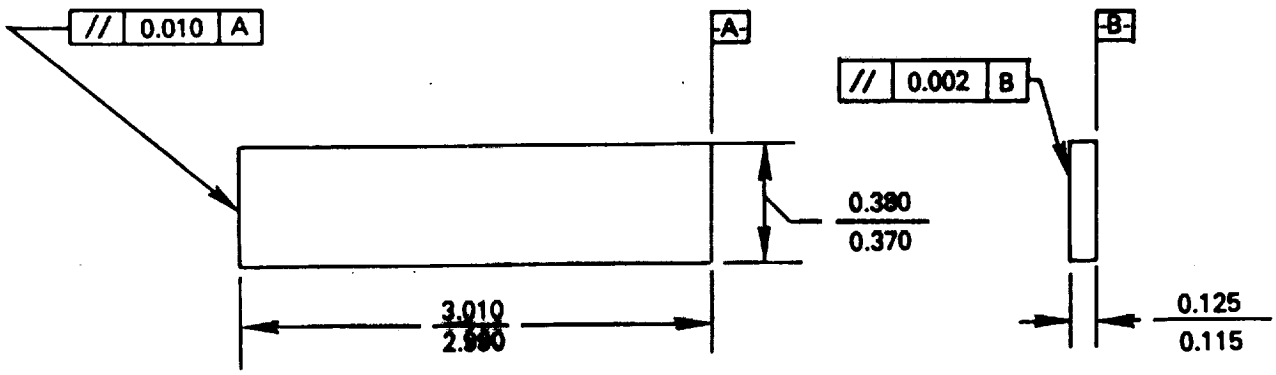

All Dimensions Shown In Inches

Figure 63 Bulk Four Point Bend Specimen Geometry

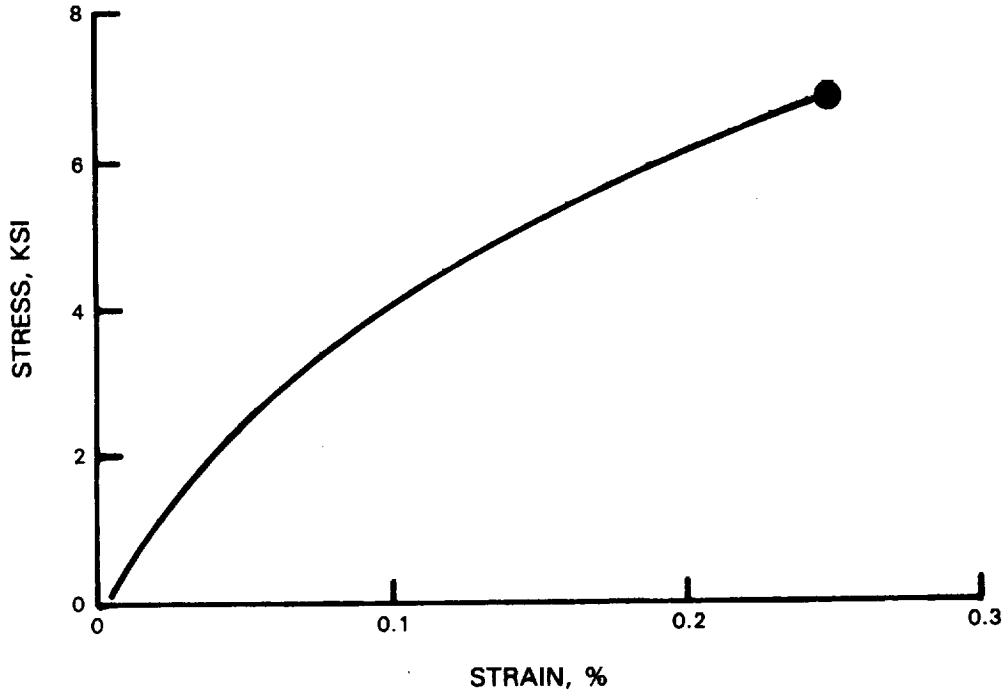

Figure 64a Significant Inlastic Deformation Observed, Room Temperature Four Point Bend Test results for Bulk Plasma Sprayed 7 w/o Y_2O_3 - ZrO_2

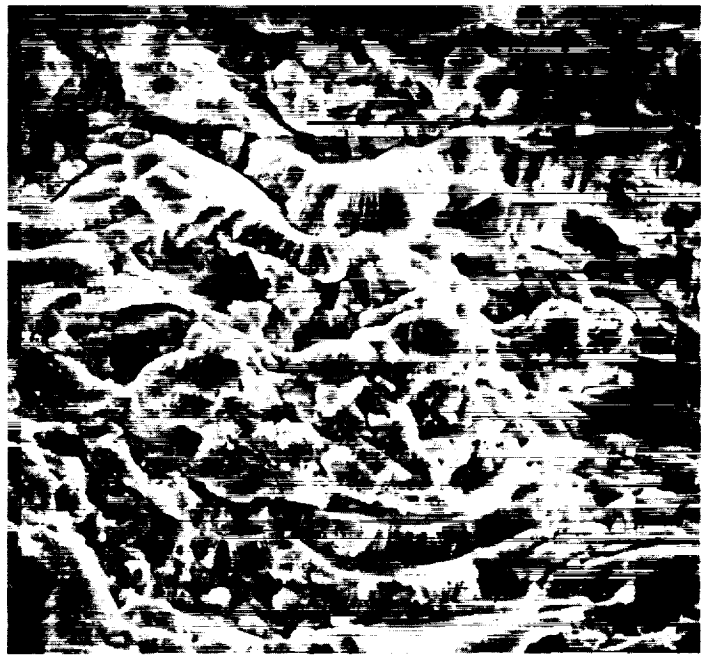

1000X

Figure 64b Fracture Surface of Four Point Bend Test Specimen

	Number of Tests Planned (Conducted)				
Test Temperature	1000°F	1600°F	1800°F	2000°F	2200°F
Test Type					
Stress-Strain Response Test					
Tension	1(3)	1(2)		1(2)	1(2)
Compression	0(1)	1(1)			1(2)
Creep/Stress Rupture Test					
Tension	1(1)		1(2)		1(1)
Compression			1(3)		1(4)
Fatigue (Wafer) Test	3(5)	3(5)			
Fracture Toughness Test	2(2)	2(2)			

Figure 65 Mechanical Property Test Plan for Bulk Ceramic

Uniaxial compression tests were conducted on right circular cylinders (Figure 66) loaded along the cylinder axis between flat and parallel alumina anvils having self locking tapered ends mounted in water cooled adapters (Figure 67). A 500 pound capacity load cell was used to provide good resolution (.05 lb) at the relatively small loads involved in this testing. Loading of the specimens was performed under displacement control of the actuator shaft at a constant displacement rate approximating a strain rate of 1×10^{-3} in/in/sec. Displacement was measured to an accuracy of 5 micro inches on the actuator shaft near the loading fixture attachment point. A machine compliance calibration was obtained at each test temperature by measuring the load-deflection characteristics of the compression apparatus without the test specimen. All data was corrected by subtracting the appropriate calibration values from the recorded displacement. Alignment of the system was confirmed by plastically deforming aluminum rodlets and measuring the resulting height variation around the circumference; this variation and less than .0002 inches. Compression specimens were heated inductively with a cylindrical graphite susceptor. To prevent rapid deterioration of the susceptor, a water cooled copper jacket with a viewing port were placed over the specimen and flooded with Argon gas (Figure 68). Test temperature was determined from the averaged output of two thermocouples located adjacent to the opposing loading pattens.

The configuration of the specimen used for testing with uniaxial tensile loading is shown in Figure 69. The tapered portion of this specimen was gripped with boron nitride coated split ceramic collets constrained with a superalloy shield and loaded by superalloy shear pins (Figure 70). Specimen strain was inferred from actuator displacement using machine compliance corrections generated from a strain gaged tensile specimen loaded to failure at room temperature. A static pre-loading apparatus was used to seat the grip section without application of significant preload to the gage section of the specimen.

Fracture toughness was measured by single edge notching the tensile specimen to a depth of about 20 mils using a 9 mil diameter diamond coated wire. While plane strain conditions were not fully satisfied in this test, it is felt to provide a reasonable indication of the general toughness capability of the material.

Derived tensile fatigue testing was conducted in the previously described compression test apparatus by compressive edge loading of the wafer geometry specimen illustrated in Figure 71. Based on the analysis of Shaw, Braiden, and DeSalvo, (Ref. 39: on Figure 72), this loading produces a biaxial stress state with a low level of tensile loading in the plane of the disk perpendicular to the compression axis (Figure 72). For materials such as ceramics where the tensile strength is substantially less than the compressive strength, tensile failure will occur in the center of the disk at loads below the compressive strength of the material. By cyclically loading this specimen, tension-tension fatigue testing was conducted on the ceramic, using a small positive R ratio (0.1) to maintain the specimen firmly seated between the anvils at all times.

3.1.3.3.1 SWRI Test Results

Results of mechanical property tests are summarized in Tables XXV through XXX. Stress-strain and creep curves for each test are included in Appendix E.

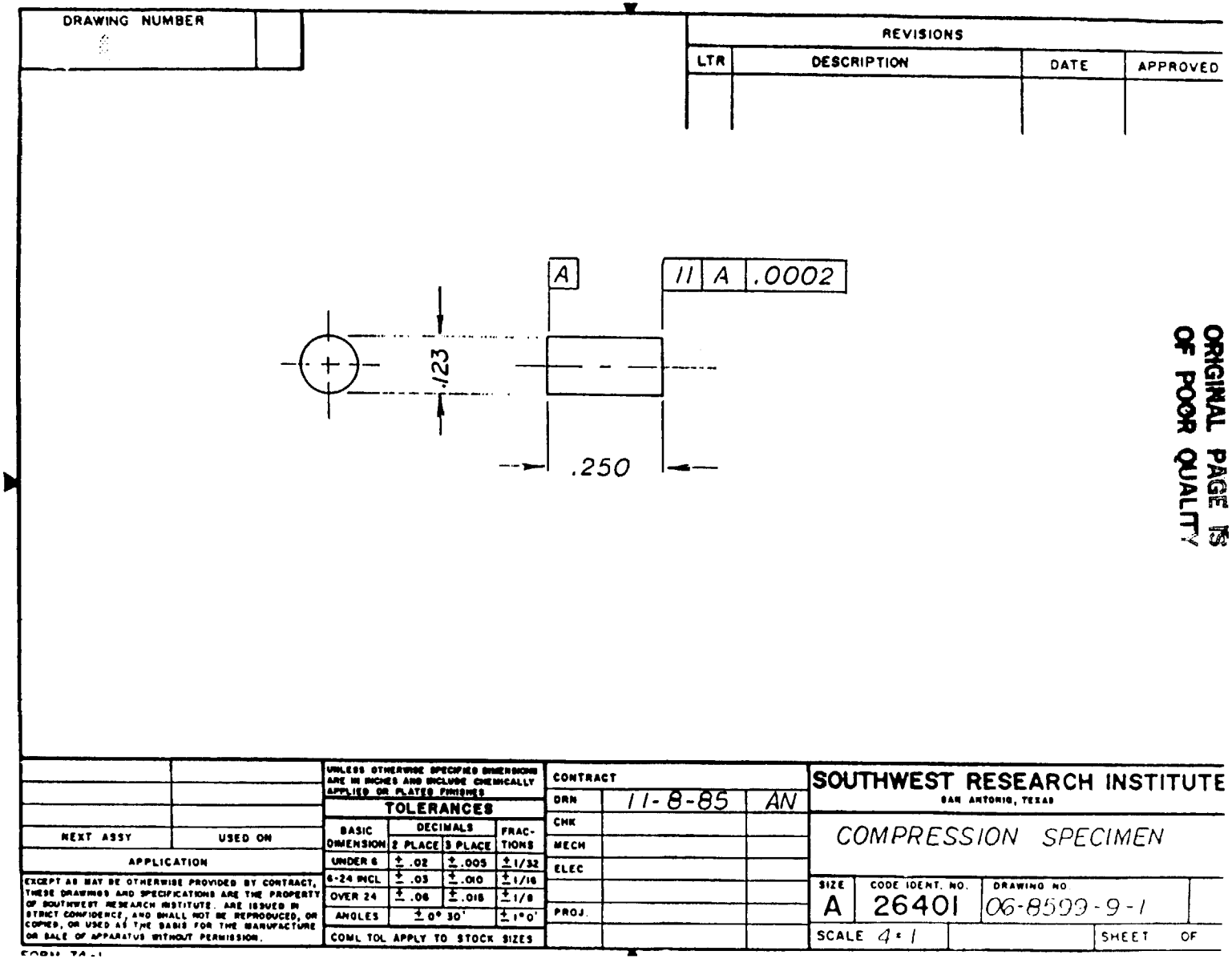

Figure 66 Compression Specimen

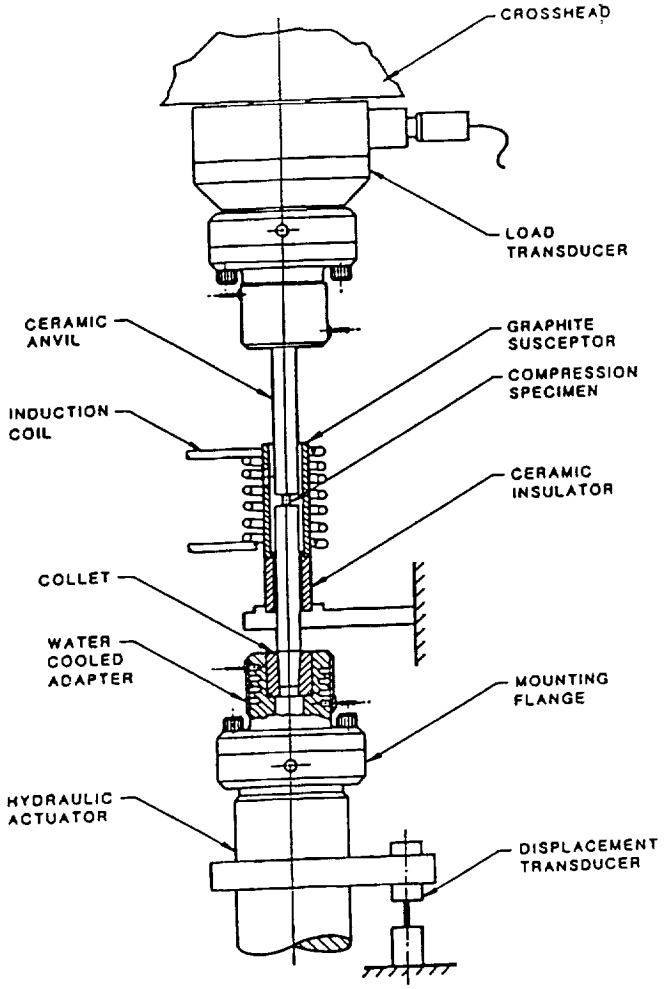

Figure 67 Compression Test Apparatus

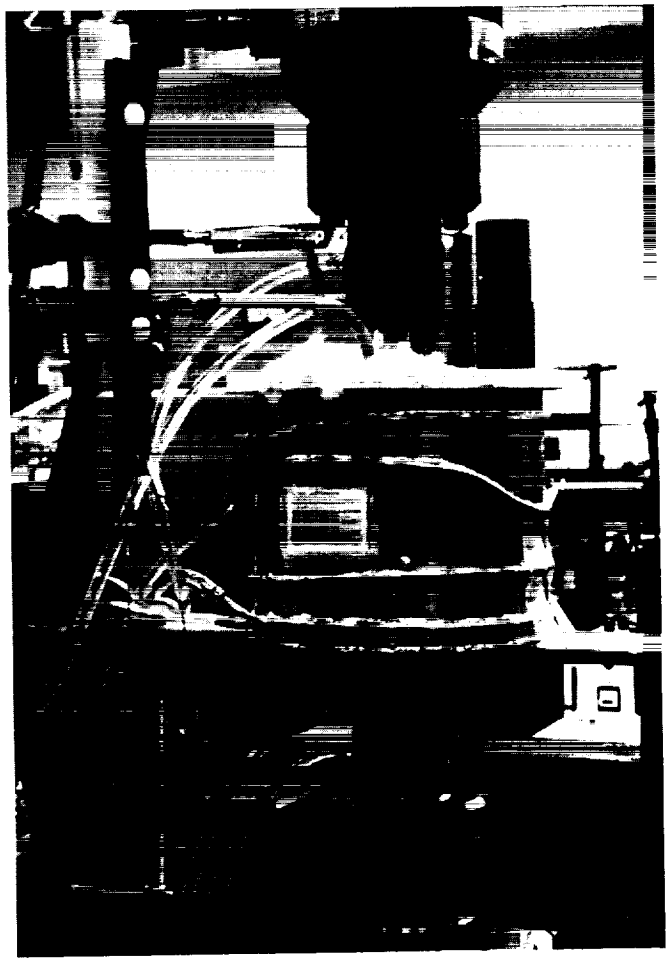

Figure 68 Test Rig

3.1.3.3.1.1 Uniaxial Tension and Compression Test Results

The most significant result of these property tests is confirmation of the non-linear deformation behavior observed in the previously discussed preliminary bend testing. Shown in Figure 73 is a room temperature tensile stress-strain curve generated from the strain gaged machine calibration specimen mentioned earlier. As with the previously discussed bend test, the strain tolerant ceramic exhibits non-linear deformation behavior throughout the loading history. Because of this non-linear behavior, it is difficult to define an "elastic modulus"; "initial stiffness" values, noted in Table XXVI, are graphical estimates of the tangent to the stress strain curve near zero load. Because elevated temperature stiffness values are based on crosshead displacement, some caution must be used in interpreting these data, despite all of the precautions taken in testing to minimize seating and machine compliance effects. For example, the slight upward curvature seen in the initial portion of most of the elevated temperature curves is assumed to be an artifact and has been ignored in measurement of initial slopes.

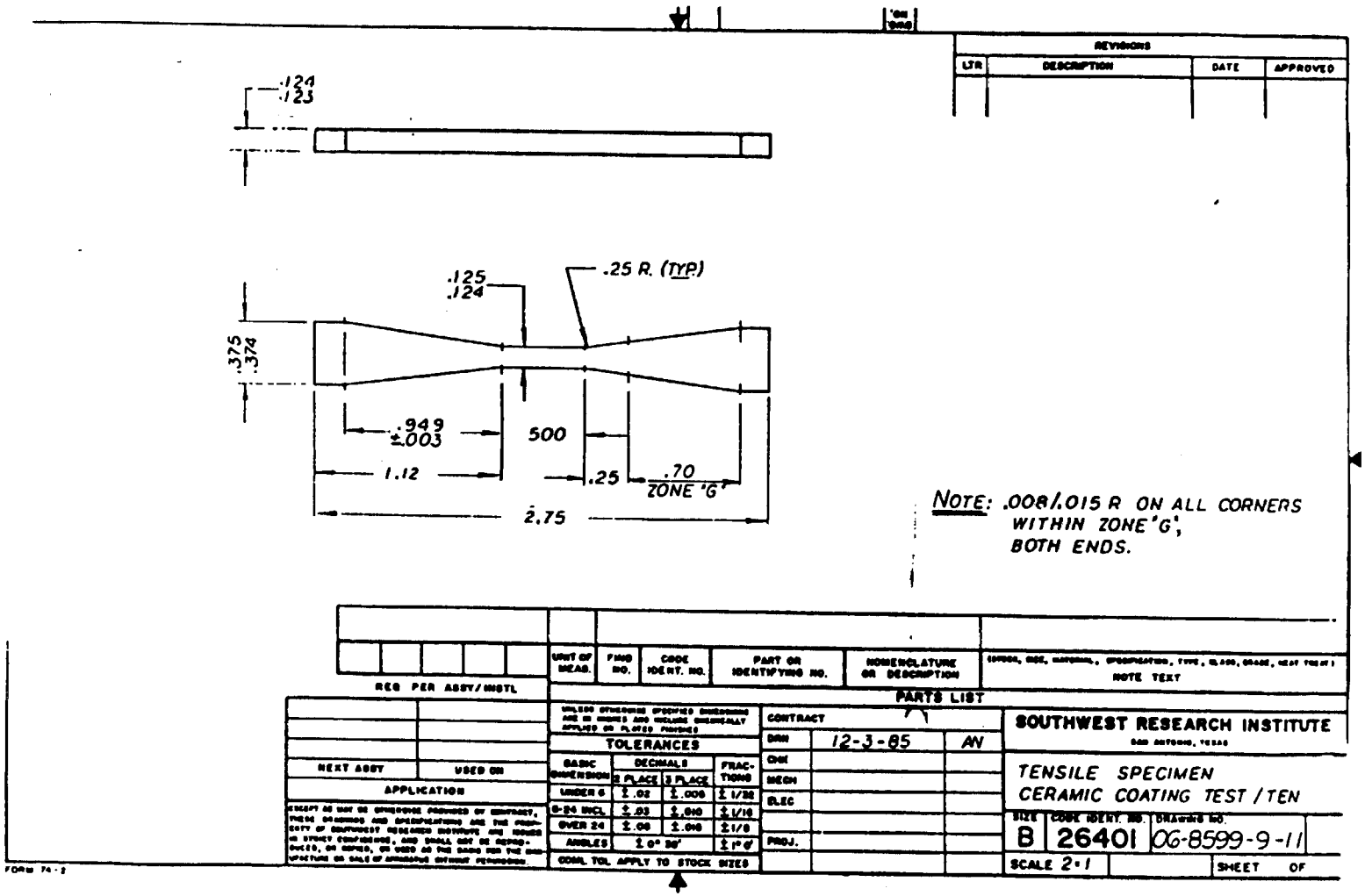

Figure 69 Tensile Specimen Geometry

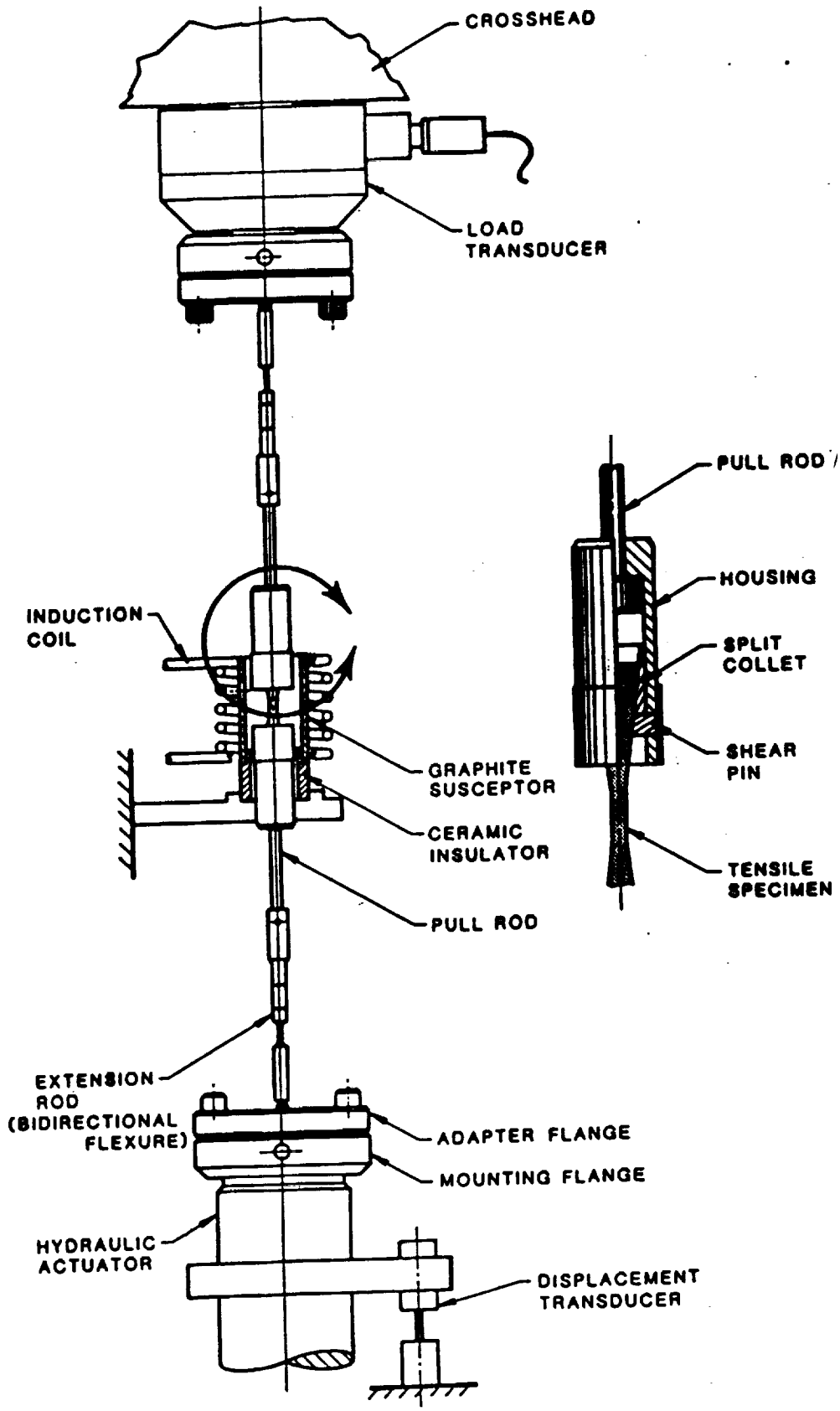

Figure 70 Tensile Test Apparatus

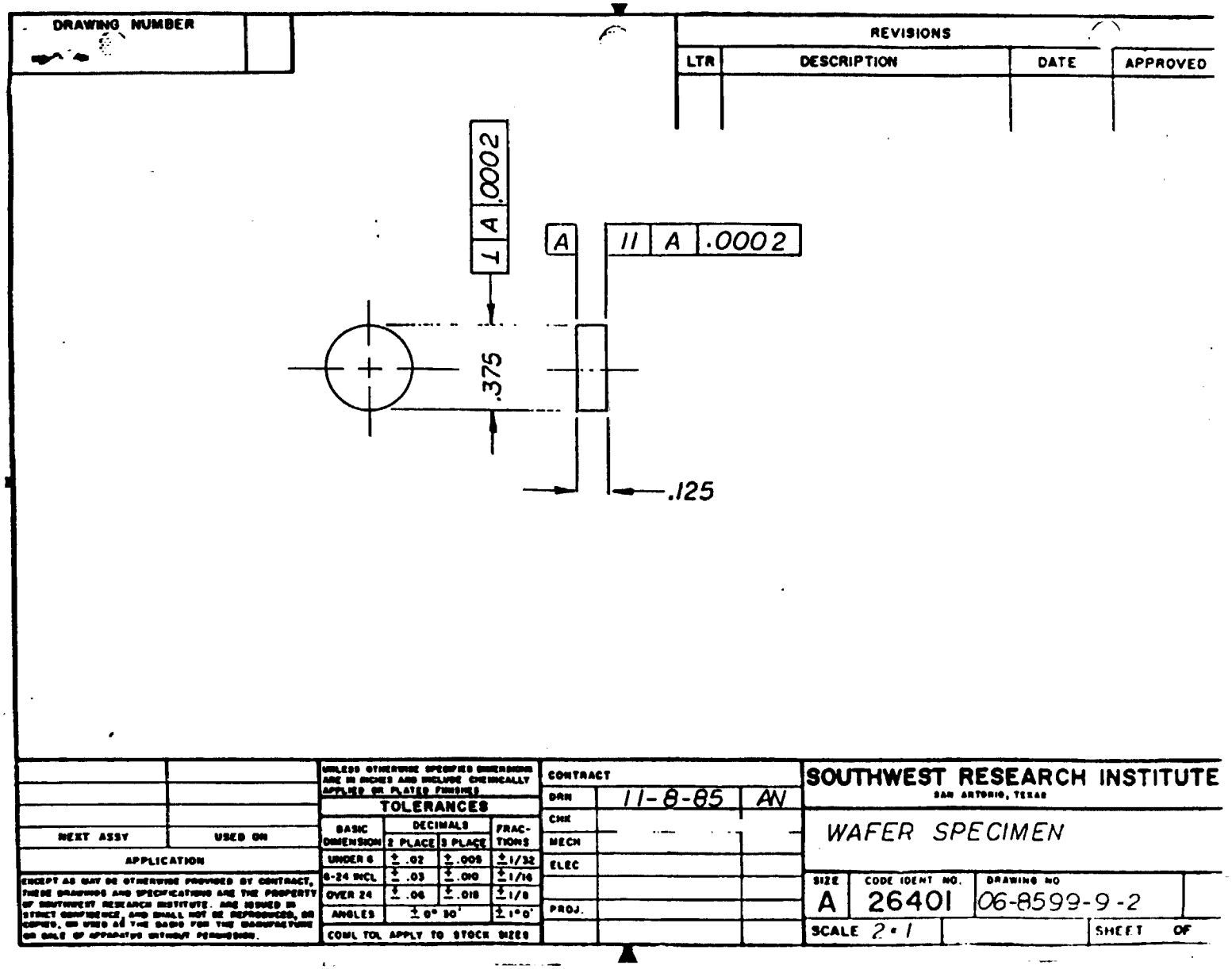

Figure 71 Wafer Specimen

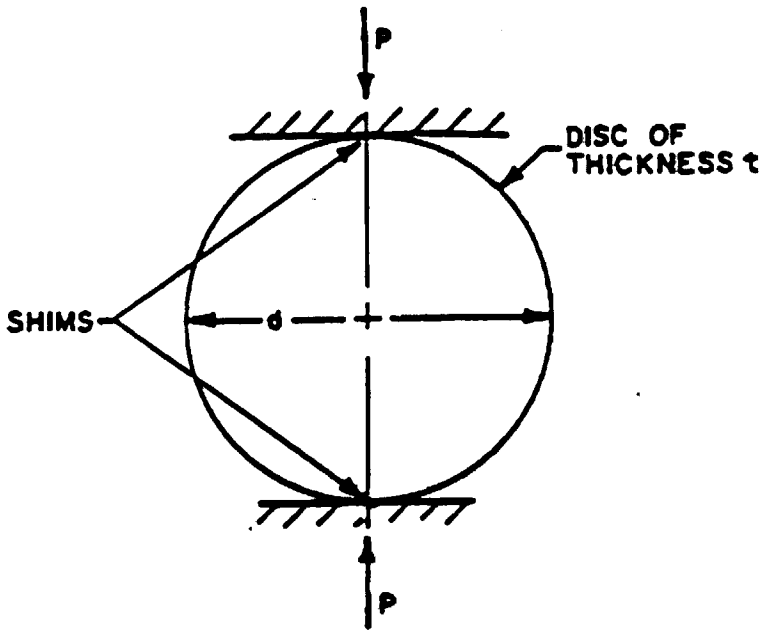

a Diametral Compression Specimen

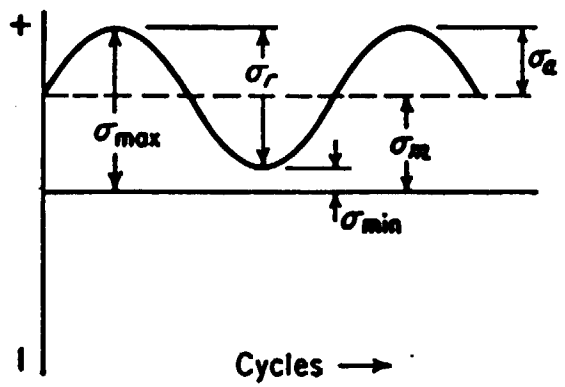

c Fatigue Stress Cycle; Repeated Stress

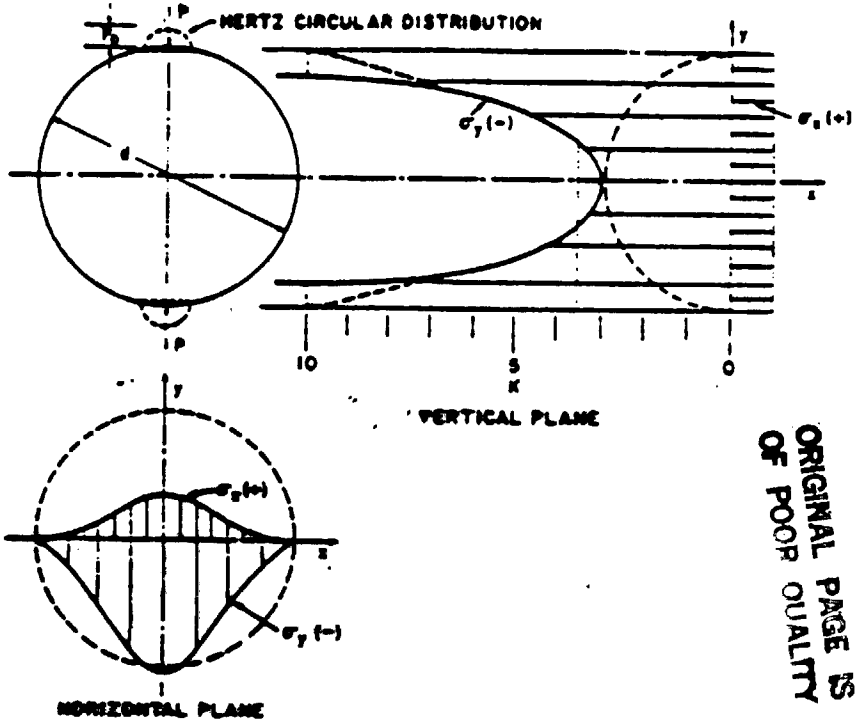

b Stress Distribution for Transversely Loaded Disk

Figure 72 Fatigue Stress Cycle

TABLE XXV
UNIAXIAL COMPRESSION PROPERTY TEST DATA

Specimen Identification Number	Test Temperature	Ultimate Compressive Strength (ksi)	Strain Ultimate (%)	Strain at Fracture (%)	Initial Stiffness E X10^6 (PSI)
Δ-2-CP-27-1	1600°F	44.0			1.64
	2175°F	28.7		2.46	3.15
Δ-2-CP-27-11	1000°F	54.6	2.61	2.61	1.96
Δ 2-CP-27-3	1600°F	39.7	1.90	1.90	1.80
Δ 2 CP 27 2	2200°F	31.6	3.54	4.38	1.95
Δ-2-CP-27-4	2196°F	39.6	4.32	5.14	1.50

TABLE XXVI
UNIAXIAL TENSION PROPERTY TEST DATA

Specimen Identification Number	Test Temperature (°F)	Initial Stiffness, E x 10^6(psi)[3]	Ultimate Tensile Strength (ksi)	Apparant[1] Failure Strain, %
EC-1	75	2.90	3.08	0.196[2]
EC-2	1000	3.08	2.65	0.158
EC-10	1000	Data Unavailable	2.60	Data Unavailable
CP-24	1000	6.31	2.58	0.056
CP-13	1600	6.31	2.58	0.077
CP-14	1600	1.80	2.68	0.283
CP-21	2000	3.08	3.08	0.215
CP-23	2000	3.73	3.18	0.188
EC-4	2200	4.01	2.45	0.296
EC-5	2200	4.01	2.32	0.265

[1] Except as noted, measured from crosshead displacement at failure, compensated for machine stiffness
[2] Measured from strain gage
[3] Tangent slope at zero load

TABLE XXVII
COMPRESSION-CREEP PROPERTY TEST DATA

Specimen Identification Number	Test Temperature	Applied Stress (ksi)	Accumulated Strain (%)	Creep Time (Minutes)	Comments
△-2-CP-27-5	1800°F	38.4	2.22	5.9	Same Specimen No Failure
		40.6	2.48	4.6	
		42.6	2.82	6.3	
△ 2-CP-27-12	1800°F	13.0	1.88	295.2	No Failure, Minimum Creep Rate = 0.24% ε/hrs
△ 2-CP-27-6	1800°F	40.1	2.32	8.8	Minimum Creep Rate = 1.27 % ε/hr, Same Specimen
		42.4	2.76	20.0	Minimum Creep Rate = 0.62 % ε/hr, No Failure
△ 2-CP-27-7	2200°F	34.5	5.17	1.90	Initial Creep Rate = 68.5% ε/hr
△ 2-CP-27-8	2200°F	31.5	6.35	3.40	Initial Creep Rate = 40.8% ε/hr
△ 2-CP-27-9	2200°F	9.5	4.5	106.1	No Failure, Minimum Creep Rate = 1.42% ε/hr
△-2-CP-27-10	2200°F	9.95	6.34	111.4	No Failure, Minimum Creep Rate = 1.83% ε/hr

TABLE XXVIII
TENSION-CREEP PROPERTY TEST DATA

Specimen Identification Number	Test Temperature	Applied Stress (ksi)	Accumulated Strain (%)	Creep Time (Minutes)	Comments
CP-12	1000	2.10	0.048	1.94	No failure, no creep response
CP-19	1800	2.17	0.140	3.75	Failed, M.C.R. 0.0038% ε/hr[1]
CP-20	1800	2.07	0.160	5.28	Failed, M.C.R. 0.0011% ε/hr [1]
EC 6	2200	1.96	0.80	0.61	Failed

[1] M.C.R - Minimum Creep Rate

TABLE XXIX
FATIGUE PROPERTY TEST DATA

Specimen Identification Number	Test Mode	Test Temperature	Maximum Applied Stress (ksi)	R	Number of Cycles	
Δ-2-CP-26-2	Fatigue	1000°F	2.5	0.1	20,000	No Failure
Δ-2-CP-26-2*	"Tensile"	1000°F	3.4	---	1/4	
Δ-2-CP-26-5	Fatigue	1000°F	2.6	0.1	307	
Δ-2-CP-26-3	Fatigue	1000°F	2.7	0.1	410	
Δ-2-CP-26-4	Fatigue	1000°F	2.7	0.1	195	
Δ-2-CP-25-2	Fatigue	1600°F	2.12	0.1	60,000	Same Specimen No Failure
			2.67	0.1	10,000	
			2.93	0.1	10,452	
			3.15	0.1	11,000	
			3.3	0.1	10,050	
Δ-2-CP-25-5	Fatigue	1600°F	2.64	0.1	407	
Δ-2-CP-26-1	Fatigue	1600°F	2.64	0.1	158	
Δ-2-CP-25-1	"Tensile"	1600°F	3.2	---	1/4	
Δ-2-CP-25-3	"Tensile"	1600°F	3.3	---	1/4	

*Specimen uploaded to failure

TABLE XXX
FRACTURE MECHANICS PROPERTY TEST DATA

Specimen Identification Number	Test Temperature	Failure Stress (ksi)	a(in.)[1]	b(in.)[2]	K_Q(ksi $\sqrt{in}$)[3]
CP-22	1000	1.76	0.0175	0.124	0.578
CP-9	1000	1.49	0.0182	0.122	0.454
CP-15	1600	1.90	0.0183	0.124	0.579
CP-18	1600	1.51	0.0212	0.124	0.517

Notes:
1. Crack (notch) depth
2. Total specimen depth
3. Apparent (not valid) critical stress intensity factor

Examination of the elevated temperature tensile curves included in Appendix E indicates that while there is substantial variability of initial and overall stiffness, The basic non-linear shape of the stress-strain curve is similar at all temperatures up to 2000°F. Both the shape similarity and the stiffness variability are illustrated by comparison of the room temperature and the two 1600°F curves reproduced in Figure 73. At 2200°F there is substantially more curvature than at the lower temperatures, as shown by the high temperature curve reproduced in Figure 73.

Both ultimate tensile strength and tensile failure strains are relatively low at all temperatures. As shown in Figure 74, strength appears to exhibit a slight decreasing trend between room temperature and 1000°F, rising again to about room temperature levels at 2000°F, and again decreasing at 2200°F. The reason for this apparent increase at 2000°F is not presently understood and may reflect data scatter, although reproducibility at each temperature appears to be quite good. It is possible that this strength peak is related to subtile phase changes (very slight monoclinic to tetragonal transformation) in this temperature range, but such interpretation must be viewed as highly speculative at the present time.

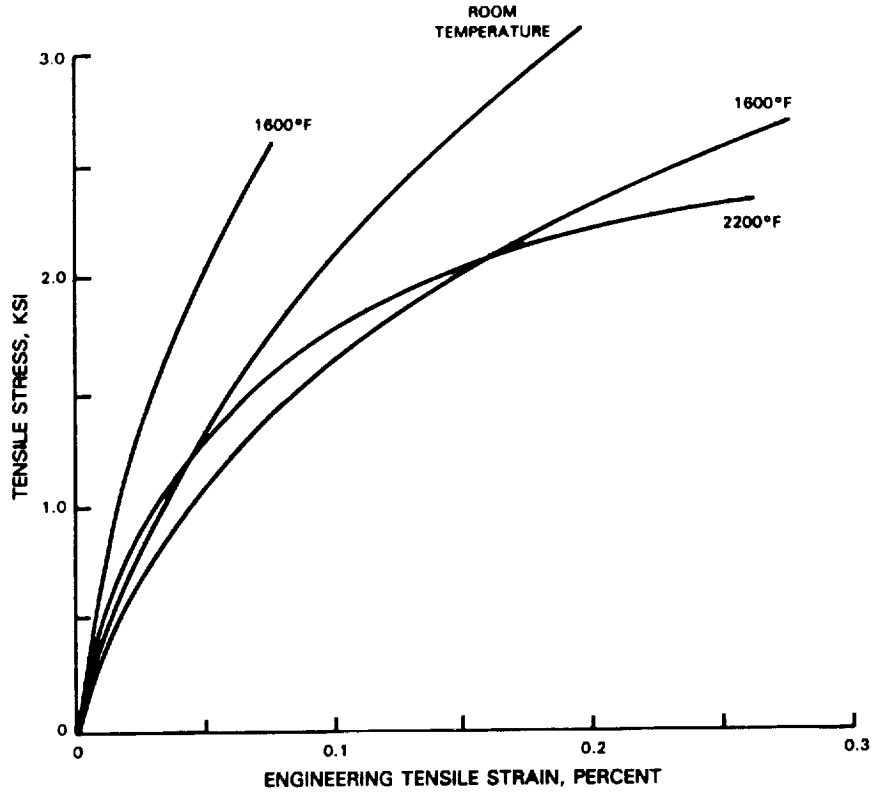

Figure 73 Representative Strain Tolerant Ceramic Tensile Stress Strain Curves at Various Temperatures. Room temperature strain data measured by strain gage; temperature curves obtained from corrected cross head displacement.

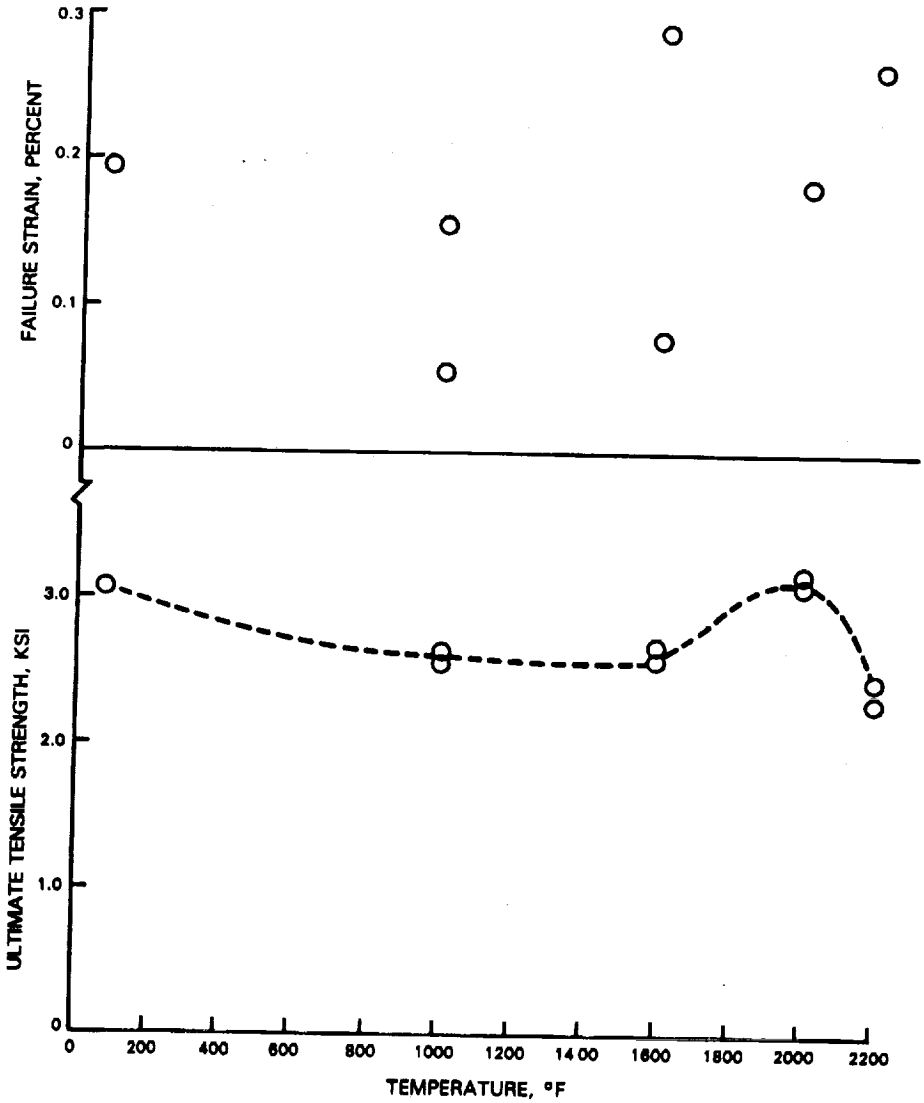

Figure 74 Inplane Temperature Elevated Tensile Properties of Strain Tolerant Ceramic

Because of substantial data scatter, it is difficult to identify any trend for temperature dependence of tensile failure strain. It should be noted that all tensile failures occurred in the fillet region of the specimen where stress concentration is calculated to be on the order of 1.15, suggesting that some caution should be exercised in interpretation of the strength and "ductility" data discussed above.

Compressive stress-strain behavior, summarized in Figure 75 and Table XXV, differs significantly from tensile behavior; compressive strengths are much higher than tensile strengths, and there appear to be distinct linear and non-linear segments to the stress-strain curves. Because corrected crosshead displacement was used to measure strain, with attendant seating effects at low loads, this latter observation is made with some reservation. This reservation not withstanding, the 1000 and 1600°F compressive stress strain curves clearly are shaped differently than corresponding tensile stress-strain curves. At 2200°F, compressive deformation begins to resemble tensile deformation, departing from linearity at relatively low stress levels. Within accuracy limits improved by use of corrected crosshead displacement, initial stiffness appears to be essentially independent of temperature in the range studied.

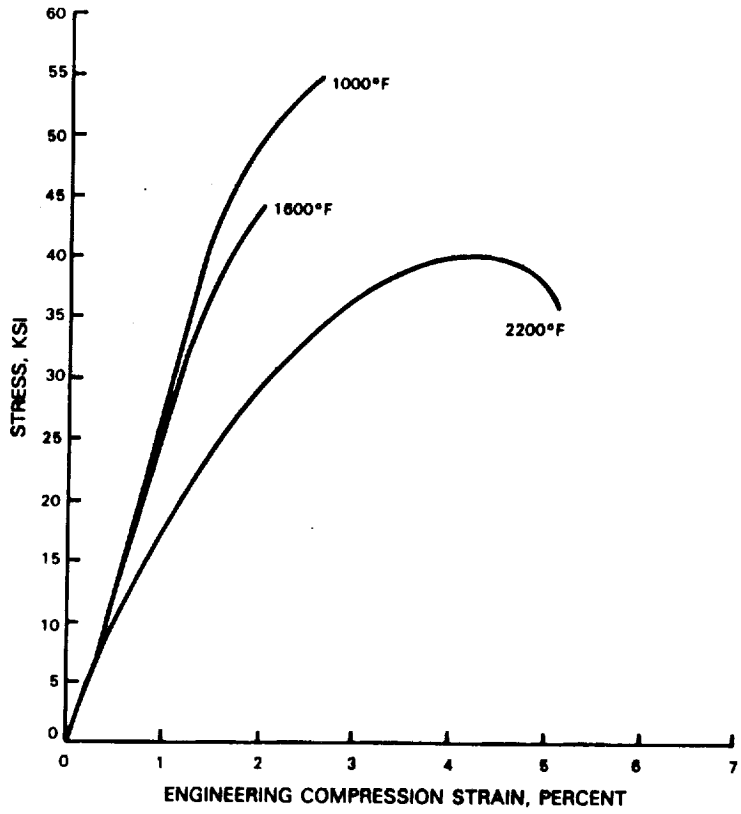

Figure 75 Representative Strain Tolerant Ceramic Compressive Stress-Strain Curves at Various Temperatures. Compressive strains calculated from corrected crosshead displacement.

The compressive failure mode was observed to be of the classical shear type (Figure 76). Compressive stresses and strains at failure are plotted in Figure 77. Because compressive tests were not conducted at 2000°F, the occurrence of a strength peak, such as that seen at this temperature in tensile loading, could not be verified.

3.1.3.3.1.2 Creep Behavior

The creep test results are listed in Tables XXVII and XXVIII for compression and tension respectively. All strain-time curves for these tests are presented in Appendix E. As shown in Table XXVII, uniaxial-compression creep tests were conducted for two stress levels at 1800°F and 2200°F, on a total of seven specimens.

Compression creep tests showed a strong creep response at 1800°F and 2200°F for low and high stress levels. At 1800°F a larger amount of compressive straining occurred in the higher stress level test.

Compression creep tests conducted at 2200°F showed a significant increase in creep response as compared with the 1800°F test results. In both the low stress and high stress level tests, at 2200°F, the initial creep rates are very high but in the lower stress level tests, the creep rates diminish significantly with time. However, the high stress level tests at 2200°F reach very large compressive strain values very quickly.

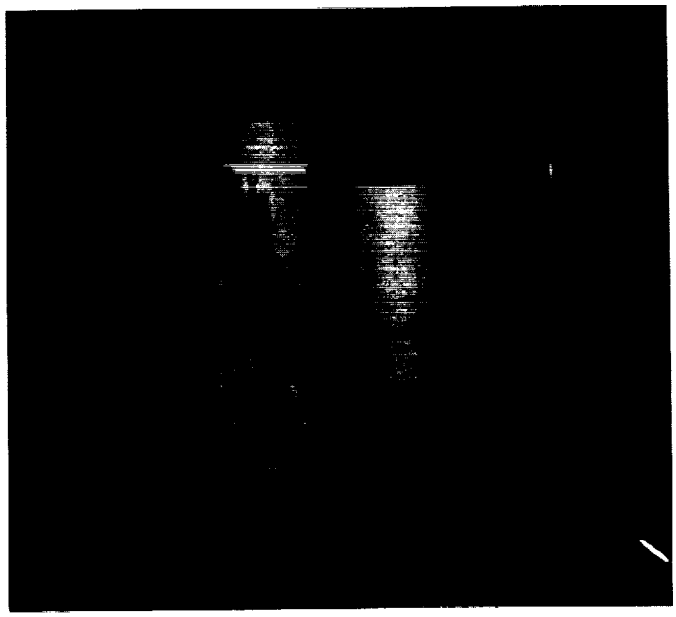

Figure 76 Typical Compressive Failure Mode

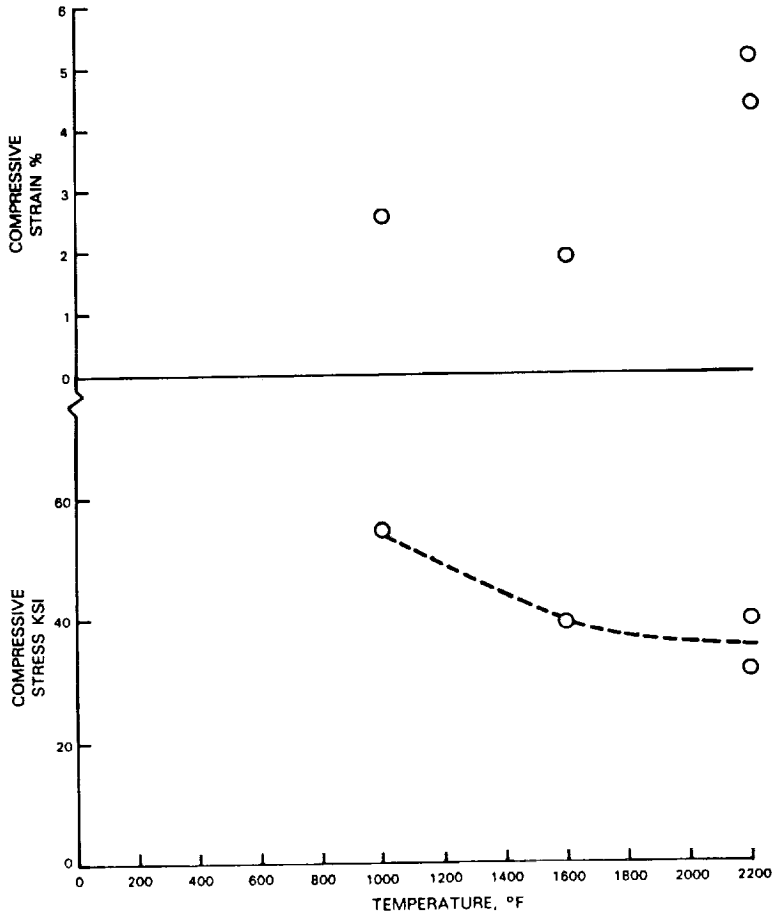

Figure 77 Inplane Elevated Temperature Compressive Properties of Strain Tolerant Ceramic

Uniaxial tension-creep tests were conducted for high stress levels (≈ 80% UTS) at 1000°F, 1800°F and 2200°F on a total of four specimens.

No tension-creep response was seen at 1000°F after testing for over two hours. However, test data at 1800°F and 2200°F revealed a significant tensile-creep response suggesting that a time-temperature dependent material response will be important in the advanced modeling effort.

Minimum creep rates were estimated graphically for a significant portion of the compression-creep and tensile-creep data. The compression minimum creep rate values were much higher than these calculated for tension and were seen to be strongly dependent on stress level and temperature. At 1800°F, minimum creep rates for compression at the lower stress level were on the order of 2.5 X $10^{-3}hr^{-1}$ and at higher stress levels were greater than $10^{-2}hr^{-1}$. Tensile minimum creep rate values averaged ≈ 7 X $10^{-5}hr^{-1}$ strain/hour at 1800°F.

At 2200°F, minimum creep rate values for compression approached 2 X $10^{-2}hr^{-1}$ at low stress levels. At higher stress levels, it appears as though only primary creep occurred and creep rates were ≈ 5 X $10^{-1}hr^{-1}$ for compression and $10^{-3}hr^{-1}$ for tension. Minimum creep rates are plotted verses stress in Figure 78; Figure 79 shows the creep rate-temperature dependence.

3.1.3.3.1.3 Fatigue Behavior

Fatigue test results are listed in Table XXIX and plotted in S-N form in Figure 80. As shown in the table, five specimens were cycled directly to failure; three at 1000°F and two at 1600°F. Three additional specimens were failed in monotonic loading to compare tensile strength as measured in the wafer test with previous uniaxial results, and to provide a "one quarter cycle" data point. One of these specimens was exposed to 20,000 cycles at an intermediate stress prior to uploading to failure at 1000°F.

Comparison of the "quarter cycle" strength values with those plotted in Figure 74 indicates reasonably good agreement between the two test methods, despite the highly biaxial stress state in the wafer specimen. This observation adds a significant level of confidence to the fatigue test results plotted in Figure 80.

The data plotted in Figure 80 show an apparently real fatigue response in the strain tolerant ceramic, but with a stress dependence substantially different from that observed in metals. Whereas metallic materials typically exhibit slopes ranging from ≈ - 1.5 with reversed plasticity to ≈ -8 in the fully elastic range, the data in Figure 80 appears to have a slope on the order of -50. Specific degradation and failure mechanisms responsible for this very stress sensitive fatigue behavior are not presently understood.

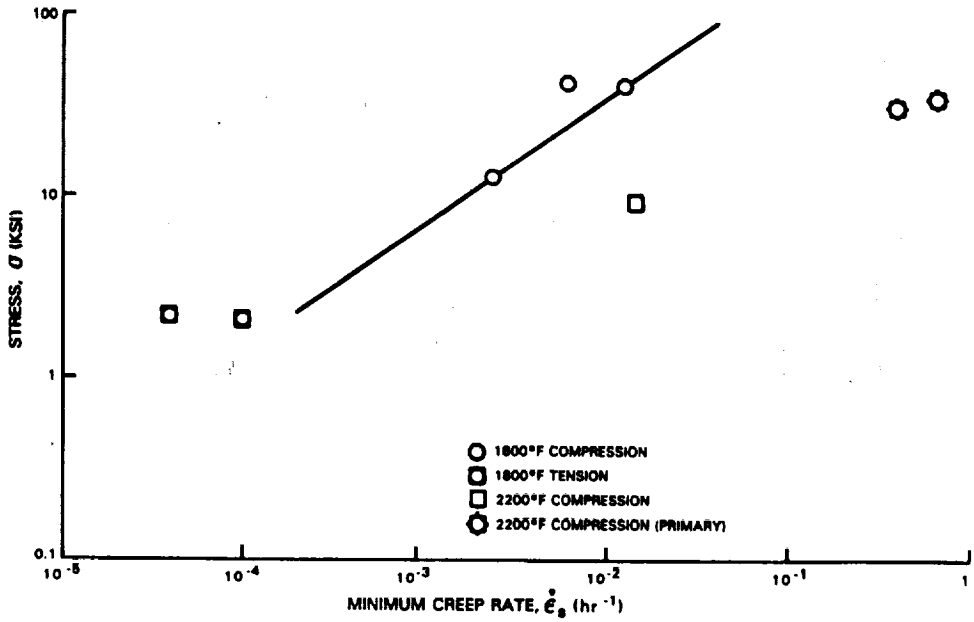

Figure 78 Stress Versus Creep Rate

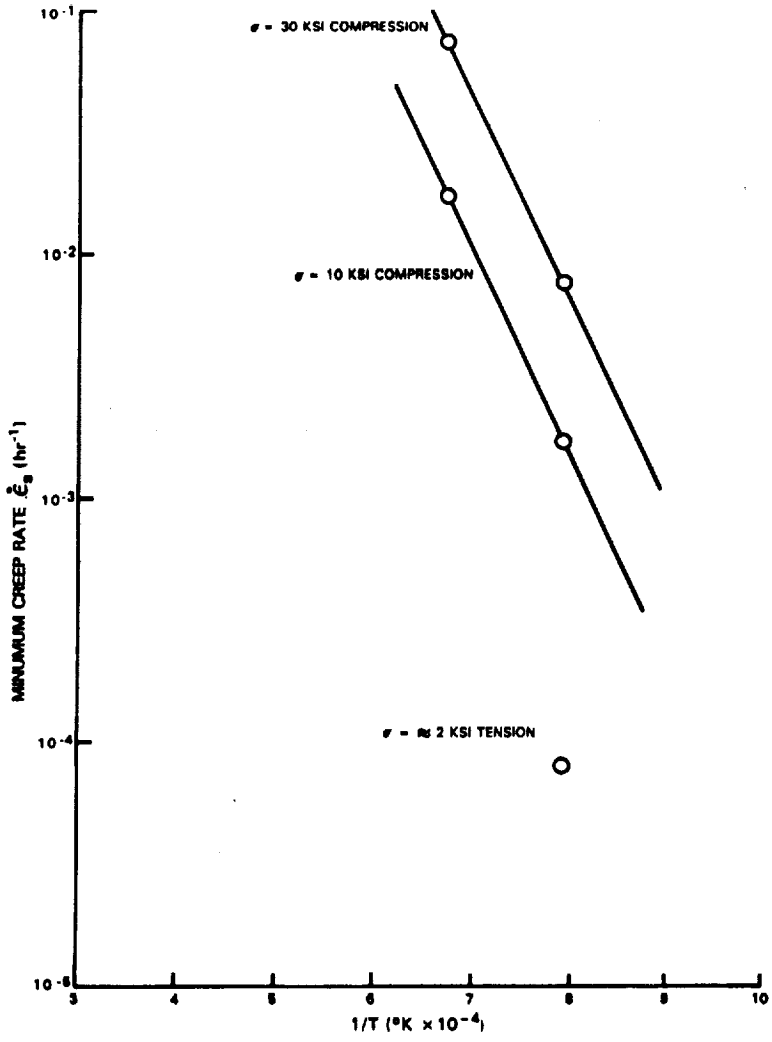

Figure 79 Creep Rate Versus Temperature

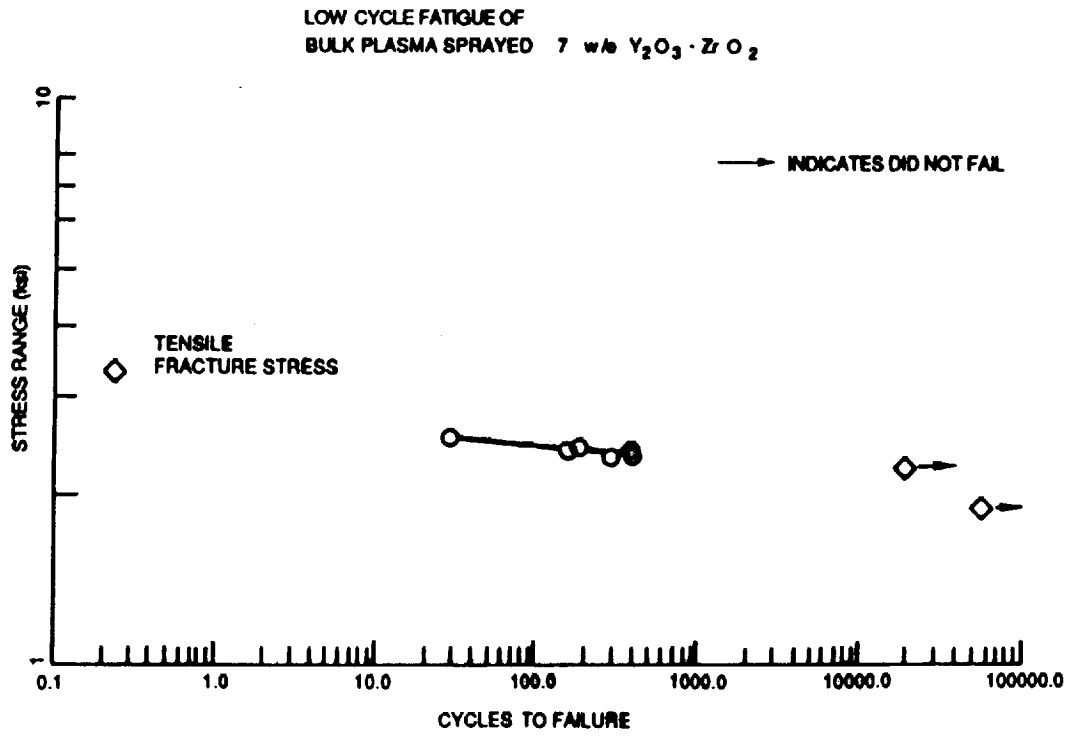

Figure 80 S-N Curve for 7YsZ (1000°F and 1600°F data plotted together)

A very surprising result was obtained on a specimen which was incrementally uploaded at 1600°F. As seen in Table XXIX, this specimen (Δ-2-CP-25-2) was uploaded five times, with 10,000 run-out cycles being applied after the fifth upload to the quarter cycle failure stress. This apparent "coaxing" behavior is not understood.

3.1.3.3.1.4 Fracture Toughness

Results of four fracture toughness tests at 1000 and 1600°F are presented in Table XXX. While plane strain conditions were not fully satisfied in these tests, the values presented are believed to provide some indication of the inherent toughness of the strain tolerant ceramic, and would probably serve as upper limit values. Inspection of the data indicates the toughness to be very low, on the order of 0.5 ksi$\sqrt{\text{in}}$ in the temperature range investigated. It should be noted that this toughness was measured with the plane and direction of propagation of the crack perpendicular to the ceramic splat structure; it is expected that toughness in the plane of the splat structure, where predominant failure cracks are located in the cyclic thermal exposure specimen, would be lower than the value measured in these tests.

3.1.4 Task IC - Predominant Mode Determinations

Based on the information generated in Tasks 1A and 1B, the relative importance of the thermomechanical and thermochemical failure modes were determined. An empirically based correlative life prediction model was developed to independently predict life for the predominant failure modes. Three predominant failure mode verification tests were conducted to determine the applicability and limits of the preliminary life prediction model.

3.1.4.1 Task IC. 1 Develop Preliminary Life Prediction System

The objective of this subtask is to develop a preliminary thermal barrier coating life prediction system based on coating life test results generated in Task IB. These results identified two important modes of coating degradation. The first of these is mechanical, and is assumed to involve an accumulation of fatigue damage resulting from thermally induced cyclic strains. The second degradation mode involves prolonged thermal exposure, and appears on the basis of phenomenological evidence to involve oxidative degradation of the metal coating system component. The approach described below to accomplish the objective of this subtask was developed at Southwest Research Institute under the direction of Dr. T. A. Cruse.

Following the approach of Miller (Ref. 18), an existing fatigue life correlation model was selected as the basis for the thermal barrier coating life model. The specific analytical form used is based on a Manson-Coffin type relationship, where the number of inelastic strain cycles to failure (N_f) is linearly related to applied inelastic strain range ($\Delta\epsilon_i$) raised to a power (b):

$$N = A\ (\Delta\epsilon_i)^b$$

Where A is a constant of proportionality. The exponent, (b), typically has a value on the order of -1.5 for metallic materials. The use of inelastic strain range as a mechanical damage driver in the ceramic coating layer is justified on the basis of substantial inelasticity observed in the previously discussed mechanical test program.

To facilitate incorporation of an environmental damage driver in the Manson-Coffin relationship, the proportionality constant is expressed in the form:

$$A = \left(\frac{1}{\Delta\epsilon_f}\right)^b$$

with $\Delta\epsilon_f$ (the inelastic strain range which causes failure in a single cycle) being made dependant on accumulated oxide thickness:

$$\Delta\epsilon_f = \Delta\epsilon_{f_o}\ (1 - \delta/\delta_c)^c + \Delta\epsilon_i\ (\delta/\delta_c)^d$$

The constant $\Delta\epsilon_{f_o}$ is failure strain in the absence of oxidation, δ_c is a constant representing the "critical" oxide thickness which would cause ceramic spallation failure in a single thermal cycle, and c and d are emperically determined constants. For the preliminary analysis, these two constants were set equal to unity. (In one run of the subsequently discussed correlation program, the coefficients c and d were allowed to vary; the "optimized" values of these coefficients did not deviate significantly from the initially assigned value of unity.)

To establish values of the constants; $b, \Delta\epsilon_{f_o}$, and δc, the spallation life data generated in Task IB were correlated with the proposed model. To accomplish this, it was necessary to establish analytical relationships between the two independent model variables (oxide thickness and inelastic strain range) and physically measurable test parameters such as time(t), temperature (T), and cycles (N). For the preliminary analysis, oxide scale thickness was calculated from the classical exponential temperature and parabolic time relationship:

$$\delta = c\,(Kpt)^{1/2}$$

Where Kp is the parabolic rate constant:

$$Kp \cong A\, e^{-\Delta H/RT}$$

Best estimate values of the constants A, c, and ΔH based on prior Pratt & Whitney and literature data were used for this initial analysis:

$A = 0.06760\ gm^2/cm^4\text{-}sec$
$c = 0.5358\ cm^3/gm$
$\Delta H = 66{,}430\ cal/mole$

As discussed in a later section, actual oxide accumulation data obtained on the PWA 264 system at the NASA Lewis Research Center will be used for the Task II improvement on this preliminary model.

The most difficult and complex value to obtain for this analysis is inelastic strain range for each of the tests conducted in Task IB. To calculate this value, relatively coarse finite element thermal and stress-strain analyses of the TBC coated test bar configuration were conducted. The finite element break-up for this analysis is shown in Figure 81.

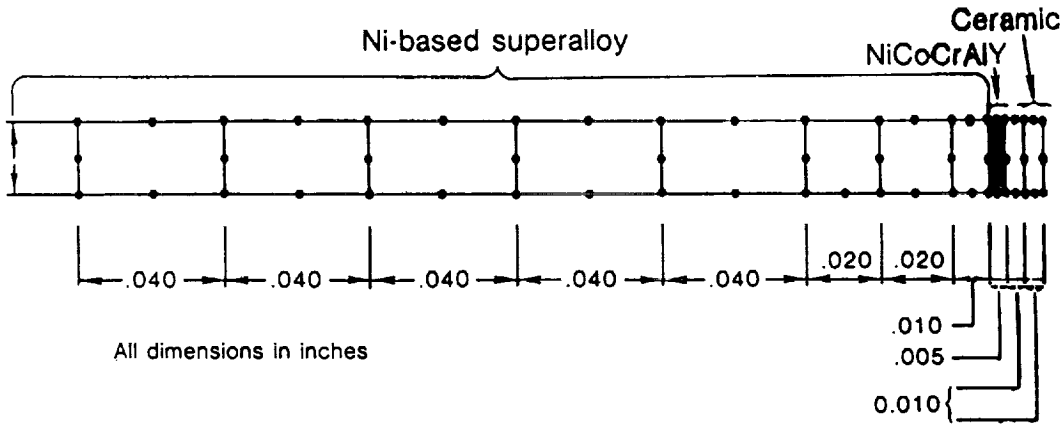

Figure 81 Axisymmetric Finite Element Model Breakup of Substrate, Bond Coat, and TBC

To approximate the non-linear tensile and compressive stress-strain behavior discussed previously, the ceramic material was modeled as being ideally inelastic, as illustrated in Figure 82. This material model assumes elastic behavior up to the yield point, followed by inelastic deformation with zero strain hardening. Because this model was formulated prior to testing which

showed a large difference in tensile and compressive strength, both tensile and compressive yield strengths were assumed equal to 5.5 KSI independent of temperature. Results of the SWRI tension and compression tests, which show a significant dependence of yield stress on stress state, will be incorporated to refine the model in Task II.

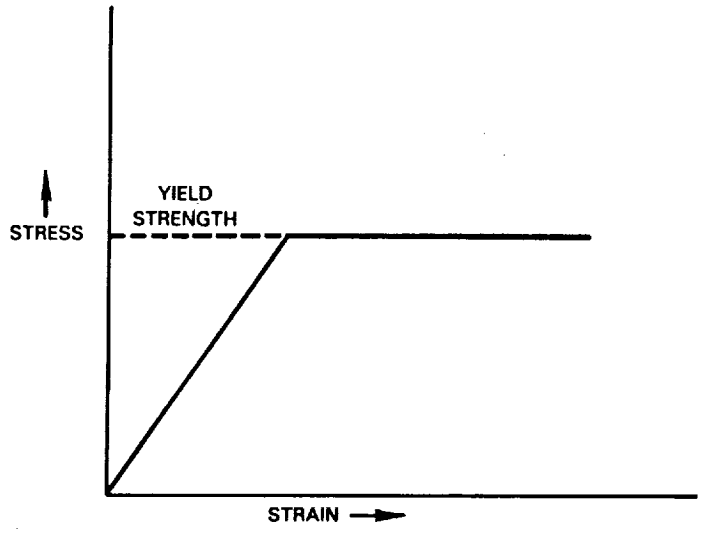

Figure 82 Idealy Inelastic Behavioral Model Used to Represent Ceramic Stress-Strain Behavior

Using the assumption of ideal inelasticity, results of the thermal and stress-strain analyses predict a ceramic hysteresis loop as illustrated in Figure 83. Initially the ceramic is assumed to be in slight compression as a result of the fabrication process (point 1 in Figure 83). During the initial portion of other thermal cycle the ceramic heats more rapidly than the underlying metal layer; since it is constrained from expanding by the much stiffer metallic substrate, the ceramic deforms compressively, elastically at first and then inelastically as thermally imposed strain exceeds the assumed compressive yield point (Point 2 on Figure 83). As the underlying metal begins to heat and the substrate temperature begins to "catch-up" with the ceramic temperature, differential expansion reverses the ceramic deformation and forces it toward tension, elastically until the tensile yield point is reached (point 3 to point 4), then inelastically until the entire system equilibrates the maximum exposure temperature (point 4 to point 5). Upon initial cool down, as the ceramic cools (and shrinks) more rapidly than the underlying metal, additional tensile going inelastic strain is accumulated in the ceramic (point 5 to point 6 in Figure 83). As the metal starts to cool and the transient through ceramic-thickness gradient decreases, differential contraction forces the ceramic into compression, elastically at first (point 6 to point 7), and then inelastically until the entire system approaches equilibrium at the minimum exposure temperature (point 8), thus completing the thermal cycle. It should be noted in Figure 83 that at completion of the initial thermal cycle the ideally inelastic hysteresis loop does not close. While multiple cycles were not modeled analytically for this preliminary analysis, it is assumed that multiple cycling would result in development of a stable hysteresis loop shifted laterally along the strain axis from that illustrated in Figure 83.

The total inelastic strain range for the hysteresis loop illustrated in Figure 83 may be analytically expressed as follows:

$$\Delta\epsilon_i = \Delta(\alpha\Delta T) + \Delta\epsilon_n + \Delta\epsilon_c - 2(\sigma_{y.s.} / E)$$

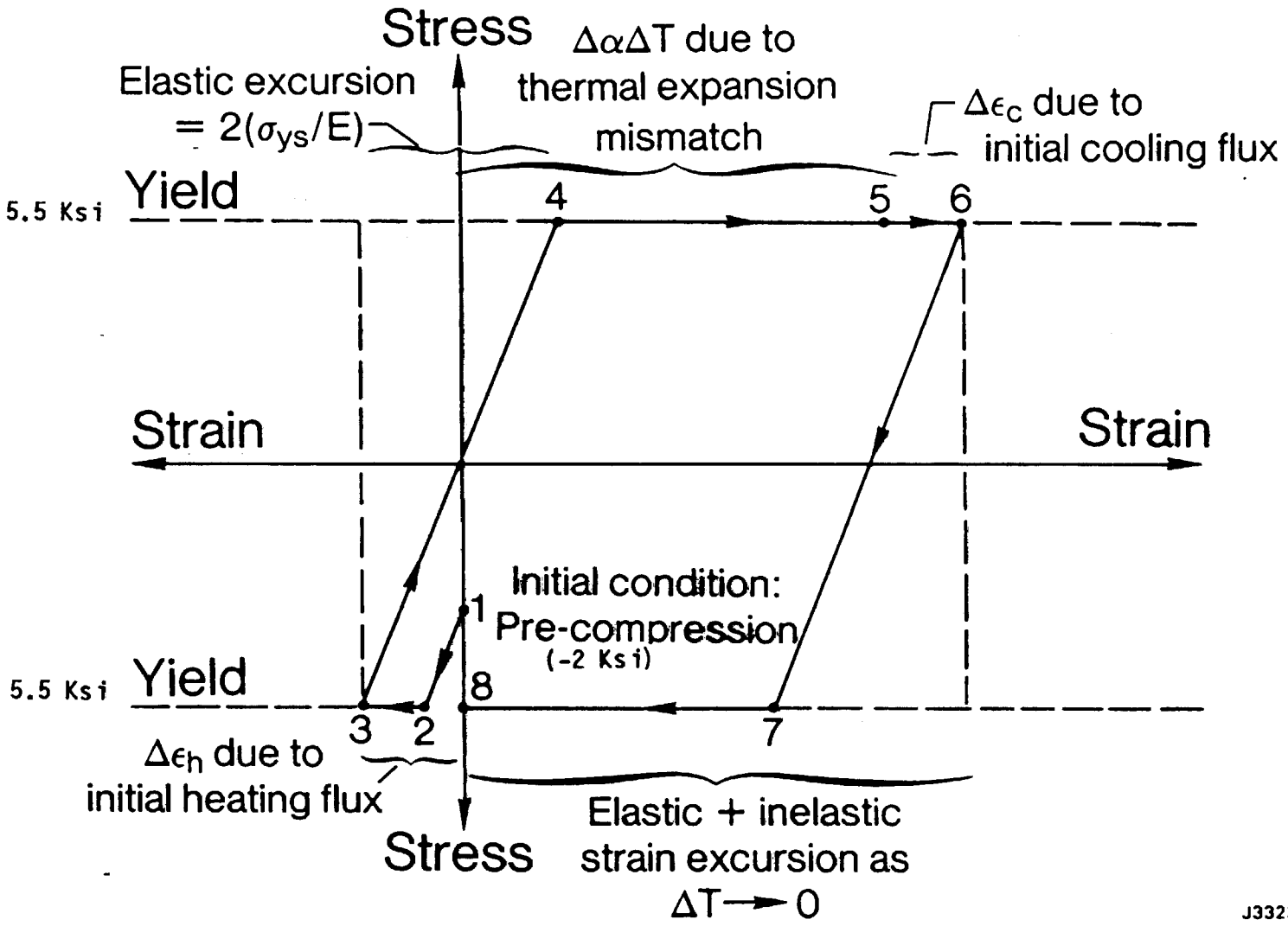

Figure 83 Conceptual Model of Thermally Driven Ceramic Stress-Strain Cycle

where $\Delta\epsilon_h$ is the inelastic strain resulting from the heating transient and $\Delta\epsilon_c$ is that resulting from the cooling transient. It is important to note that, depending on the severity of the transients, the total inelastic strain range can be larger than the nominal $\Delta(\alpha\Delta T)$ driving force.

To establish values of the constants b, $\Delta\epsilon_{fo}$, and δ_c in the preliminary model, life data from the Task IB cyclic burner rig tests were correlated with values of $\Delta\epsilon$, and δ calculated for each set of test conditions. The approach to computation involved computerized linear summation of fractional mechanical and oxidative damage accumulated in successive "blocks" of exposure at specific conditions. Results of this correlation are shown in Figure 84 together with best fit values of the three constants. Based on a computed correlation coefficient $\approx$0.9, the fit of the experimental data must be considered quite good for this initial model. It is reassuring to note that the best-fit critical oxide thickness and oxide-free failure strain constants have physically reasonable values, on the order of 0.3 mil and 1% strain respectively. It is of interest to note that the slope of the correlation (b) is extremely high when compared to typical metal values mentioned previously. This observation is consistent with the previously discussed isothermal fatigue slope, which was estimated to be on the order of 50 (Figure 80).

3.1.4.2 Task IC.2 Verification Tests

The objective of this subtask is to experimentally verify the preliminary life prediction model described in the previous section. The approach to verification testing involves cyclic burner rig testing as conducted in Task IB, modified as described below to more closely simulate engine operation conditions. Three tests have been conducted at three sets of exposure conditions which are different from one another and from the condition used to establish the correlation in Task IB.

The test method used for life model verification involves clean fuel cyclic burner rig testing with a single, internally cooled hollow specimen. This specimen permits exposure of the ceramic with a steady state through thickness gradient to more closely simulate engine exposure of the coating, and also allows more precise instrumentation and control of the thermal environment. As shown in Figure 85, the hollow verification test specimen is twice the diameter of the previously utilized specimen, and rotates about it's own axis to assure circumferential temperature uniformity. These substantial changes from the Task IB experimental condition assure that the preliminary model will be effectively challenged by the verification testing.

Specific test conditions and results of the verification tests are presented in Table XXXI; comparisons between observed and predicted cyclic life are made graphically in Figure 86. It is clear from this plot that the model predicts the uncooled test result more accurately than the two cooled test results. Prediction of the uncooled test indicates that the radial stress model accurately accounts for changes associated with the change in specimen radius from 0.25 in. to 0.5 inch. Also, the relatively accurate prediction for the uncooled verification test indicates that for tests emphasizing cyclic strain damage, the fatigue based model is a good functional form for life prediction.

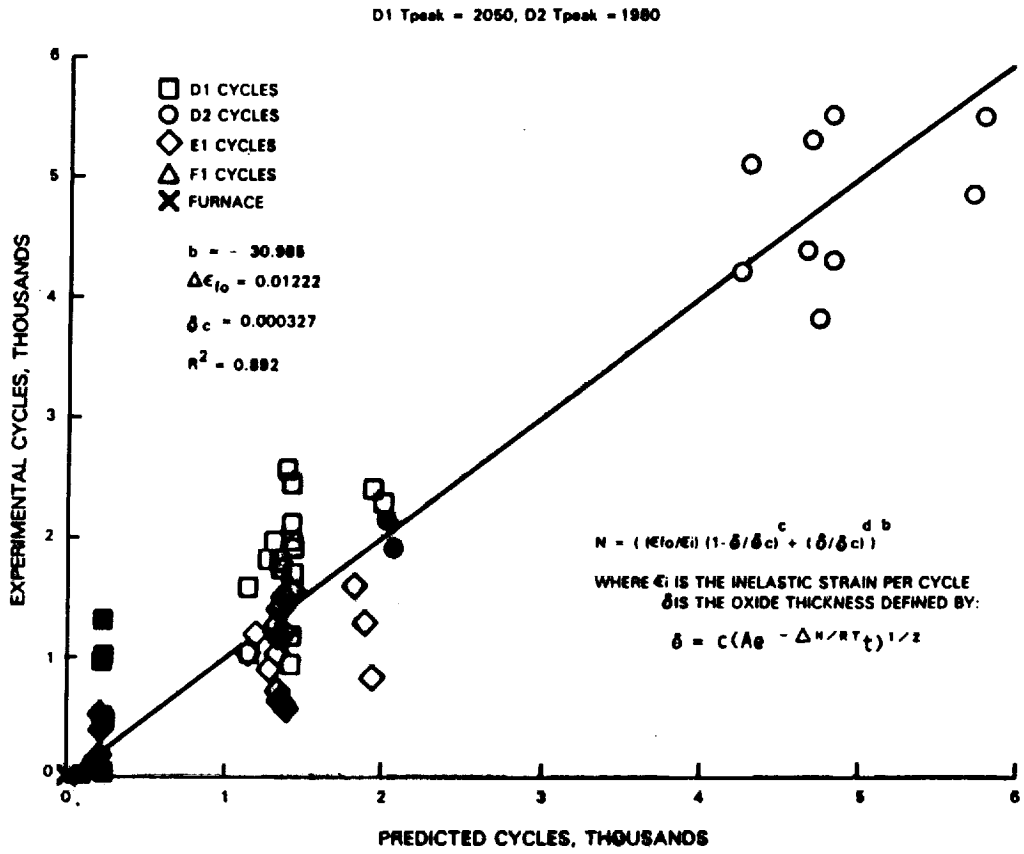

Figure 84 Preliminary Life Model Correlation

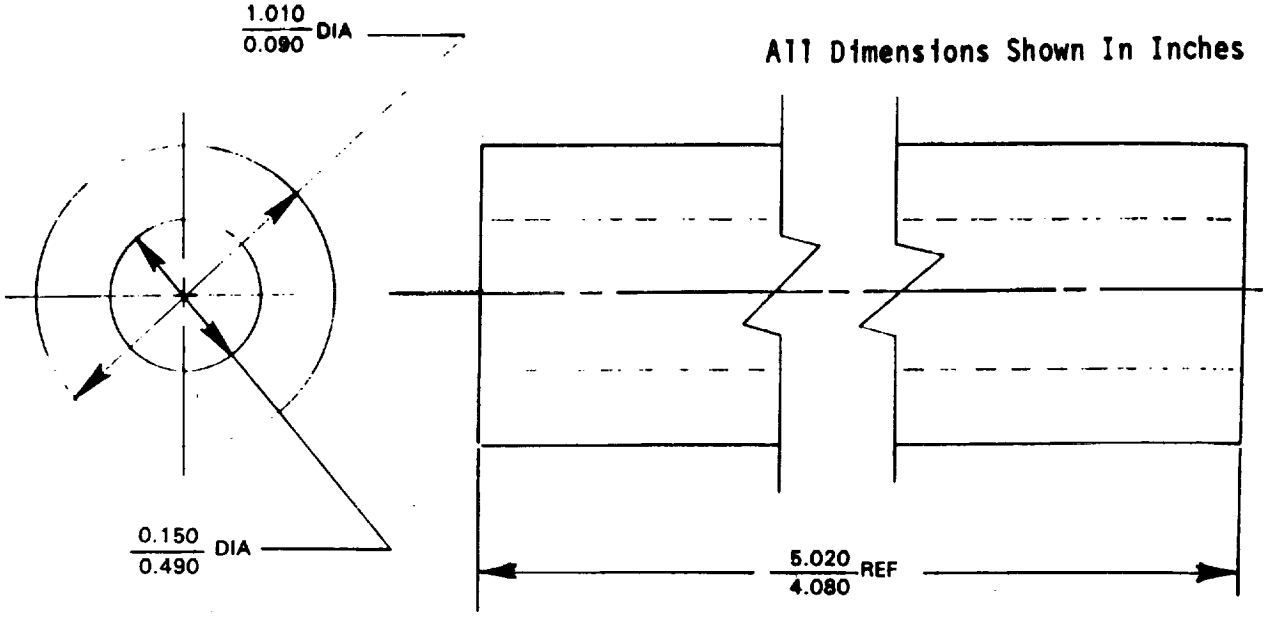

Figure 85 Single Rotating, Internally-Cooled Tube Tests Specimen Geometry

TABLE XXXI
VERIFICATION TEST RESULTS

Specimen Identification Number	T.C. Temperature	Interface Temperature (Calculated)	Ceramic Surface Temperature (Estimated)	Test Condition	Test Hours	Hot Hours (Estimated)	Experimental Number of Cycles Accumulated	Predicted Number of Cycles	Predicted Cycles/ Experimental Cycles
HT-05	1935°F	2005°F	2145°F	12 min. cycle - Cooled I.D.	105.87	70.58	524	1907	3.6
HT-06	1960°F	2035°F	2175°F	6 min. cycle - Cooled I.D.	88.37	29.45	884	4290	4.9
HT-12	2050°F	2050°F		12 min. cycle - uncooled I.D.	138	97.75	686	619	0.9

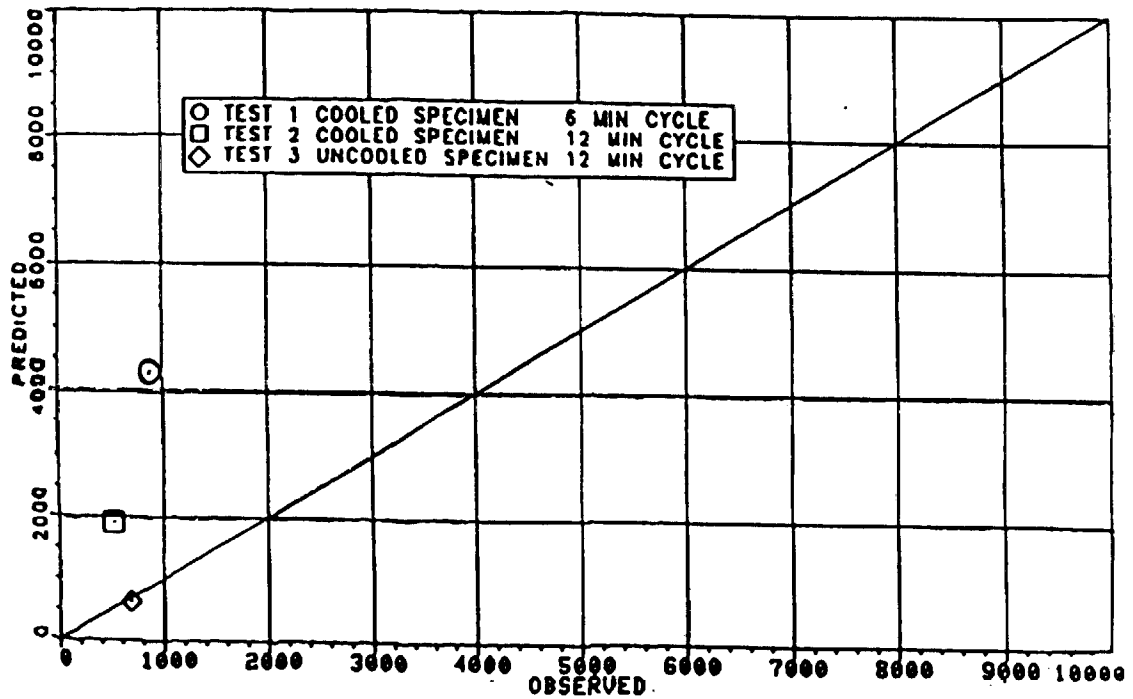

Figure 86 Predicted Cycles Versus Observed Cycles for the Task IC Verification Tests

Two possible explanations for the inaccuracy of cooled test predictions are: 1) the model is inadequate to account for the complex stress distribution which would result from the through thickness ΔT. 2) the inaccuracy of the relatively simple instrumentation used. The initial Task II results from much worse sophisticated instrumentation indicated possible errors in the temperature readings taken in Task I. Both of the above mentioned sources of error are being addressed in Task II. Consistent with the purpose of this Task, the model is being upgraded and much better instrumentation is being used for Task II testing.

It is of interest to examine damage predictions versus number of cycles for the three verification tests. Figure 87 indicates that for the verification test conditions, the model predicts very little mechanical damage early in life, with damage accumulating rapidly for the last few hundred cycles. This result is really a reflection of the steep slope being used in the model. It should be noted that on Figure 87, the inflections in the two uncooled verification test curves, have no physical meaning but are merely a result of how temperature data blocks were sequenced and inputted. A plot of the predicted oxide thickness ratio versus number of cycles, shown in Figure 88, indicates that the uncooled test is accumulating oxide at a greater rate than the two cooled tests, presumably because of the higher interface temperature.

Failure modes were examined for comparison with these observed on the smaller, solid bar specimens and on engine parts. All three specimens exhibited typical, near interface spallation. The crack morphology was, in general, similar except in one case, described below where more fine cracks are seen. Specific metallographic observations are described in the succeeding paragraphs and the post-test microstructures are presented in Figures 89 through 91.

Figure 89a and 89b show the post-test specimen and microstructure after 105.87 test hours/524 cycles. This specimen was tested in the burner rig using a 12-minute cycle with internal cooling. The specimen exhibited ceramic spallation completely around the bar in the hot zone. The specimen microstructure shown in Figure 89b is of the upper portion of the hot zone on the test bar and an area where the ceramic had not been spalled off yet was included. Two types of near interface cracks are observed in the area where the ceramic remains adherent. There are some very large cracks which do not appear to be directly associated with the bond coat oxide but which do appear to follow the general bond coat topology. The other type of crack which is observed is directly associated with bond coat oxide. They are finer, smaller cracks which are either extending from the oxidized bond coat asperity or are within the bond coat oxide layer itself. These cracks do not appear to directly result in ceramic spallation because they are still present in the area where spalling has occurred. Another interesting observation in Figure 89b is that there is a very large crack $\approx$ 3-4 mils down from the ceramic surface. This crack may well be consequential damage i.e., crack started by the large chip spalling off.

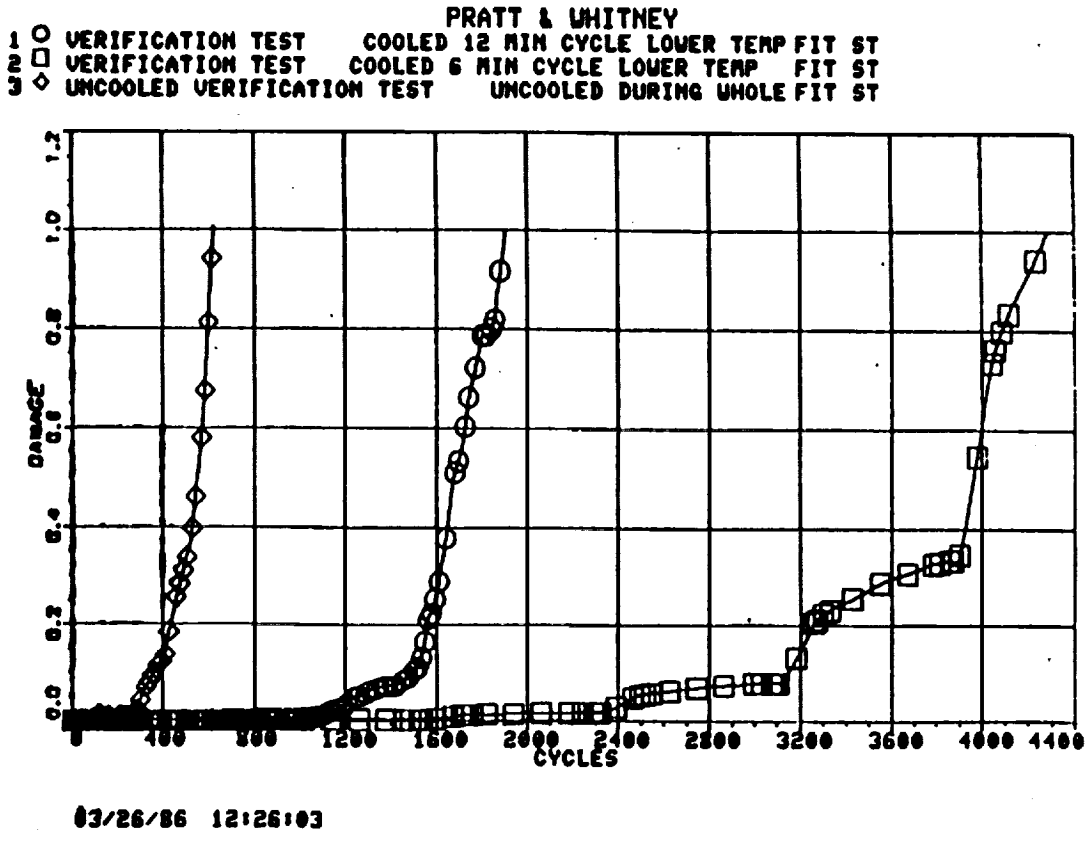

Figure 87 Damage Versus Cycle Number Plot Showing All Three Verification Tests

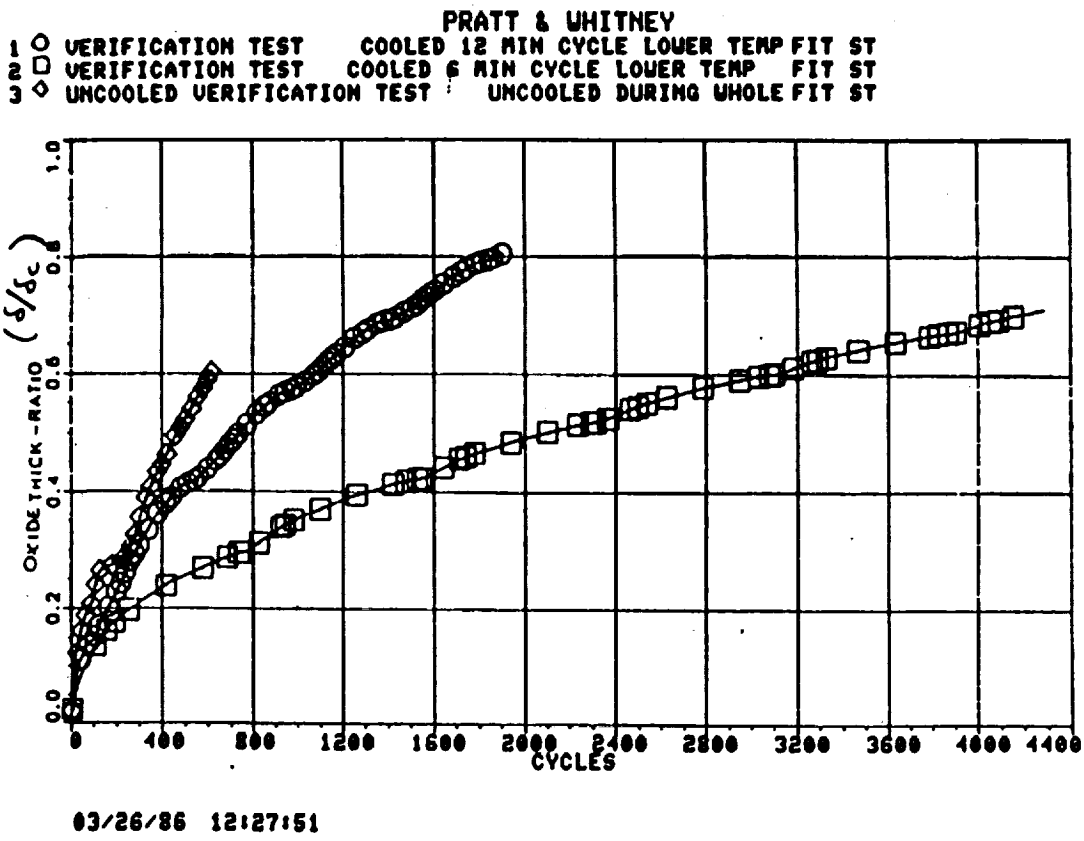

Figure 88 Ratio of Accumulated Oxide Thickness to Predicted Critical Oxide Thickness at Failure Versus Cycle Number Plot for the Three Verification Tests

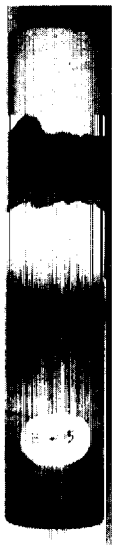

(a) .64X

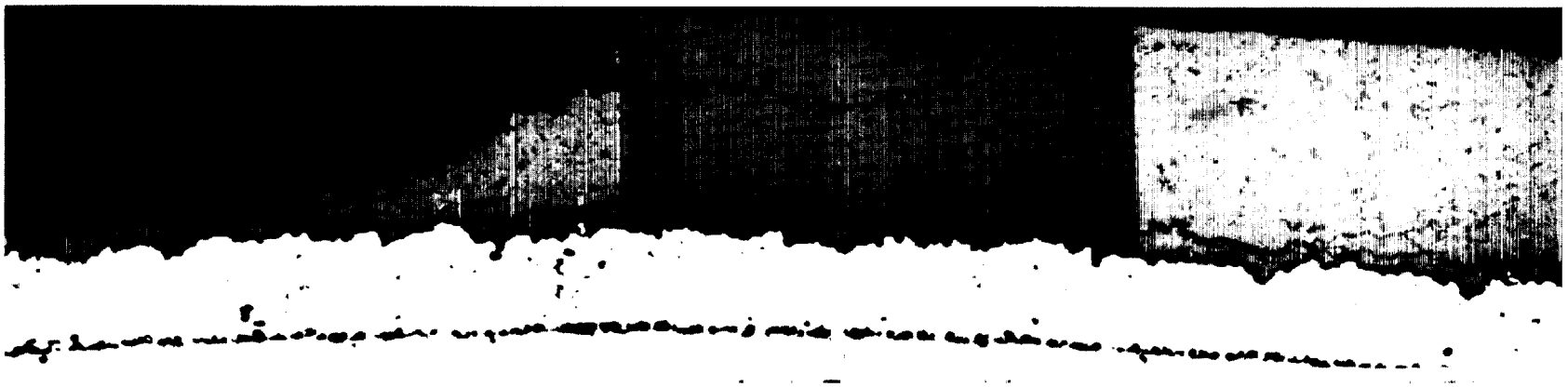

(b) 128X

Figure 89 (a) Post-Test Specimen After 105.87 Test Hours/524 Cycles, 12 Minute Burner Rig Cycle, Cooled I.D.
(b) Post-Test Microstructure Near Spalled Area

Figures 90a and 90b show the post-test specimen for the second verification tests, and its microstructure. This specimen had accumulated 88.37 hours of test time/884 cycles. The burner rig cycle was 6 minutes, and the specimen was internally cooled. The microstructure of the specimen shows less "subcritical" cracking than the 12-minute cycle, internally cooled test specimen. While it survived less time at the peak temperature than the latter specimen, it did accumulate a greater number of cycles. The microstructure shows some oxidized islands of NiCoCrAlY at the interface that are not apparent in the other internally cooled specimen, but these areas do not appear to be associated with any major cracks.

Figures 91a and 91b show the post-test specimen and microstructure of the uncooled test specimen after 138 test hours/686 cycles. A 12-minute burner rig cycle was used. This specimen spalled in two areas in the hot zone of the bar approximately 90° apart. In the area where ceramic is still adherent, the microstructure shows a large number of subcritical cracks such that if exposed for a longer period of time, ceramic spalling may have occurred 360° around the bar. These cracks appear to follow the bond coat topology. In the spalled area the bond coat topology does not seem to be as complex as in the area where the ceramic is still adherent. Perhaps localized changes in the bond coat geometry cause the ceramic to spall in that particular area first.

3.2 Task II - Major Mode Life Prediction Model

The objective of this task is refinement of the preliminary life prediction model developed in Task I. The approach involves refinement of both the analytical and the experimental approaches utilized to develop the preliminary model. Analytical enhancements will involve better modeling of the ceramic constitutive and time dependent behavior, as well as refinement of the finite element calculation of temperature and stress-strain distribution. Improvements to the experimental approach involve improved simulation of engine exposure conditions and expansion of the parameter envelope to cover a broader range of mechanical and oxidation forcing functions. The improved test method will involve well characterized testing of the single internally cooled specimen used for Task IC verification testing.

3.2.1 Task IIA - Experimental Design

The objective of Task IIA is to design experiments to obtain data for correlation with the refined major mode life prediction model. To accomplish this objective a matrix of twenty tests has been defined based on the Task I model and verification test results (Table XXXII). Shown in Figure 92 are the relative mechanical and oxidation damage fractions calculated for each of these twenty tests. Tests 1 through 6 minimize mechanical damage and emphasize oxidation damage by reducing the cycle temperature range. Tests 7 through 12 will emphasizes mechanical damage while minimizing oxide growth by minimizing exposure to the maximum cycle temperature. Tests 13 through 18 are mixed mode tests designed to improve capability of the model to handle interactive effects. Tests 19 and 20 will duplicate the test 7 and 8 conditions using a smaller specimen diameter (0.84 in. versus 1.0 in.) to access the effect of component geometry on life.

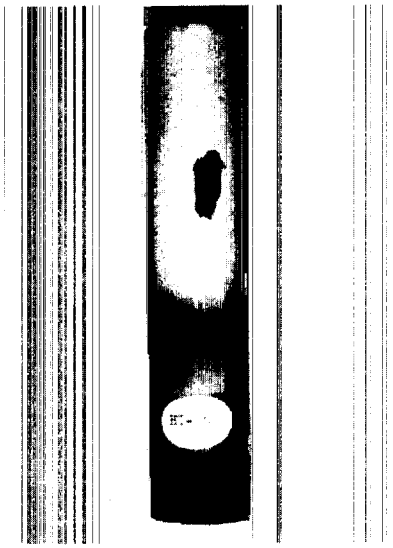

(a) .64X

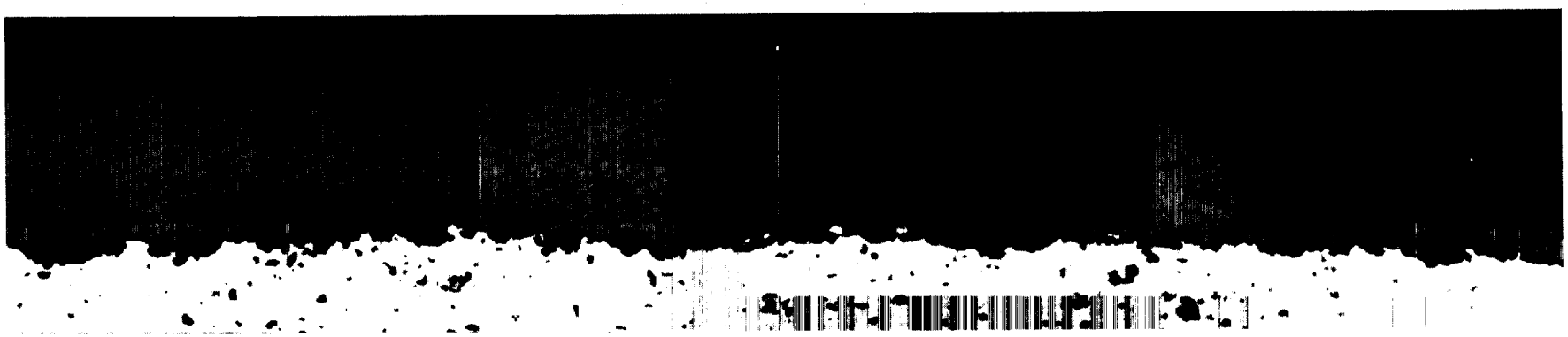

(b) 128X

Figure 90 (a) Post-Test Specimen After 88.37 Test Hours/884 Cycles, 6 Minute Burner Rig Cycle, Cooled I.D.
(b) Post-Test Microstructure Near Spalled Area

(a) .64X

(b) 128X

Figure 91 (a) Post-Test Specimen After 138 Test Hours/686 Cycles, 12 Minute Burner Rig Cycle, Uncooled I.D. (b) Post-Test Microstructure Near Spalled Area

TABLE XXXII
TASK II EXPERIMENTS

Test	Emphasis	Interface Temp(°F) Max	Min	Cycle Time (Min)	Purpose of Test is to Establish
1	Oxide	2025	800	6	
2	↓	↓	↓	6	
3				12	
4				12	Critical Oxide Thickness
5				24	
6	↓	↓	↓	24	
7	Strain	2050	70	6	
8	↓	2050	↓		
9		2100			Static Failure Strain
10		2100			
11		2150			
12	↓	2150	↓		
13	Mixed	1975	135	6	
14	Mode		↓	6	
15	↓			12	
16				12	Rate of Oxide Growth
17		2025		6	
18	↓	2025	↓	12	
19	0.42" Radius	2050	70	6	Direct Effect of
20	0.42" Radius	2050	70	6	Radial Stress

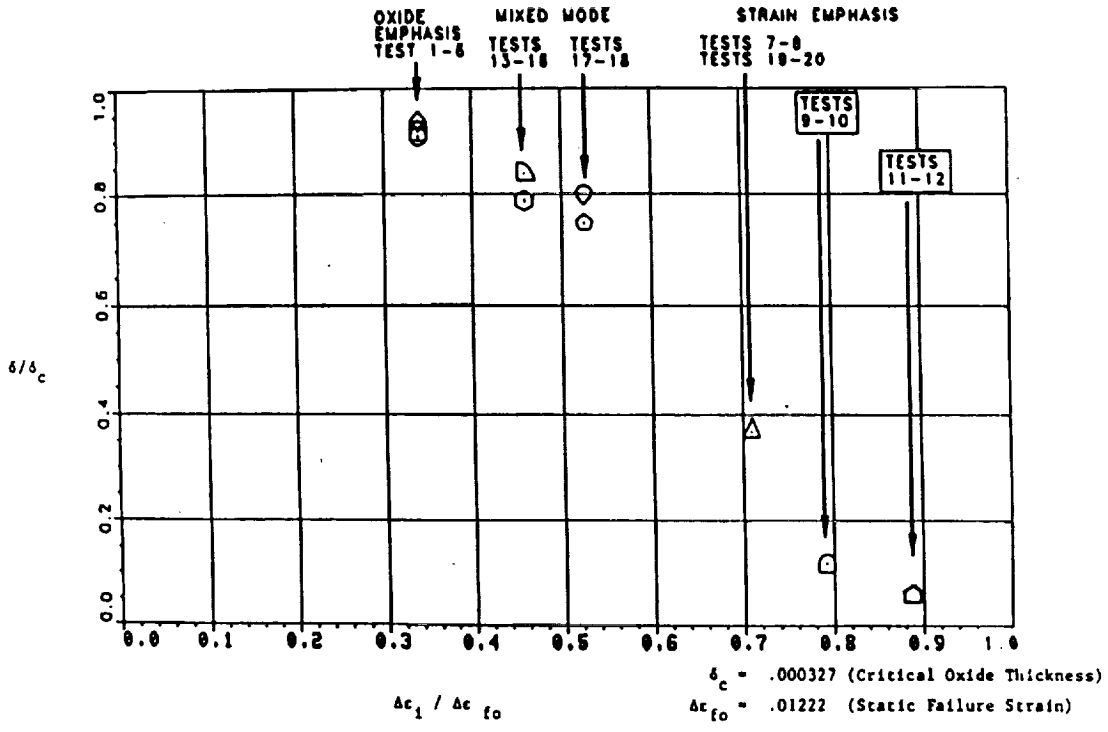

Figure 92 Task II Predictions Ratio of Accumulated Oxide Thickness to Predicted Critical Oxide Thickness at Failure Versus Strain Ratio

Task IIB - Experiments/Analysis and Model Development

The objective of the subtask is to conduct the experiments and model refinements described above.

One test, designated number 11 in Table XXXII and shown as a solid data point in Figure 92, has been conducted to date. The test cycle consisted of 110 seconds of heat up to 2150°F metal temperature and ≈ 4 minutes of forced air cooling to 70°F. Internal cooling was not used. As indicated previously, the purpose of this test was to emphasize mechanical damage while minimizing oxide accumulation. The coating spallation life was 28 cycles in the test, versus a predicted life of 26 cycles calculated from the Task I preliminary model, indicating relatively good model performance when damage is predominantly mechanical. During the coming year the remaining 19 tests will be completed and the model will be refined to improve prediction capability over the entire mechanical-oxidation damage envelope. These refinements then will be substantiated in Task III with bench mark engine mission simulation testing.

4.0 CONCLUSIONS

The Task I program approach was designed to assess the predominant TBC failure mechanisms. The laboratory test program included the study of the influence of driving forces such as interface temperature, thermal cycle frequency, environment and coating thickness on ceramic spalling life. The predominant failure mode was determined to be ceramic spallation resulting from ceramic cracking parallel and adjacent to, but not coincident with, the metal-ceramic interface.

The Task I initiative included furnace exposure tests in air and argon, clean fuel cyclic burner rig tests, cyclic hot corrosion testing and physical/mechanical property testing of the bulk ceramic and metallic bond coat materials.

In the Task I testing coating life was found not only to be driven by interfacial temperature but is also a function of cyclic content such that shorter thermal cycles with larger transients will spall the coating before its equivalent full furnace (long cycle) life is achieved. Also for all tests a thermal transient was required to spall the ceramic; i.e., furnace test specimens failed upon cool down during a particular thermal cycle. Consistent with the hypothesis that bond coat oxidation is an important factor effecting coating durability, it was found that thermal exposure in an inert environment does not cause coating degradation while pre-exposure in air reduces coating durability significantly.

Interrupted burner rig tests conducted as part of the Task IB.1 critical experiments showed that subcritical microcrack link-up was occurring, resulting in a progressive damage mode. The role of bond-coat oxidation in initiating these cracks is not yet clear since direct evidence of oxide initiating subcritical cracks was difficult to find. However, since the phenomenological evidence shows conclusively that oxidation is a major life driver, it is presumed that oxidation may play a less direct role in crack propagation.

Ceramic thickness effects were also found to play a role in coating longevity. Thin ceramic coatings, nominal 5 mils thick, showed an increase in coating spalling life as compared to the baseline 10 mil coating, while 15 mil thick ceramic spalled earlier than the baseline.

Cyclic hot corrosion is considered to be a secondary failure mode. As indicated by the engine exposed part evaluation, the characteristic "multi-level" type failure mode is generally not observed. In laboratory testing, TBC failures due to hot corrosion were observed only at high corrodent levels (35 ppm which is above the level typically encountered in engine service) in which the TBC failure life is considered to be more a function of thermomechanical damage than thermochemical interactions.

As part of the Task I effort physical and mechanical property testing was conducted to acquire data required for thermal and stress analysis and life prediction model development. The bulk ceramic was observed to have complex

property characteristics. The bulk ceramic exhibits a non-linear stress-strain response which is attributed to the unique plasma sprayed microstructure. The tension and compression stress strain responses were different in terms of their achieved ultimate strength levels which were an order of magnitude apart. The plasma sprayed ceramic also exhibits a strong creep response.

Another important finding is that the material also has low cycle fatigue characteristics response over an extremely narrow stress range. Above a critical stress level rapid damage is accumulated in the system.

Based on Task I test results, a preliminary life prediction model has been developed. It focuses on two major damage modes as identified in laboratory testing. The first of these modes involves a mechanical driving force, resulting from cyclic strain and stresses caused by thermally induced and externally imposed loads. The second is an environmental driving force, which from the experimental results is related to "oxidation damage", attributed to the in-service growth of a NiCoCrAlY oxide scale at the metal ceramic interface. Based on the apparently "mechanical" mode of ceramic failure, it is presumed that the oxide scale may influence the intensity of the mechanical driving force.

Verification tests were conducted to challenge the preliminary model. It was concluded from these tests that the fatigue based model is a good functional form for life prediction of the TBC. A Task II test matrix was designed to aggressively pursue parametric refinements to the model which may include accounting for ceramic creep. Additional inelastic/non-linear stress analysis is also planned.

REFERENCES

1. Stecura, S., "Effects of Plasma Spray Parameters on Two-Layer Thermal Barrier Coating System Life", NASA TM 81724, 1981.

2. Summer, I. E., "Development of Improved-Durability Plasma Sprayed Ceramic Coatings for Gas Turbine Engine", AIAA/SAE/ASME 16th Joint Propulsion Conference, AIAA-80-1193, 1980.

3. Cassenti, B. N., Brickley, A. M., "Thermal and Stress Analysis of Thermal Barrier Coatings", AIAA-81-1402, 1981.

4. Grot, A. S., Martin, J. K., "Behavior of Plasma Sprayed Ceramic Thermal Barrier Coating for Gas Turbine Engines", American Ceramic Society Bulletin, Vol. 60 No. 8, pp. 807-811, 1981.

5. Anderson, N. P., Sheffler, K. D., "Development of Stain Tolerant Thermal Barrier Coating Systems" Final Report, Tasks I-III, Contract No. NAS3-22548, NASA CR 168251, PWA-5777-29, 1983.

6. Miller, R. A., Levine, S. R., Stecura, S., "Thermal Barrier Coatings for Aircraft Gas Turbines", AIAA 80-0302, 1980.

7. Sheffler, K. D., Graziani, R. A., Sinko, G. C., "JT9D Thermal Barrier Coated Vanes," Final Report, Contract No. NAS3-20630, NASA CR 167964, 1982.

8. Becher, P. F., Rice, R. W., Wu C. Cm., Jones, R. L. "Factors in the Degradation of Ceramic Coating for Turbine Alloys" Thin Solid Films 53, pp. 225-232, 1978.

9. Gladden, H. J., "Thermal Performance of a Ceramic Coated Turbine Vane Under Transient Gas Conditions" SAE preprint N810205, presented at International Congress and Exposition, Detroit, Michigan Feb. 23-27, 1981.

10. Duvall, D. S., Ruckle, D. L., "Ceramic Thermal Barrier Coatings for Turbine Engine Components" ASME, International Gas Turbine Conference and Exhibit ASME Paper 82-GT-322, 27th, London, England, Apr. 18-22, 1982.

11. Ruckle, D. L., "Plasma-Sprayed Ceramic Thermal Barrier Coatings for Turbine Vane Platforms" Thin Solid Films 73, pp. 455-461, 1980.

12. Stecura, S., "Two-Layer Thermal Barrier Coating for Turbine Airfoils - Furnace and Burner Rig Test Results", NASA TM X-3425, Sept. 1976.

13. Stecura, S., "Two-Layer Thermal Barrier Coating for High Temperature Components" American Ceramic Society Bulletin, Vol. 56, No. 12, pp. 1082-1089, 1977.

14. Levine S. R., Miller, R. A., Hodge, P. E., "Thermal Barrier Coatings for Heat Engine Components" SAMPE Quarterly, pp. 20-26, 1980.

15. Miller, R. A., Lowell C. E., "Failure Mechanisms of Thermal Barrier Coatings Exposed to Elevated Temperatures", Thin Solid Films, 95, pp. 265-273, 1982.

16. Stecura, S., "Effects of Yttrium, Aluminum and Chromium Concentrations in Bond Coatings on the Performance of Zirconia-Yttria Thermal Barriers" Thin Solid Films, 73, pp. 481-489, 1980.

17. Andersson, C. A., Lau, S. K., Bratton, R. J., Lee, S. Y., Rieke, K. L., "Advanced Ceramic Coating Development for Industrial/Utility Gas Turbine Applications", Final Report DOE/NASA 0110-1, NASA CR-165619, 1982.

18. Miller, R. A., "Oxidation - Based Model for Thermal Barrier Coating Life" J. Am. Cer. Soc. Vol. 67, No.8 pp. 517-521, 1984.

19. McDonald, G., Hendricks R. C., "Effects of Thermal Cycling on ZrO_2-Y_2O_3 Thermal Barrier Coatings" Thin Solid Films, 72 (2), pp. 491-496, 1980.

20. Gedwill, M. A., "Burner Rig Evaluation of Thermal Barrier Coating Systems for Nickel Base Alloys", NASA TM 81685, Feb. 1981.

21. Andersson, C. A., "Thermal Stress Fracture of Ceramic Coatings", Fracture Mechanics of Ceramics, Vol. 6, Measurements, Transformation, and High Temperature Fracture, N.Y., Plenum Press, pp. 497-509, 1983.

22. Miller, R.A., Berndt, C.C., "Performance of Thermal Barrier Coatings in High Heat Flux Environments," Thin Solid Films 119, pp. 195-202, 1984.

23. Harding, A. G., Adam, T. "Thermal Stress in Ceramics Applied as Thermal Barrier Layers to Turbine Blades", British Ceramic Society Transactions, Vol. 65, No. 5, pp. 289-307, 1965.

24. Miller, R. A., Smialek, J. L., Garlick, R. G., "Phase Stability in Plasma Sprayed Partially Stability in Plasma Sprayed Partially Stablized Zirconia-Yttria" Advances in Ceramics, Vol. 3, pp. 241-253, 1981.

25. Miller, R. A., Garlick, R. G., Smialek, J. L., "Phase Distributions in Plasma Sprayed Zirconia-Yttria" American Ceramic Society Bulletin, Vol. 62, No. 12, pp. 1355-1358, 1983.

26. Rice, R. W., Pahanke, R. C., McDonough, W. J., "Effect of Stresses from Thermal Expansion Anisotropy, Phase Transformation and Second Phases on the Strength of Ceramics", J. Am. Cer. Soc., Vol. 63, No. 11-12, pp. 703-710, 1980.

27. Berndt, C. C., Herman, H., "Anisotropic Thermal Expansion Effects in Plasma Sprayed ZrO_2-8%Y_2O_3 Coatings", Ceramic Engineering and Science Proceedings, Vol. 4, pp. 792-801, 1983.

28. Stecura, S., "Two-Layer Thermal Barrier Systems for Ni-Al-Mo Alloy and Effects of Alloy Thermal Expansion on System Life", American Ceramic Society Bulletin, Vol. 61, No.2, pp. 256-262, 1982.

29. Bevan, C. E., "Development of Advanced Plasma Sprayed Ceramic Coatings for Industrial Gas Turbine Engines" Final Report, DOE/Batelle Subcontract B-A0747-A-Z, PWA 5906, 1982.

30. Miller, R. A., "Analysis of the Response of a Thermal Barrier Coating to Sodium and Vanadium Doped Combustion Cases", DOE/NASA 2593-79/7, NASA TM 79205, 1979.

31. Hodge, P. E., Stecura, S., Gedwell, M. A., Zaplatynsky, I., Levine, S. R., "Thermal Barrier Coating: Burner Rig Hot Corrosion Test Results", J. Materials for Energy Systems, 1, pp. 47-58, March 1980.

32. Hodge, P. E., Miller, R. A., Gedwill, M. A., "Evaluation of Hot Corrosion Behavior of Thermal Barrier Coatings", Thin Solid Films, Vol. 73, No. 2, pp. 447-453, 1980.

33. Pettit, F. S., Goward, G. W., "High Temperature Corrosion and use of Coatings for Protection", Metallurgical Treatises, Metallurgical Society of AIME, pp. 603-619, 1983.

34. Lau, S. K., Bratton, R. J., "Degradation Mechanisms of Ceramic Thermal Barrier Coatings in Corrosion Environments", High Temperature Protective Coatings Proceedings of the Symposium, Atlanta, Georgia, March 7, 8, 1983 Metallurgical Society of AIME, pp. 305-317, 1984, .

35. Barkalow, R. H., "Hot Corrosion of Ceramic Coating Materials for Industrial/Utility Gas Turbines", DOE No.DE-AC-03-78ET15236, Ref. No. 81-200-7003-FR, Jan. 1981.

36. Hamilton, J. C., Nagelberg, A. S., "In Situ Raman Spectroscopic Study of Yttria-Stablilized Zirconia Attack by Molten Sodium Vanadate", J. Am. Cer. Soc., Vol. 67, No. 10, pp. 686-690, 1984.

37. Miller, R. A., Argarwal, P., Duderstadt, E. C., "Life Modelling of Atmospheric and Low Pressure Plasma Sprayed Thermal Barrier Coatings", Ceramic and Engineering Science Proceedings, Vol. 5, No. 7-8, pp. 470-478, July-Aug. 1984.

38. Shankar, R. N., Berndt, C. C., Herman, H., "Phase Analysis of Plasma Sprayed Zirconia-Yttria Coatings", Ceramic Engineering and Science Proceedings, Vol. 4, pp. 784-787, 1983.

39. Shaw, M. C., Braiden, P. M., DeSalvo, G. J., "The Disk Test for Brittle Materials". Transactions of the ASME, Journal of Engineering for Industry Paper No. 73-WA/Prod-17, pg 1-11, 1973.

APPENDIX A

SUMMARY OF WEIGHT GAIN DATA FOR FURNACE EXPOSED SPECIMENS

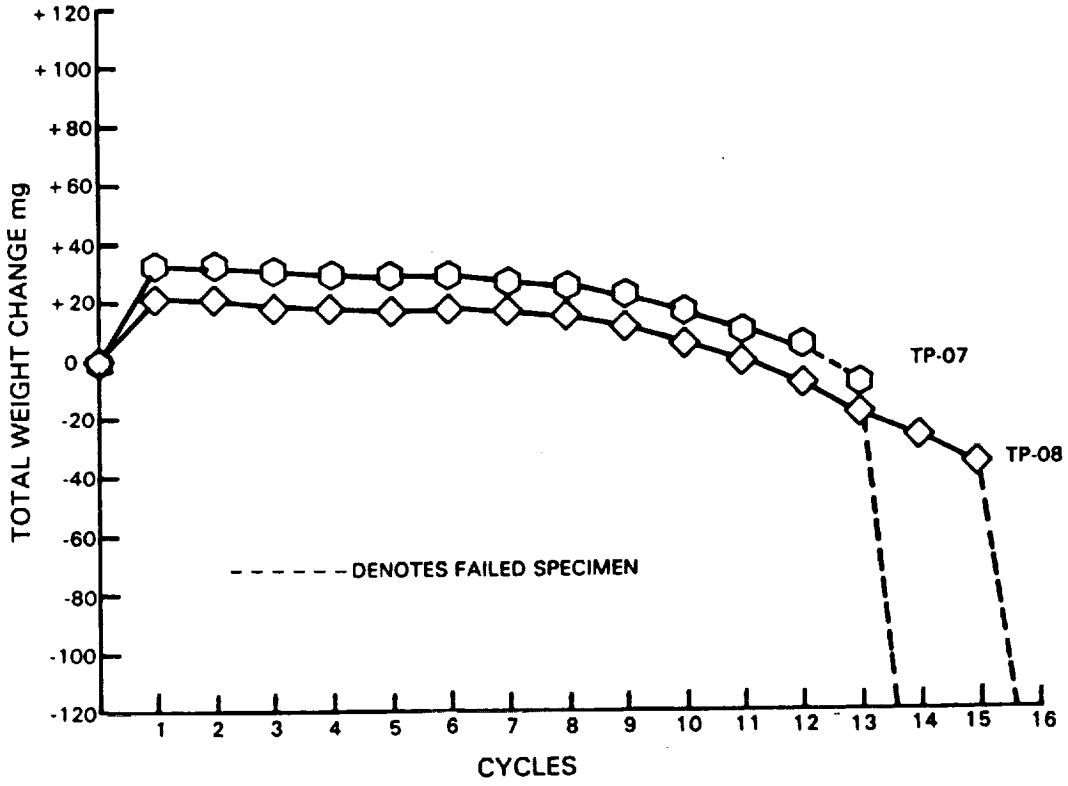

Figure A-1 Task I Furnace Test Results; Weight Change Versus Cycles for 2100°F, Air, 10 Hour Cycle

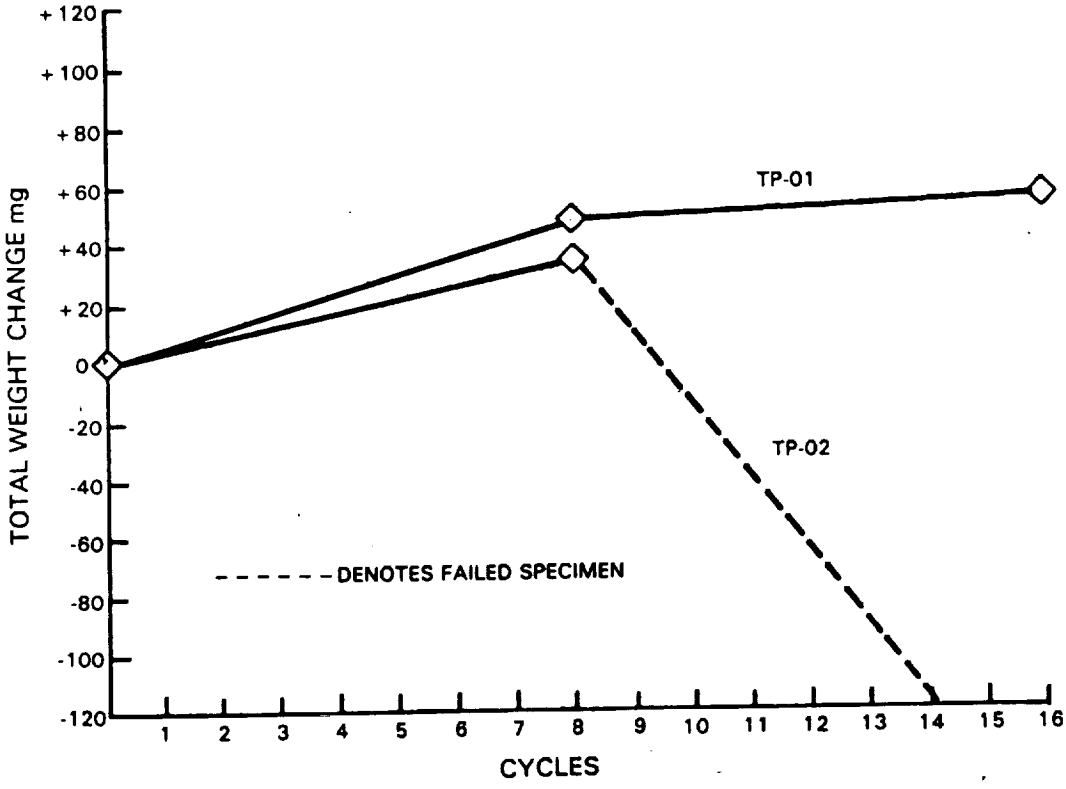

Figure A-2 Task I Furnace Test Results; Weight Change Versus Cycles for 2100°F, Air, 80 Hour Cycle

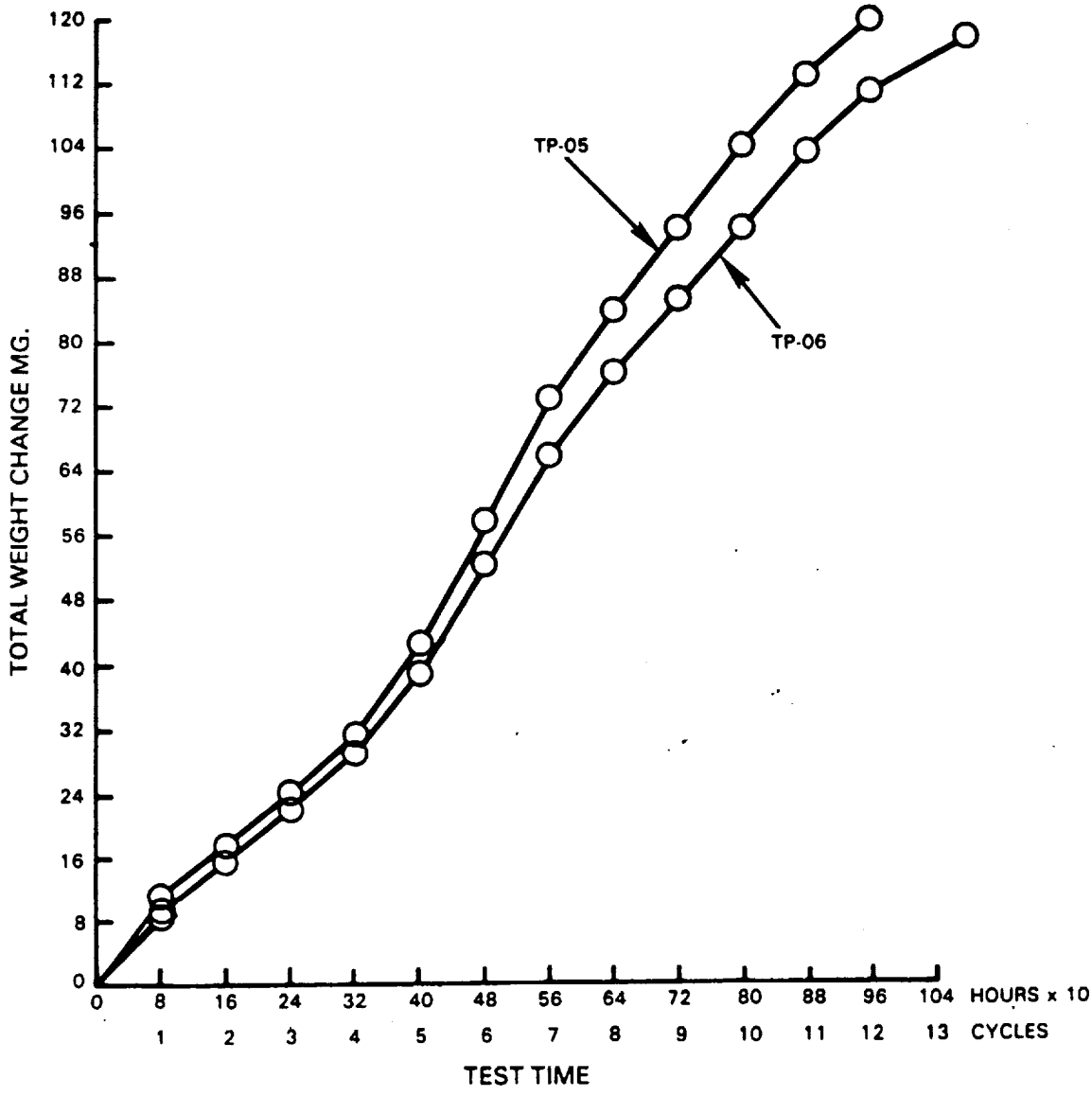

Figure A-3 Task I Furnace Test Results; Weight Change Versus Cycles for 2100°F, Argon, 80 Hour Cycle

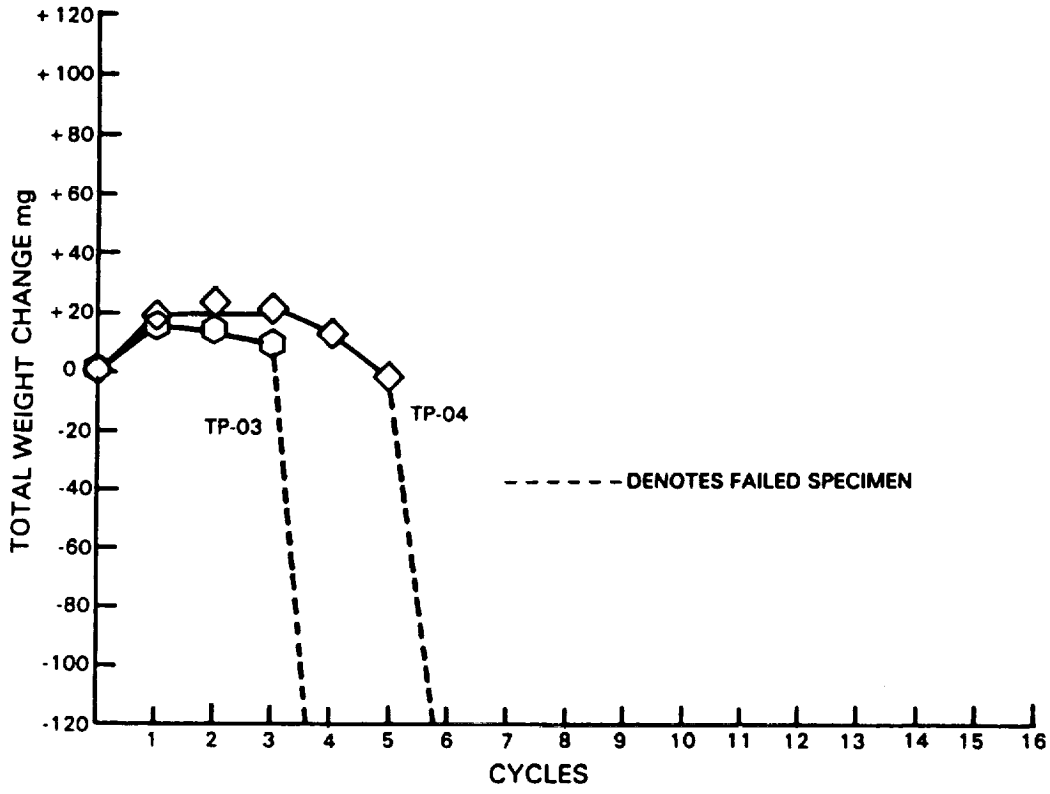

Figure A-4 Task I Furnace Test Results; Weight Change Versus Cycles for 2200°F, Air, 10 Hour Cycle

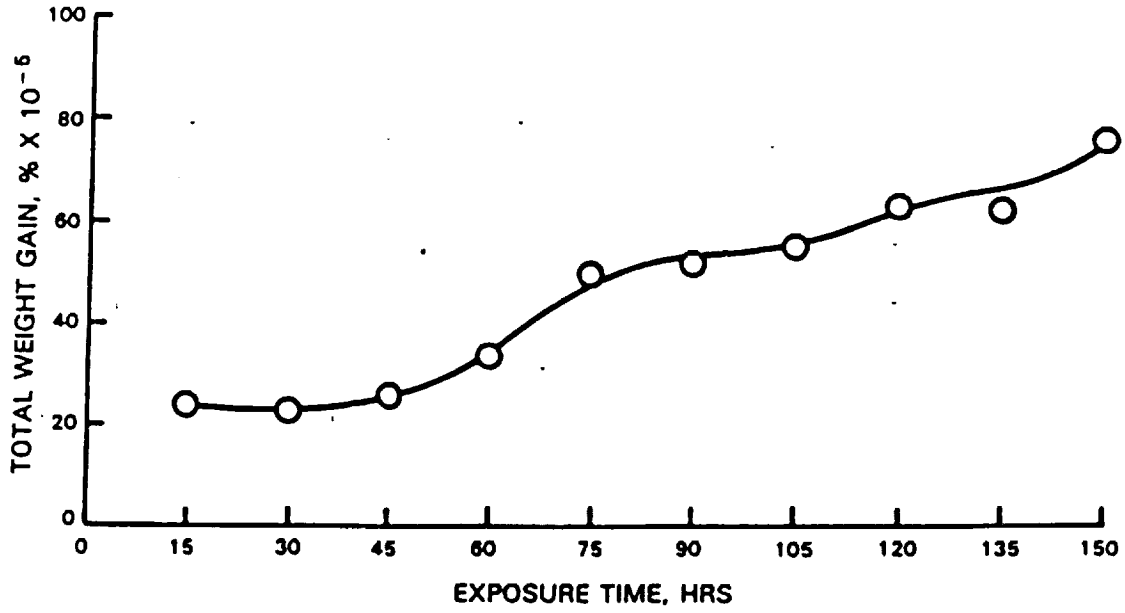

Figure A-5 Task I Furnace Test Results; Weight Change Exposure Time for Fractional Exposure Test, 2100°F, Air, 15 Hour Cycle

APPENDIX B

CYCLIC BURNER RIG TEST DETAILS

The uncooled burner rig test employed in Task I involves cyclic flame heating and forced air cooling of coated cylindrical test specimens. A set of 12 specimens are installed on a spindle per test set at one time. These bars are rotated in the exhaust gases of a jet fuel burner rig to provide a uniform temperature for all specimens. The exhaust gases are the combustion products of Jet A fuel and air, with a velocity of Mach 0.3. Specimen temperature is controlled using an optical pyrometer and automatic feedback controller.

During rig operation the fuel pressure is regulated automatically to maintain the desired temperature. To provide cyclic cooling, the burner is automatically moved away from the specimens for the cool-down portion of the cycle, during which a compressed air blast is applied to the specimens. The test rig is shown in Figure B-1. Testing is interrupted approximately every 20 hours to allow for visual examination of the specimens. Failure is considered to have occurred when spallation occurs over approximately 50 percent of the "test" zone of the bar. The "test" zone includes an area which is approximately 2.5 cm (1 inch) long at the center of the exposed portion of the bar, having a uniform temperature during testing. This failure criterion recognizes that some ceramic loss may occur without severe degradation of the protective nature of the ceramic. It should be noted that once initiated, spallation failure propagates relatively rapidly, so that the stated coating life is not highly sensitive to end point definitions.

In order to further maintenance of reliable test temperatures with good repeatability, one of the twelve 0.5" diameter test bars was replaced with a coated specimen with two internal passages for the routing of thermocouple sensors. One passage was an axial hole 0.170" diameter through the entire length of the specimen. The other hole also penetrated the bar parallel to the axis, but located 50% of the distance between the circumference of the aforementioned 0.170" hole and the outside diameter of the specimen. This passage extended approximately 1.25" down from the tip of the bar and was of 0.040" diameter to accept a 0.032" thermocouple sensors. The specimen geometry is shown in Figure B-2. This specimen is installed in the test cluster with the sensor located in the trailing edge or inside diameter wall of the bar. Thermocouple leads are routed down the specimen drive unit through a slip-ring and finally to a recording device.

By correlating optical pyrometer values with thermocouple readings, optical controller set points are established daily with the thermocouple, thus avoiding drift of test specimen temperature resulting from gradual ceramic emissivity changes.

An alternate specimen was also designed and has seen limited application. Essentially, this specimen is utilized similar to the previously described type, except there is no 0.170" I.D. center hole, and there are three, rather than one, thermocouple holes, each terminating within different longitudinal points in the specimen/cluster hot zone.

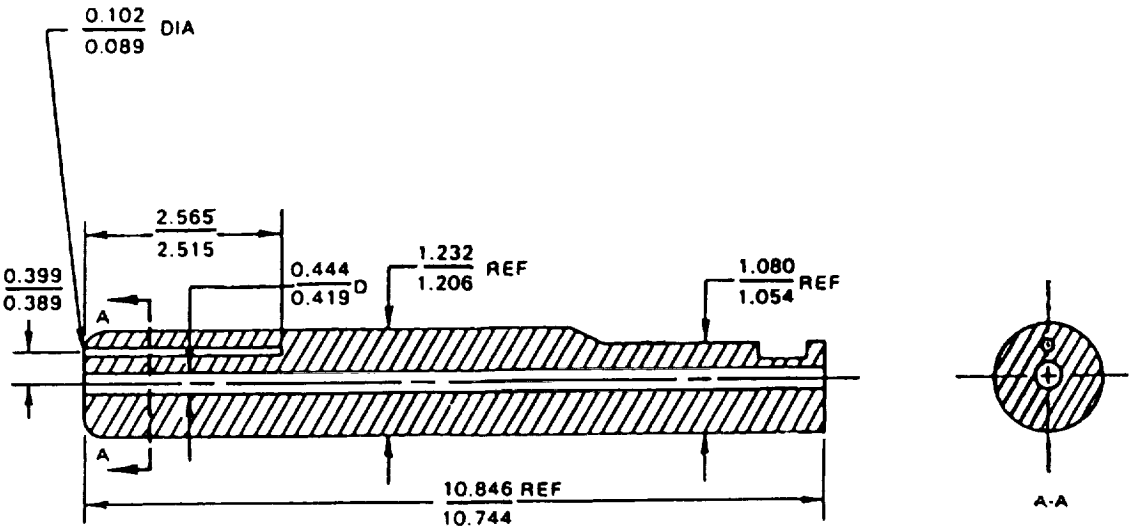

Figure B-1 Diagram of Thermocoupled Specimen Used for Burner Rig Testing. Dimension are expressed in centimeters.

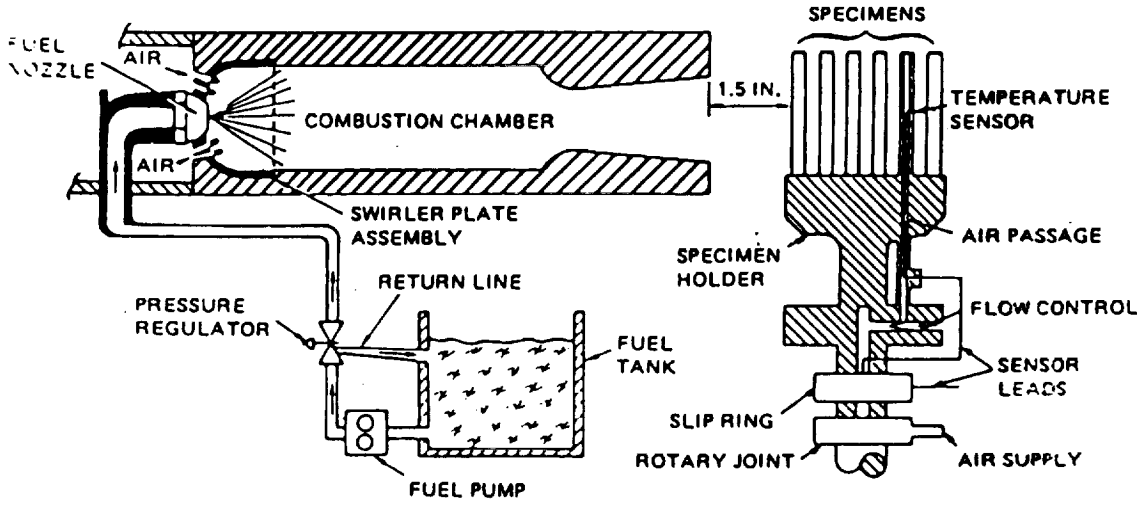

Figure B-2 Schematic Diagram of Cyclic Burner Rig Test Apparatus for Task I

APPENDIX C

CORROSION BURNER RIG TEST DETAILS

A cyclic hot corrosion test was utilized in Task I to aid in defining the capability of the coating system under simulated field service conditions. Specific test conditions were selected to model a mixed oxidation-hot corrosion type of exposure encountered in relatively high temperature aircraft turbine exposure with "clean" fuels and moderate atmospheric contaminants.

Intensive study of hot corrosion phenomena at Pratt & Whitney has shown that the primary contaminants responsible for hot corrosion attack in aircraft turbine engines operating on clean fuels are sea salt from near ground level air (ingested during take-off) and sulfur trioxides from the combustion gases. A comprehensive analysis of hot corrosion mechanisms has shown conclusively that acidification of contaminant salt deposits by sulfur trioxide is critically related to turbine hot corrosion and that meaningful laboratory hot corrosion testing requires that the activity of SO_3 be maintained at levels characteristic of turbine operation. Accordingly, the hot corrosion test rig used in Task I provides for control of both salt contaminant loading and for control of combustion gas composition by effectively limiting excess dilution air.

The test rig used in the hot corrosion exposure evaluation was specifically designed for evaluation of turbine materials in contaminated environmental conditions. The rig is similar to that previously described in Appendix A for oxidation test evaluation in that it maintains full automatic control of test temperature and cooling cycles and features a special rotating specimen mounting fixture with internal specimen cooling air. This fixture provides for simultaneous test of twelve air-cooled specimens. There is also provision for metered injection of contaminants to allow accurate simulation of aircraft turbine environments. Temperature control of the hot corrosion test rig is conducted in the same manner as previously discussed for oxidation test rigs.

The major modification in the hot corrosion test rig is that the cooled specimen cluster is operated inside a burner exhaust gas duct as shown schematically in Figure C-1. This duct exhaust allows specific restriction of ambient air dilution and consequently provides for optimum control of the level of exhaust gas sulfur and air contaminants.

The hot corrosion test conditions used in Task I simulate typical hot corrosion conditions encountered in near ground aircraft engine operation. Selection of the 899°C (1650°F) ceramic surface temperature were based on conditions that exist where major salt loading from atmosphere contamination occurs. The test cycle was the same as that used for cyclic oxidation testing, i.e., 57 minutes in the flame and three minutes for air cooling.

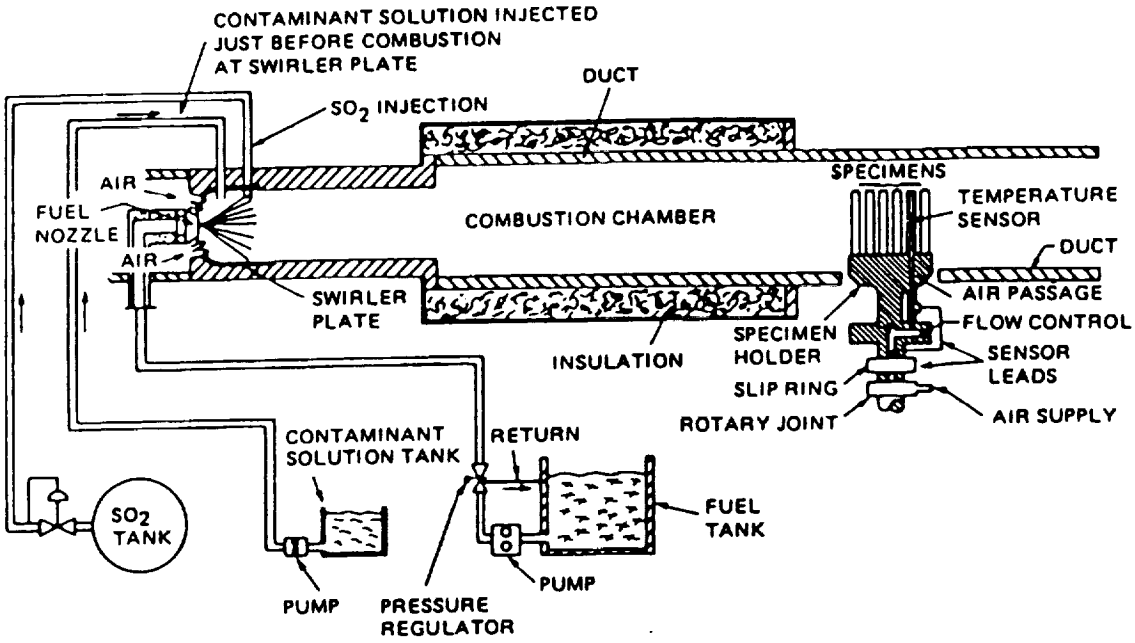

Figure C-1 Schematic Diagram of Ducted Burner Rig Test Apparatus for Task I Hot Corrosion Exposure. Test specimens are enclosed to allow precise control of SO_3 and other contaminants.

APPENDIX D

EXPERIMENTAL PROCEDURES USED TO MEASURE PHYSICAL PROPERTIES

Thermal Conductivity - A comparative method was used to determine thermal conductivity. The sample was instrumented with thermocouples and placed between two instrumented reference standards of identical geometry to the sample. The composite stack was fitted between an upper heater and lower heater and the complete system placed on a liquid cooled heat sink. A load was applied to the top of the system and a thermal guard which could be heated or cooled was placed around the system.

A temperature gradient was established in the stack; radial heat loss was minimized by establishing a similar gradient in the guard tube. The system reached equilibrium after which successive readings of temperatures at various points were averaged and evaluated. From this data, heat flux was determined and specimen thermal conductivity calculated. The results are shown in the text Tables XIX, XXII for the bulk ceramic and metallic specimens respectively.

Specific Heat - The specific heat was determined using a high temperature calibrated copper drop calorimeter. The sample was attached to a 3mm platinum support wire and suspended vertically at the center of a three-zone controlled temperature furnace with the sample resting upon the receiver below it. Thermocouples were attached such that junctions touched the sample near the top and bottom.

The sample was allowed to attain a selected equilibrium temperature for a period of time on the order of 1-2 hours then regular readings of the thermocouple were taken. At a given time, the radiation shields moved to allow the sample to fall and come to rest in the receiver. When the sample came to rest, these shields returned to the original position to reduce any radiation heat transfer from the furnace to the receiver or convective and radiant heat transfer from the receiver to the outside. The temperature of the copper receiver was taken regularly. Following a drop the receiver system was allowed to come to equilibrium for the order of two hours. The specific heat was calculated at selected temperature by differentiation and substitution and is shown in the text Tables XX and XXIII for the bulk ceramic and metallic specimens.

Thermal Expansion - The room temperature length of each specimen was measured before the test. The specimen was then placed in an electronic automatic recording dilatometer and a thermocouple placed in contact with the center of the sample. An environmental chamber which controlled the temperature at constant rates surrounded the system. The dilatometer was allowed to run with length and the temperature recorded continuously and autographically. The results for the bulk ceramic and metallic specimens tested are given in the text Tables XXI and XXIV respectively.

APPENDIX E

STRESS-STRAIN AND CREEP CURVES FOR ALL MECHANICAL PROPERTY TESTS CONDUCTED AT SOUTHWEST RESEARCH INSTITUTE

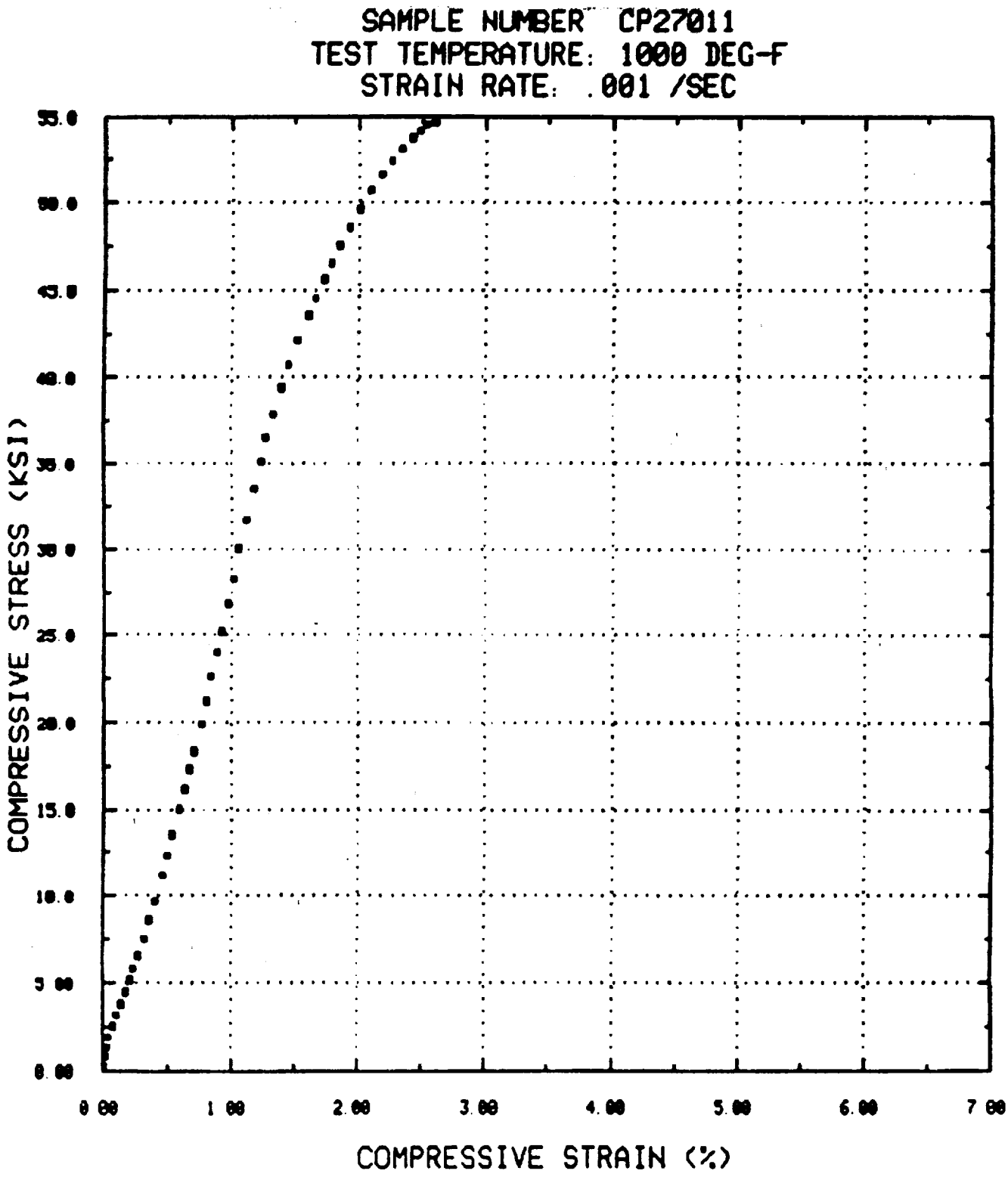

Figure E-1 Compression Stress-Strain (1000°F)

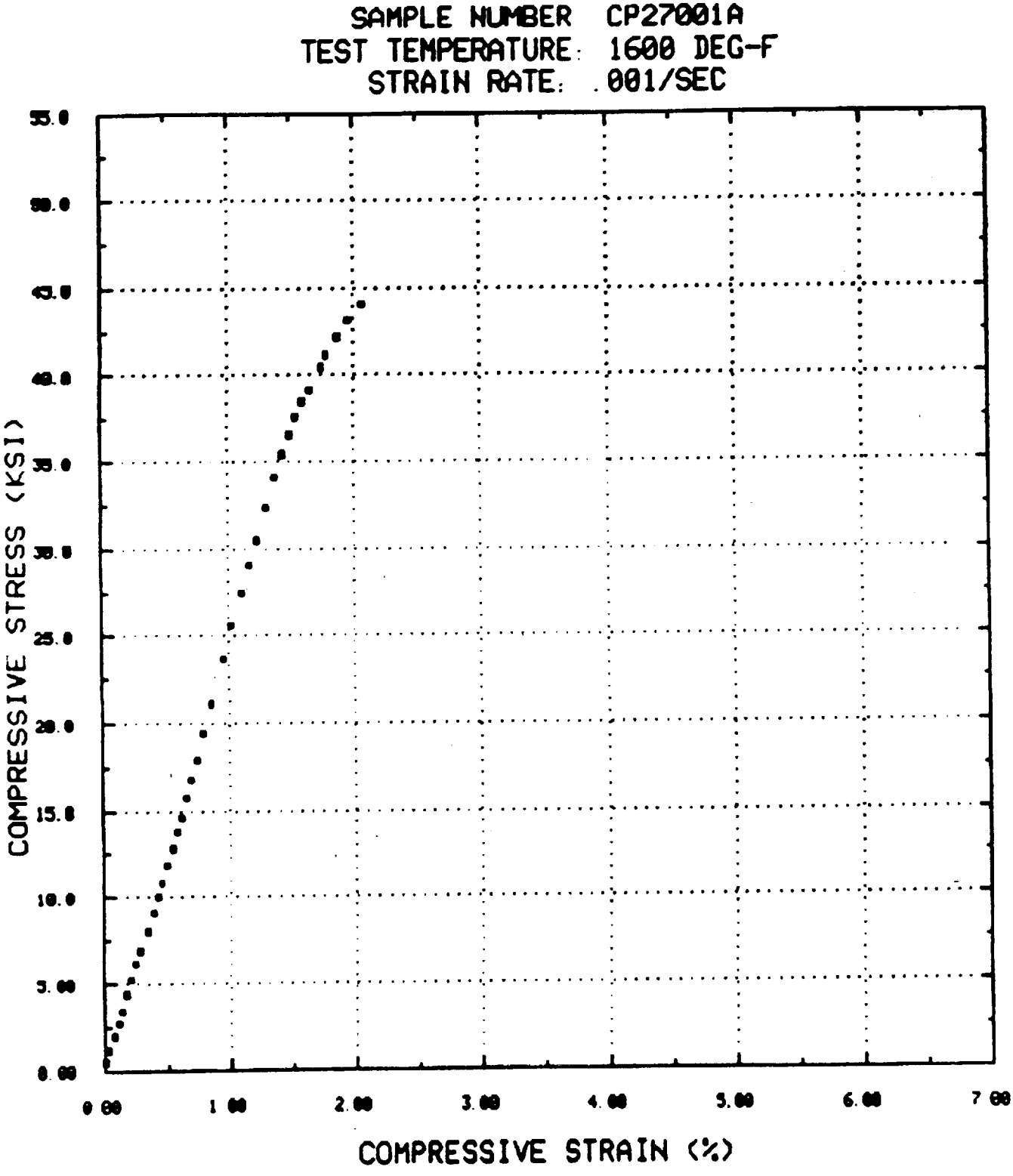

Figure E-2 Compression Stress-Strain (1600°F)

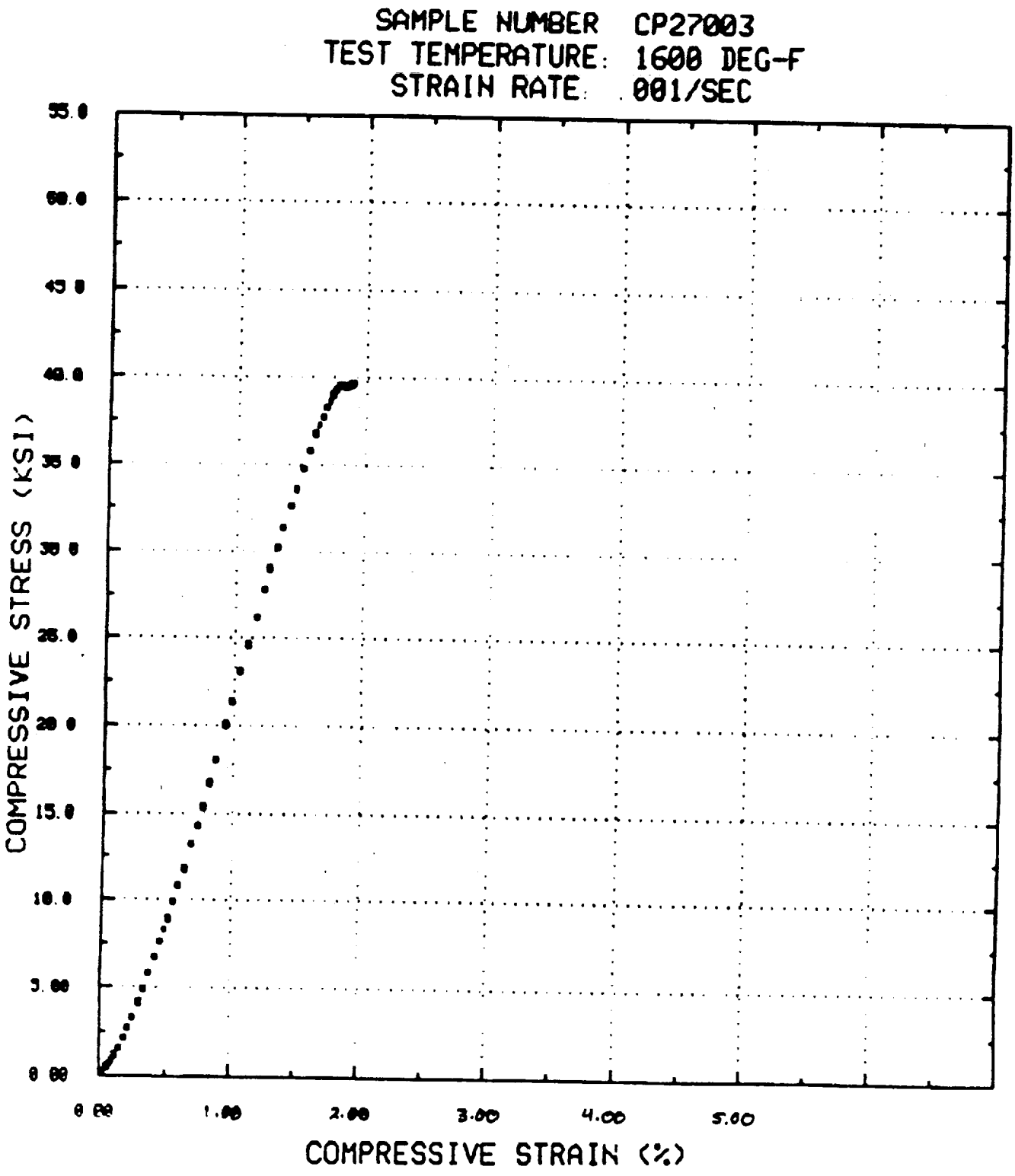

Figure E-3 Compression Stress-Strain (1600°F)

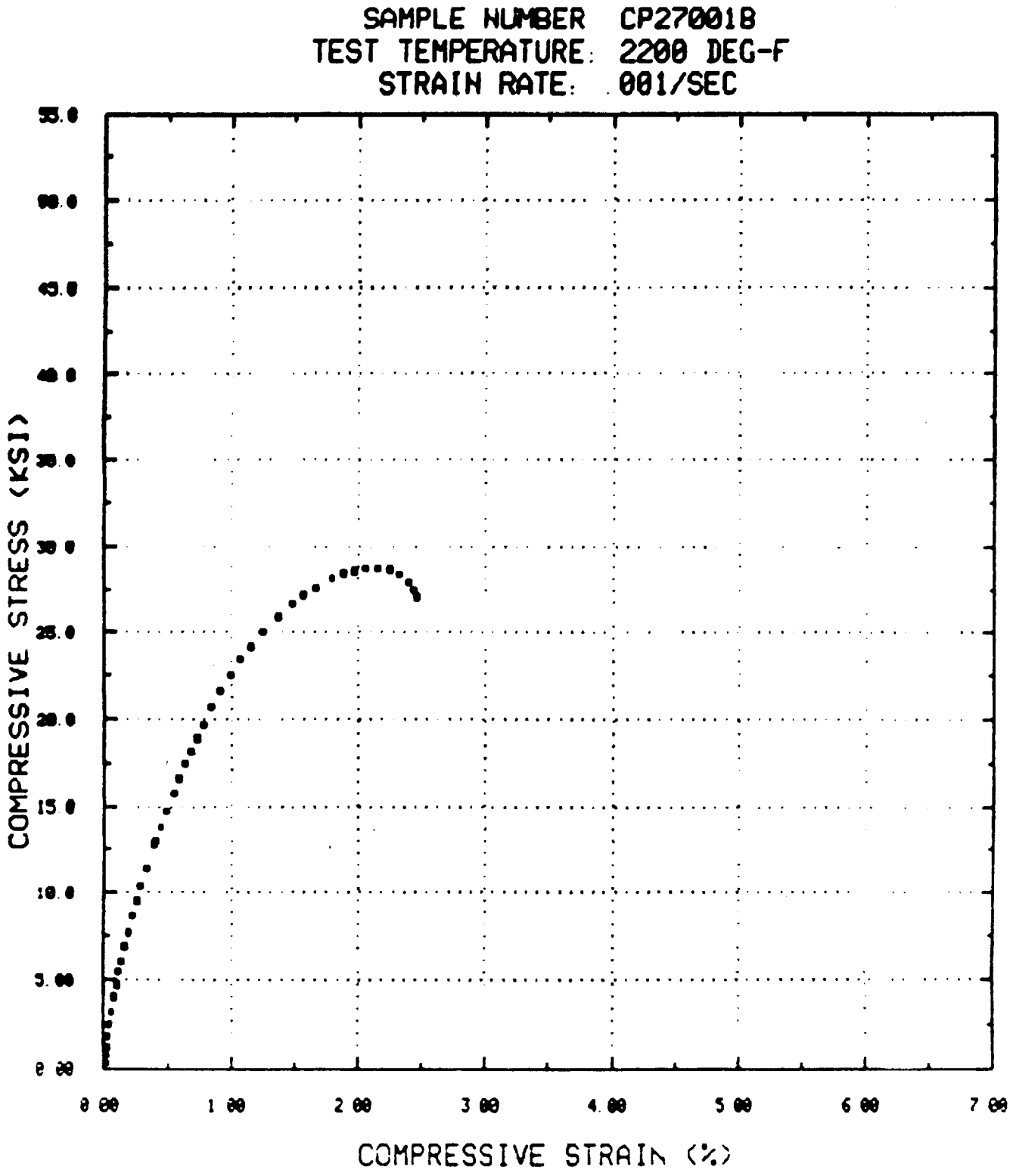

Figure E-4 Compression Stress-Strain (2200°F)

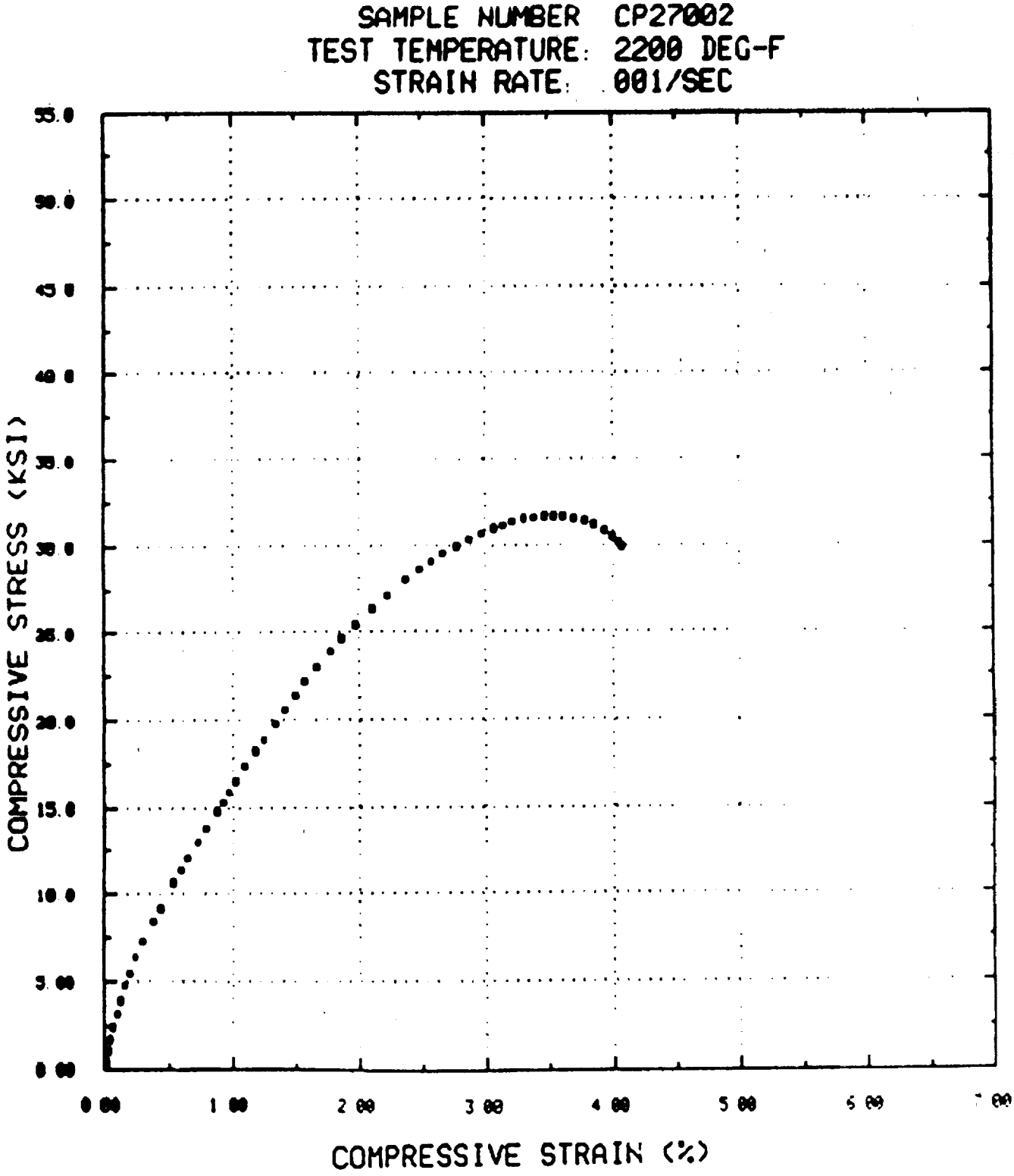

Figure E-5 Compression Stress-Strain (2200°F)

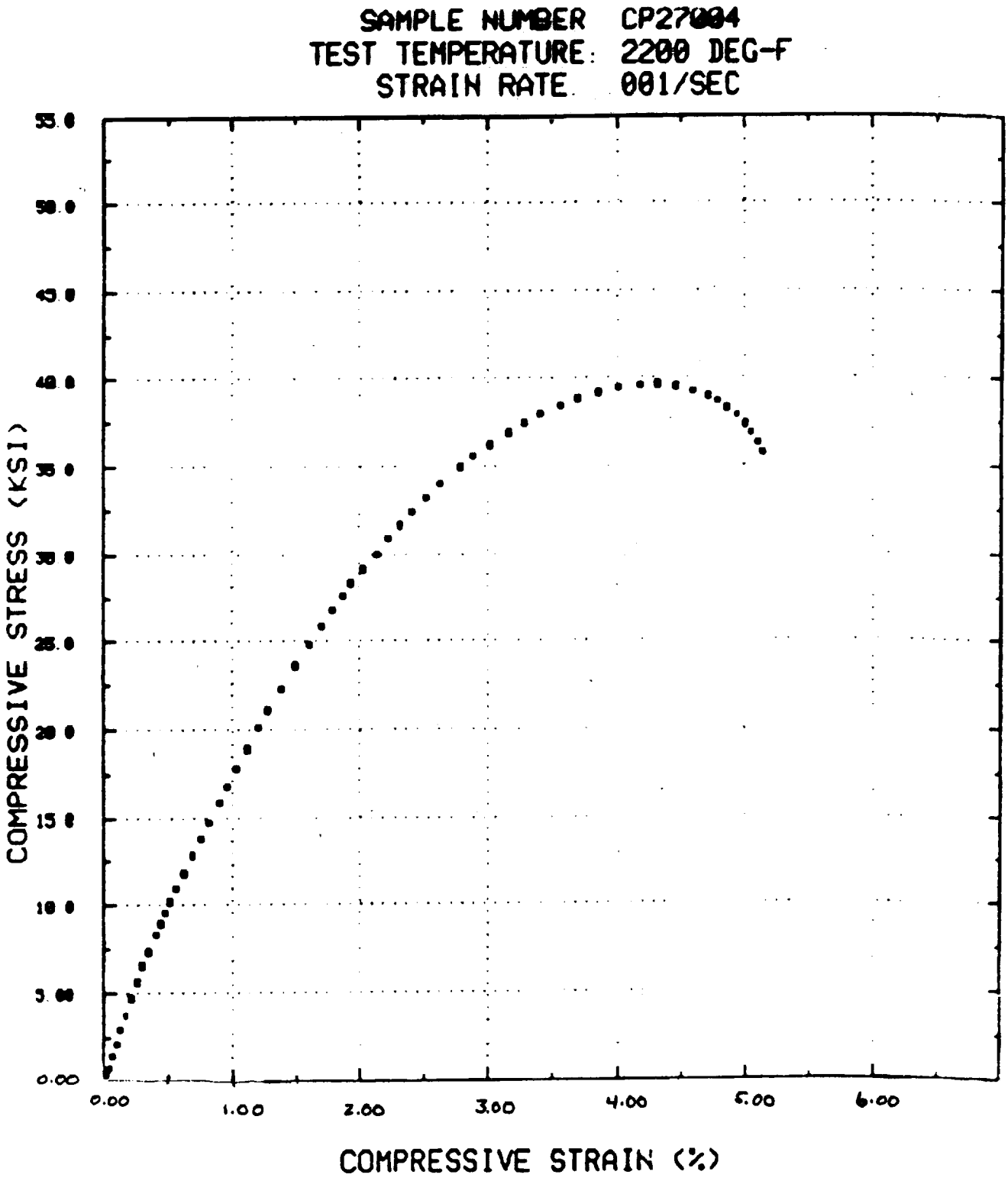

Figure E-6 Compression Stress-Strain (2200°F)

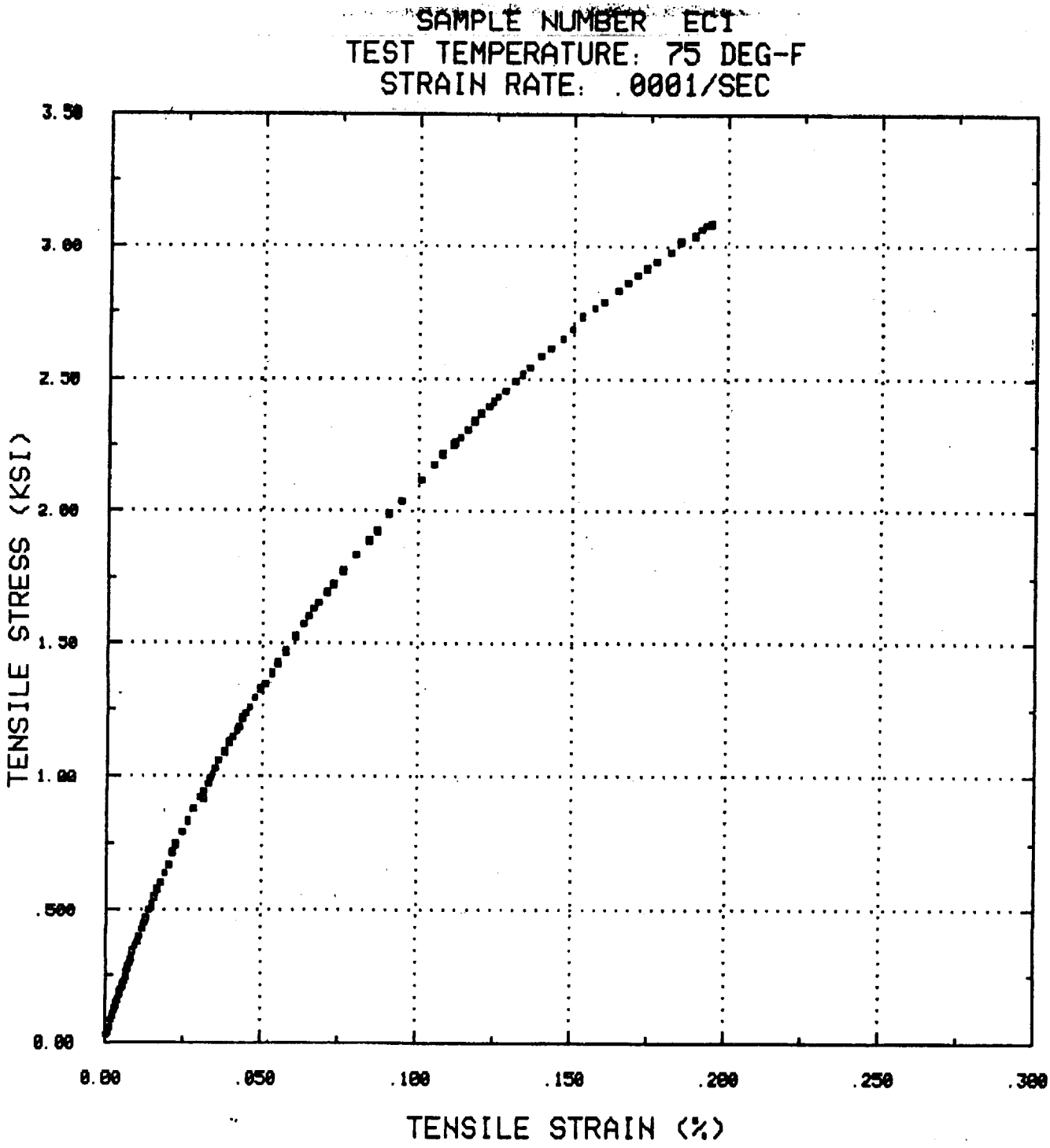

Figure E-7 Tension Stress-Strain (75°F)

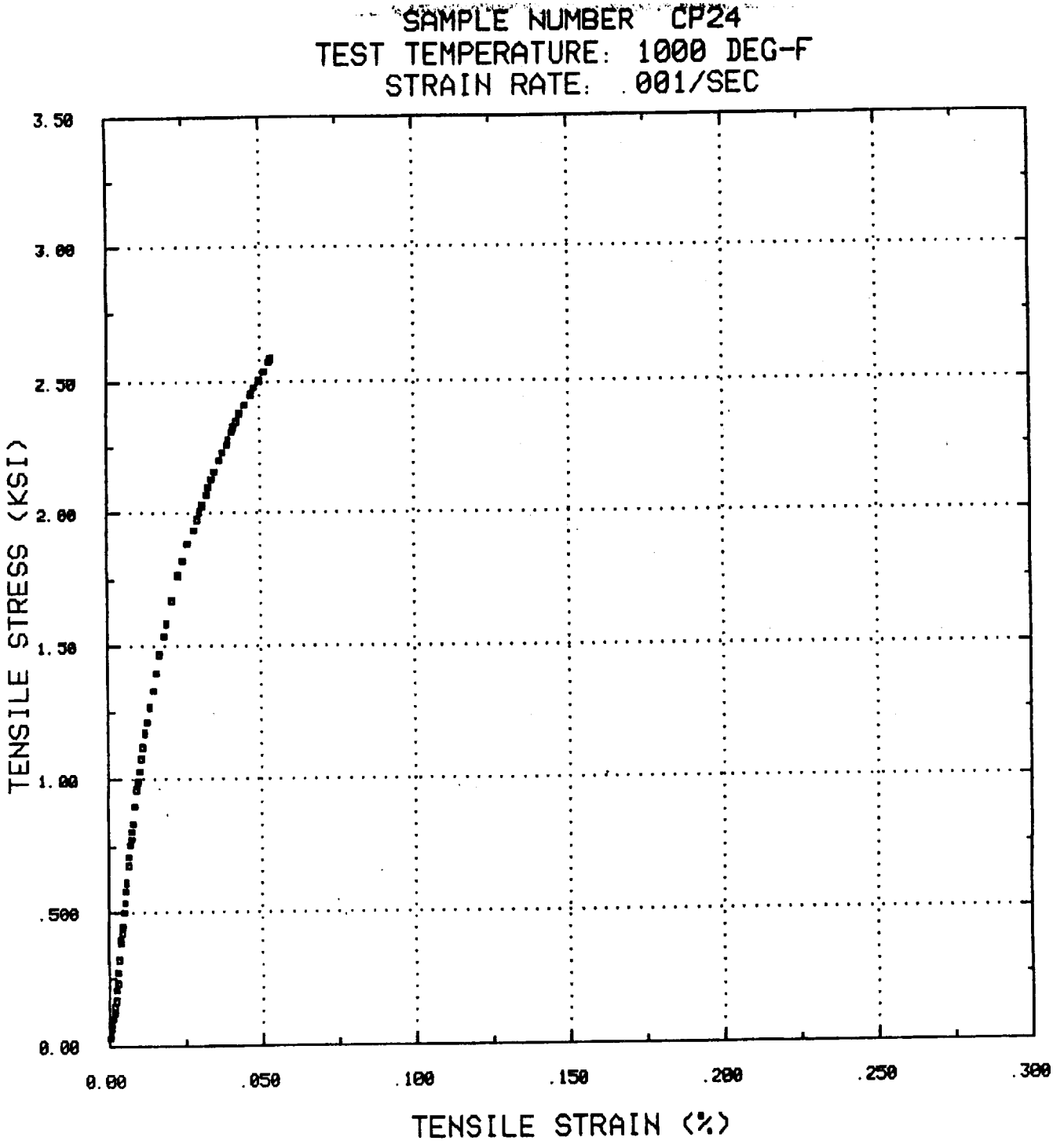

Figure E-8 Tension Stress-Strain (1000°F)

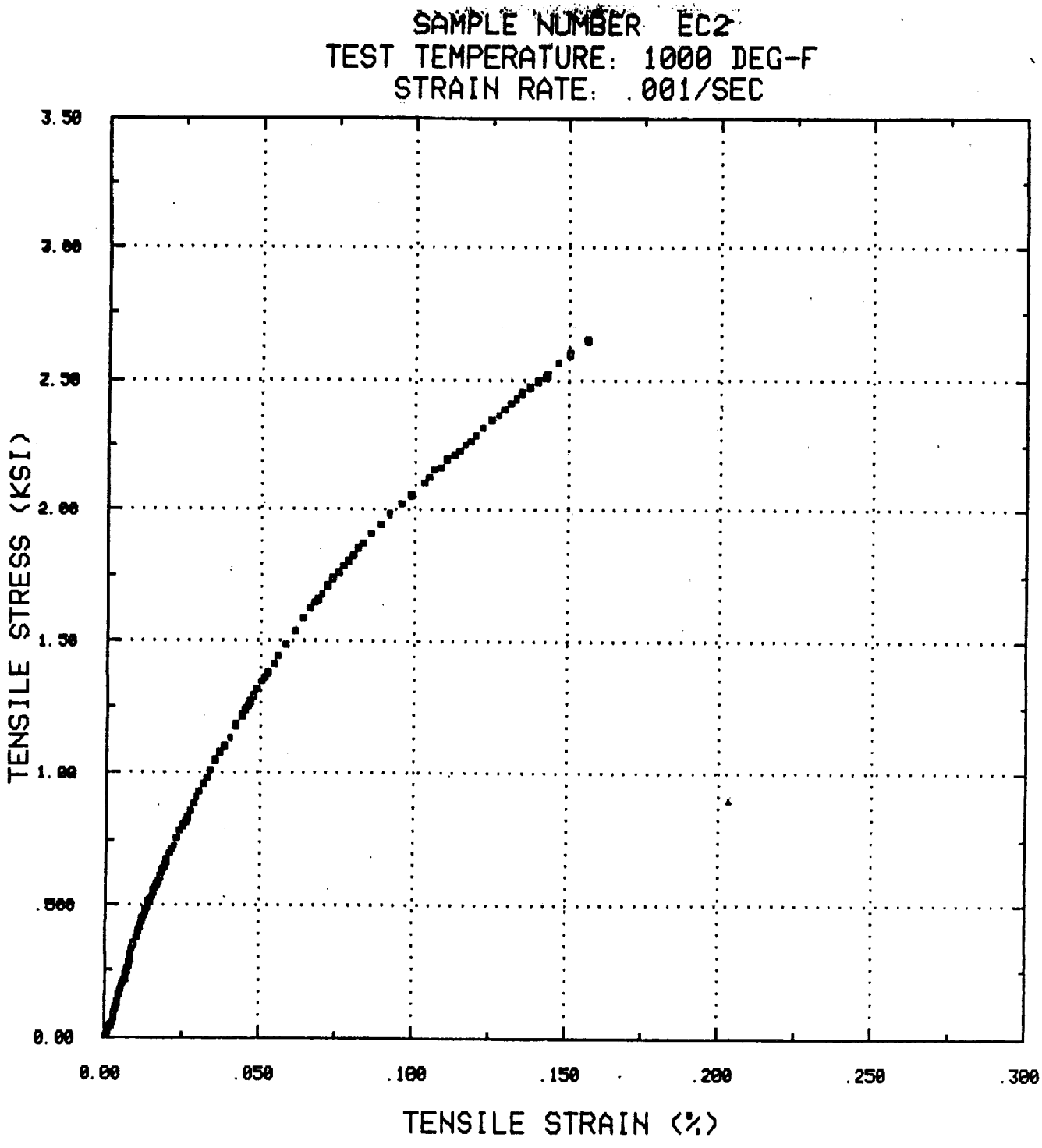

Figure E-9 Tension Stress-Strain (1000°F)

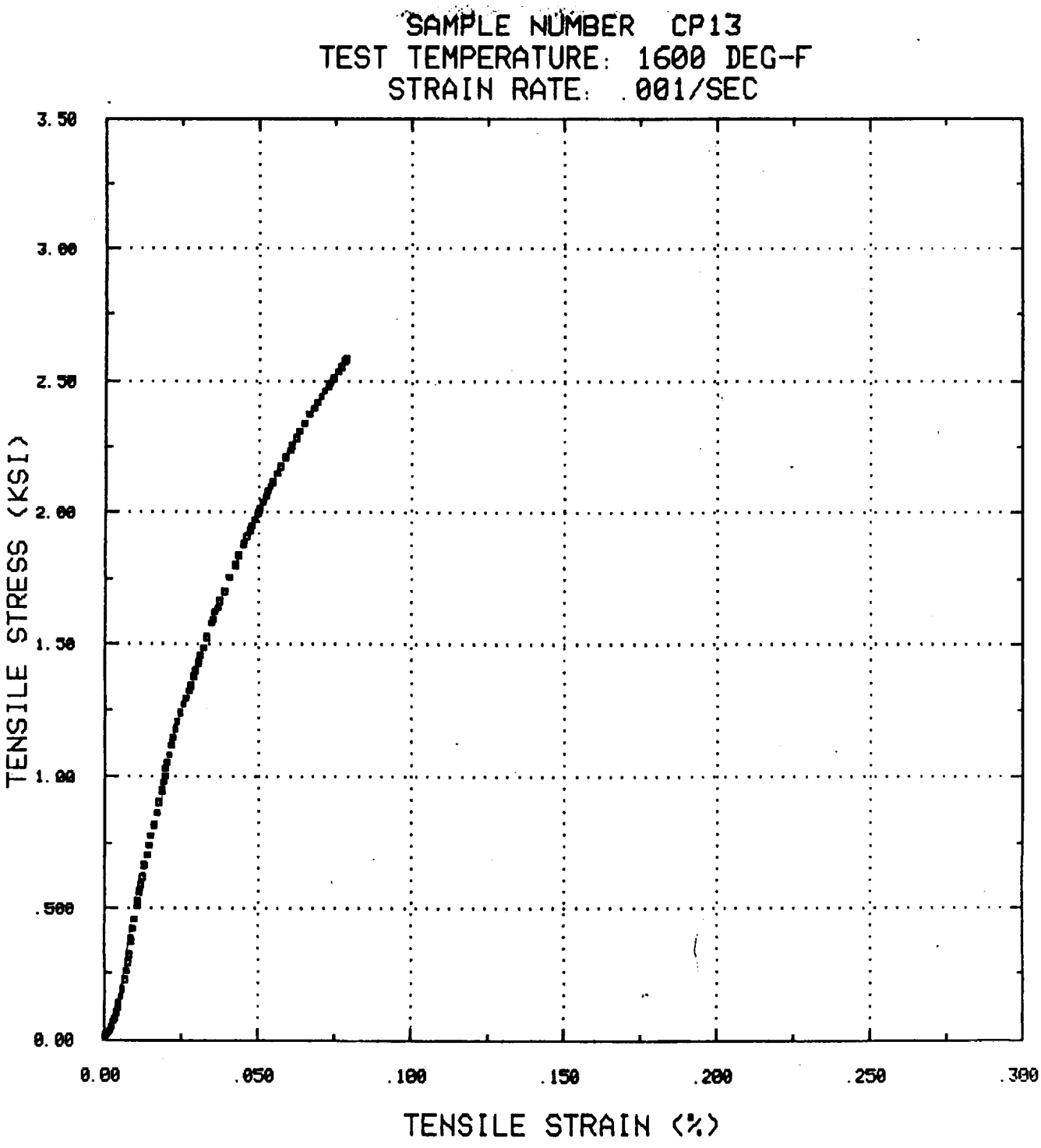

Figure E-10 Tension Stress-Strain (1600°F)

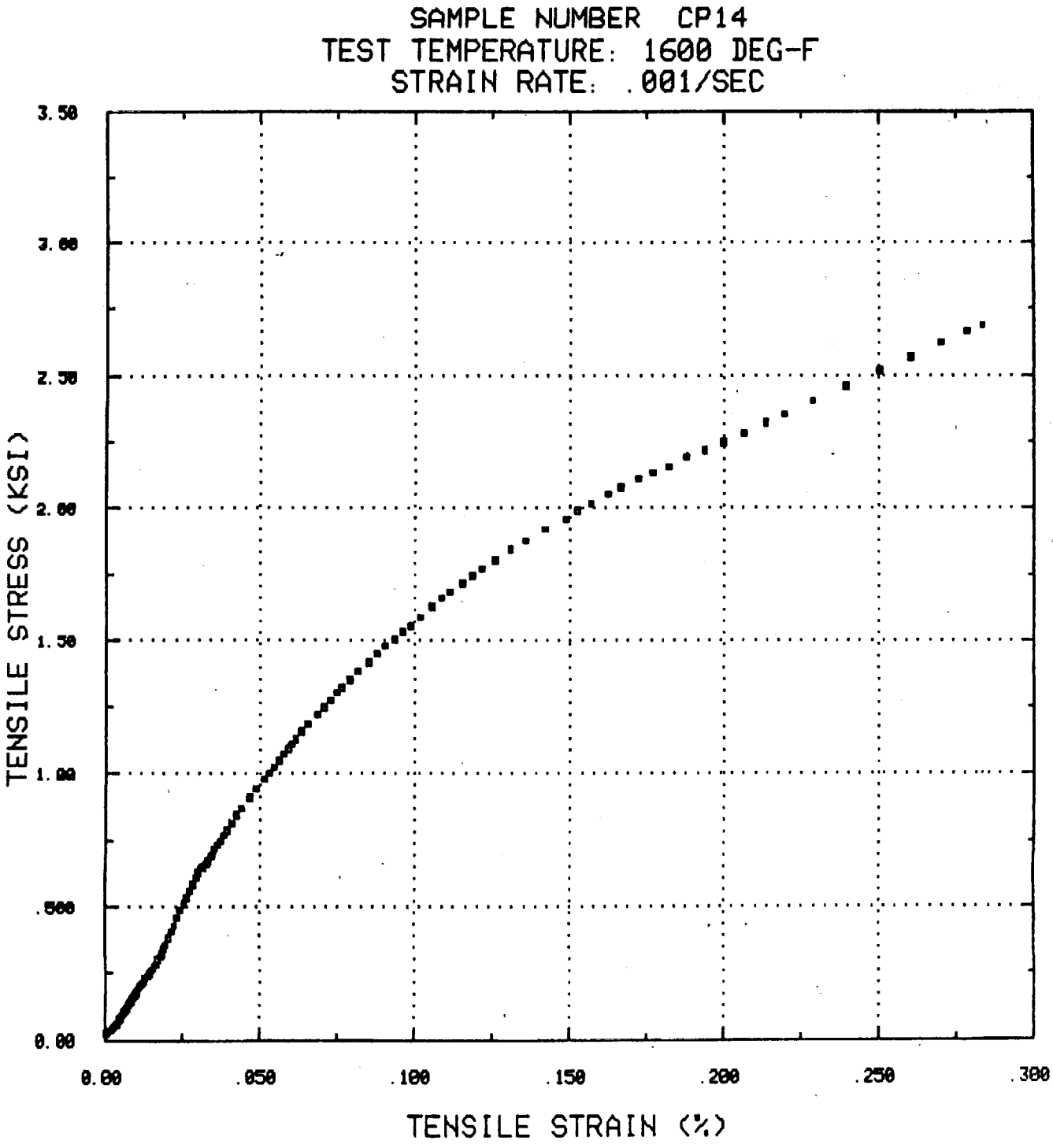

Figure E-11 Tension Stress-Strain (1600°F)

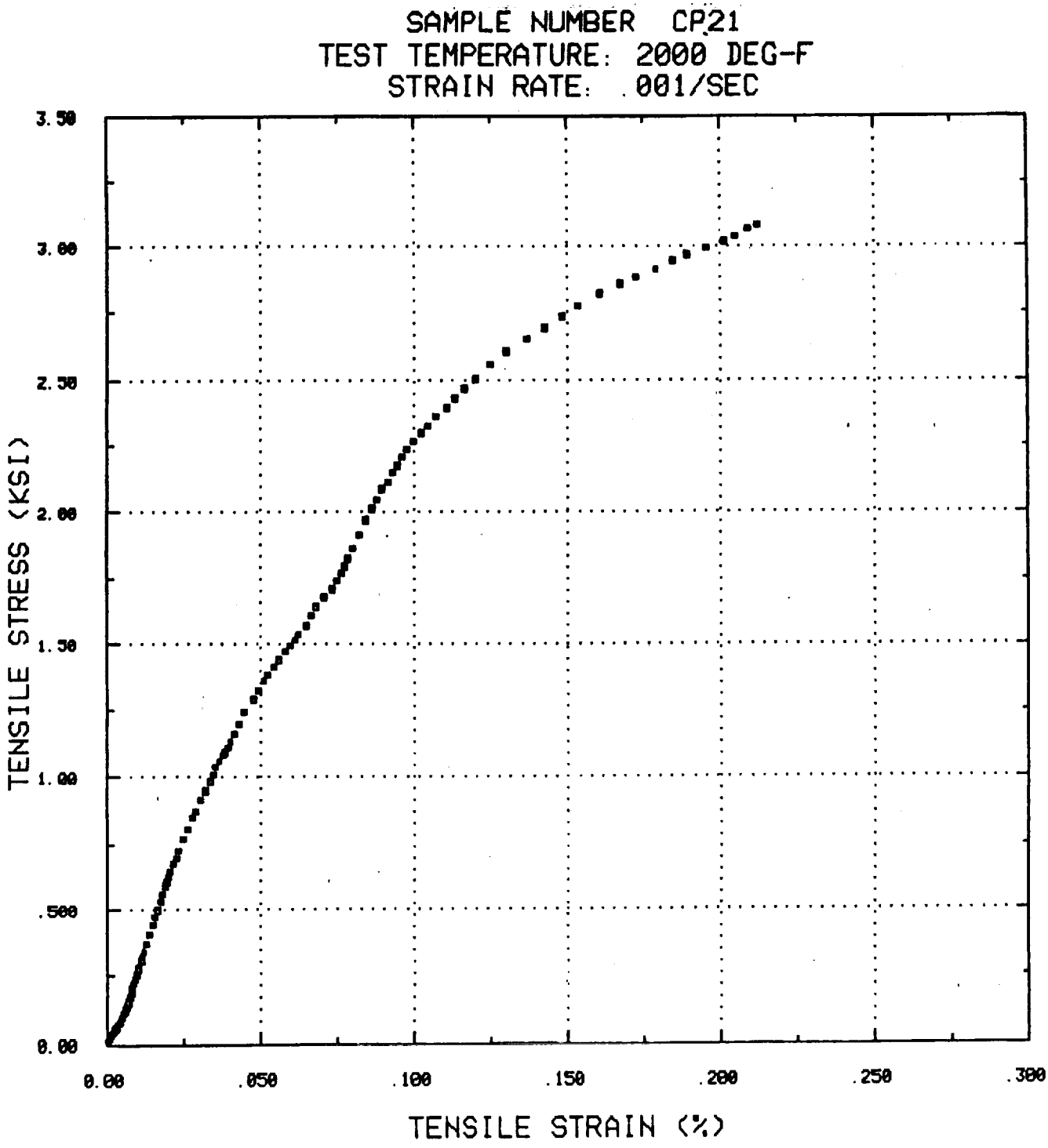

Figure E-12 Tension Stress-Strain (2000°F)

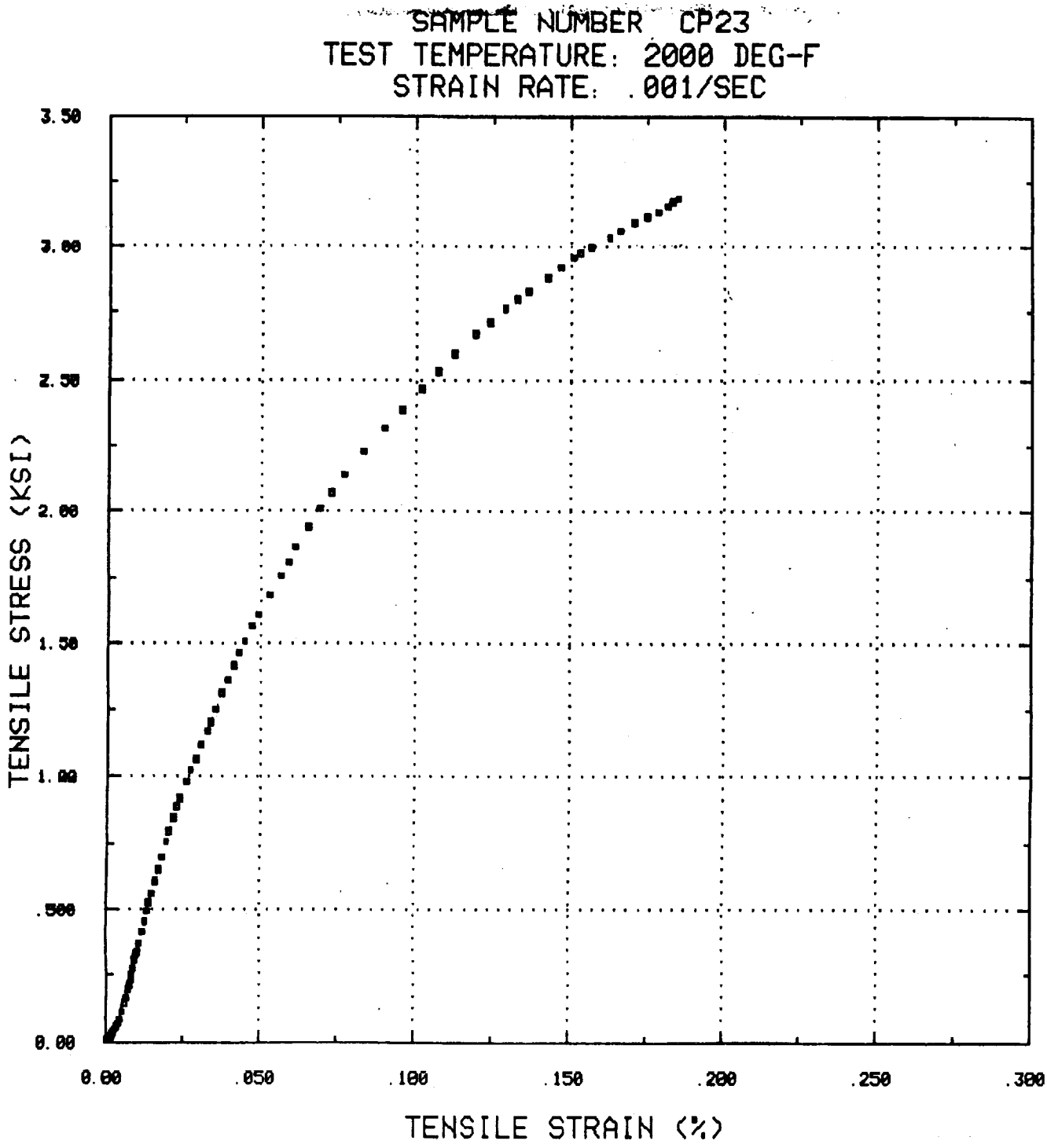

Figure E-13 Tension Stress-Strain (2000°F)

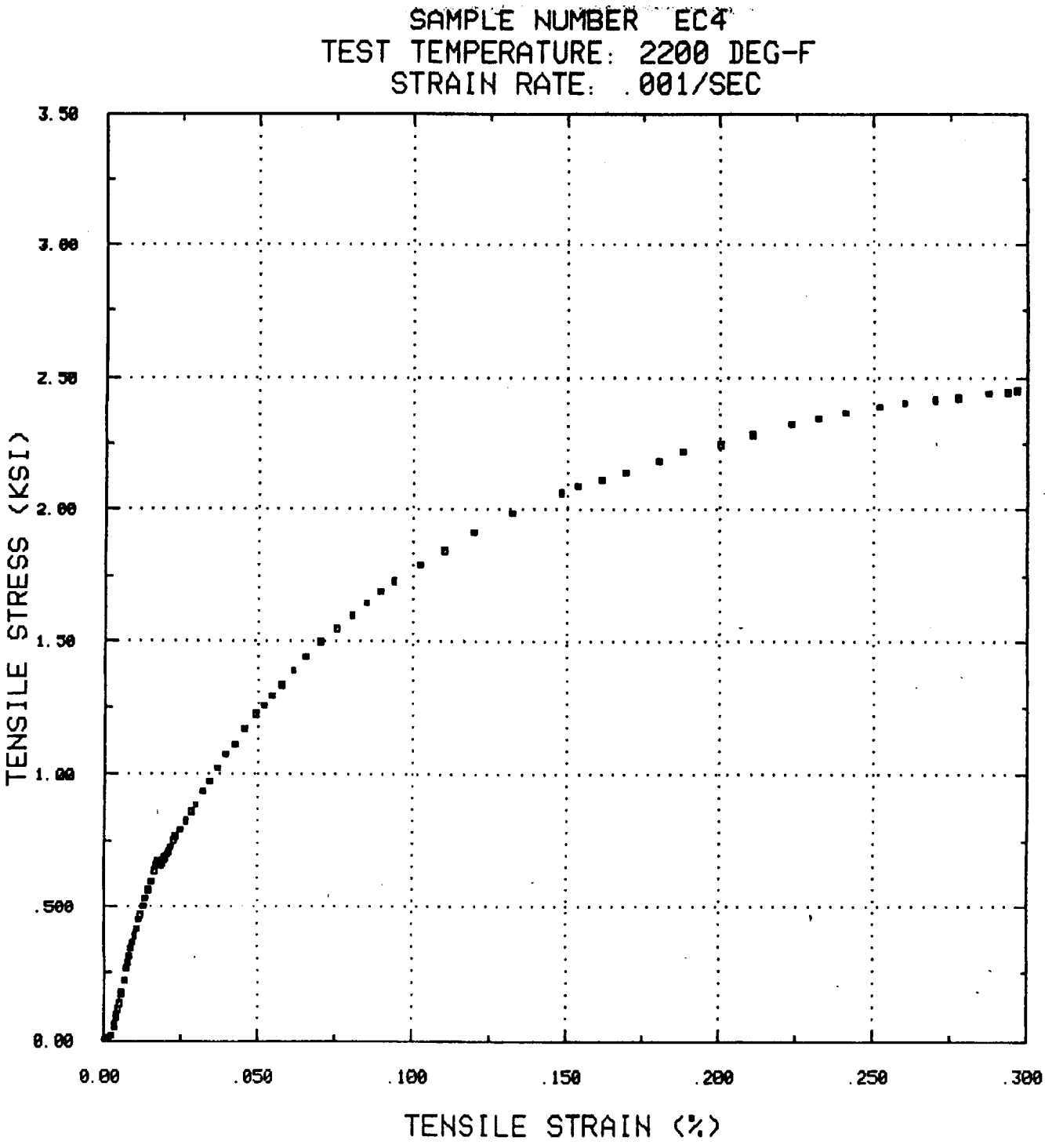

Figure E-14 Tension Stress-Strain (2200°F)

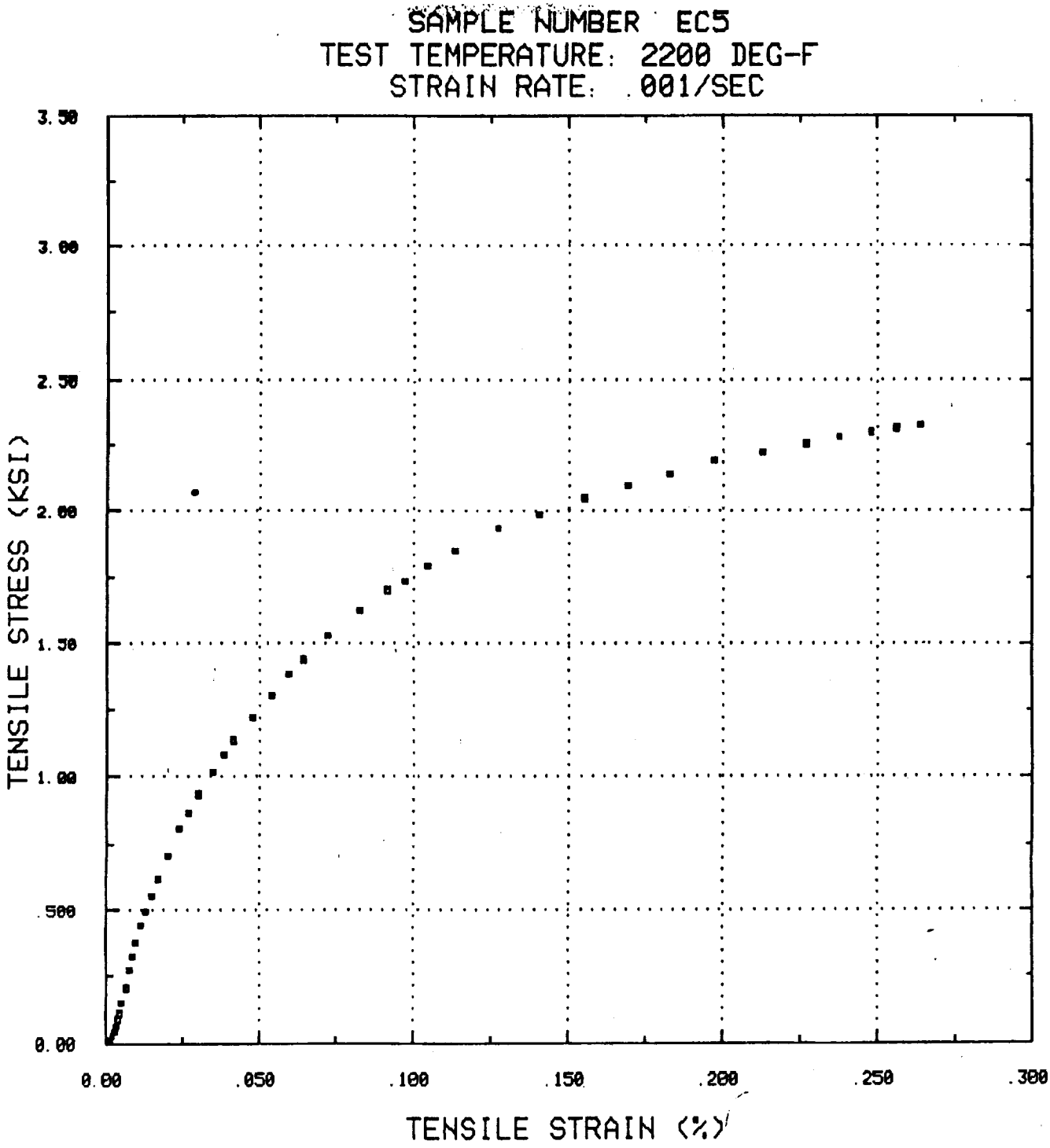

Figure E-15 Tension Stress-Strain (2200°F)

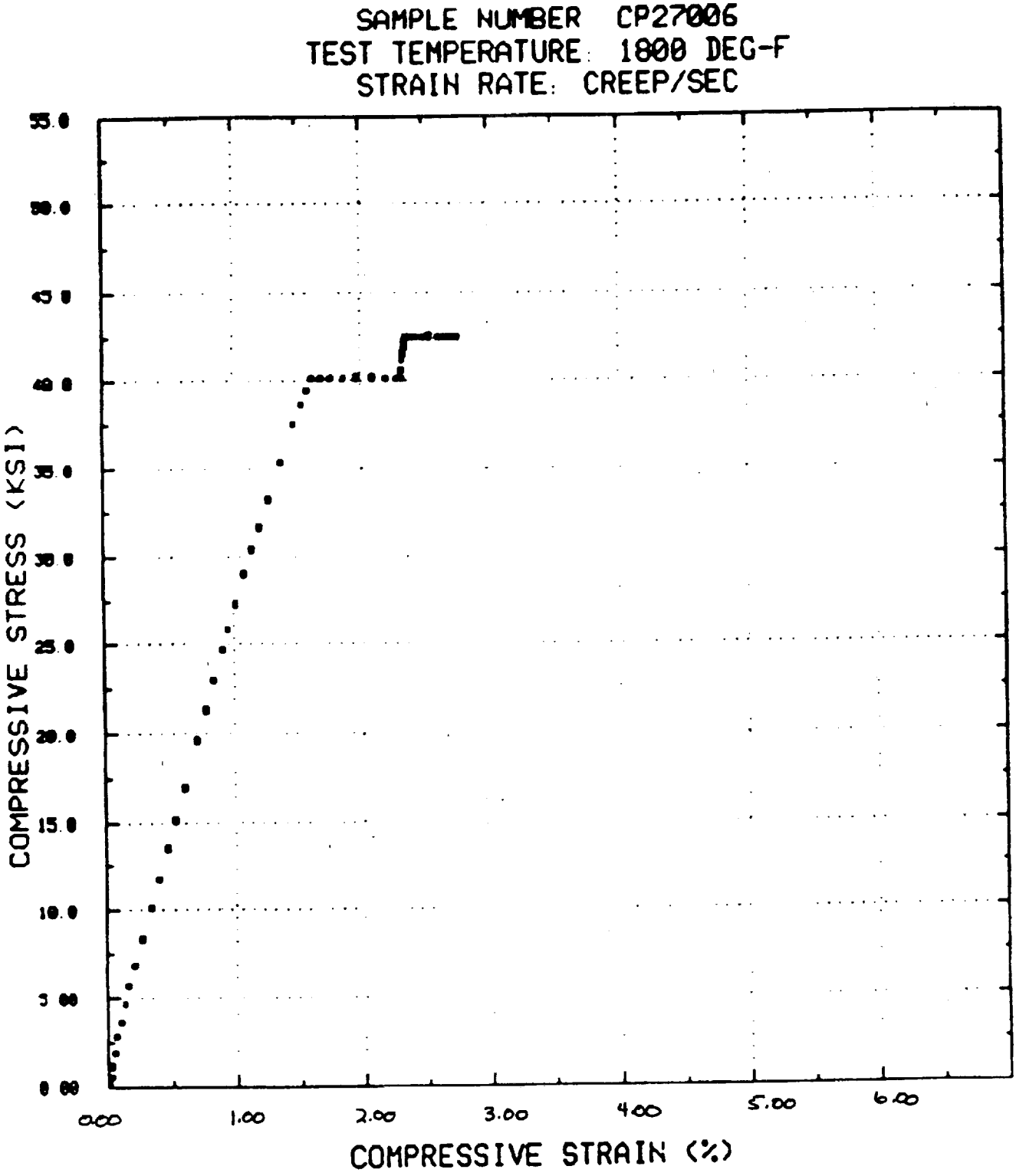

Figure E-16 Compression Creep Stress-Strain (1800°F)

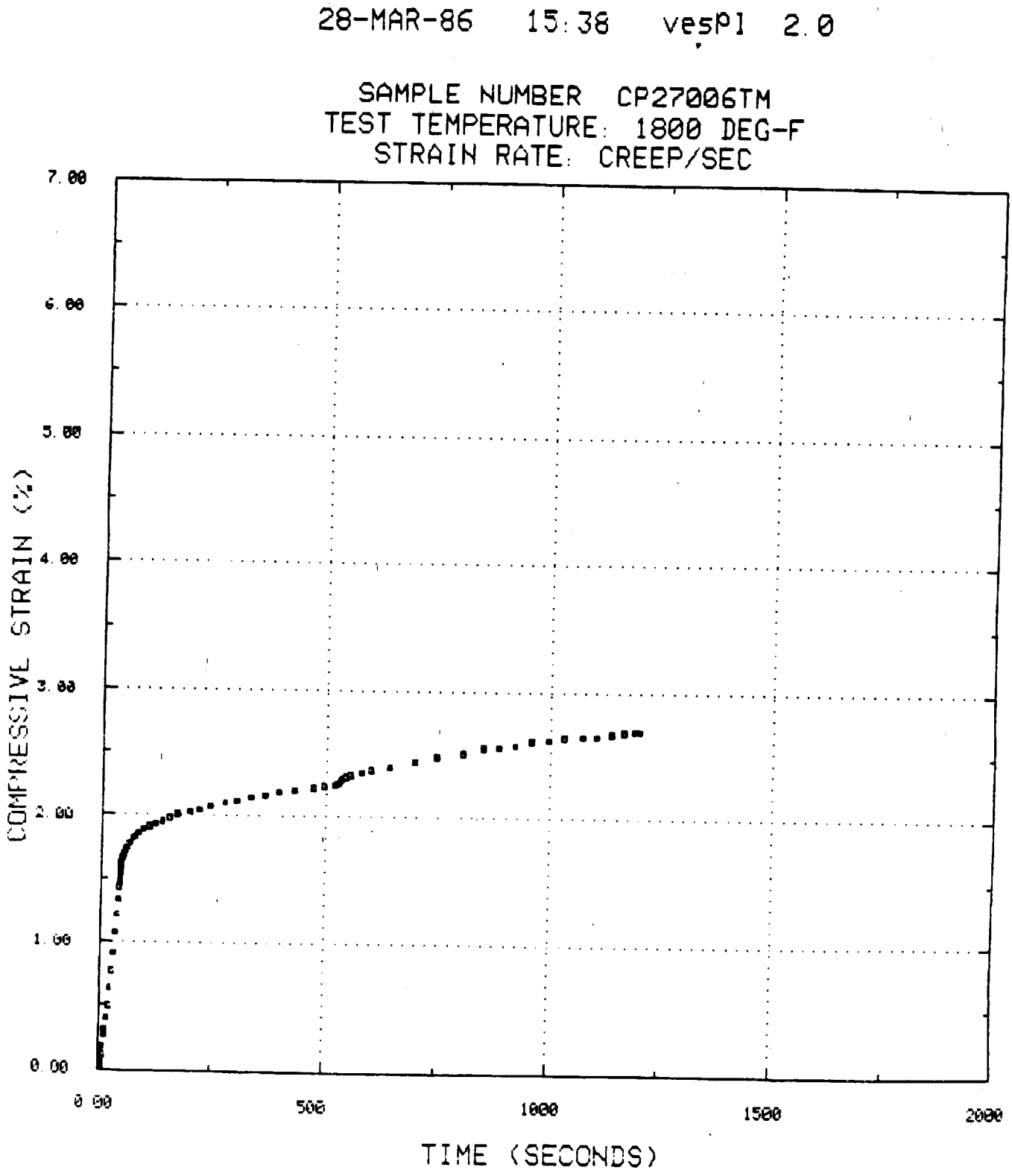

Figure E-17 Compression Creep Strain-Time (1800°F)

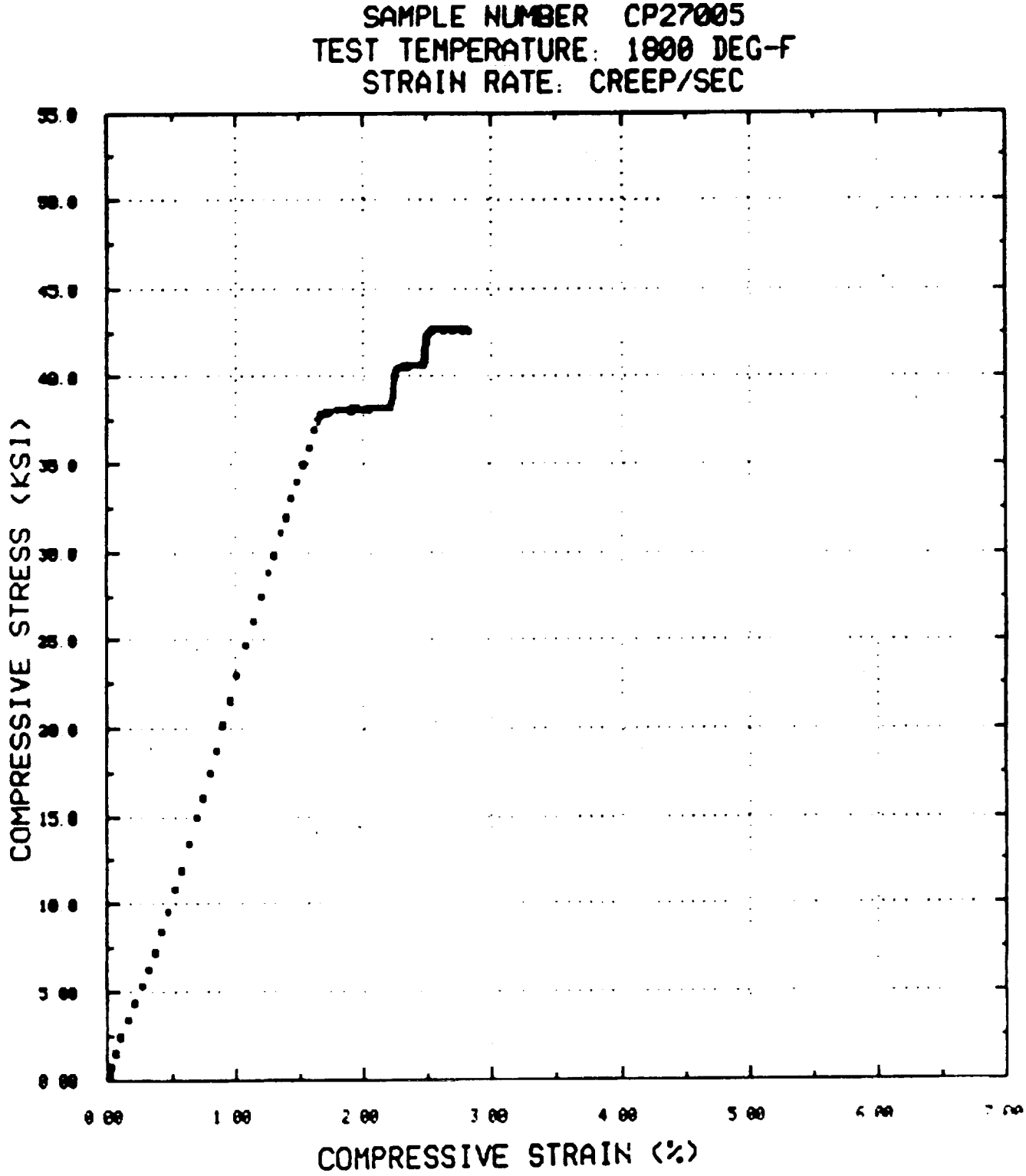

Figure E-18 Compression Creep Stress-Strain (1800°F)

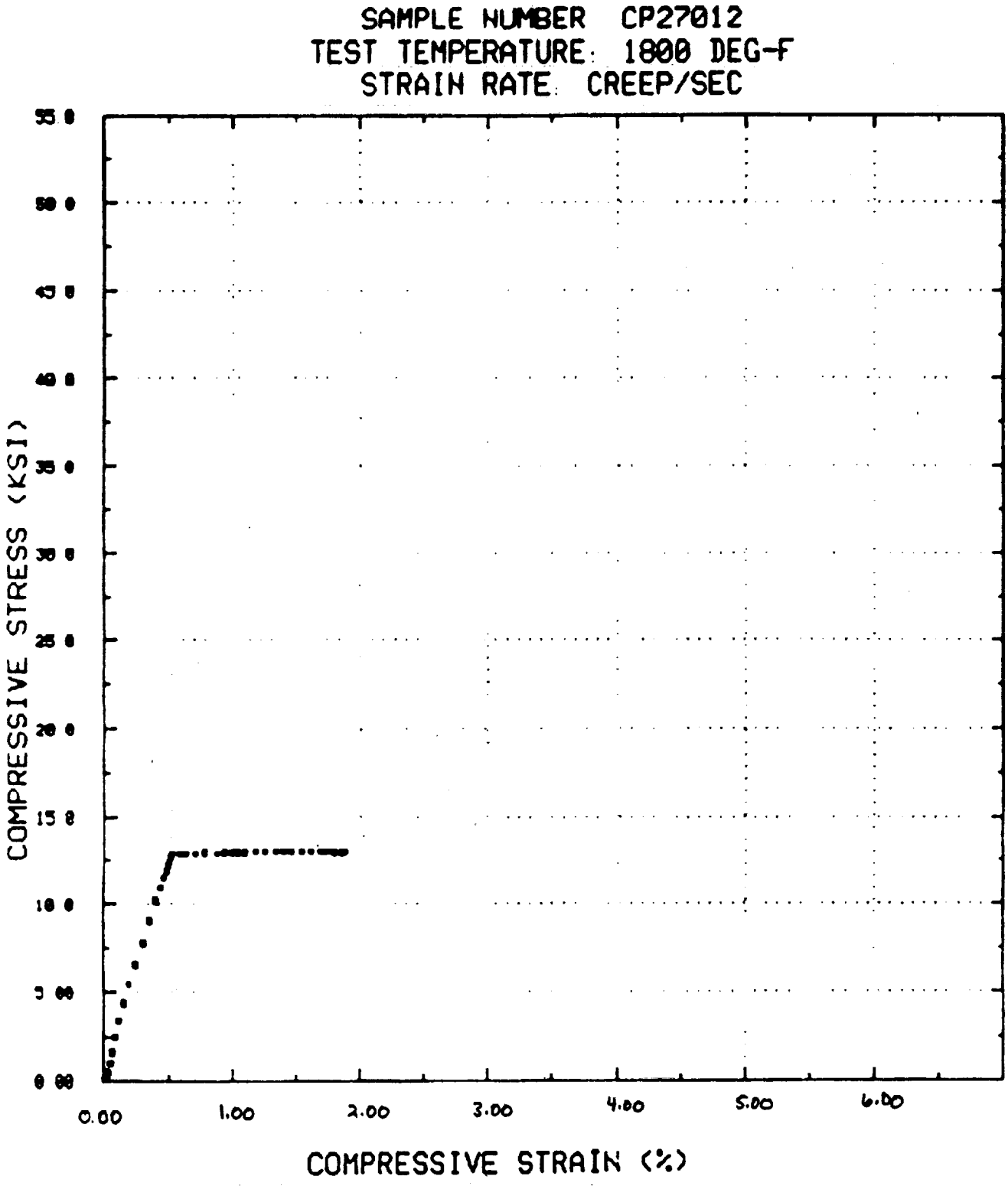

Figure E-19 Compression Creep Stress-Strain (1800°F)

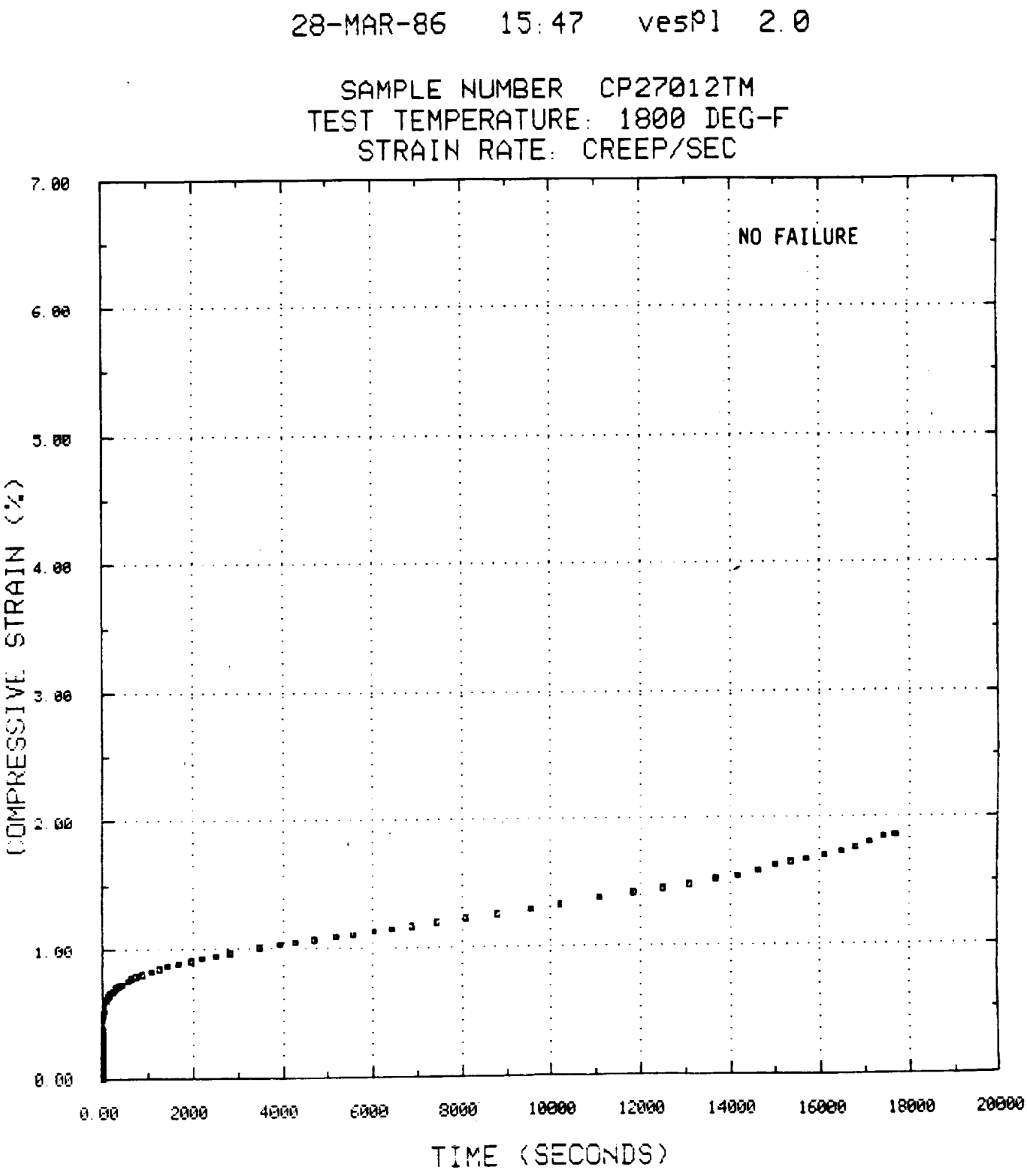

Figure E-20 Compression Creep Strain-Time (1800°F)

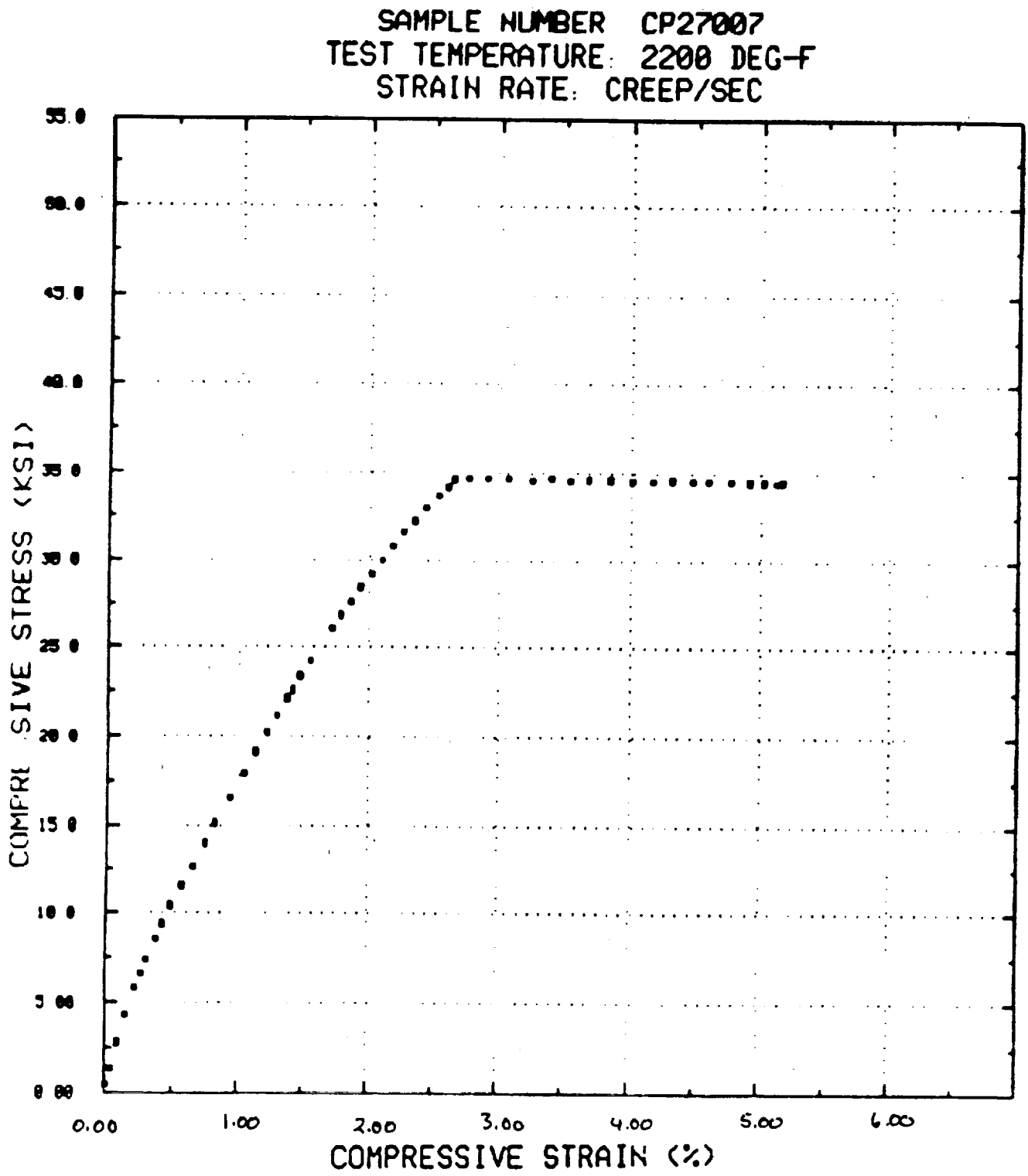

Figure E-21 Compression Creep Stress-Strain (2200°F)

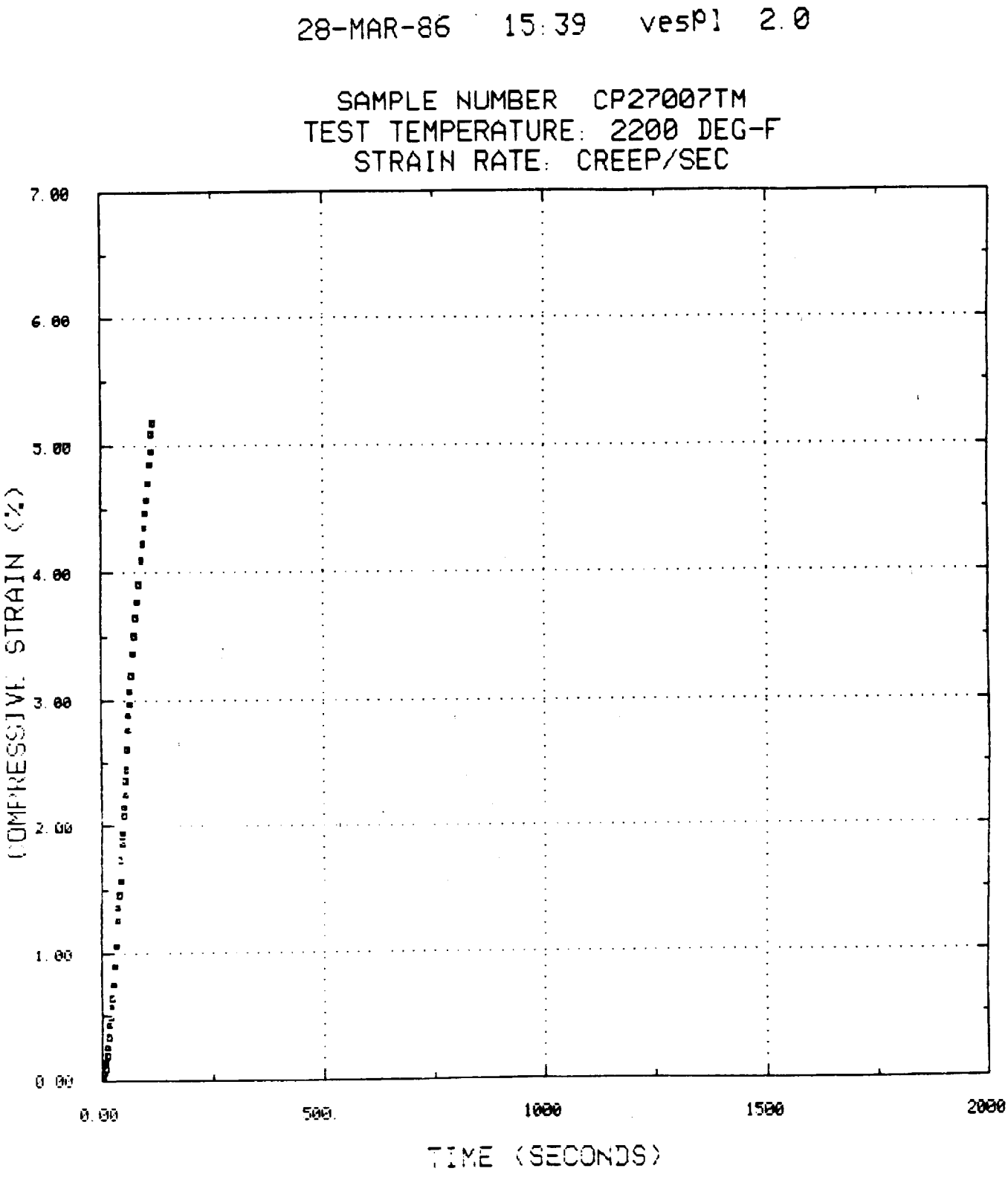

Figure E-22a Compression Creep Strain-Time (2200°F)

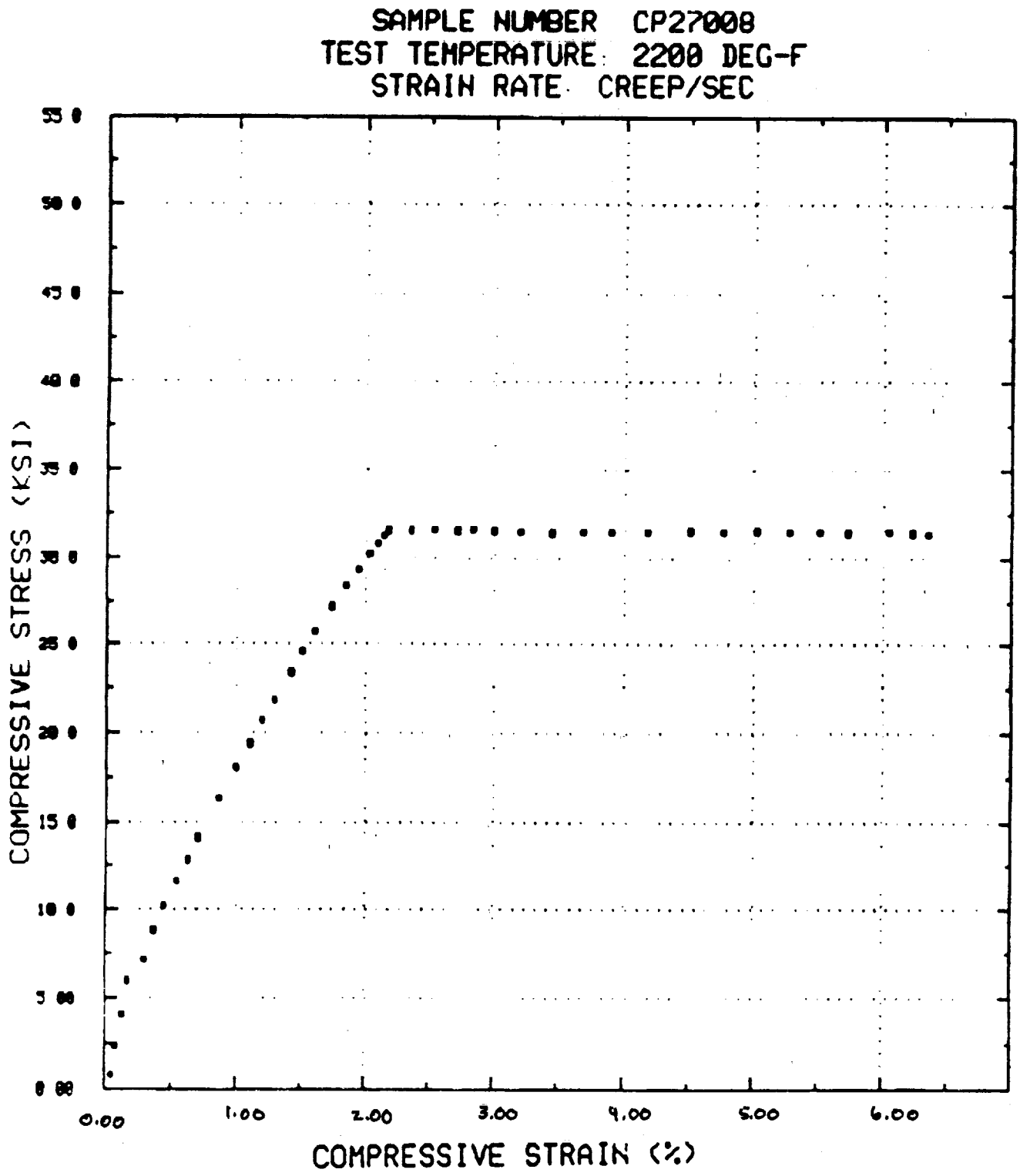

Figure E-22b Compression Creep Stress-Strain (2200°F)

C-3

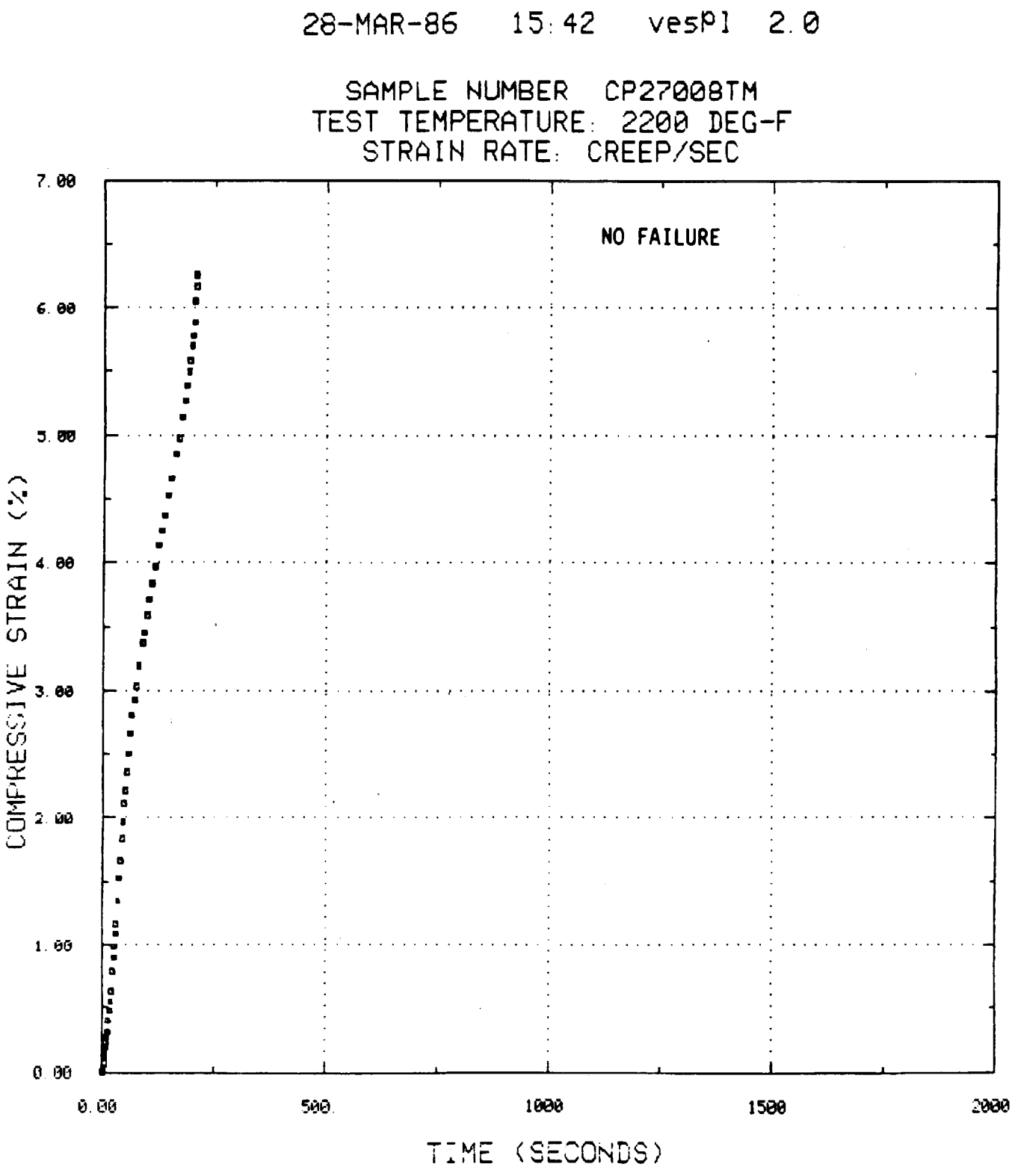

Figure E-23 Compression Creep Strain-Time (2200°F)

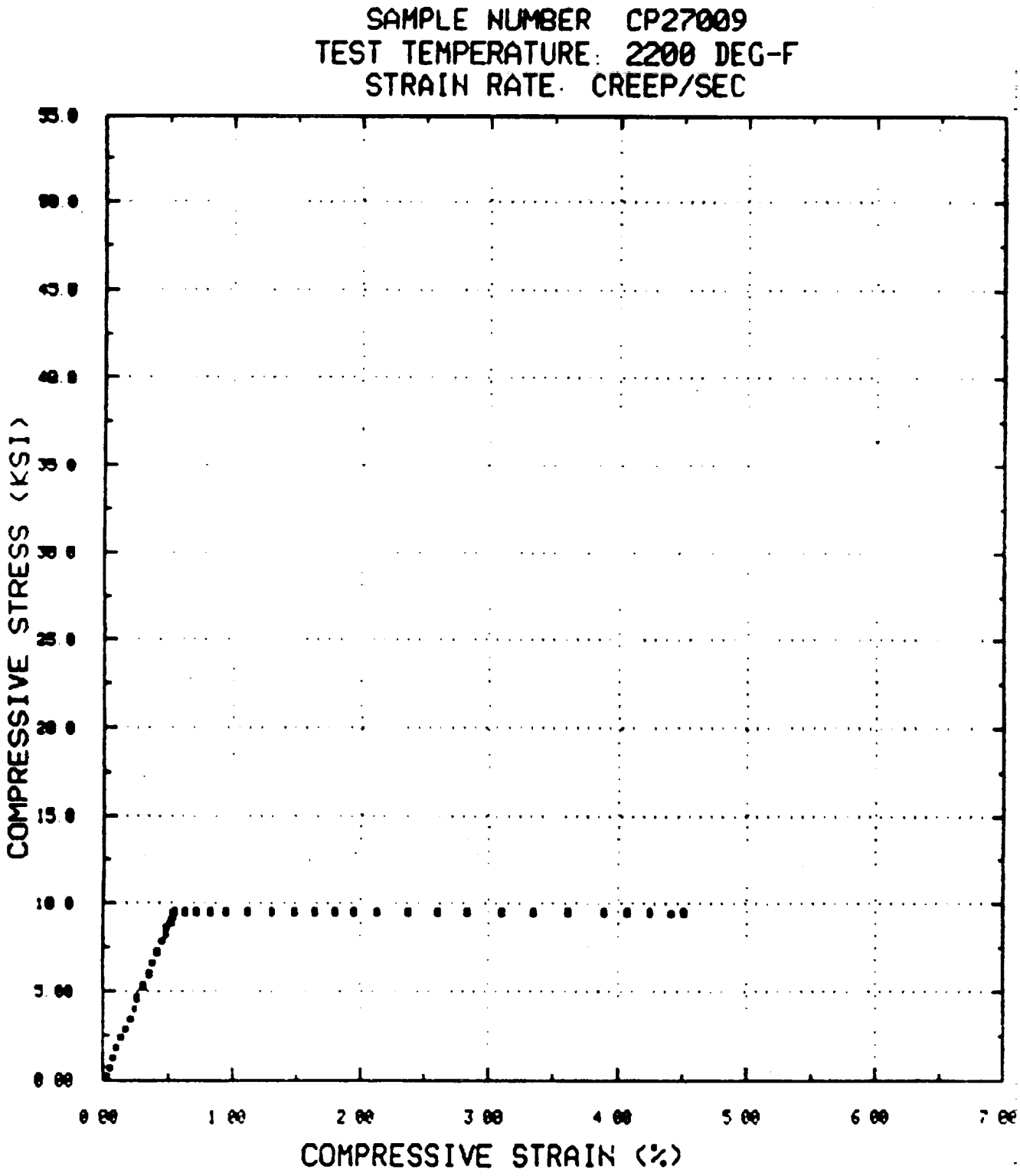

Figure E-24 Compression Creep Stress-Strain (2200°F)

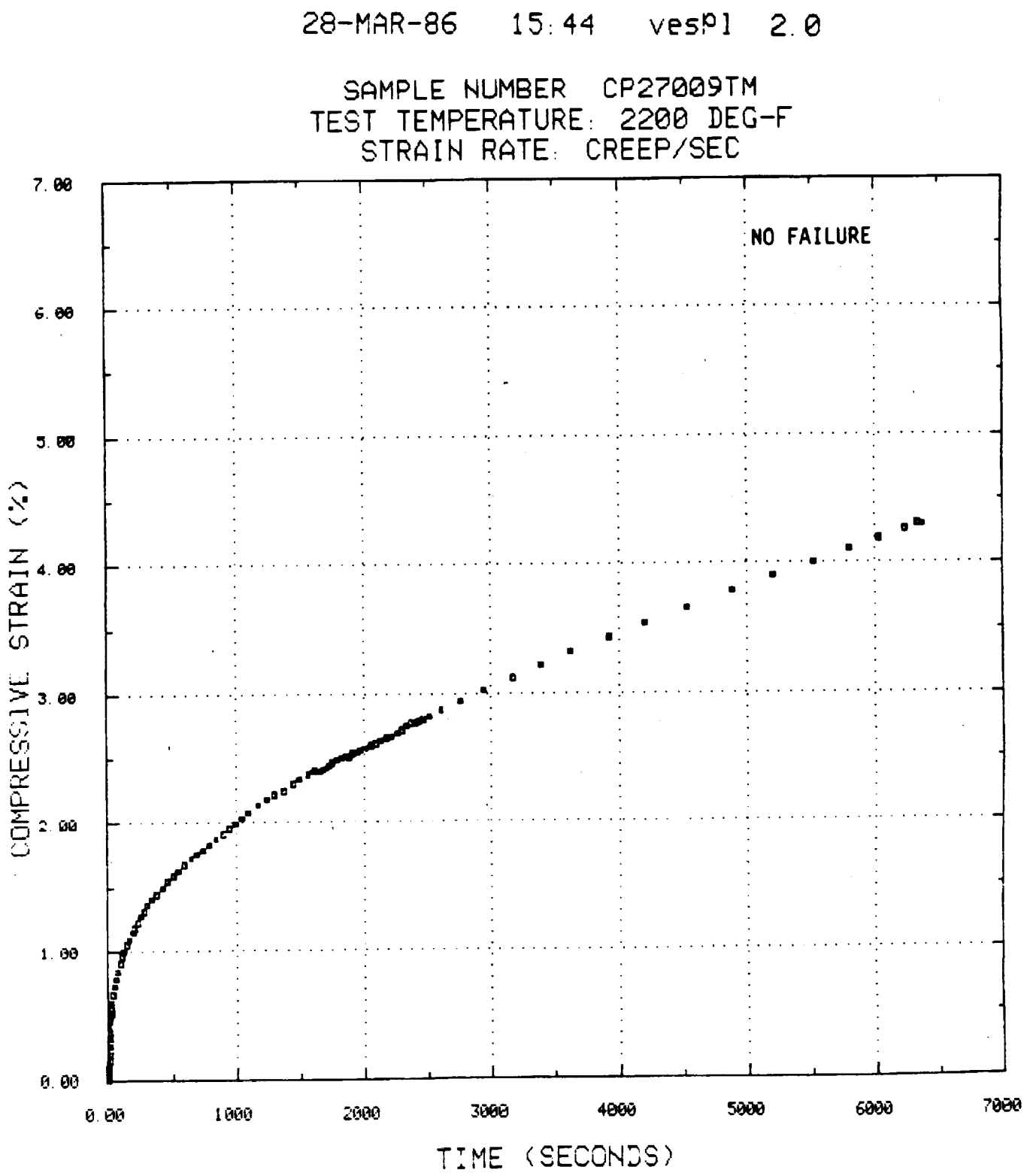

Figure E-25 Compression Creep Strain-Time (2200°F)

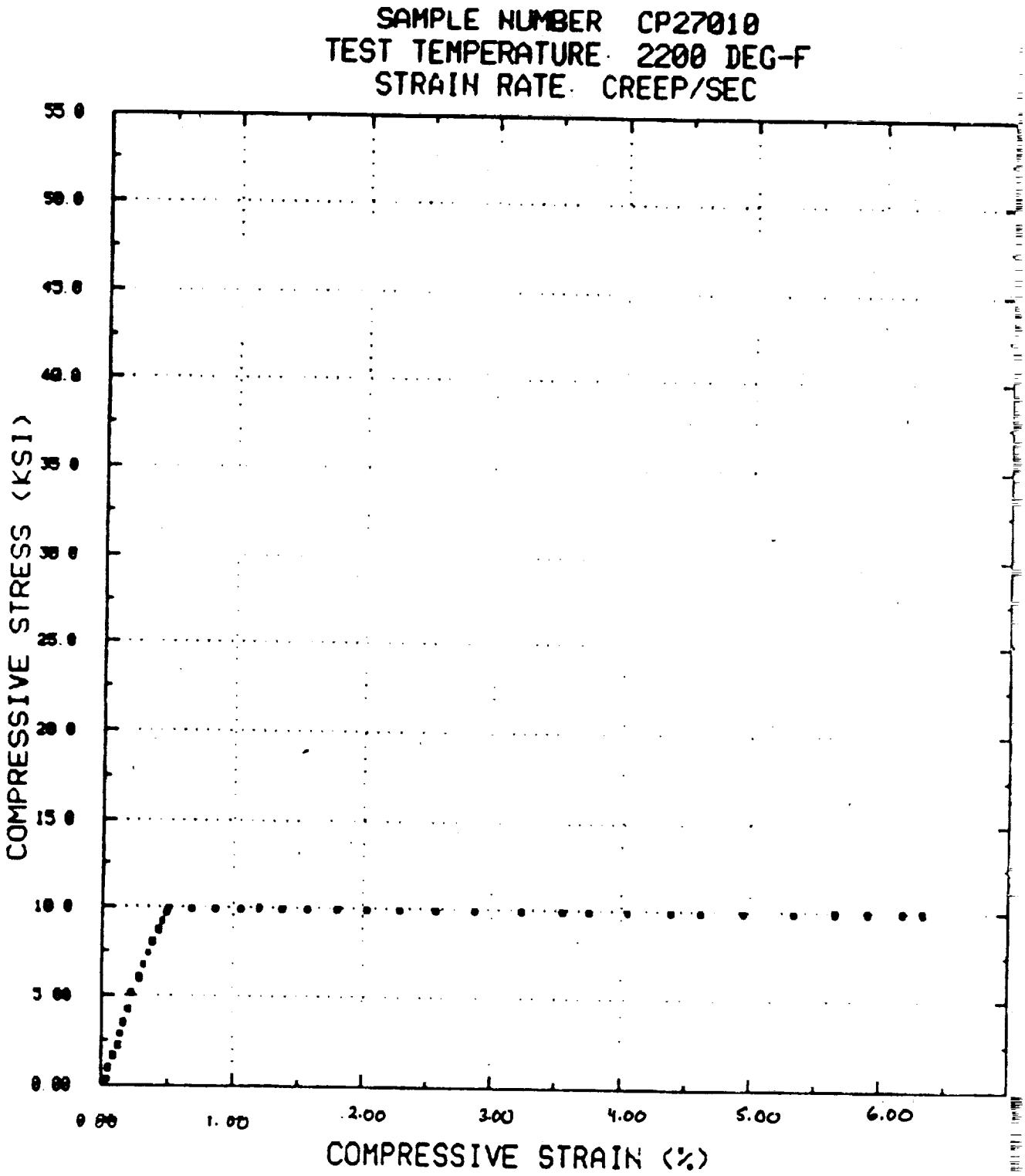

Figure E-26 Compression Creep Stress-Strain (2200°F)

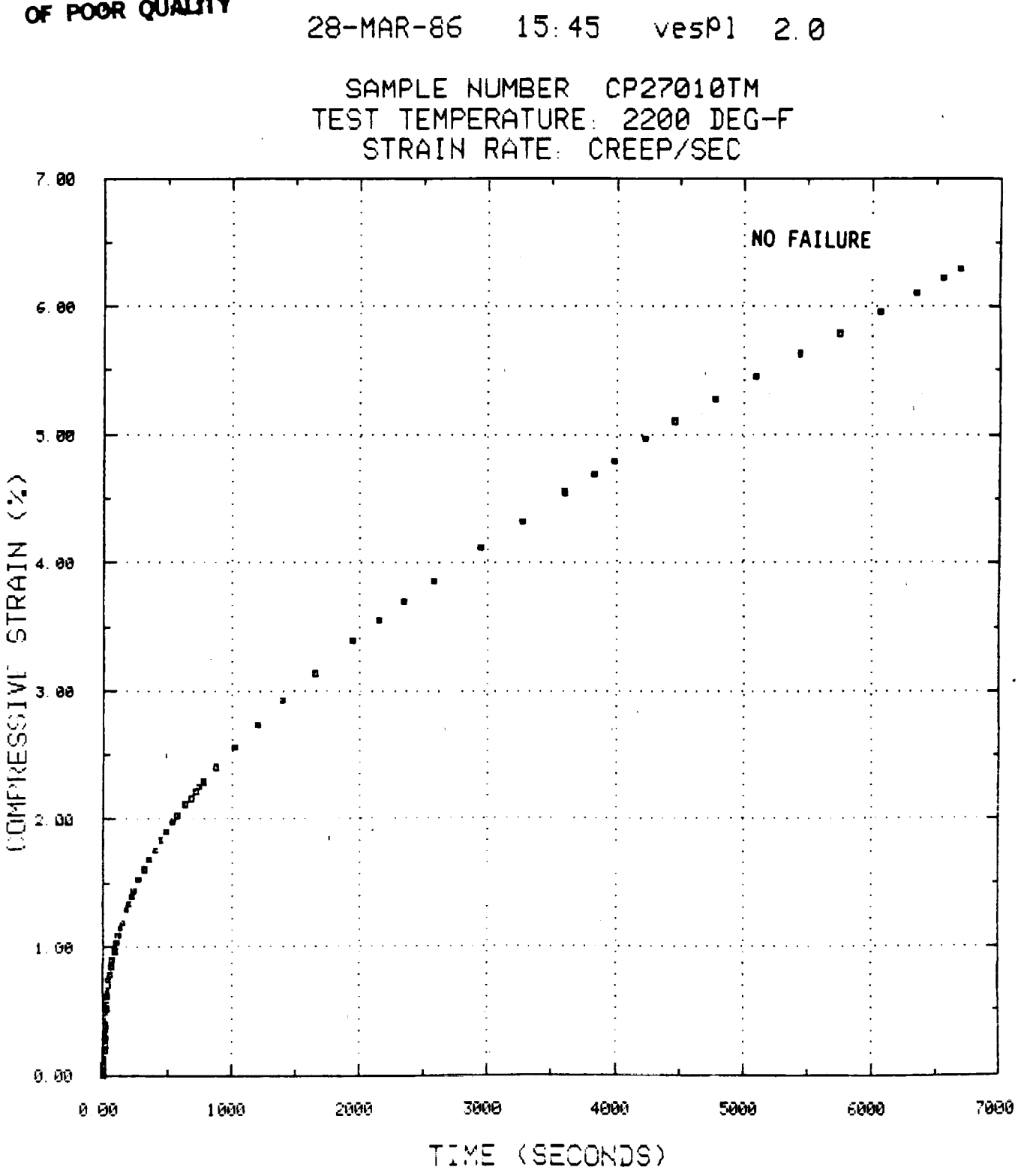

Figure E-27 Compression Creep Strain-Time (2200°F)

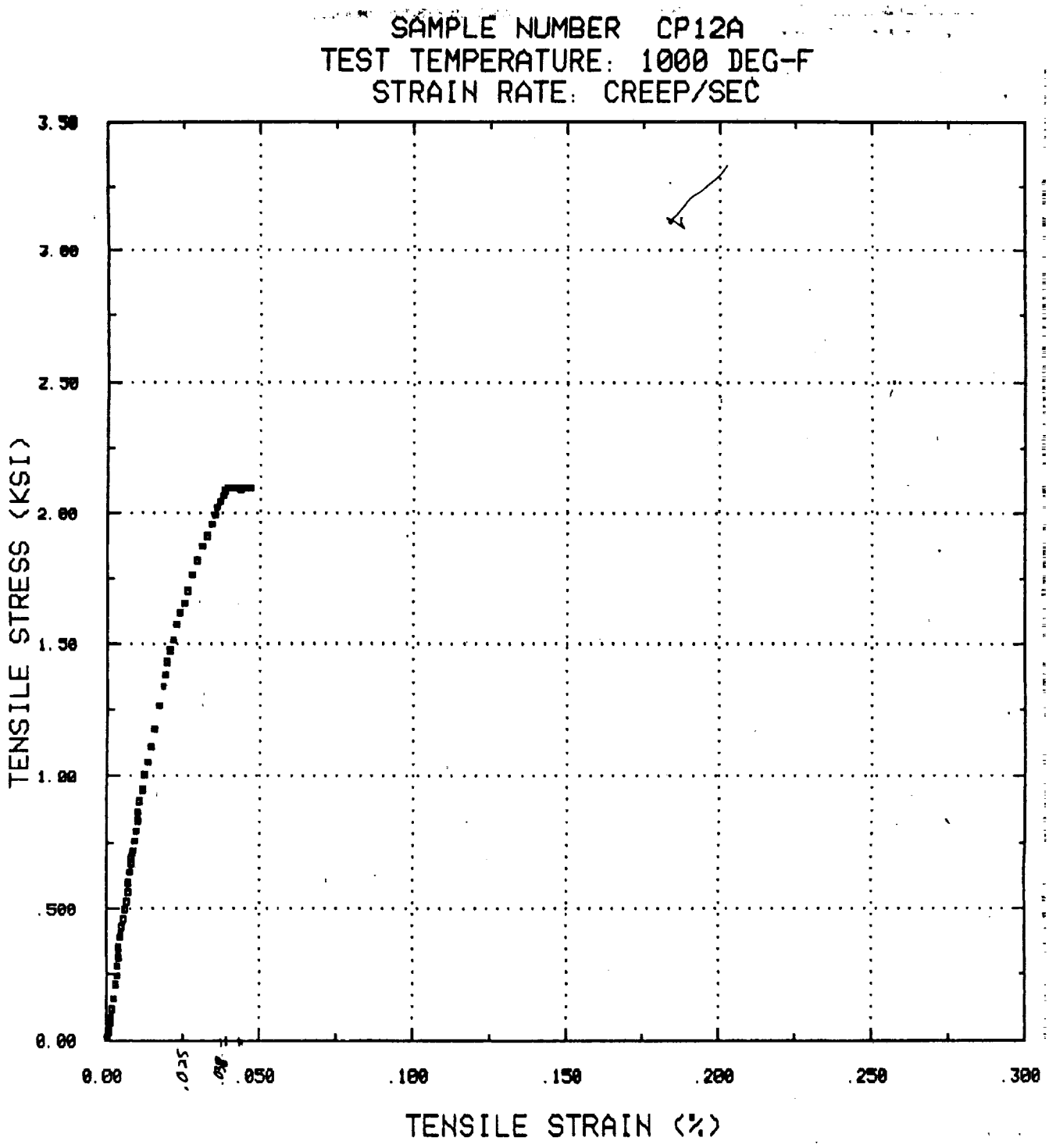

Figure E-28 Tension Creep Stress-Strain (1000°F)

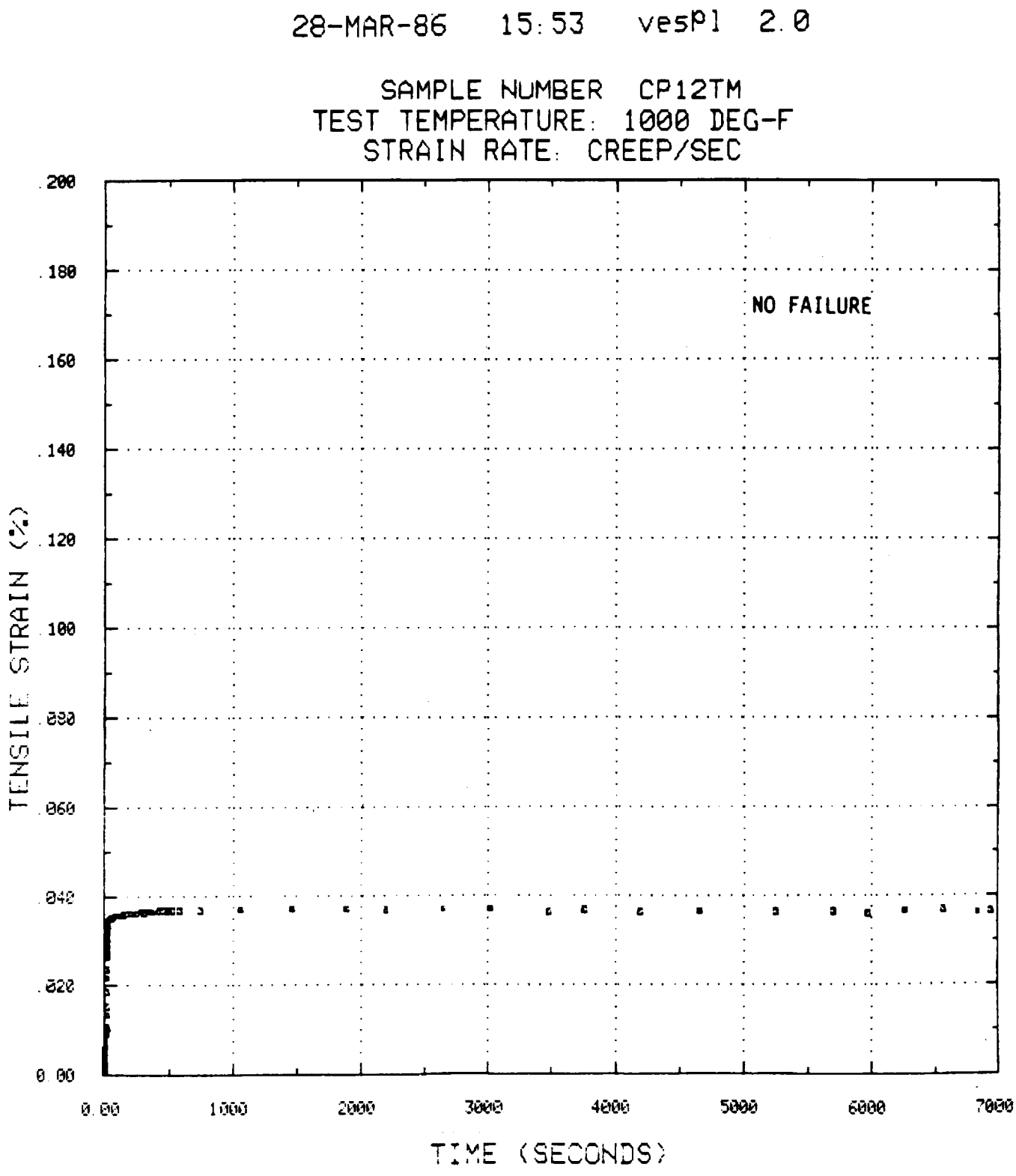

Figure E-29 Tension Creep Strain-Time (1000°F)

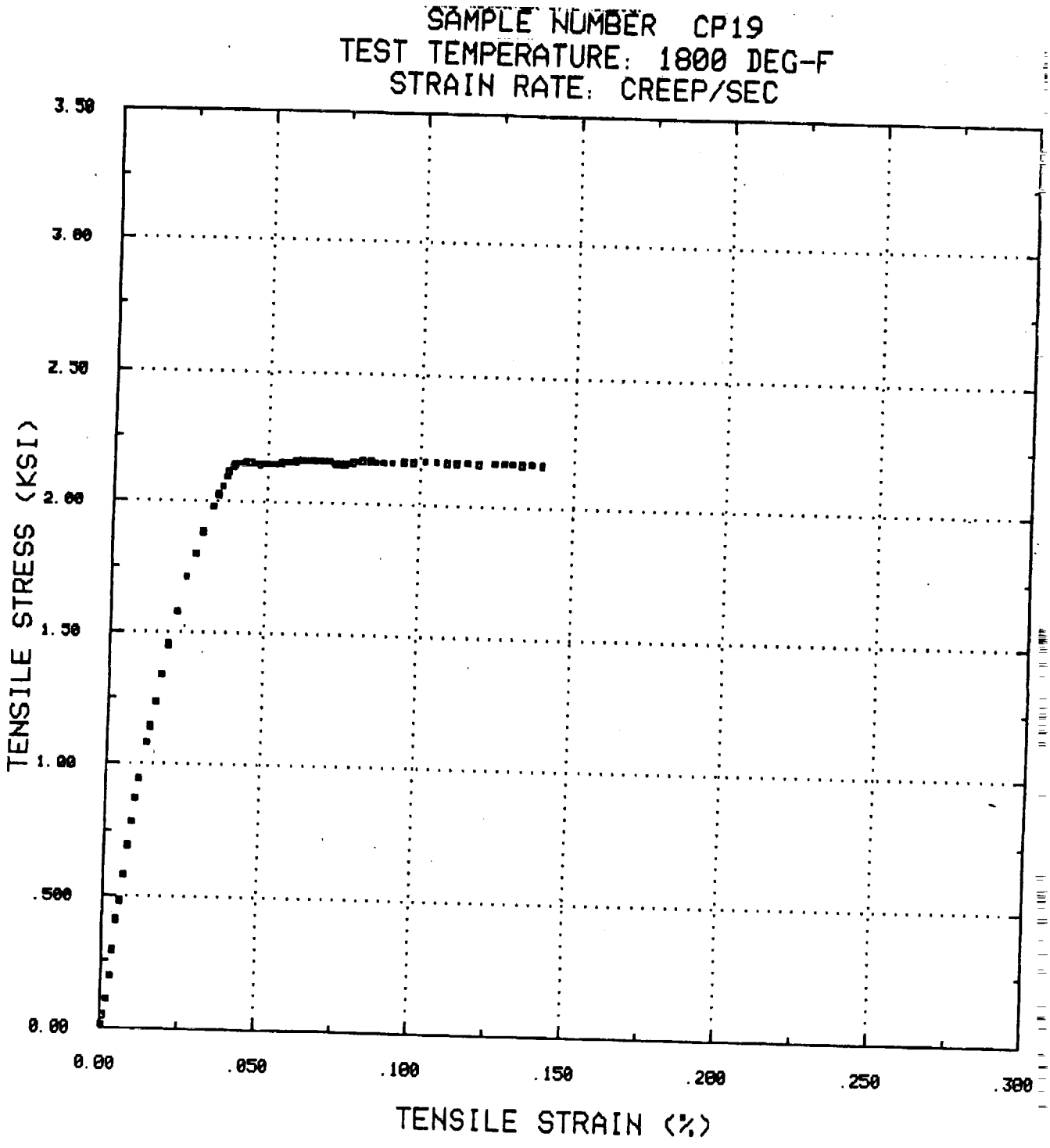

Figure E-30 Tension Creep Stress-Strain (1800°F)

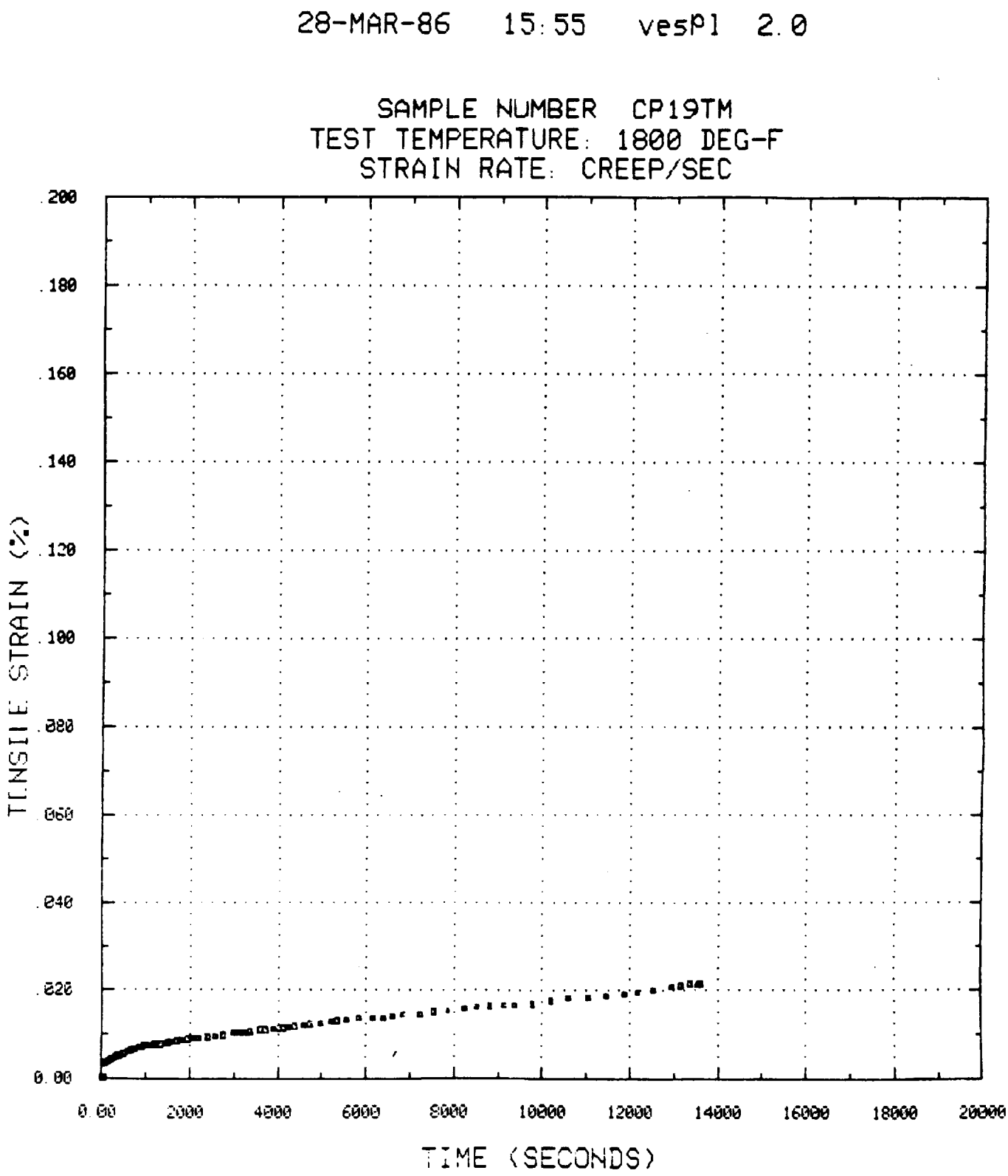

Figure E-31 Tension Creep Strain-Time (1800°F)

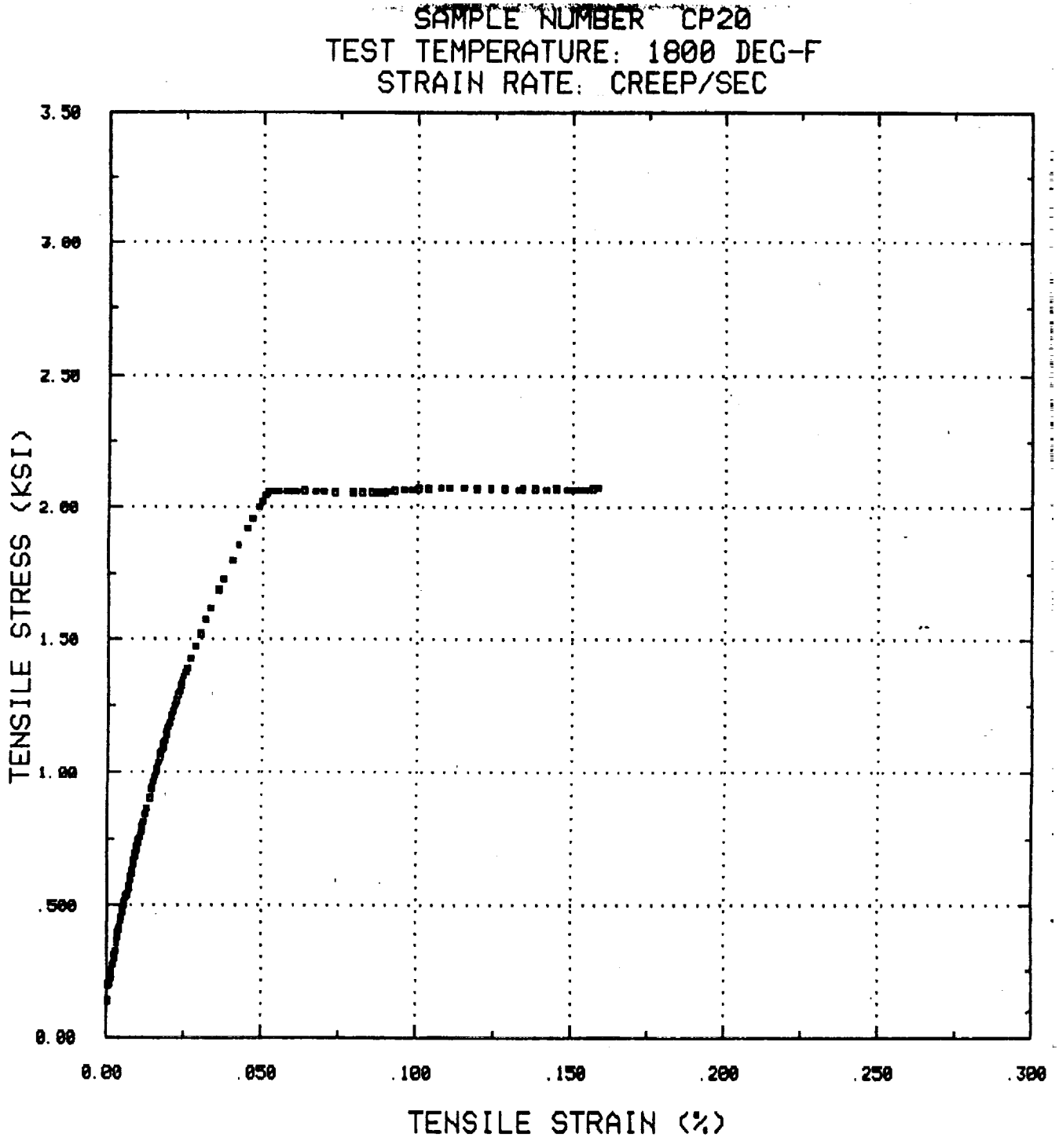

Figure E-32 Tension Creep Stress-Strain (1800°F)

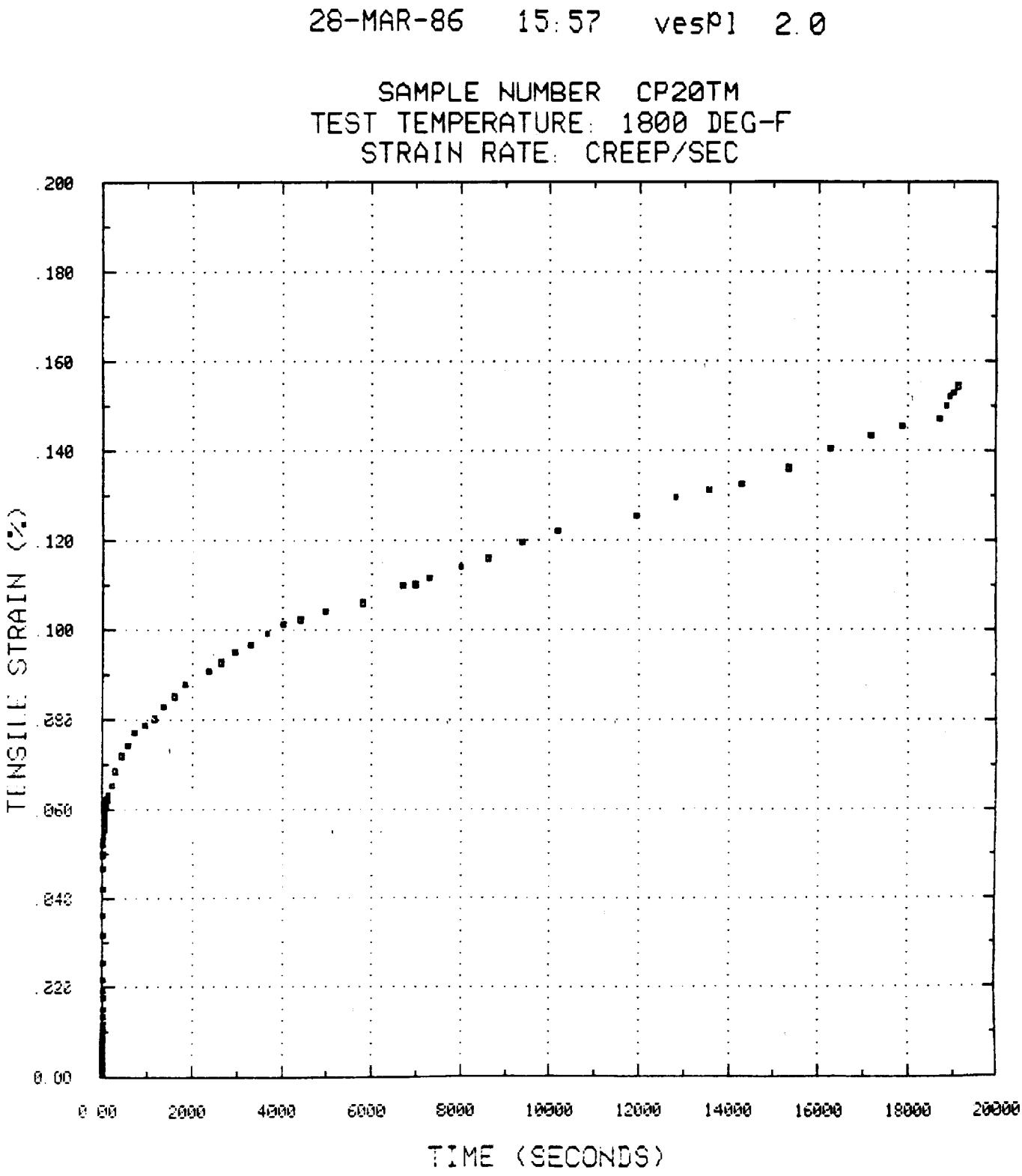

Figure E-33 Tension Creep Strain-Time (1800°F)

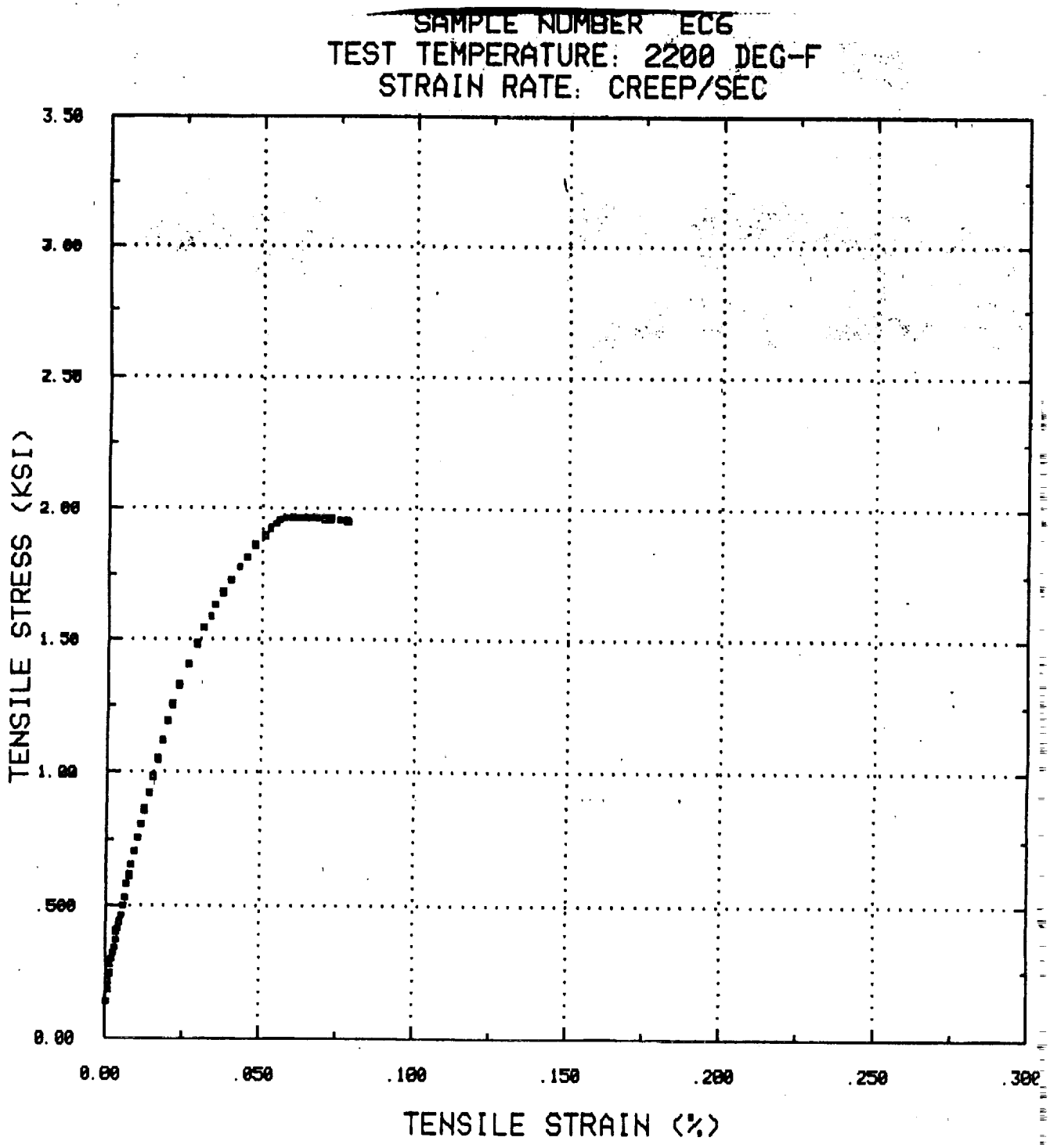

Figure E-34 Tension Creep Stress-Strain (2200°F)

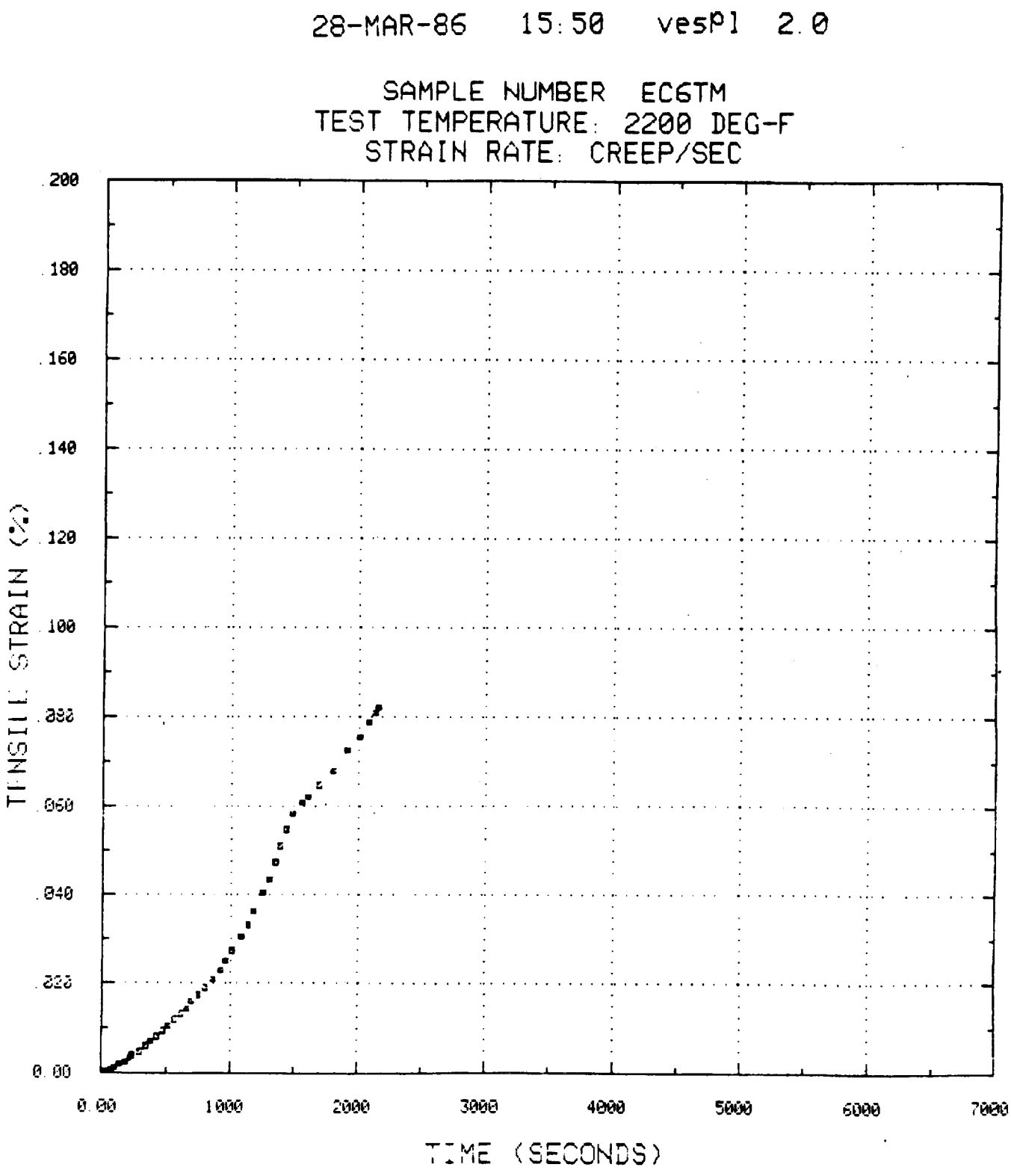

Figure E-35 Tension Creep Strain-Time (2200°F)

DISTRIBUTION LIST

NASA Scientific and Technical
Information Facility
Attn: Acquisition Branch
P.O. Box 8757
Baltimore Washington Inter. Airport
Baltimore, MD 21240

D. L. Alger (301-2)
NASA Lewis Research Center
21000 Brookpark Road
Cleveland, OH 44135

L. F. Aprigliano
D. Taylor Shipyard
R&D Center
Annapolis, MD 21402

M. M. Bailey (77-6)
NASA Lewis Research Center
21000 Brookpark Road
Cleveland, OH 44135

Michael Bak (5-16)
Williams International
P.O. Box 200
Walled Lake, MI 48088

H. Beale
Applied Coatings, Inc.
775 Kaderly Drive
Columbus, OH 43228

Robert Beck
Teledyne - CAE
1330 Laskey Road
Toledo, OH 43612

Biliyar N. Bhat (EH-23)
NASA Marshall Space
Flight Center
Huntsville, AL 35812

Donald H. Boone
University of California
Bldg. 62, Room 351
Berkeley, CA 94720

David Bott
Muscle Shouls Mineral Company
1202 East 2nd Street
Muscle Shoals, AL 35661

R. J. Bratton
Westinghouse Electric R&D
1310 Buelah Road
Pittsburgh, PA 15235

Sherman D. Brown
Chemical Engineering Dept.
University of Illinois
Urbana, IL 61801

Walter Bryzik (RGRD)
U.S. Army Tank-Auto. Command
Diesel Engine Research RMSTA
Warren, MI 48397

R. F. Bunshah
University of California
6532 Boelter Hall
Los Angeles, CA 90024

George C. Chang (MC 219)
Cleveland State University
Cleveland, OH 44115

Ted Chase
Elliot Support Services Division
of United Technologies Corporation
2001 West Belt Drive North
Houston, Texas 77043

Jerry Clifford
U.S. Army Applied Tech. Lab.
SAVDL-ATL-ATP
Fort Eustis, VA 23604

DISTRIBUTION LIST (cont'd)

Dave Clingman
Detroit Diesel Allison - GMC
Engineering Operations
Indianapolis, IN 46206

Arthur Cohn
E P R I
3412 Hillview Avenue
Palo Alto, CA 94303

Thomas A. Cruse
Southwest Research Institute
P.O. Box 28510
San Antonio, TX 78284

Keith Duframe
Battelle Labs.
Columbus, OH 43216

Mrityunjoy Dutta
U.S. Army AMSAV-EAS
4300 Goodfellow Blvd.
St. Louis, MO 63120

D. S. Engleby
Naval Air Rework Facility
Mail Drop 9, Code 017
Cherry Point, NC 28533

John Fairbanks (FE-22)
Department of Energy
Office of Fossil Energy
Washington, DC 20545

N. Geyer
AFWAL/MLLM
Wriaght Patterson AFB
Dayton, OH 45433

J. W. Glatz
NAPTC R&D Division
Naval Air Prop. Test Center
Trenton, NJ 08628

G. W. Goward
Coatings Technology Corp.
2 Commercial Street
Branford, CT 06405

M. A. Greenfield (RM)
NASA Headquarters
600 Independence Avenue
Washington, DC 20546

S. J. Grisaffe (49-1)
NASA Lewis Research Center
21000 Brookpark Road
Cleveland, OH 44135

D. K. Gupta
Pratt & Whitney Group
400 Main Street
East Hartford, CT 06108

William K. Halman
Temescal
2850 Seventh Street
Berkeley, CA 94710

D. Hanink
Detroit Diesel Allison-GMC
Engineering Operations
Indianapolis, IN 46206

Doug Harris
APS - Materials Inc.
153 Walbrook
Dayton, OH 45405

Harold Herman
Argonne National Lab.
9700 South Cass Avenue
Argonne, IL 60439

H. Herman (W-8)
Detroit Diesel Allison-GMC
P.O. Box 894
Indianapolis, IN 46206

M. Herman
Dept. of Materials Science
State Univ. of New York
Stonybrook, NY 11794

Frank Hermanek
Alloy Metals, Inc.
501 Executive Drive
Troy, MI 48084

R. Hillery (M-85)
General Electric Company
MPTL
Cincinnati, OH 45215

J. Stan Hilton
University of Dayton
300 College Park
Dayton, OH 45469

Richard R. Holmes (EH-43)
Marshall Space
Flight Center
Hunstville, AL 35812

Lulu Hsu
Solar Turbines, Inc.
2200 Pacific Highway
San Diego, CA 92138

Larry A. Junod
Allison Gas Turbine Division
P.O. Box 420, Plant 8-T12
Indianapolis, IN 46206

C. Kortovich
TRW Inc.
23355 Euclid Avenue
Cleveland, OH 44117

Propulsion Laboratory (302-2)
U.S. Army Res. & Tech. Lab.
21000 Brookpark Road
Cleveland, OH 44135

Sylvester Lee
AFWAL-MLTM
Wright Patterson AFB
Dayton, OH 45433

A. V. Levy
Lawrence Berkely Lab.
University of California
Berkely, CA 94720

C. H. Liebert (77-2)
NASA Lewis Research Center
21000 Brookpark Road
Cleveland, OH 44135

E. L. Long, Jr.
Oak Ridge National Lab.
P.O. Box X, Bldg. 4508
Oak Ridge, TN 37831

Frank N. Longo
Metco, Inc.
1101 Prospect Avenue
Westbury, L.I., NY 11590

DISTRIBUTION LIST (cont'd)

Richard Martin (9W-61)
Boeing Commercial Airplane Co.
P.O. Box 3707
Seattle, WA 98124

R. A. Miller (105-1)
NASA Lewis Research Center
21000 Brookpark Road
Cleveland, OH 44135

T. E. Mitchell
Case Western Reserve Univ.
10900 Euclid Avenue
Cleveland, OH 44106

S. Naik
AVCO-Lycoming Division
550 South Main Street
Stratford, CT 06497

Dr. J. A. Nesbitt (105-1)
NASA Lewis Research Center
21000 Brookpark Road
Cleveland, OH 44135

J. W. Patten
Cummins Engine Company
Box 3005
Columbus, IN 47202

Ronne D. Proch
Corning Glass Works
31501 Solon Road
Solon, OH 44139

R. J. Quentmeyer (500-220)
NASA Lewis Research Center
21000 Brookpark Road
Cleveland, OH 44135

Gopal Revanton
Deer & Company
3300 River Drive
Moline, IN 61265

David Rigney (D-83)
General Electric Company
Cincinnati, OH 45215

Joseph Scricca
AVCO-Lycoming Division
550 South Main Street
Stratford, CT 06497

Keith Sheffler
Pratt & Whitney Group
400 Main Street
East Hartford, CT 06108

T. P. Shyu
Caterpiller Tractor Company
100 N.E. Adams
Peoria, IL 61629

R. W. Soderquist (165-03)
Pratt & Whitney Group
400 Main Street
East Hartford, CT 06108

D. E. Sokolowski (49-7)
NASA Lewis Research Center
21000 Brookpark Road
Cleveland, OH 44135

C. A. Stearns (106-1)
NASA Lewis Research Center
21000 Brookpark Road
Cleveland, OH 44135

S. Stecura (105-1)
NASA Lewis Research Center
21000 Brookpark Road
Cleveland, OH 44135

T. E. Strangman
Garrett Turbine Engine Co.
111 South 24th Street
Phoenix, AZ 85034

T. N. Strom (23-2)
NASA Lewis Research Center
21000 Brookpark Road
Cleveland, OH 44135

T. A. Taylor
Linde Division
Union Carbide Corporation
Indianapolis, IN 46224

Robert P. Tolokan
Brunswick Corporation
2000 Brunswick Lane
DeLand, FL 32724

F. C. Toriz
Rolls Royce, Inc.
1985 Phoenix Blvd.
Atlanta, GA 30349

Donald Whicker
GM Research Laboratory
GM Technical Center
Warren, MI 48090

Volker Wilms
Chromalloy R&T
Chromalloy Amer. Corp.
Orangeburg, NY 10962

I. Zaplatynsky (105-1)
NASA Lewis Research Center
21000 Brookpark Road
Cleveland, OH 44135